UNIVERSITY OF CALIFORNIA SAN DIEGO

Structural and mechanistic studies of the proline-rich domain of ALIX

A Dissertation submitted in partial satisfaction of the requirements
for the degree Doctor of Philosophy

in

Chemistry

by

Ruben D. Elias

Committee in charge:

Professor Lalit Deshmukh, Chair
Professor Joseph Adams
Professor Itay Budin
Professor Patricia Jennings
Professor Andrew Kummel

2023

The Dissertation of Ruben D. Elias is approved, and it is acceptable in quality and form for publication on microfilm and electronically.

University of California San Diego

2023

DEDICATION

The whole of this work is dedicated to Samantha. You are my best friend and role model. You are the color and texture which paints my worldview. Whatever worries might come, in whichever corner of the world we might find ourselves, will fuzz and fade into the background so long as you are my focus.

EPIGRAPH

Te vi sin que me vieras
Te hable sin que me oyeras
Y sin embargo sigues
Unida a mi existencia
Y si vivo cien años
Cien años pienso en ti

-Pedro Infante, on his relationship to proteins

TABLE OF CONTENTS

LIST OF FIGURES

LIST OF TABLES

LIST OF SUPPLEMENTARY FILES

Elias_Lists of all peptides identified in LC-MSMS analyses.xlsx

Tables listing all identified peptides in LC-MS/MS analyses used for Figures 3.3.2, 3.3.3, 3.4 C. For experimental details, see section 3.9.5 and Table 3.2

Elias_Src-mediated dissolution of ALIX condensates monitored by fluorescence microscopy.mp4

Timelapse of dissolution of $ALIX^{Strep}_{1\text{-}868*}$ (50 μM) condensates in the presence of Src (5 μM) and ATP (5 mM). Microscopy images of the condensates were collected every min (30min total). Video playback is 10 images/s. Buffer and experimental conditions were as follows: 50mM Tris, pH 7.5, 50 mM NaCl, 5 mM $MgCl_2$, 2 mM DTT, 5% (w/v) PEG-4000, and 0.02 mg/mL Streptavidin Alexa-Fluor488, at room temperature.

Elias_Dissolution of ALIX-PRD condensates monitored by TIRF microscopy.mp4

Condensates of ATTO488-labeled $PRD^{Strep}_{703\text{-}868*}$(100 μM) were incubated with Src (10 μM) and ATP (5 mM). TIRF images of the condensates were collected every 15 s (80 min total). Video playback is sped up 450 times. Buffer and experimental conditions were as follows: 50 mM Tris, pH 7.5, 50 mM NaCl, 5 mM $MgCl_2$, 2 mM DTT, and 5% (w/v) PEG-4000, at room temperature.

ACKNOWLEDGEMENTS

I would like to acknowledge Professor Lalit Deshmukh for his support as the chair of my committee. His support, insight, and guidance have been paramount to any success I have seen throughout my years at UC San Diego. To my fellow lab members, past and present: Dr. Bhargavi Ramaraju, Spencer Nelson, Aman Shihora, Chenrong Yu, and John Brown- I am truly thankful that I have had the opportunity to know each of you and am nothing short of ecstatic for the bright futures that lay ahead of each of you. To my lab neighbors Hyesoo Kim and Israel Juarez-Contreras, I admire and am grateful for the warmth and friendliness you showed me daily.

I could not have persisted through grad school without support from my family. Josh and Sarah, whose genuine care has provided a respite during difficult stretches of graduate school; Ronnie and Mario, who place me on a pedestal too high, and whose loving outstretched arms wore me to a mutually grandiose affection; my siblings Nicole, who has unknowingly shown me how to be accepting of myself, and Lydia, who I attempt to mimic whenever I feel meek, and the wonderful nieces and nephews which they have brought into my life, who remind me the indescribable beauty it is to simply exist; and my parents, who have exemplified what it means to be truly dedicated in compassion to the needs of the local community.

I am also appreciative of those whose encouragement led me to my current position. Dr. Scott Herrick, who showed me Kazuhiko Kinosita's video of ATPase rotation in my first biology course at Riverside Community College, sparking my interest in biophysics; Dr. Russ Hille, who welcomed me into his lab at UC Riverside as an unseasoned undergraduate; Dr. Joeseph Genereux who welcomed me into his lab at UC Riverside as a slightly more seasoned undergraduate, and who continues to be a source of guidance and optmism; Dr. Ernst Martinez and Rebecca Brown who supported me through the MARC U-STAR program at UC Riverside; and lastly and most

unlikely Dr. Brian Zid, who came across my application for an entirely different program at UC San Diego and lured me instead towards the chemistry department.

Chapter 2, in full, is a reprint of the material as it appears in: Elias, R. D., Ma, W., Ghirlando, R., Schwieters, C. D., Reddy, V. S., and Deshmukh, L. (2020) Proline-rich domain of human ALIX contains multiple TSG101-UEV interaction sites and forms phosphorylation-mediated reversible amyloids. Proc Natl Acad Sci U S A, 117 (39), 24274-24284. The dissertation author was the primary investigator and author of this paper.

Chapter 3, in full, is a reprint of the material as it appears in: Elias, R. D., Ramaraju, B., and Deshmukh, L. (2021) Mechanistic roles of tyrosine phosphorylation in reversible amyloids, autoinhibition, and endosomal membrane association of ALIX. J Biol Chem, 297 (5), 101328. The dissertation author was the primary investigator and author of this paper.

Chapter 4, in part, has been submitted for publication of the material as it may appear in: Elias, R. D., Zhu, Y., Su, Q., Ghirlando, R., Zhang, J., and Deshmukh, L. (2023) Reversible phase separation of ESCRT-protein ALIX through tyrosine phosphorylation. (Accepted). The dissertation author was the primary researcher and author of this paper.

VITA

2018 Bachelor of Science in Biochemistry, University of California Riverside

2020 Master of Science in Chemistry, University of California San Diego

2023 Doctor of Philosophy in Chemistry, University of California San Diego

PUBLICATIONS

Elias, R. D., Ma, W., Ghirlando, R., Schwieters, C. D., Reddy, V. S., and Deshmukh, L. (2020) Proline-rich domain of human ALIX contains multiple TSG101-UEV interaction sites and forms phosphorylation-mediated reversible amyloids. Proc Natl Acad Sci U S A, 117 (39), 24274-24284.

Elias, R. D., Ramaraju, B., Deshmukh, L. (2021) Mechanistic roles of tyrosine phosphorylation in reversible amyloids, autoinhibition, and endosomal membrane association of ALIX. J Biol Chem, 297 (5), 101328.

Elias, R. D., Zhu, Y., Su, Q., Ghirlando, R., Zhang, J., and Deshmukh, L. (2023) Reversible phase separation of ESCRT-protein ALIX through tyrosine phosphorylation. Sci. Adv. (Accepted)

Elias, R. D.; Shihora, A.; Hammond, J.; Ghirlando, R.; Deshmukh, L. (2023) ALS variants of annexin A11's proline-rich domain impair its S100A6-mediated fibril dissolution. (Under revision)

ABSTRACT OF THE DISSERTATION

Structural and mechanistic studies of the proline-rich domain of ALX

by

Ruben D. Elias

Doctor of Philosophy in Chemistry

University of California San Diego, 2023

Professor Lalit Deshmukh, Chair

The biological roles and functional utility of disorder within proteins is poorly understood relative to globular domains despite the predicted presence of disorder within over 50% of the human proteome. Disorder is generally characterized to facilitate protein-protein interactions; however many biophysical investigations employ only a small fragment from a disordered region to characterize a given biological interaction, likely overlooking any possible contributions from the remainder of the disordered region. In this respect, this dissertation discusses biophysical characterization and mechanistic insights into the functions of the intact proline-rich domain belonging to ALIX, a central ESCRT component protein critical to the fundamental process of cell division.

Chapter 1 provides perspective over the biological roles of disordered proteins and proline-rich domains, and relevant open questions surrounding the molecular biology of ALIX. Chapter 2 begins an exploration of the ALIX proline-rich domain, describing its multifaceted interaction with partner TSG101-UEV domain, and its novel formation of phosphorylation-reversible amyloid. Chapter 3 continues with a characterization of the phosphorylation-dependent intramolecular association between ALIX Bro1 and proline-rich domains to modulate membrane binding and spatial localization of ALIX. Chapter 4 then concludes the present work on ALIX by characterizing the intact protein, focusing on the contributions of the proline-rich domain towards ALIX phosphorylation-reversible phase separation, and regulation of cytokinetic abscission machinery CHMP4B and CHMP4C. Altogether the observations made here display the propensity of the proline-rich domain of ALIX to mediate the formation of phosphorylation-reversible amyloids and condensates, and rationally propose biological functions and molecular mechanisms in which such behavior is utilized.

Chapter 1: Introduction

1.1 Disordered proteins

A foundational tenet of molecular biology is the causal link between the three-dimensional structure of a protein and its function. However, outside of this paradigm exists a large set of biologically active proteins with either minimal structural order, termed intrinsically disordered proteins (IDPs), or who are composed of both structured and intrinsically disordered regions (IDRs) (1). The amount of disorder in a given proteome is generally positively correlated with organism complexity (2-4), with an estimated >50% of the human proteome containing at least on extended IDR (5,6). IDPs and IDRs are broadly implicated in mediating complex signaling networks (7-11), where their structural plasticity facilitates protein-protein interactions (12) and complex regulation through posttranslational modification (13).

Dysfunction of IDPs and IDRs, and the consequent dysregulation of their respective signaling networks, is a common feature in the development and progression of many cancers and neurodegenerative disease (9,14-17). Yet, our overall understanding of IDP and IDR function lags behind that of structured proteins, as their inherent lack of a defined three-dimensional structure excludes them from most modern technical advances in structural biology. In this lens, disordered proteins represent underutilized wells of information towards our overall understanding of diverse pathologies and cellular functions. In this dissertation, efforts are focused on studying a single type of IDR termed proline-rich domains.

1.2 Proline-rich domains

While IDRs do not face the evolutionary pressure to maintain a globular fold and thus evolve at a faster rate than structured domains (18,19), proline is among the most frequent and most conserved residues found in disordered regions (20). Proline-rich domains (PRDs) are a common flavor of IDR, loosely defined as having ≥ 30% proline abundance and containing multiple short, repeating proline-rich motifs (21,22). Proline is the most disorder-promoting amino acid (23,24), and polyproline tracts favor the formation of rigid, extended loops termed polyproline II helices (25,26). As interactions between ordered and disordered proteins are primarily driven by hydrophobic contacts (25), the combined hydrophobic character of proline and conformational rigidity of proline-rich motifs define their propensity to act as signal recognition elements for common signaling modules such as SH3, WW, and UEV domains (11,21,27,28). The interest of this body of work centers around ALIX and its proline-rich domain, who functions as key component in cell division and cell proliferation networks, and whose depletion leads to incomplete cytokinesis and cell death (29,30).

1.3 ALIX

ALIX (Apoptosis-linked gene-2 interacting protein X, or PDCD6IP) is a multifunctional protein involved in membrane remodeling processes such as endocytosis (31), multivesicular body and exosome biogenesis (32-35), membrane repair (36-38), enveloped virus budding (39,40), and cytokinetic abscission (29,41-43). These processes are carried out by the evolutionarily conserved ESCRT pathway, composed of five distinct complexes termed ESCRT-0, -I, -II, -III, and the AAA ATPase Vps4 (44). In brief, ESCRTs -0, -I, and -II localize and recruit cargo and downstream ESCRT machinery to the affected phospholipid membrane, while ESCRT-III and VPS4 constrict

and sever the membrane. The propensity for ALIX to function through the ESCRT pathway in a wide spectrum of cellular process stems from its domain architecture (45,46).

ALIX consists of three domains: structured N-terminal and central domains, respectively termed Bro1 and V, and an unstructured C-terminal PRD (47). The Bro1 domain localizes to late endosomal membranes through interaction with the phospholipid LBPA (48), and binds and activates ESCRT-III machinery, an interaction which defines an ESCRT-I and -II-independent arm of ESCRT initiation (49,50). The V domain recruits ubiquitylated cargoes (51,52) and a consensus motif YPXnL (where X is any amino acid and n=1-3) found in endogenous ESCRT-associated proteins and exogenous retroviral Gag proteins (34,53,54). It can be summarized then that both the Bro1 and V domains drive the spatial localization of ALIX, downstream ESCRT factors, and cargoes, however the function of the C-terminal PRD appears more complex.

Through its multiple proline-rich motifs, ALIX-PRD interacts with ESCRT-I machinery, calcium signaling proteins like ALG2, and multiple ubiquitous signaling modules such as SH3 and WW domains (21,55,56). ALIX-PRD is also implicated as an autoregulatory element, controlling the activity of ALIX by mediating an autoinhibited conformation (57-60) and directing ALIX multimerization (61,62). Multiple reports have observed that the phosphorylation of ALIX-PRD defines a change in activity, localization, binding interactions, and function of ALIX (56,63,64). Thus, the functional complexity of ALIX appears to be derived from its C-terminal PRD, however molecular details of how ALIX-PRD mediates these activities are sparse.

1.4 Concluding remarks

A molecular comprehension of protein function, down to the atomic level, is critical towards the complete understanding of disease pathology and production of effective therapies. The aim of this body of work is to provide molecular mechanisms for observed biological

phenomena and functions associated with the disordered PRD of ALIX. As intrinsically disordered proteins are refractory to many conventional structural and biophysical techniques, solution-state nuclear magnetic resonance (NMR), which excels at characterizing disordered proteins (65), was the workhorse technique utilized here. Throughout the investigations presented here, we uncover novel behaviors of ALIX mediated by its PRD, specifically the wholly reversible formation of phase-separated condensates and solid amyloid fibrils controlled by posttranslational modification, namely tyrosine phosphorylation. The dissolution of amyloid fibrils is particularly striking, as the sheer number of intermolecular interactions between individual monomer units which compose the amyloid fold has been demonstrated to impart a high degree of rigidity and stability to the superstructure (66,67). It should be noted, however, that ALIX has not yet been observed in vivo to utilize the amyloid fold during the course of its routine biological functions. However, the work presented here provides the foundations to consider and explore such a possibility.

Similarly, these works lay out a framework to discover similarly labile or reversible amyloids. As such, further investigation within the Deshmukh group have identified and characterized a mechanism to dissolve amyloid fibrils derived from the PRD of annexin A11 (68). Similarity in primary sequence between the ALIX and annexin A11 PRDs suggests the existence of these behaviors in other similarly proline- and tyrosine rich IDRs such as that found in annexin A7. We anticipate further investigation into such IDRs will reveal a new family of proteins with the propensity to form labile, reversible, and functional amyloids and condensates, and define the molecular characteristics which encode for such behaviors.

1.5 References

1. Wright, P. E., and Dyson, H. J. (1999) Intrinsically unstructured proteins: re-assessing the protein structure-function paradigm. J Mol Biol 293, 321-331

2. Ward, J. J., Sodhi, J. S., McGuffin, L. J., Buxton, B. F., and Jones, D. T. (2004) Prediction and functional analysis of native disorder in proteins from the three kingdoms of life. J Mol Biol 337, 635-645

3. Schad, E., Tompa, P., and Hegyi, H. (2011) The relationship between proteome size, structural disorder and organism complexity. Genome Biol 12, R120

4. Gao, C., Ma, C., Wang, H., Zhong, H., Zang, J., Zhong, R., He, F., and Yang, D. (2021) Intrinsic disorder in protein domains contributes to both organism complexity and clade-specific functions. Sci Rep 11, 2985

5. Deiana, A., Forcelloni, S., Porrello, A., and Giansanti, A. (2019) Intrinsically disordered proteins and structured proteins with intrinsically disordered regions have different functional roles in the cell. PLoS One 14, e0217889

6. Niklas, K. J., Dunker, A. K., and Yruela, I. (2018) The evolutionary origins of cell type diversification and the role of intrinsically disordered proteins. J Exp Bot 69, 1437-1446

7. Uversky, V. N., Oldfield, C. J., and Dunker, A. K. (2005) Showing your ID: intrinsic disorder as an ID for recognition, regulation and cell signaling. J Mol Recognit 18, 343-384

8. Brodsky, S., Jana, T., Mittelman, K., Chapal, M., Kumar, D. K., Carmi, M., and Barkai, N. (2020) Intrinsically Disordered Regions Direct Transcription Factor In Vivo Binding Specificity. Mol Cell 79, 459-471 e454

9. Iakoucheva, L. M., Brown, C. J., Lawson, J. D., Obradovic, Z., and Dunker, A. K. (2002) Intrinsic disorder in cell-signaling and cancer-associated proteins. J Mol Biol 323, 573-584

10. Bondos, S. E., Dunker, A. K., and Uversky, V. N. (2022) Intrinsically disordered proteins play diverse roles in cell signaling. Cell Commun Signal 20, 20

11. Wright, P. E., and Dyson, H. J. (2015) Intrinsically disordered proteins in cellular signalling and regulation. Nat Rev Mol Cell Biol 16, 18-29

12. Seoane, B., and Carbone, A. (2021) The complexity of protein interactions unravelled from structural disorder. PLoS Comput Biol 17, e1008546

13. Pejaver, V., Hsu, W. L., Xin, F., Dunker, A. K., Uversky, V. N., and Radivojac, P. (2014) The structural and functional signatures of proteins that undergo multiple events of post-translational modification. Protein Sci 23, 1077-1093

14. Uversky, V. N., Dave, V., Iakoucheva, L. M., Malaney, P., Metallo, S. J., Pathak, R. R., and Joerger, A. C. (2014) Pathological unfoldomics of uncontrolled chaos: intrinsically disordered proteins and human diseases. Chem Rev 114, 6844-6879

15. Meszaros, B., Hajdu-Soltesz, B., Zeke, A., and Dosztanyi, Z. (2021) Mutations of Intrinsically Disordered Protein Regions Can Drive Cancer but Lack Therapeutic Strategies. Biomolecules 11

16. Santamaria, N., Alhothali, M., Alfonso, M. H., Breydo, L., and Uversky, V. N. (2017) Intrinsic disorder in proteins involved in amyotrophic lateral sclerosis. Cell Mol Life Sci 74, 1297-1318

17. Uversky, V. N. (2015) Intrinsically disordered proteins and their (disordered) proteomes in neurodegenerative disorders. Front Aging Neurosci 7, 18

18. Forcelloni, S., and Giansanti, A. (2020) Evolutionary Forces and Codon Bias in Different Flavors of Intrinsic Disorder in the Human Proteome. J Mol Evol 88, 164-178

19. Ahrens, J. B., Nunez-Castilla, J., and Siltberg-Liberles, J. (2017) Evolution of intrinsic disorder in eukaryotic proteins. Cell Mol Life Sci 74, 3163-3174

20. Brown, C. J., Johnson, A. K., and Daughdrill, G. W. (2010) Comparing models of evolution for ordered and disordered proteins. Mol Biol Evol 27, 609-621

21. Ren, X., and Hurley, J. H. (2011) Proline-rich regions and motifs in trafficking: from ESCRT interaction to viral exploitation. Traffic 12, 1282-1290

22. Morgan, A. A., and Rubenstein, E. (2013) Proline: the distribution, frequency, positioning, and common functional roles of proline and polyproline sequences in the human proteome. PLoS One 8, e53785

23. Campen, A., Williams, R. M., Brown, C. J., Meng, J., Uversky, V. N., and Dunker, A. K. (2008) TOP-IDP-scale: a new amino acid scale measuring propensity for intrinsic disorder. Protein Pept Lett 15, 956-963

24. Williams, R. M., Obradovi, Z., Mathura, V., Braun, W., Garner, E. C., Young, J., Takayama, S., Brown, C. J., and Dunker, A. K. (2001) The protein non-folding problem: amino acid determinants of intrinsic order and disorder. Pac Symp Biocomput, 89-100

25. Gunasekaran, K., Tsai, C. J., and Nussinov, R. (2004) Analysis of ordered and disordered protein complexes reveals structural features discriminating between stable and unstable monomers. J Mol Biol 341, 1327-1341

26. Williamson, M. P. (1994) The structure and function of proline-rich regions in proteins. Biochem J 297 (Pt 2), 249-260

27. Adzhubei, A. A., Sternberg, M. J., and Makarov, A. A. (2013) Polyproline-II helix in proteins: structure and function. J Mol Biol 425, 2100-2132

28. Zarrinpar, A., Bhattacharyya, R. P., and Lim, W. A. (2003) The structure and function of proline recognition domains. Sci STKE 2003, RE8

29. Morita, E., Sandrin, V., Chung, H. Y., Morham, S. G., Gygi, S. P., Rodesch, C. K., and Sundquist, W. I. (2007) Human ESCRT and ALIX proteins interact with proteins of the midbody and function in cytokinesis. EMBO J 26, 4215-4227

30. Christ, L., Wenzel, E. M., Liestøl, K., Raiborg, C., Campsteijn, C., and Stenmark, H. (2016) ALIX and ESCRT-I/II function as parallel ESCRT-III recruiters in cytokinetic abscission. Journal of Cell Biology 212, 499-513

31. Laporte, M. H., Chi, K. I., Caudal, L. C., Zhao, N., Schwarz, Y., Rolland, M., Martinez-Hernandez, J., Martineau, M., Chatellard, C., Denarier, E., Mercier, V., Lemaitre, F., Blot, B., Moutaux, E., Cazorla, M., Perrais, D., Lante, F., Bruns, D., Fraboulet, S., Hemming, F. J., Kirchhoff, F., and Sadoul, R. (2022) Alix is required for activity-dependent bulk endocytosis at brain synapses. PLoS Biol 20, e3001659

32. Hikita, T., Kuwahara, A., Watanabe, R., Miyata, M., and Oneyama, C. (2019) Src in endosomal membranes promotes exosome secretion and tumor progression. Sci Rep 9, 3265

33. Zhang, Y., Liu, Y., Liu, H., and Tang, W. H. (2019) Exosomes: biogenesis, biologic function and clinical potential. Cell Biosci 9, 19

34. Baietti, M. F., Zhang, Z., Mortier, E., Melchior, A., Degeest, G., Geeraerts, A., Ivarsson, Y., Depoortere, F., Coomans, C., Vermeiren, E., Zimmermann, P., and David, G. (2012) Syndecan-syntenin-ALIX regulates the biogenesis of exosomes. Nat Cell Biol 14, 677-685

35. Larios, J., Mercier, V., Roux, A., and Gruenberg, J. (2020) ALIX- and ESCRT-III-dependent sorting of tetraspanins to exosomes. J Cell Biol 219

36. Scheffer, L. L., Sreetama, S. C., Sharma, N., Medikayala, S., Brown, K. J., Defour, A., and Jaiswal, J. K. (2014) Mechanism of Ca(2)(+)-triggered ESCRT assembly and regulation of cell membrane repair. Nat Commun 5, 5646

37. Sonder, S. L., Boye, T. L., Tolle, R., Dengjel, J., Maeda, K., Jaattela, M., Simonsen, A. C., Jaiswal, J. K., and Nylandsted, J. (2019) Annexin A7 is required for ESCRT III-mediated plasma membrane repair. Sci Rep 9, 6726

38. Shukla, S., Larsen, K. P., Ou, C., Rose, K., and Hurley, J. H. (2022) In vitro reconstitution of calcium-dependent recruitment of the human ESCRT machinery in lysosomal membrane repair. Proc Natl Acad Sci U S A 119, e2205590119

39. Strack, B., Calistri, A., Craig, S., Popova, E., and Gottlinger, H. G. (2003) AIP1/ALIX is a binding partner for HIV-1 p6 and EIAV p9 functioning in virus budding. Cell 114, 689-699

40. Fujii, K., Hurley, J. H., and Freed, E. O. (2007) Beyond Tsg101: the role of Alix in 'ESCRTing' HIV-1. Nat Rev Microbiol 5, 912-916

41. Carlton, J. G., and Martin-Serrano, J. (2007) Parallels between cytokinesis and retroviral budding: a role for the ESCRT machinery. Science 316, 1908-1912

42. Addi, C., Presle, A., Fremont, S., Cuvelier, F., Rocancourt, M., Milin, F., Schmutz, S., Chamot-Rooke, J., Douche, T., Duchateau, M., Giai Gianetto, Q., Salles, A., Menager, H., Matondo, M., Zimmermann, P., Gupta-Rossi, N., and Echard, A. (2020) The Flemmingsome reveals an ESCRT-to-membrane coupling via ALIX/syntenin/syndecan-4 required for completion of cytokinesis. Nat Commun 11, 1941

43. Strohacker, L. K., Mackay, D. R., Whitney, M. A., Couldwell, G. C., Sundquist, W. I., and Ullman, K. S. (2021) Identification of abscission checkpoint bodies as structures that regulate ESCRT factors to control abscission timing. Elife 10

44. Vietri, M., Radulovic, M., and Stenmark, H. (2020) The many functions of ESCRTs. Nat Rev Mol Cell Biol 21, 25-42

45. Bissig, C., and Gruenberg, J. (2014) ALIX and the multivesicular endosome: ALIX in Wonderland. Trends Cell Biol 24, 19-25

46. Odorizzi, G. (2006) The multiple personalities of Alix. J Cell Sci 119, 3025-3032

47. Fisher, R. D., Chung, H. Y., Zhai, Q., Robinson, H., Sundquist, W. I., and Hill, C. P. (2007) Structural and biochemical studies of ALIX/AIP1 and its role in retrovirus budding. Cell 128, 841-852

48. Matsuo, H., Chevallier, J., Mayran, N., Le Blanc, I., Ferguson, C., Faure, J., Blanc, N. S., Matile, S., Dubochet, J., Sadoul, R., Parton, R. G., Vilbois, F., and Gruenberg, J. (2004) Role of LBPA and Alix in multivesicular liposome formation and endosome organization. Science 303, 531-534

49. Tang, S., Buchkovich, N. J., Henne, W. M., Banjade, S., Kim, Y. J., and Emr, S. D. (2016) ESCRT-III activation by parallel action of ESCRT-I/II and ESCRT-0/Bro1 during MVB biogenesis. Elife 5

50. McCullough, J., Fisher, R. D., Whitby, F. G., Sundquist, W. I., and Hill, C. P. (2008) ALIX-CHMP4 interactions in the human ESCRT pathway. Proc Natl Acad Sci U S A 105, 7687-7691

51. Joshi, A., Munshi, U., Ablan, S. D., Nagashima, K., and Freed, E. O. (2008) Functional replacement of a retroviral late domain by ubiquitin fusion. Traffic 9, 1972-1983

52. Keren-Kaplan, T., Attali, I., Estrin, M., Kuo, L. S., Farkash, E., Jerabek-Willemsen, M., Blutraich, N., Artzi, S., Peri, A., Freed, E. O., Wolfson, H. J., and Prag, G. (2013) Structure-based in silico identification of ubiquitin-binding domains provides insights into the ALIX-V:ubiquitin complex and retrovirus budding. EMBO J 32, 538-551

53. Zhai, Q., Fisher, R. D., Chung, H. Y., Myszka, D. G., Sundquist, W. I., and Hill, C. P. (2008) Structural and functional studies of ALIX interactions with YPX(n)L late domains of HIV-1 and EIAV. Nat Struct Mol Biol 15, 43-49

54. Dores, M. R., Chen, B., Lin, H., Soh, U. J., Paing, M. M., Montagne, W. A., Meerloo, T., and Trejo, J. (2012) ALIX binds a YPX(3)L motif of the GPCR PAR1 and mediates ubiquitin-independent ESCRT-III/MVB sorting. J Cell Biol 197, 407-419

55. von Schwedler, U. K., Stuchell, M., Muller, B., Ward, D. M., Chung, H. Y., Morita, E., Wang, H. E., Davis, T., He, G. P., Cimbora, D. M., Scott, A., Krausslich, H. G., Kaplan, J., Morham, S. G., and Sundquist, W. I. (2003) The protein network of HIV budding. Cell 114, 701-713

56. Schmidt, M. H. H., Dikic, I., and Bogler, O. (2005) Src phosphorylation of Alix/AIP1 modulates its interaction with binding partners and antagonizes its activities. J Biol Chem 280, 3414-3425

57. Zhou, X., Pan, S., Sun, L., Corvera, J., Lin, S. H., and Kuang, J. (2008) The HIV-1 p6/EIAV p9 docking site in Alix is autoinhibited as revealed by a conformation-sensitive anti-Alix monoclonal antibody. Biochem J 414, 215-220

58. Zhou, X., Pan, S., Sun, L., Corvera, J., Lee, Y. C., Lin, S. H., and Kuang, J. (2009) The CHMP4b- and Src-docking sites in the Bro1 domain are autoinhibited in the native state of Alix. Biochem J 418, 277-284

59. Zhou, X., Si, J., Corvera, J., Gallick, G. E., and Kuang, J. (2010) Decoding the intrinsic mechanism that prohibits ALIX interaction with ESCRT and viral proteins. Biochem J 432, 525-534

60. Sun, S., Zhou, X., Corvera, J., Gallick, G. E., Lin, S. H., and Kuang, J. (2015) ALG-2 activates the MVB sorting function of ALIX through relieving its intramolecular interaction. Cell Discov 1, 15018

61. Carlton, J. G., Agromayor, M., and Martin-Serrano, J. (2008) Differential requirements for Alix and ESCRT-III in cytokinesis and HIV-1 release. Proc Natl Acad Sci U S A 105, 10541-10546

62. Qiu, X., Campos, Y., van de Vlekkert, D., Gomero, E., Tanwar, A. C., Kalathur, R., Weesner, J. A., Bongiovanni, A., Demmers, J., and d'Azzo, A. (2022) Distinct functions of dimeric and monomeric scaffold protein Alix in regulating F-actin assembly and loading of exosomal cargo. J Biol Chem 298, 102425

63. Dejournett, R. E., Kobayashi, R., Pan, S., Wu, C., Etkin, L. D., Clark, R. B., Bogler, O., and Kuang, J. (2007) Phosphorylation of the proline-rich domain of Xp95 modulates Xp95 interaction with partner proteins. Biochem J 401, 521-531

64. Sun, S., Sun, L., Zhou, X., Wu, C., Wang, R., Lin, S. H., and Kuang, J. (2016) Phosphorylation-Dependent Activation of the ESCRT Function of ALIX in Cytokinetic Abscission and Retroviral Budding. Dev Cell 36, 331-343

65. Dyson, H. J., and Wright, P. E. (2021) NMR illuminates intrinsic disorder. Curr Opin Struct Biol 70, 44-52

66. Smith, J. F., Knowles, T. P., Dobson, C. M., Macphee, C. E., and Welland, M. E. (2006) Characterization of the nanoscale properties of individual amyloid fibrils. Proc Natl Acad Sci U S A 103, 15806-15811

67. Knowles, T. P., Fitzpatrick, A. W., Meehan, S., Mott, H. R., Vendruscolo, M., Dobson, C. M., and Welland, M. E. (2007) Role of intermolecular forces in defining material properties of protein nanofibrils. Science 318, 1900-1903

68. Elias, R. D.; Shihora, A.; Hammond, J.; Ghirlando, R.; Deshmukh, L. (2023) ALS variants of annexin A11's proline-rich domain impair its S100A6-mediated fibril dissolution. (Under revision)

Chapter 2: Proline-rich domain of human ALIX contains multiple TSG101-UEV interaction sites and forms phosphorylation-mediated reversible amyloids

2.1 Introduction

Proline-rich domains (PRDs) are ubiquitous in the eukaryotic proteome and function as docking sites for a multitude of signaling protein modules (1-4). Prolines are also favored in intrinsically disordered proteins (IDPs), which lack a well-defined structure (5, 6). The relative abundance of proline is primarily due to its unusual structural properties. The proline sidechain is fused to its backbone amide nitrogen, which imposes unique conformational constraints and provides a distinct entropic advantage for binding to its signaling partners. The most common structure formed by consecutive proline residues is a left-handed helix, termed polyproline type II (PPII), with an extended rigid conformation that favors entropy-driven protein-protein interactions (7-9). A PPII structure can tolerate various combinations of proline and non-proline residues without compromising its structural integrity. PRDs are predicted to be disordered (10) and contain strategically placed short segments comprising proline residues and polyproline stretches. These contiguous functional segments, termed linear motifs (11), maintain the structural plasticity of PRDs where the presence of prolines results in extended conformations, rendering the linear motifs accessible for interactions with their signaling partners. A typical PRD contains sequentially similar linear epitopes, and this multivalency results in an increase in the avidity of protein-protein interactions and solution-to-gel phase transitions (12). Such interactions have been less studied in the context of intracellular signaling networks as compared with the interactions between extracellular ligands and their receptors, namely antibody-receptor and carbohydrate-lectin systems (13-15). To make use of ubiquitous PRDs, eukaryotes employ an array of proline-recognition domains (16, 17), which comprise several well-known motifs, including Src homology

3 (SH3), WW, GYF, and ubiquitin E2 variant (UEV), as well as many others. The interactions between proline-recognition domains and PRDs create dynamic signaling networks where a PRD can rapidly switch between binding partners and form multivalent complexes that dictate cell growth, transcription, cell signaling, and other essential cellular functions. Despite their importance, however, PRDs are usually removed from the protein constructs used for X-ray crystallography and NMR studies, due to the problems associated with their recombinant expression and their lack of structure. Since prolines lack amide protons, they are not amenable to conventional ^{1}H-detected NMR methods used to study IDPs at atomic resolution (18). As a result, there are clear gaps in our current understanding of how PRDs regulate cellular functions.

The apoptosis-linked gene-2 interacting protein X (ALIX), a human cellular protein, functions within the endosomal-sorting complexes required for transport (ESCRT) pathway (19, 20). The ESCRT pathway comprises a collection of proteins that form polymeric filaments and mediates membrane scission to facilitate cytokinetic abscission, biogenesis of multivesicular bodies, plasma membrane repair, and budding of enveloped viruses such as HIV-1 and Ebola. The ESCRT machinery consists of five functionally distinct protein complexes, ESCRT-0, -I, -II, and -III and AAA ATPase VPS4. ESCRT-0, -I, and -II are involved in sorting ubiquitinated proteins to endosomes. ESCRT-III filaments comprising polymeric assemblies of charged multivesicular body proteins (CHMPs) and ATPase VPS4 are involved in membrane scission. ALIX, also known as programmed cell death 6 interacting protein (PDCD6IP), interacts with ESCRT-I protein tumor susceptibility gene 101 (TSG101) and recruits ESCRT-III proteins to carry out membrane scission. In addition to ESCRT-mediated membrane remodeling, ALIX is involved in apoptosis, cell adhesion, and endocytosis (21). ALIX consists of an amino (N)-terminal Bro1 domain, a central V-domain, and a carboxy (C)-terminal PRD containing ~30% prolines (Fig. 2.1 A). The Bro1 and

V domains have been extensively studied by structural methods (22, 23). Relatively little is known about the PRD, despite its functional importance. ALIX-PRD is highly conserved among vertebrates (Fig. 2.1.1) and is known to interact with multiple binding partners (21), including the UEV domain of TSG101 (TSG101-UEV) (24, 25), tyrosine kinases such as Src (26) and Hck (27), endocytic proteins endophilins (28), and many others. The interactions between ALIX-PRD and TSG101-UEV are mediated by the N-terminal portion of PRD, which is also implicated in the autoinhibition of ALIX (29). The C-terminal tyrosine-rich portion of PRD is implicated in ALIX multimerization (30). The biological importance of ALIX-PRD and the lack of prior biophysical studies make it a prototypical system to study the mechanistic role of PRDs in cell signaling.

By dividing it into two recombinant constructs, representing the N- and the C-terminal portions of ALIX-PRD, we carry out a detailed investigation using a range of biophysical methods, including heteronuclear NMR spectroscopy, fluorescence spectroscopy, analytical ultracentrifugation (AUC), negative-stain electron microscopy (EM), and mass spectrometry (MS). Note that poor bacterial expression (31) and the overall size of the full-length protein (~96 kDa) do not allow for a similar biophysical investigation of PRD in the context of full-length ALIX. We show that the three tandem proline-rich motifs of the N-terminal portion of ALIX-PRD compete for binding with TSG101-UEV, suggesting that a PRD-mediated multimerization of ALIX will result in enhanced functional affinity for its binding partner, TSG101-UEV. We demonstrate that the C-terminal tyrosine-rich portion of ALIX-PRD forms amyloid fibrils and viscous gels under near-physiological conditions, as evidenced by dye-binding assays with amyloid-specific probes, congo red (CR) and thioflavin T (ThT), and visualized by negative-stain EM. Remarkably, the fibril formation is reversible as the fibrils dissolve at low temperatures (2 to 6 °C) or upon Src kinase mediated hyperphosphorylation of ALIX-PRD. This reversible

polymerization is strikingly different from those exhibited by pathological amyloids, including the ones associated with Alzheimer's and Parkinson's diseases that resist disassembly. We show that amyloid formation is driven by the hydrophobic effect, likely mediated by intra- and intermolecular interactions between tyrosine and proline residues, whereas phosphorylation-mediated dissolution is governed by charge repulsion.

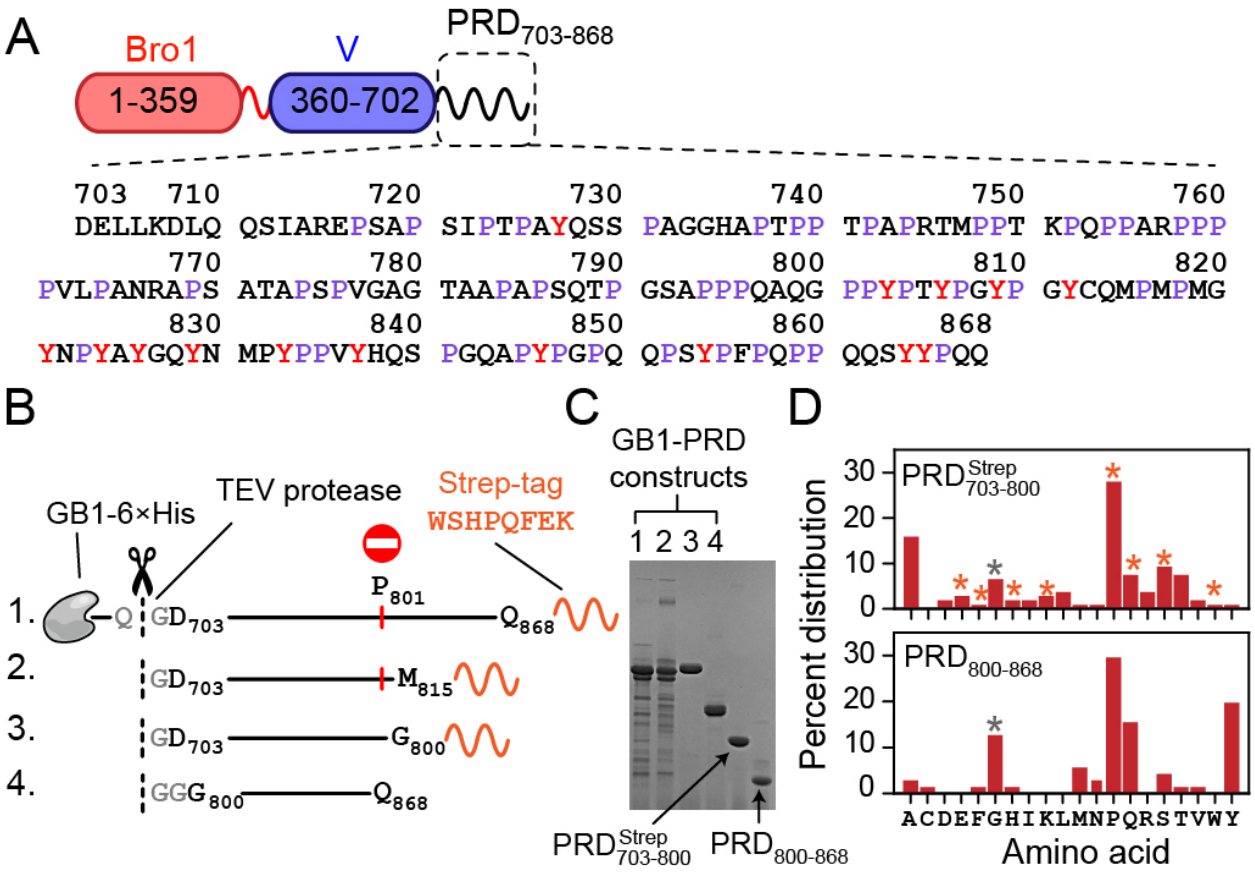

Figure 2.1: ALIX domain organization and summary of ALIX-PRD constructs used in the current work

(A) Schematic of ALIX organization. Primary sequence of PRD is shown with prolines (~30%) and tyrosines (~9%) labeled in purple and red, respectively. **(B)** Recombinant PRD constructs, namely GB1-PRD$^{Strep}_{703-868}$, GB1-PRD$^{Strep}_{703-815}$, GB1-PRD$^{Strep}_{703-800}$, and GB1-PRD$_{800-868}$. The positions of purification tags, 6×His and strep, are marked (primary sequence of strep tag is shown). TEV protease cutting sites are shown in gray and marked with dashed lines and scissors. Recombinant expression of GB1-PRD$^{Strep}_{703-868}$ and GB1-PRD$^{Strep}_{703-815}$ resulted in truncated fragments because of ribosomal stalling induced by polyproline stretches, especially at residue P801, marked by a red circle and vertical red line. **(C)** SDS-PAGE analysis of purified PRD constructs [16% wt/vol tris(hydroxymethyl)aminomethane-glycine gel]; the order of GB1-PRD fusion constructs is the same as the one depicted in B. TEV-cleaved products, namely PRD$^{Strep}_{703-800}$ and PRD$_{800-868}$ are marked with arrows. **(D)** Amino acid composition of PRD$^{Strep}_{703-800}$ (top) and PRD$_{800-868}$ (bottom). Vertical bars marked with orange and gray asterisks denote contributions from nonnative strep tag and remnant-glycine residues of TEV cleavage sites, respectively.

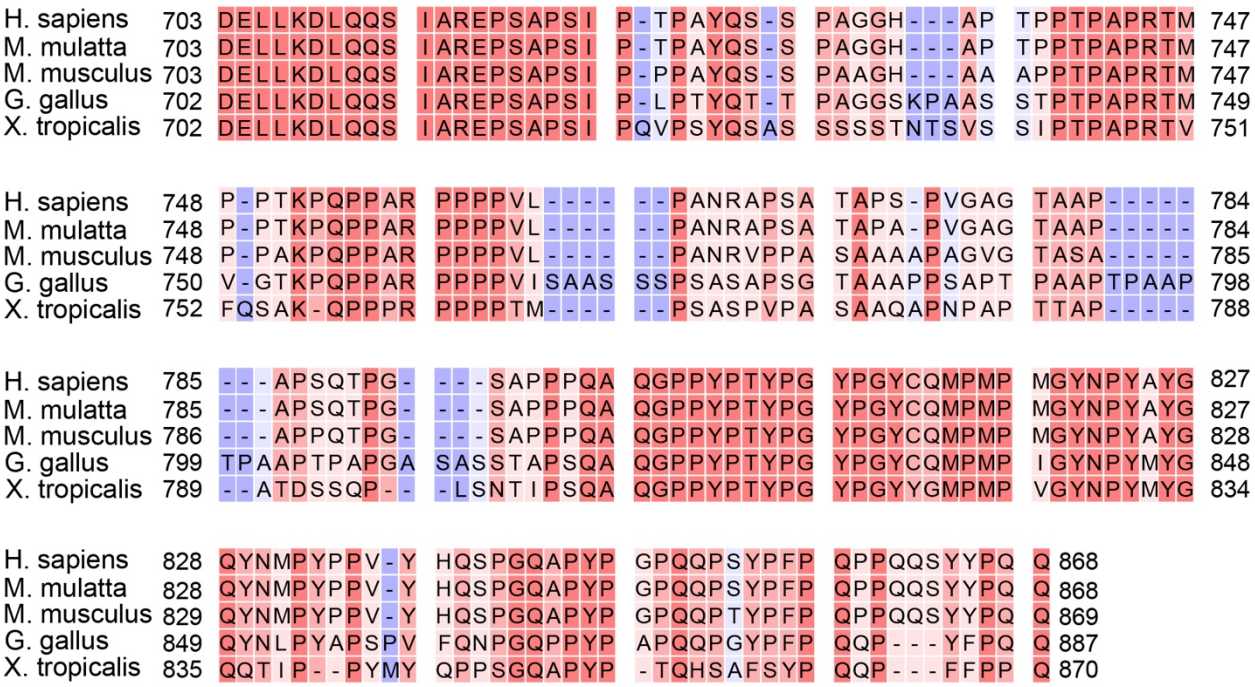

Figure 2.1.1: Primary sequence comparison of representative ALIX-PRDs among vertebrate species

A blue to red gradient is used to denote conservation with blue and red colors depicting the least and the most conserved residues, respectively. The following sequences were used for analysis: H. sapiens (Uniprot accession no. Q8WUM4), M. mulatta (Uniprot accession no. H9Z3W8), M. musculus (Uniprot accession no. Q9WU78), G. gallus (Uniprot accession no. A0A1D5PLK6) and X. tropicalis (Uniprot accession no. Q5XGJ5).

2.2 Recombinant constructs

The current work made use of two codon-optimized PRD constructs, namely the N-terminal fragment, $PRD^{Strep}_{703\text{-}800}$, and the C-terminal fragment, $PRD_{800\text{-}868}$ (Fig. 2.1 B-D). This "divide-and-conquer" strategy was employed since we were unable to express intact full-length PRD as well as its shorter truncated counterpart in Escherichia coli ($PRD^{Strep}_{703\text{-}868}$ and $PRD^{Strep}_{703\text{-}815}$, respectively). Sodium dodecyl sulphate-polyacrylamide gel electrophoresis (SDS-PAGE) (Fig. 2.1 C) and liquid chromatography-electrospray ionization-time-of-flight mass spectrometry (LC-ESI-TOFMS) (Fig. 2.2) analyses of the expression patterns of the latter two constructs revealed ribosomal stalling and subsequent translational arrest induced by polyproline stretches that are ubiquitous in ALIX-PRD, with regions ^{758}PPPP^{761} and ^{801}PPYP^{804} being particularly problematic. Essentially no intact proteins were produced as both $PRD^{Strep}_{703\text{-}868}$ and $PRD^{Strep}_{703\text{-}815}$ did not express beyond residue P801. These results agree with prior reports that show that translation of consecutive proline residues leads to ribosomal stalling (32-34). Each PRD construct carried a cleavable N-terminal fusion tag comprising B1 domain of protein G, GB1 (35), followed by a polyhistidine affinity tag (6xHis) and a tobacco etch virus (TEV) protease cleavage site; GB1-6xHis-TEV, hereafter referred to as GB1. In the case of $PRD^{Strep}_{703\text{-}800}$, a non-cleavable strep affinity tag (36) was engineered at the C terminus (^{801}WSHPQFEK^{808}), which served two purposes. It allowed a ready separation of intact protein from its truncated fragments using affinity chromatography and facilitated precise measurements of protein concentrations using ultraviolet absorbance; extinction coefficient at 280 nm (37): 6,970 versus 1,280 M-1cm-1, with and without the C-terminal strep tag, respectively (see Fig. 2.1 D for the amino acid composition of the two PRD constructs used in current work). We also made use of recombinant human full-length Src

kinase and TSG101-UEV (see Fig. 2.2.1 for LC-ESI-TOFMS characterization of the constructs used in current work).

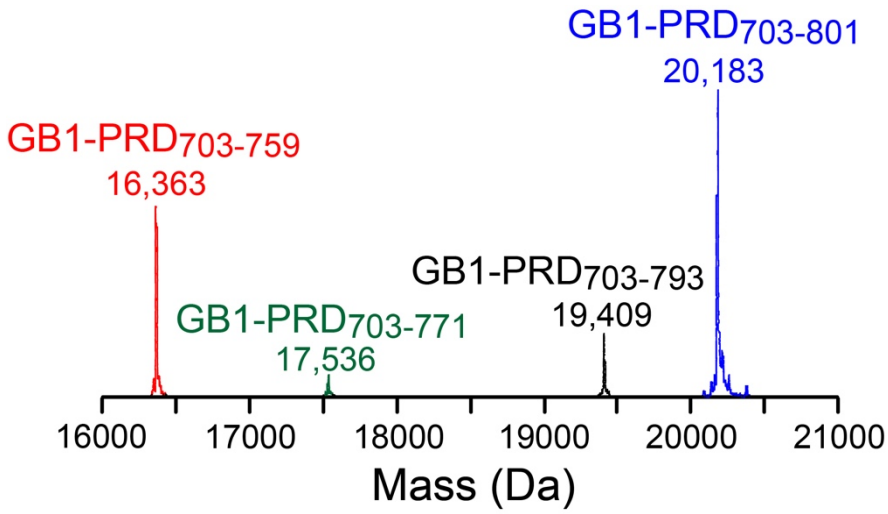

Figure 2.2: LC-ESI-TOFMS analysis of GB1-PRD$^{Strep}_{703-868}$ expression in E. coli

Recombinant expression of GB1-PRD$^{Strep}_{703-868}$ construct produced truncated fragments due to ribosomal stalling arising from polyproline stretches. Mass-spectrometry analysis of these fragments revealed four problematic regions - ^{758}PPP^{760}, ^{769}PSA^{771}, ^{791}GSAPPP^{796}, and ^{799}QGPPPP^{804} (underlined residues denote the termination residue for each fragment).

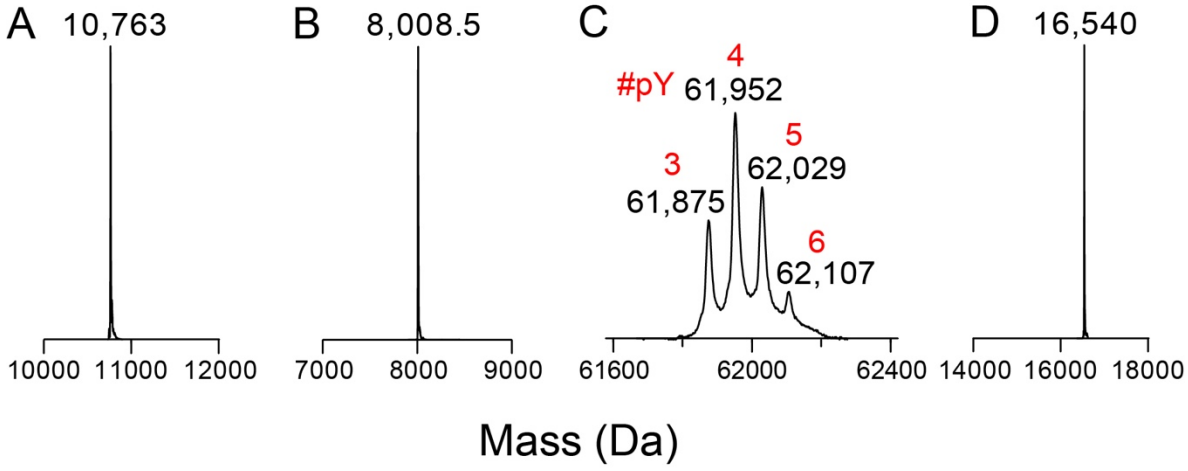

Figure 2.2.1: LC-ESI-TOFMS analysis of recombinant constructs used in current study

(A) PRD$^{Strep}_{703-800}$, calculated mass: 10,764 Da; **(B)** PRD$_{800-868}$, calculated mass: 8008.8 Da; **(C)** full-length human Src kinase, calculated mass: 61,635 Da. Mass-spectrometry analysis of Src revealed multiple (tyrosine) phosphorylated states, labeled in red (each phosphorylated tyrosine residue accounts for additional 80 Da); **(D)** TSG101-UEV, calculated mass:16,540 Da.

2.3 NMR analysis of $PRD^{Strep}_{703-800}$

$PRD^{Strep}_{703-800}$ yielded a high-quality ^{1}H-^{15}N transverse relaxation-optimized spectroscopy-heteronuclear single quantum coherence spectroscopy (TROSY-HSQC) spectrum (Fig. 2.3 A). The chemical shifts of the backbone amide proton resonances were clustered in a narrow 1 part per million (ppm) window (~7.7 to ~8.7 ppm), a hallmark of random-coil conformation. To further explore the structural propensity of $PRD^{Strep}_{703-800}$ in solution, we recorded NMR-backbone chemical shifts, three bond 3JHNHα couplings, and ^{15}N-longitudinal and transverse relaxation rates (R_1 and R_2, respectively). Nearly complete (~97%) backbone resonance assignments were achieved using a combination of three-dimensional conventional ^{1}H-detected and modern ^{13}C-detected NMR methods (18) (Fig. 2.3 B). Differences between observed chemical shifts and the corresponding random-coil values, referred to as secondary chemical shifts (Δδ), are sensitive indicators of local secondary structure. By using the random-coil values corrected for pH, ionic strength, and temperature (38, 39), rms values of 0.19, 0.35, 0.29, and 0.64 ppm were obtained for secondary chemical shifts of $^{13}C_\alpha$, $^{13}C_\beta$, $^{13}C'$, and ^{15}N, respectively (Fig. 2.3.1 A). Note that the chemical shifts of the last C-terminal residue, K808, were not considered for rms calculations. $\Delta\delta(^{13}C\alpha)$ values, the best reporters of local secondary structure, were evenly distributed around 0 ppm, indicative of a random-coil conformation. The absence of structural ordering was confirmed by analysis of backbone chemical shifts using the program δ2D (40), which yielded low values of the average secondary-structure propensities, ~2% of α-helix and ~11% of β-sheet (Fig. 2.3.1 B). For nearly all residues of $PRD^{Strep}_{703-800}$, the population of PPII fell in the ~20 to 30% range. A few notable exceptions were regions ^{752}PQPPAR^{757} and ^{782}AAP^{784}, which showed elevated PPII propensities (~30 to 40%). Finally, nothing definitive can be said about the conformation of the two polyproline stretches, namely ^{758}PPPP^{761} and ^{794}PPP^{796}, due to the lack of δ2D predictions for

these regions. These results are in excellent agreement with experimental CheZOD Z-scores (41), which indicated that nearly all residues of $PRD^{Strep}_{703-800}$ are disordered with Z-scores of <3 (Fig. 2.3.1 C). Note that the ^{734}GHAPTP^{739} motif showed slightly elevated Z-scores (~3 to 6), indicating a possible presence of a transient ordered structure in that region. $^{3}J_{HNH\alpha}$ couplings of $PRD^{Strep}_{703-800}$ were highly correlated with the random-coil $^{3}J_{HNH\alpha}$ values predicted using nearest-neighbor effects (42), with a Pearson's correlation coefficient of ~0.8 (Fig. 2.3.1 D). Analysis of ^{15}N-relaxation rates, measured at 800 MHz at 30 °C, revealed average R_1 and R_2 values of ~1.2 and ~2.1 s-1, respectively, indicating rapid backbone dynamics in the pico- to nanosecond regime (Fig. 2.3.1 E). Taken together, NMR results establish that $PRD^{Strep}_{703-800}$ is disordered in solution with the lack of dominant PPII population(s).

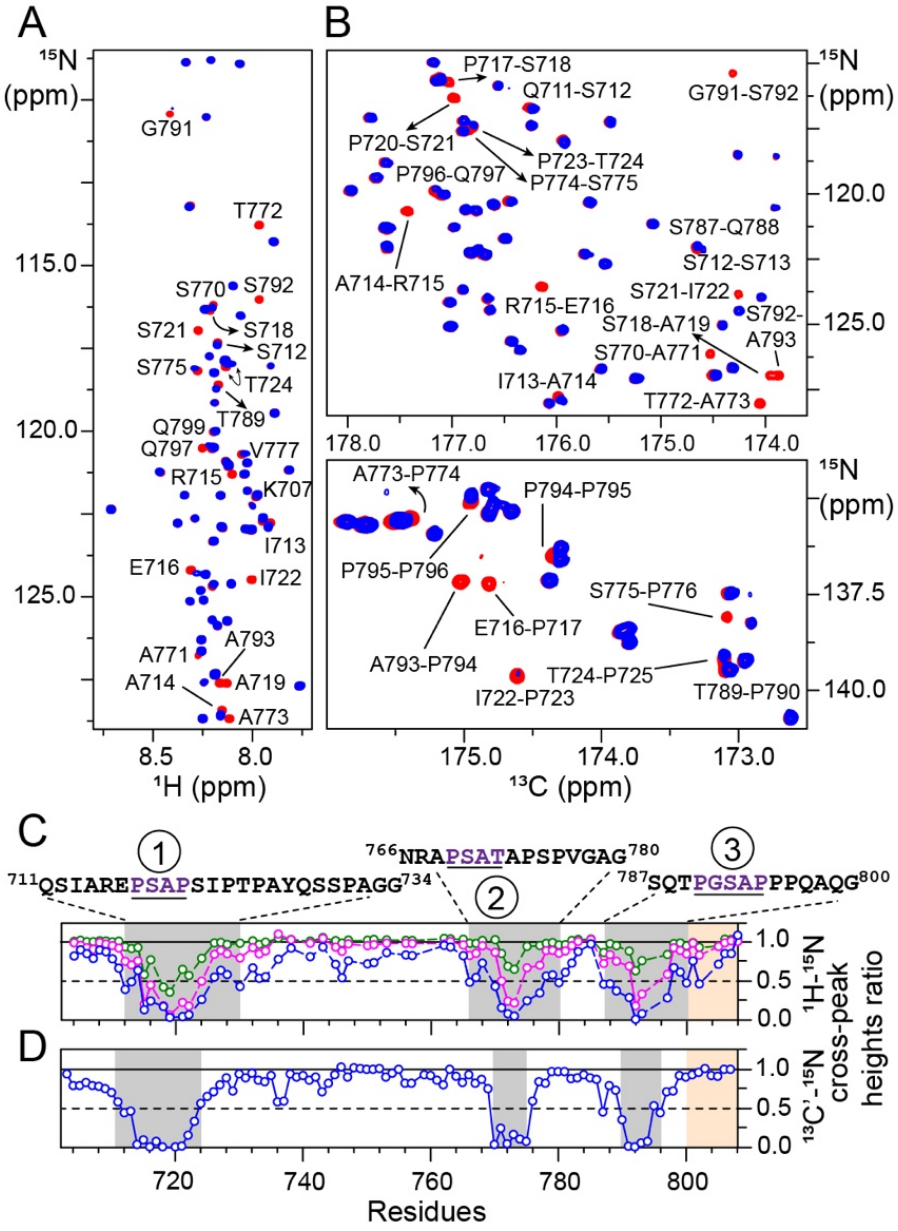

Figure 2.3: NMR analyses of interactions of $PRD^{Strep}_{703-800}$ with TSG101-UEV

(A and B) Overlay of expanded regions of the ^{1}H-^{15}N TROSY **(A)** and ^{13}C-^{15}N CO-N **(B)** correlation spectra of 100 μM $PRD^{Strep}_{703-800}$ in the absence (red) and presence (blue) of TSG101-UEV (molar ratio: 1:3). Some isolated cross-peaks that exhibit significant reduction in intensities on addition of TSG101-UEV are labeled. **(C and D)** The reduction in ^{1}H-^{15}N **(C)** and ^{13}C′-^{15}N **(D)** cross-peak intensities of $PRD^{Strep}_{703-800}$ on addition of TSG101-UEV is indicative of intermediate exchange on the chemical-shift time scale. Color scheme is as follows: $PRD^{Strep}_{703-800}$ + TSG101-UEV molar ratio: green, 1:0.25; magenta, 1:1.5; blue, 1:3. Affected regions are highlighted with semitransparent gray rectangles; primary sequences of each interacting PRD site (1, 2, and 3) are shown above the graphs, with recurring PTAP-like motifs underlined and labeled in dark purple. The position of the C-terminal strep tag (residues 801 to 808) is denoted by semitransparent orange rectangles.

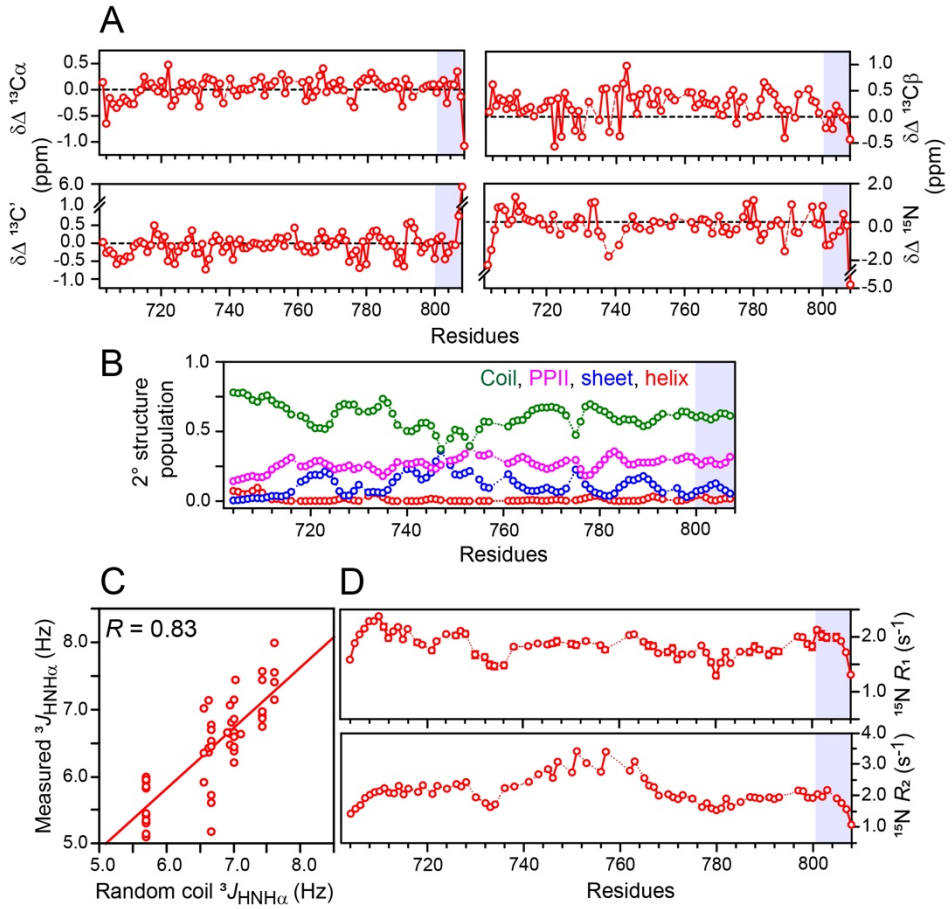

Figure 2.3.1: NMR analyses of $PRD^{Strep}_{703-800}$

(A) Secondary chemical shifts of $PRD^{Strep}_{703-800}$, namely Cα, C', Cβ and N, were derived from random coil values and correction factors of Poulsen and co-workers (38,39). **(B)** Secondary structure population of $PRD^{Strep}_{703-800}$ derived from the backbone shifts using δ2D (40). **(C)** Experimental CheZOD Z-scores (41,95). Residues of $PRD^{Strep}_{703-800}$ which show Z-scores ≥ 3 are highlighted with semi-transparent grey rectangles (namely 703-705, 723, 734-739, 742, 784, 793-794). **(D)** Correlation plot of $^{3}J_{HNH\alpha}$ couplings measured for $PRD^{Strep}_{703-800}$ against random coil values predicted using the newly derived nearest-neighbor effects (42). **(E)** Relaxation analysis of $PRD^{Strep}_{703-800}$ construct. All spectra were recorded in an interleaved manner. The following relaxation delays were used: R_1 (0, 120, 200, 360, 520, 680, 800, 1400 ms); $R_1\rho$ (0, 23, 55, 73, 106, 145, 193, 260 ms). R_2 is given by $[R_1\rho - R_1 \cos^2(\theta)/\sin^2(\theta)]$ where θ is the angle between the effective spin-lock field and the external magnetic field (and a value of 90° represents a resonance exactly on-resonance with the spin-lock field). The strength of the radiofrequency spin-lock field (ν_{RF}) employed in the $R_1\rho$ experiment was 1.5 kHz. Region highlighted in semi-transparent blue rectangle indicates the C-terminal strep purification tag (residues 801-808). All data were acquired at a spectrometer ^{1}H frequency of 800 MHz at 30 °C.

2.4 Interactions of NMR-visible $PRD^{Strep}_{703-800}$ with unlabeled TSG101-UEV

TSG101-UEV binds to P(T/S)AP motifs found in both cellular and viral proteins, including the p6 domain of HIV-1 Gag polyprotein (43). Direct interactions between the ^{717}PSAP^{720} motif of ALIX-PRD and TSG101-UEV were reported using yeast-two hybrid and surface plasmon resonance (SPR) measurements (25). The latter were carried out using recombinant TSG101-UEV and an 11-residue peptide analog of ALIX-PRD, $PRD_{714-723}$, and yielded an equilibrium dissociation constant, K_D, of 142 ± 0.5 μM. To explore interactions between $PRD^{Strep}_{703-800}$ and TSG101-UEV, we made use of NMR-titration experiments, where an increasing concentration of unlabeled TSG101-UEV was added to NMR-visible $PRD^{Strep}_{703-800}$ (Fig. 2.3 A and B and Fig. 2.4). Significant reductions in $^{1}H_N/^{15}N$ and $^{13}C'/^{15}N$ cross-peak intensities were observed for residues surrounding the ^{717}PSAP^{720} motif on the addition of unlabeled TSG101-UEV, a manifestation of intermediate-exchange regime on the chemical-shift time scale. The affected PRD region encompassed residues 711 to 734. As expected for an intermediate-exchange regime, only a few residues exhibited small but detectable $^{1}H_N/^{15}N$ and $^{13}C'/^{15}N$ chemical shift perturbations (Fig. 2.4). Surprisingly, two additional regions (residues 766 to 780 and 787 to 800) exhibited significant reductions in cross-peak intensities on the addition of TSG101-UEV, indicative of secondary interactions. Examination of primary sequences of all three affected PRD regions, namely residues 711 to 734, 766 to 780, and 787 to 800 (hereafter referred to as sites 1, 2, and 3, respectively), revealed a plausible explanation for these interactions. All three sites comprise sequentially similar motifs, namely ^{717}PSAP^{720}, ^{769}PSAT^{772}, and ^{790}PGSAP^{794} (Fig. 2.3 C), which interact with TSG101-UEV. ^{15}N-relaxation rates of $PRD^{Strep}_{703-800}$ were measured as a function of TSG101-UEV concentration (Fig. 2.4.1). Interactions between $PRD^{Strep}_{703-800}$ and TSG101-UEV are localized around the sites mentioned above as a significant increase in ^{15}N-R_2 rates on TSG101-UEV

addition was found only at these three interaction sites (Fig. 2.4.1 A and B). These results indicate that the TSG101-UEV-bound state of $PRD^{Strep}_{703-800}$ is dynamically disordered, with local ordering around the three interaction sites. These observations are in excellent agreement with the X-ray structure of the complex between TSG101-UEV and HIV-1 p6 analog comprising the PTAP motif (44) as the entire nine residue p6 analog (PEPTAPPEE) was visualized in an extended conformation in the binding groove of TSG101-UEV. Sedimentation studies of $PRD^{Strep}_{703-800}$ and TSG101-UEV demonstrated that both proteins were monodisperse and monomeric (Fig. 2.4.2). Sedimentation velocity experiments on $PRD^{Strep}_{703-800}$ returned a best-fit frictional ratio of ∼2.0, indicative of an IDP. In contrast, the frictional ratio for TSG101-UEV was ∼1.3, a value typical for globular proteins. We also carried out sedimentation-equilibrium experiments on $PRD^{Strep}_{703-800}$ (Fig. 2.4.3) and TSG101-UEV (Fig. 2.4.4), which showed that both proteins remain monodisperse at high concentrations with no indication of self-association. These results corroborate and confirm NMR-titration (cf., Fig. 2.3) and -relaxation data (cf., Fig. 2.4.1) and establish that the reduction in cross-peak intensities of $PRD^{Strep}_{703-800}$ observed on the addition of unlabeled TSG101-UEV is due to the association of the two proteins.

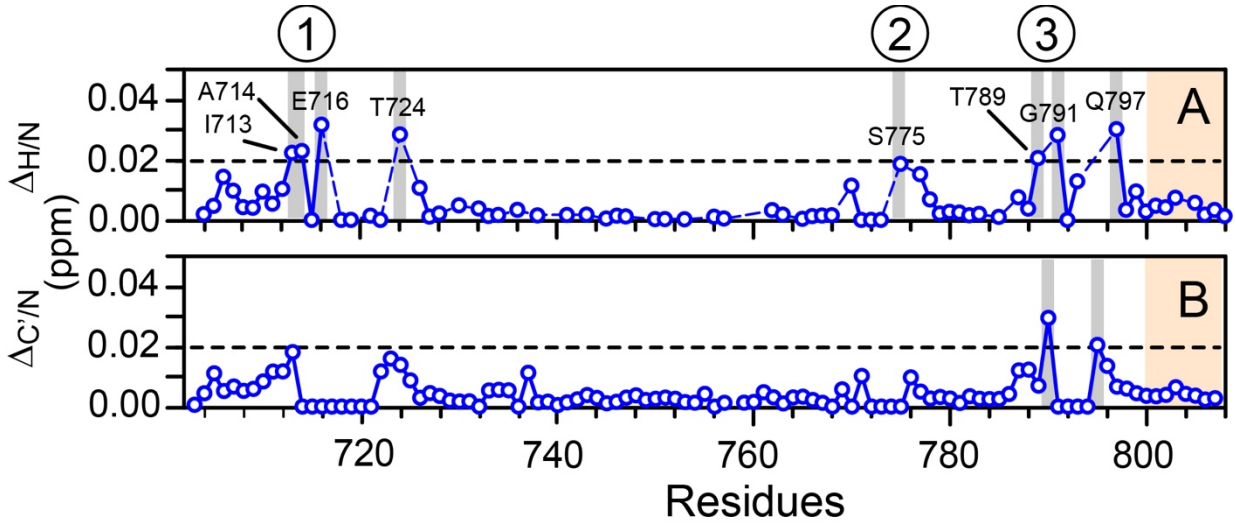

Figure 2.4: NMR chemical shift analysis of $PRD^{Strep}_{703-800}$ + TSG101-UEV interactions

(A) $^{1}H_N/^{15}N$ and **(B)** $^{13}C'/^{15}N$ chemical shift perturbation profiles of $PRD^{Strep}_{703-800}$ upon addition of TSG101-UEV (molar ratio= 1:3). Weighted combined $^{1}H_N/^{15}N$ (ΔH/N) and $^{13}C'/^{15}N$ (ΔC'/N) chemical shift perturbations resulting from the addition of TSG101-UEV were calculated as follows: $\Delta_{H/N}=\left\{(\Delta\delta_{HN})^2+(0.154\times\Delta\delta_N)^2\right\}^{1/2}$, where $\Delta\delta_{HN}$ and $\Delta\delta_N$ are the $^{1}H_N$ and ^{15}N chemical shift differences in ppm, respectively, between free and bound states, whereas $\Delta_{C'/N}=\left\{\left(0.3\times\Delta\delta_{C'}\right)^2+(0.154\times\Delta\delta_N)^2\right\}^{1/2}$, where $\Delta\delta_{C'}$ and $\Delta\delta_N$ are the $^{13}C'$ and ^{15}N chemical shift differences in ppm, respectively. Affected residues are highlighted with semi-transparent grey rectangles. Each interacting PRD site (1, 2, and 3) are shown above the panels. Region highlighted in semi-transparent orange rectangle indicates the C-terminal strep purification tag (residues 801-808). All data were acquired at a spectrometer ^{1}H frequency of 800 MHz at 30 °C. Buffer conditions were as follows: 20 mM sodium phosphate, pH 6.5, 50 mM NaCl, 1 mM TCEP, 2 mM EDTA.

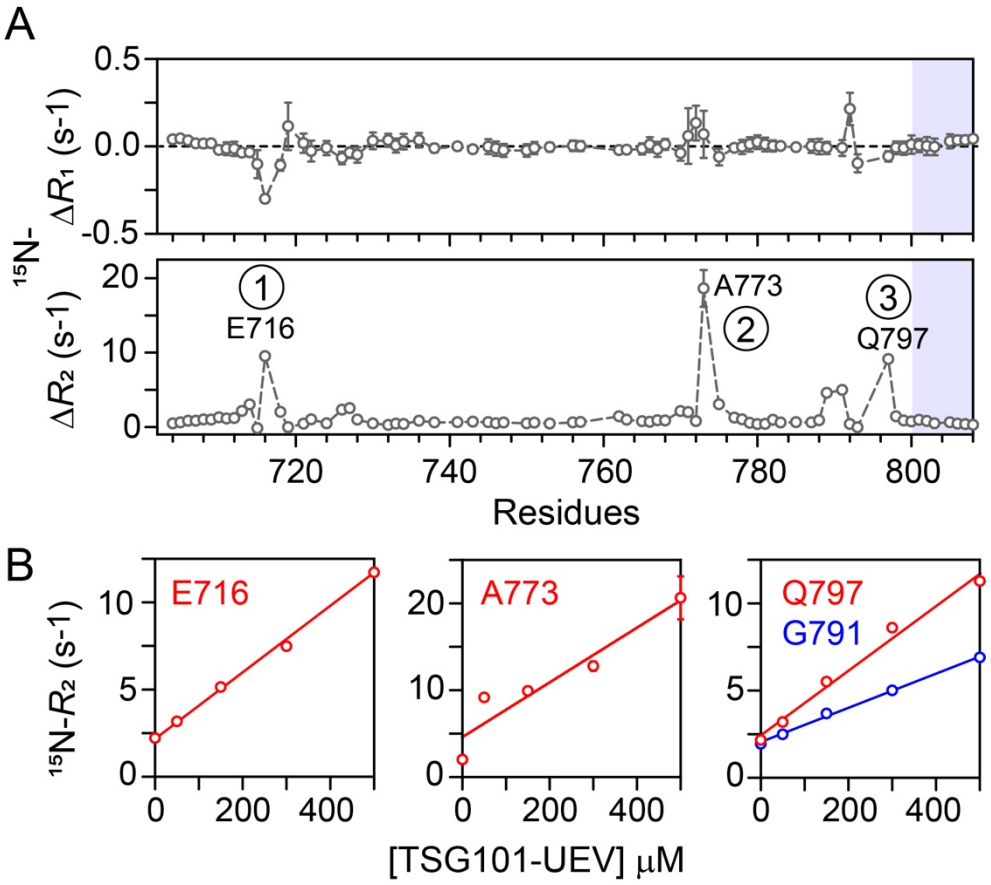

Figure 2.4.1: NMR relaxation analysis of $PRD^{Strep}_{703-800}$ + TSG101-UEV interactions

(A) ^{15}N-ΔR_1 and ΔR_2 profiles of $PRD^{Strep}_{703-800}$ upon addition of TSG101-UEV (molar ratio = 1:5), where ΔR is the difference between R_{bound} and R_{free}. Affected residues and the corresponding interacting site (1, 2, and 3) are marked. Region highlighted in semi-transparent blue rectangle indicates the C-terminal strep purification tag (residues 801-808). **(B)** ^{15}N-R_2 rates of three most-affected $PRD^{Strep}_{703-800}$ regions, each representing a distinct binding site (1, 2, and 3), plotted as a function of TSG101-UEV concentration and fitted with linear slope. All data were acquired at a spectrometer ^{1}H frequency of 800 MHz at 30 °C. Buffer conditions were as follows: 20 mM sodium phosphate, pH 6.5, 50 mM NaCl, 1 mM TCEP, 2 mM EDTA.

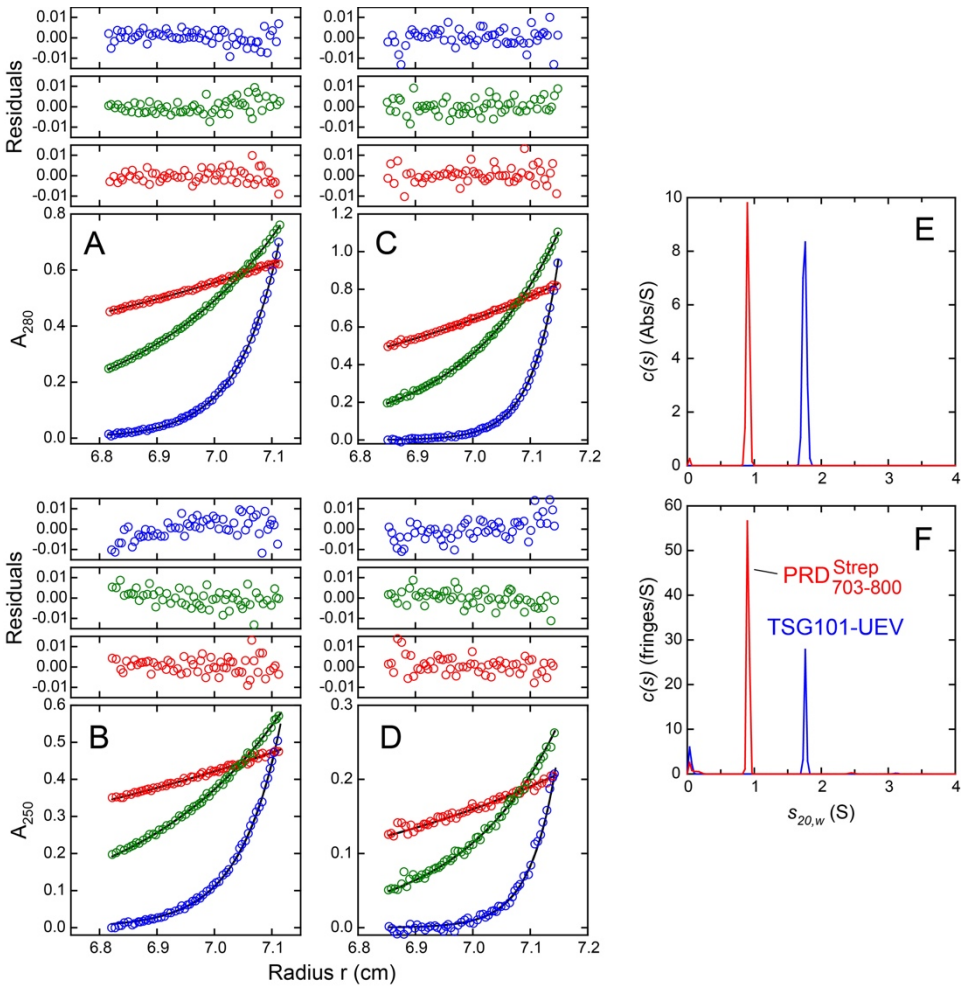

Figure 2.4.2: Characterization of $PRD^{Strep}_{703-800}$ and TSG101-UEV by analytical ultracentrifugation

(A - B) Sedimentation equilibrium analytical ultracentrifugation of $PRD^{Strep}_{703-800}$ at a loading concentration of 70 µM (12 mm cell) collected at 30 ºC and rotor speeds of 12,000 (red), 22,000 (green), and 42,000 (blue) rpm. Absorbance data collected at **(A)** 280 nm and **(B)** 250 nm were analyzed in terms of a single non-interacting species with mass conservation, returning a mass of 9.5 kDa consistent with a $PRD^{Strep}_{703-800}$ monomer. **(C - D)**. Sedimentation equilibrium analytical ultracentrifugation of TSG101-UEV at a loading concentration of 22 µM (12 mm cell) collected at 30 °C and rotor speeds of 12,000 (red), 22,000 (green), and 42,000 (blue) rpm. Absorbance data collected at **(C)** 280 nm and **(D)** 250 nm were analyzed in terms of a single non-interacting species with mass conservation, returning a mass of 16.1 kDa consistent with a TSG101-UEV monomer. Solid lines in the sedimentation equilibrium plots show the global best-fits obtained, and residuals are depicted in the panels above the data plot. For clarity, only every third experimental data point is shown. Absorbance **(E)** and interference **(F)** sedimentation velocity c(*s*) profiles for 66 µM $PRD^{Strep}_{703-800}$ (red) and 21 µM TSG101-UEV (blue) based on data collected at 20°C and 50,000 rpm, showing the presence of pure, monodisperse, monomeric species.$PRD^{Strep}_{703-800}$ is characterized by a sedimentation coefficient of 0.91 S with a molar mass of ~10.7 kDa, whereas TSG101-UEV is characterized by sedimentation coefficient of 1.75 S with a molar mass of ~17.0 kDa. Calculated monomer masses for $PRD^{Strep}_{703-800}$ and TSG101-UEV are 10.764 kDa and 16.483 kDa, respectively.

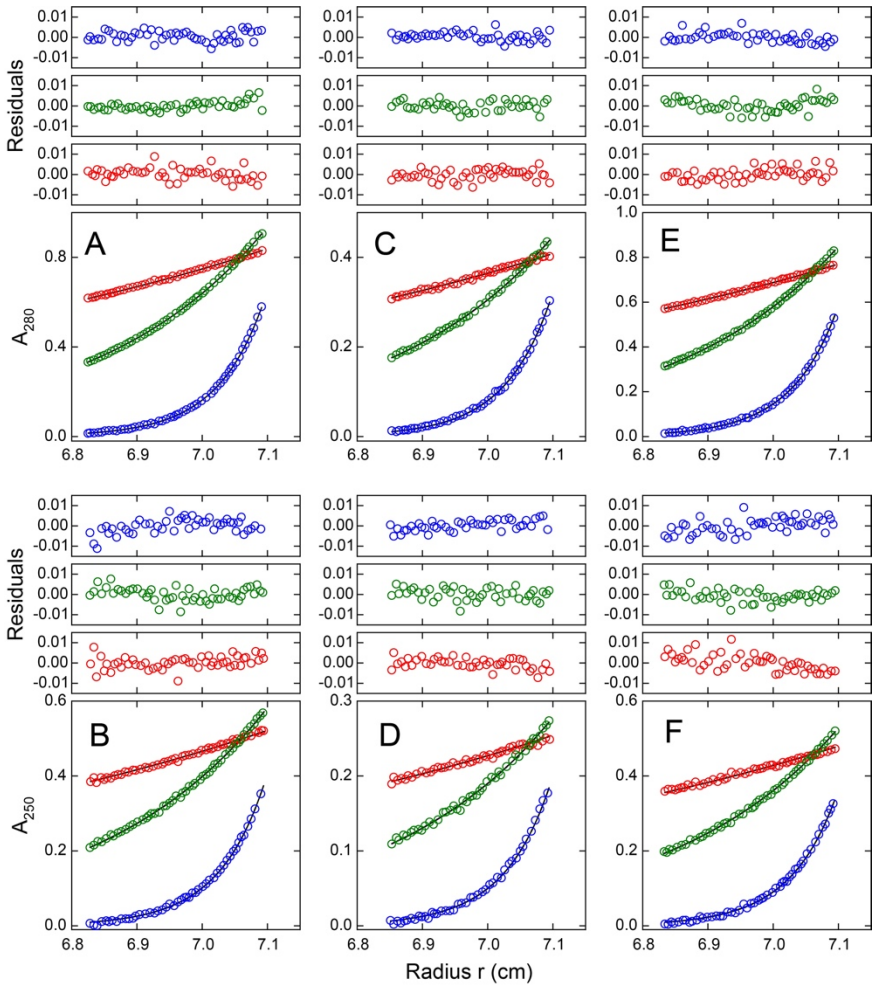

Figure 2.4.3: Characterization of $PRD^{Strep}_{703-800}$ at high concentrations by analytical ultracentrifugation

Sedimentation equilibrium analytical ultracentrifugation of $PRD^{Strep}_{703-800}$ at loading concentrations of **(A - B)** 360 µM (3 mm cell), **(C - D)** 180 µM **(3 mm cell)**, and **(E and F)** 90 µM (12 mm cell) collected at 30 ºC and rotor speeds of 12,000 (red), 22,000 (green), and 42,000 (blue) rpm. Absorbance data collected at 280 nm **(A, C, and D)** and 250 nm **(B, D, and F)** were analyzed globally in terms of a single non-interacting species with mass conservation, returning a mass of 9.5 kDa consistent with a monomeric species. Solid lines show the global best-fits obtained, and residuals are depicted in the panels above the data plot. For clarity only every third data point is shown.

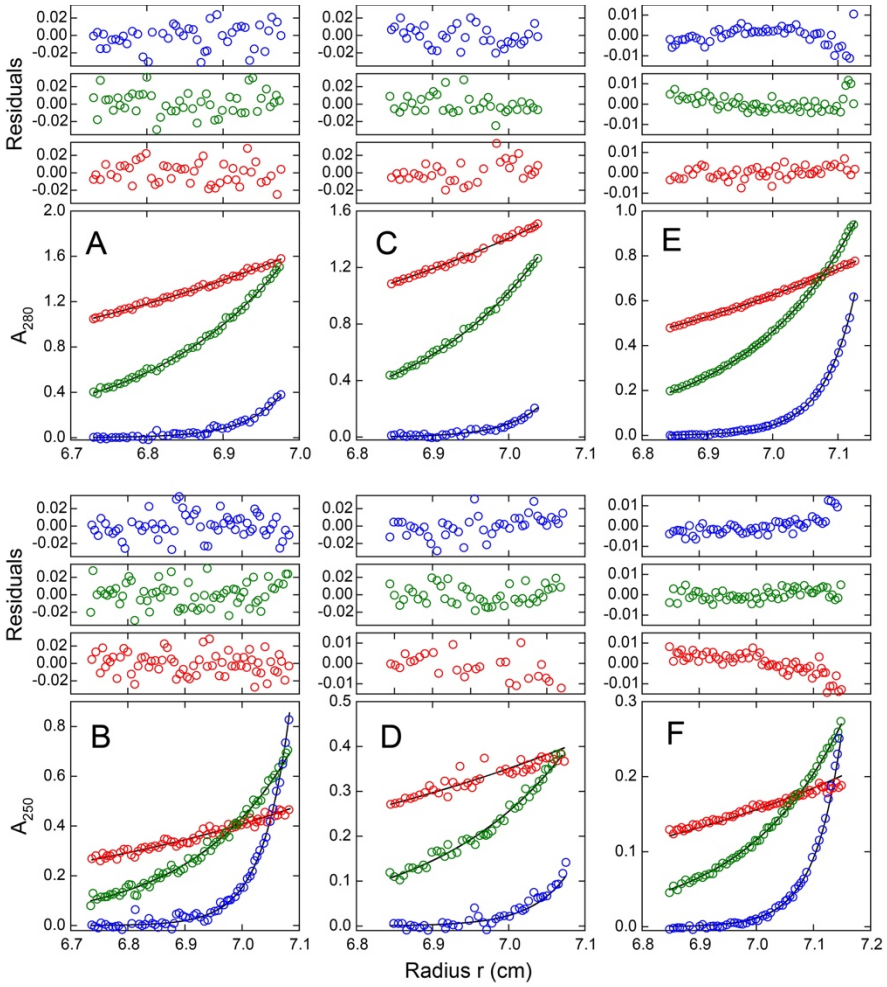

Figure 2.4.4: Characterization of TSG101-UEV at high concentrations by analytical ultracentrifugation

Sedimentation equilibrium analytical ultracentrifugation of TSG101-UEV at loading concentrations of **(A - B)** 380 μM (1.5 mm cell), **(C - D)** 190 μM (3 mm cell), and **(E and F)** 95 μM (3 mm cell) collected at 30 ºC and rotor speeds of 12,000 (red), 22,000 (green), and 42,000 (blue) rpm. Absorbance data collected at 280 nm **(A, C, and D)** and 250 nm **(B, D, and F)** were analyzed globally in terms of a single non-interacting species with mass conservation, returning a mass of 15.3 kDa consistent with a monomeric species. This slightly smaller mass observed at high concentrations shows the onset of thermodynamic non-ideality. Solid lines show the global best-fits obtained, and residuals are depicted in the panels above the data plot. For clarity only every third data point is shown.

2.5 Interactions of NMR-visible TSG101-UEV with unlabeled $PRD^{Strep}_{703-800}$

To further explore TSG101-UEV + $PRD^{Strep}_{703-800}$ interactions, NMR titration experiments were carried out on NMR-visible TSG101-UEV in the absence and presence of unlabeled $PRD^{Strep}_{703-800}$ (Fig. 2.5 A). The solution conformation of TSG101-UEV in the absence of $PRD^{Strep}_{703-800}$ was assessed using residual dipolar couplings (RDCs), which provide information on orientations of bond vectors (45-47). Excellent agreement was observed between the backbone amide ($^1D_{NH}$) RDCs, measured in polyethylene glycol/hexanol alignment medium (48), and those calculated from X-ray coordinates of TSG101-UEV (Protein Data Bank [PDB] entry 3OBS) (44), indicating that the structure of TSG101-UEV remains unaltered in solution (Fig. 2.5.1). A significant reduction in $^1H_N/^{15}N$ cross-peak intensities and small $^1H_N/^{15}N$ chemical-shift perturbations (~0.05 to 0.1 ppm) were observed for the following TSG101-UEV regions on the addition of 4 molar equivalents of $PRD^{Strep}_{703-800}$ (Fig. 2.5 B and C): residues 32 to 34, 58 to 69, 87 to 103, 110 to 111, and 134 to 144. Comparison of these results against X-ray/NMR complexes of TSG101-UEV + HIV-1 p6 analogs (43, 44) revealed that $PRD^{Strep}_{703-800}$ occupies the same binding pocket of TSG101-UEV as that of the HIV-1 p6 peptide. We, therefore, carried out docking calculations using the X-ray structure of TSG101-UEV + HIV-1 p6 peptide complex as a template (PDB entry 3OBU) (44), supplemented by distance restraints derived from NMR-titration data in Xplor-NIH (49). To simplify calculations, only a large fragment of one of the interacting sites of $PRD^{Strep}_{703-800}$, site 1, was used as a PRD analog (residues 711 to 730). The lowest-energy structure from these calculations is shown in Fig. 2.5 D. This structure confirms that TSG101-UEV carries a single binding site for a PTAP-like motif. Therefore, among the three PTAP-like motifs of $PRD^{Strep}_{703-800}$, namely ^{717}PSAP^{720}, ^{769}PSAT^{772}, and ^{790}PGSAP^{794}, only one can interact with one TSG101-UEV molecule at any given time.

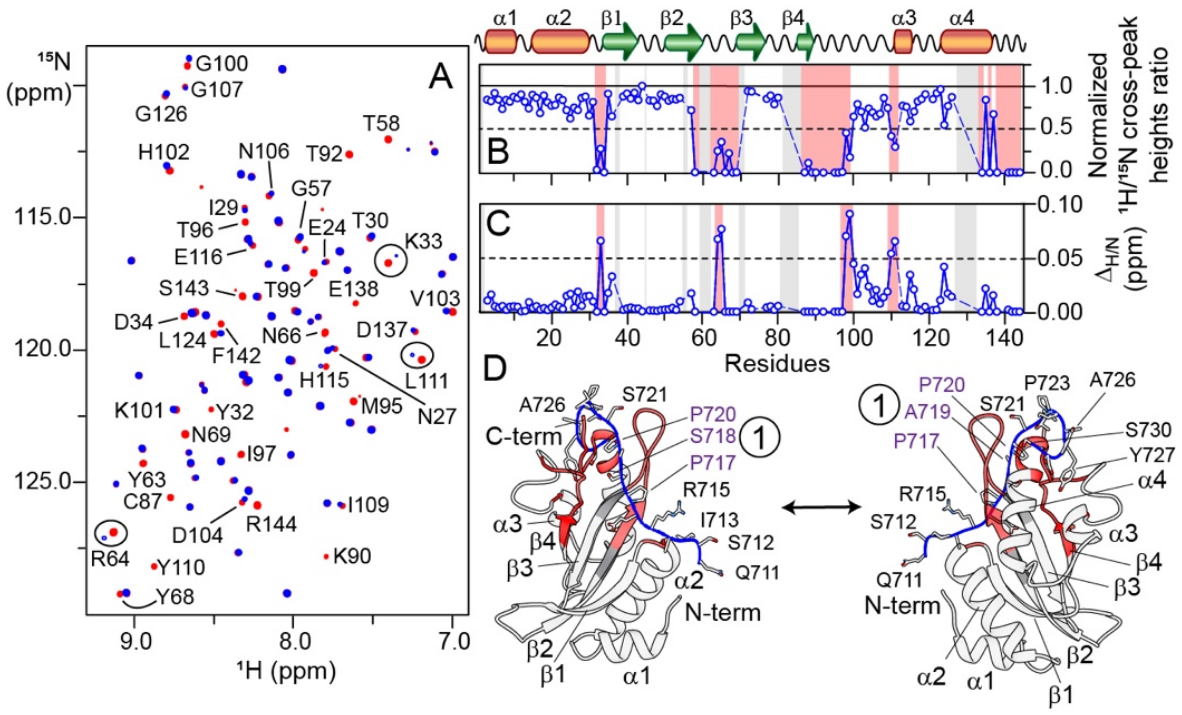

Figure 2.5: NMR and structural analyses of interactions of TSG101-UEV with $PRD^{Strep}_{703-800}$

(A) Overlay of expanded region of the ^{1}H-^{15}N TROSY correlation spectra of $^{15}N/^{2}H$-labeled 100 μM TSG101-UEV in the absence (red) and presence (blue) of $PRD^{Strep}_{703-800}$ (molar ratio: 1:4). Some isolated cross-peaks that exhibit significant reduction in intensities upon addition of $PRD^{Strep}_{703-800}$ are labeled. Cross-peaks that undergo chemical-shift changes on addition of $PRD^{Strep}_{703-800}$ are marked by circles. **(B and C)** The reduction in ^{1}H-^{15}N cross-peak intensities **(B)** and the perturbations in $^{1}H_N/^{15}N$ chemical shifts **(C)** of TSG101-UEV on addition of $PRD^{Strep}_{703-800}$. Affected regions are highlighted in semitransparent red rectangles (secondary structure elements are indicated above the graphs). Semitransparent gray rectangles and dashed blue lines indicate the residues that could not be assigned unambiguously. **(D)** A ribbon diagram of model of TSG101-UEV + $PRD_{711-730}$ complex. TSG101-UEV and $PRD_{711-730}$ are colored in white and blue, respectively. Regions marked in red represent residues of TSG101-UEV that are most affected on addition of $PRD^{Strep}_{703-800}$. Gray ribbons indicate residues around the binding site that could not be assigned unambiguously. For $PRD_{711-730}$, the side chains of individual residues are also shown; ^{717}PSAP^{720} motif (site 1) is marked with dark purple labels.

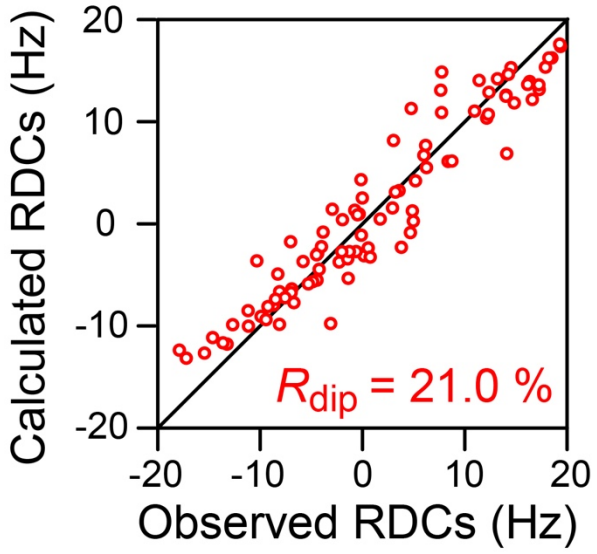

Figure 2.5.1: Backbone RDC analysis of TSG101-UEV

Panel shows best-fit agreement obtained by singular value decomposition (SVD) between $^{1}D_{NH}$ RDCs measured in 5% PEG-hexanol (5) and those calculated from a high-resolution X-ray structure of TSG101-UEV (1.5 Å, PDB ID: 3OBS) (23). The RDC R-factor, R_{dip}, is given by $\{\langle(D_{obs}-D_{calc})\rangle^2/\langle(2D_{obs}^2)\rangle^{1/2}\}$, where D_{obs} and D_{calc} are the observed and calculated $^{1}D_{NH}$ RDC values, respectively (96). Data were acquired at a spectrometer ^{1}H frequency of 600 MHz at 30 °C. Buffer conditions were as follows: 20 mM sodium phosphate, pH 6.5, 50 mM NaCl, and 1 mM TCEP.

2.6 Quantitative characterization of interactions of $PRD^{Strep}_{703-800}$ with TSG101-UEV

To quantitate $PRD^{Strep}_{703-800}$ + TSG101-UEV interactions, we collected Carr-Purcell-Meiboom-Gill (CPMG) relaxation dispersion experiments, which probe exchange between free and bound states on a time scale ranging from ~0.1 to 10 ms (50-52). Analysis of CPMG profiles via propagation of the Bloch-McConnell equations (53) yields the kinetic rate constants for the exchange process(es) and population(s) of the bound state(s). Fig. 2.6 A shows representative ^{15}N-CPMG relaxation dispersion profiles observed for each of the interaction site of NMR-visible $PRD^{Strep}_{703-800}$ in the presence of 5-molar excess of unlabeled TSG101-UEV; the corresponding profiles in the absence of TSG101-UEV are flat. Consistent with $^{1}H_N/^{15}N$ chemical-shift perturbation data (Fig. 2.4), only a few $PRD^{Strep}_{703-800}$ residues exhibited significant dispersions. Therefore, to aid the quantitative analysis, ^{15}N-CPMG measurements were recorded on NMR-visible $PRD^{Strep}_{703-800}$ in the presence of 2- and 3-molar excess of unlabeled TSG101-UEV (one at a time; Fig. 2.6.1). Because only one site of $PRD^{Strep}_{703-800}$ can interact with one TSG101-UEV at any given time, dispersion profiles for each interaction site were fit independently to a two-state exchange model, A↔B, comprising a free (State A) and a bound $PRD^{Strep}_{703-800}$ (State B). For each PRD site, all of the CPMG data collected as a function of increasing TSG101-UEV concentration were fit simultaneously. The results of the CPMG fits are shown in Fig. 2.6 A and Fig. 2.6.1. The kinetic parameters extracted from the fits are shown in Fig. 2.6 B (also see Table 2.1). The values of fitted dissociation rate constants, k_{off}, were 489 ± 11 s^{-1} (site 1) versus 1,941 ± 93 s^{-1} (site 2), and 3,281 ± 313 s^{-1} (site 3). Under the conditions of the experiment (100 μM $PRD^{Strep}_{703-800}$ + 500 μMTSG101-UEV), the k^{app}_{on} values were 344 ± 10 s^{-1} (site 1), 263 ± 42 s^{-1} (site 2), and 206 ± 105 s^{-1} (site 3), where k^{app}_{on} is the fitted pseudo first-order association rate constant. The exchange rate

constants, $k_{ex} = k_{on}^{app} + k_{off}$, between free and bound $PRD_{703-800}^{Strep}$ were ~830 s^{-1} (site 1), ~2,200 s-1 (site 2), and ~3,500 s-1 (site 3), indicating that the exchange at site 1 is ~3 and ~4 times slower than at sites 2 and 3, respectively. This is largely because the koff rates for each PRD site were significantly different even though the corresponding k_{on}^{app} values were comparable. The similarity of k_{on}^{app} values is consistent with the observations that each PRD site is composed of sequentially similar PTAP-like motifs (cf., Fig. 2.3 C), whereas differences in the corresponding k_{off} rates can be attributed to the fact that, although similar, sites 1, 2, and 3 are not identical to one another. The total amount of unbound TSG101-UEV was calculated to be 453 μM under the conditions of the experiment (100 μM $PRD_{703-800}^{Strep}$ + 500 μM TSG101-UEV; see section 2.10.6 for additional details). Because only one PRD site can bind to one TSG101-UEV at any given time, second-order association rate constants (k_{on}) were readily computed to be 76 ± 2, 58 ± 9, and 45 ± 23 (Å~ 104 $M^{-1} \cdot s^{-1}$) for sites 1, 2, and 3, respectively; $k_{on} = k_{on}^{app} \times [L]$, where [L] is the concentration of unbound TSG101-UEV. The resultant equilibrium dissociation constant, $K_D = k_{off}/k_{on}$, values were 0.64 ± 0.02 mM (site 1), 3.3 ± 0.6 mM (site 2), and 7.2 ± 3.7 mM (site 3), implying that site 1 of $PRD_{703-800}^{Strep}$ is the primary site of interaction, whereas sites 2 and 3 are secondary. Note that the K_D reported here for site 1 (~0.64 mM; measured at 30 °C) is approximately five times weaker than that reported in a previous study (25) carried out using a peptide analog of ALIX-PRD (~0.14 mM; measured using SPR at 20 °C). The discrepancy in binding affinity observed between intact $PRD_{703-800}^{Strep}$ (this work) versus its peptide analog ($PRD_{714-723}$) (25) can be attributed to differences in constructs and experimental conditions, specifically the temperature. These findings are consistent with our earlier investigations of interactions between HIV-1 Gag and protease, which demonstrated that native substrates often interact weakly with their binding partners compared with the corresponding peptide analogs (51, 54).

In addition to a 1:1 stoichiometry where one $PRD^{Strep}_{703\text{-}800}$ site is occupied by one TSG101-UEV molecule, there exists a possibility that sites 1 and 2, which are ~40 residues apart (cf., Fig. 2.3 C and D), can be occupied by two TSG101-UEV molecules at any given time: a 1:2 stoichiometry. Similarly, sites 1 and 3 are ~50 residues apart and can thus form a 1:2 complex. Sites 2 and 3, however, are mutually exclusive as they are separated by ~10 residues and, therefore, cannot simultaneously interact with two TSG101-UEV molecules due to steric hindrance. The total percentage occupancy of each $PRD^{Strep}_{703\text{-}800}$ site under the conditions of the experiment (100 μM $PRD^{Strep}_{703\text{-}800}$ + 500 μM TSG101-UEV) was calculated using corresponding K_D values for each site and mass-action law (Fig. 2.6 C and D). The bound populations for the 1:1 complex were 34 ± 3% (site 1), 7 ± 2% (site 2), and 3 ± 3% (site 3), and for the 1:2 complex were 5 ± 2% (site 1 + site 2) and 2 ± 2% (site 1 + site 3). The above observations establish that $PRD^{Strep}_{703\text{-}800}$ contains three PTAP-like motifs that compete for binding to TSG101-UEV, where site 1 is the primary site of interaction, and sites 2 and 3 are secondary. The C-terminal portion of PRD is implicated in multimerization of ALIX (30) (see Amyloids and Gels of $PRD_{800\text{-}868}$), indicating that in the event of ALIX multimerization, the sites mentioned above are likely to increase the functional affinity of ALIX-PRD for its interactions with TSG101.

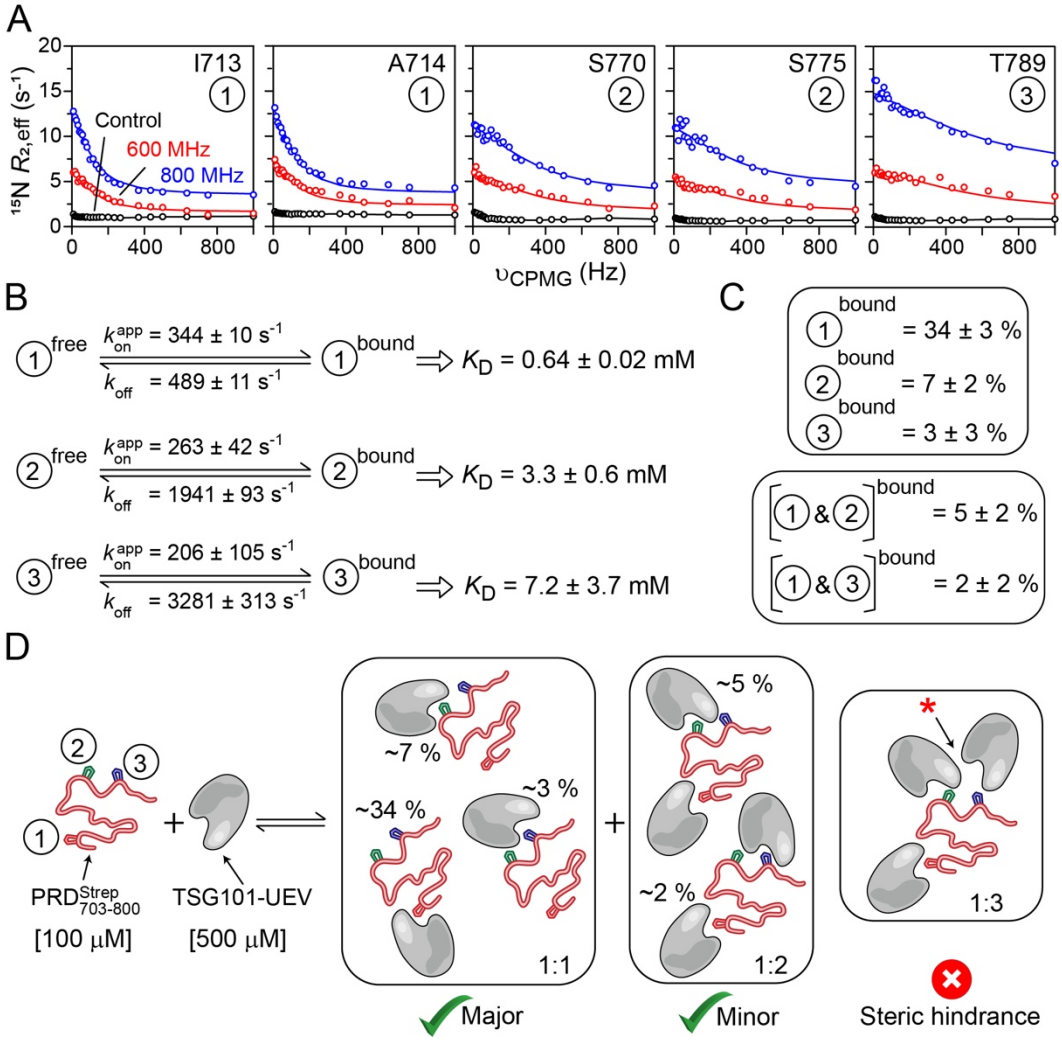

Figure 2.6: Quantitative analyses of interactions of PRD$^{Strep}_{703-800}$ with TSG101-UEV

(A) Representative backbone ^{15}N-CPMG relaxation dispersion profiles observed for 100 µM PRD$^{Strep}_{703-800}$ on addition of TSG101-UEV (molar ratio: 1:5); dispersions were recorded at 600 MHz (red) and 800 MHz (blue). The experimental data are displayed as circles, and the solid lines represent the global best fits to a two-state exchange model. Control relaxation dispersions at 800 MHz obtained in the absence of TSG101-UEV are shown in black. For the control data, black lines are used to guide the eye. **(B)** Summary of kinetic parameters obtained upon globally best fitting all CPMG data to a two-site exchange mode. Each interacting site (1, 2, and 3) is fit individually. k_{on}^{app} is an apparent pseudo-first-order association rate constant that pertains to 100 µM PRD$^{Strep}_{703-800}$ and 500 µM TSG101-UEV used in the CPMG experiments. k_{off} is the dissociation rate constant. The equilibrium dissociation constant, K_D, for each individual site is given by k_{off}/k_{on}, where $k_{on} = k_{on}^{app}/[L]$ and [L] is the concentration of unbound TSG101-UEV. **(C)** Populations of 1:1 and 1:2 complexes formed between PRD$^{Strep}_{703-800}$ and TSG101-UEV, calculated using K_D values for each individual PRD site and mass-action law. Note that sites 2 and 3 are mutually exclusive as they cannot simultaneously interact with two TSG101-UEV molecules due to steric hindrance (cf., Fig. 2.3 C). **(D)** Scheme depicting potential modes of interactions of PRD$^{Strep}_{703-800}$ with TSG101-UEV; populations of bound sites are labeled.

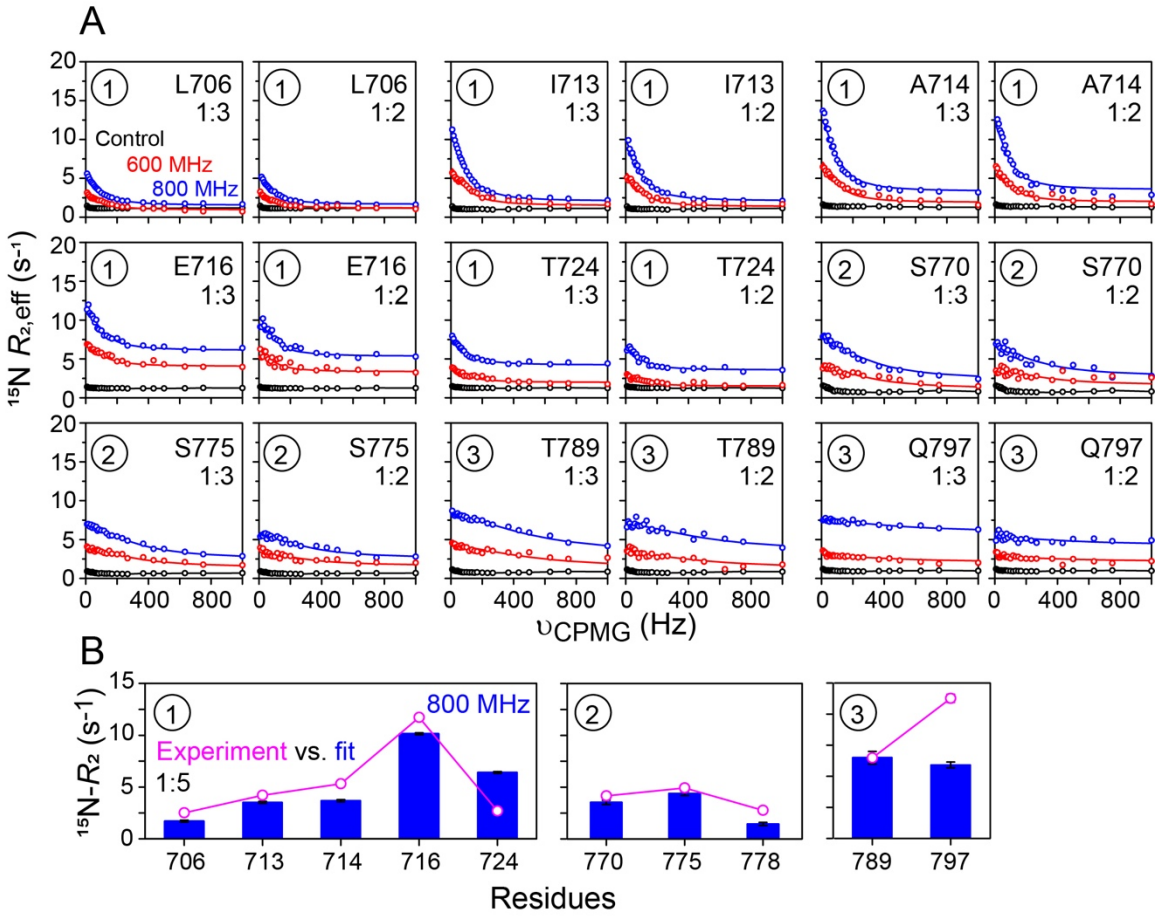

Figure 2.6.1: ^{15}N-CPMG analyses of interactions of $PRD^{Strep}_{703-800}$ with TSG101-UEV

(A) Backbone ^{15}N-CPMG relaxation dispersion profiles observed for 100 μM $PRD^{Strep}_{703-800}$ on addition of TSG101-UEV (molar ratios = 1:3 and 1:2). Each interacting site (1, 2, and 3) is marked in circles. Dispersions were recorded at spectrometer frequency of 600 MHz (red) and 800 MHz (blue). The experimental data are displayed as circles, and the solid lines represent the global best fits to a two-state exchange model. Control relaxation dispersions at 800 MHz obtained in the absence of TSG101-UEV are shown in black. For the control data, black lines are used to guide the eye. **(B)** Comparison between experimentally measured residue-specific backbone ^{15}N-R_2 rates of $PRD^{Strep}_{703-800}$ on addition of 5-molar equivalent of TSG101-UEV (magenta) and the corresponding rates obtained from CPMG fits (blue).

Table 2.1: Bound populations (p_b), exchange rates (k_{on}^{app}, k_{on} and k_{off}), and binding constants (K_D) for $PRD_{703-800}^{Strep}$ - TSG101-UEV interactions

The optimized rate constants ($k_{on}^{app}$and k_{off}) were extracted directly from CPMG fits. The corresponding second-order association rate constants (k_{on}) were calculated using the relationship $k_{on}^{app} = [L] \times k_{on}$ where [L] is the concentration of unbound TSG101-UEV. Under the conditions of the experiment, the amount of unbound TSG101-UEV was 453 µM (see section 2.10.6 for details). Bound fractions, pb, of each site were calculated using mass action law and the corresponding K_D values (see section 2.10.6 for details). Experiments were carried out at spectrometer ^{1}H frequency of 800 and 600 MHz at 30 °C. Buffer conditions were as follows: 20 mM sodium phosphate, pH 6.5, 50 mM NaCl, 1 mM TCEP, 2 mM EDTA. Protein concentrations were as follows: 100 µM $PRD_{703-800}^{Strep}$ + 500 µM TSG101-UEV (Note that CPMG measurements were also carried out on 100 µM $PRD_{703-800}^{Strep}$ and 200 / 300 µM TSG101-UEV; one at a time). Each interacting site of $PRD_{703-800}^{Strep}$ was fitted individually where all the CPMG data collected as function of increasing TSG101-UEV concentration were simultaneously fitted. k_{off} was the shared optimized parameter for each site in the fits. The K_D values are given by $K_D = k_{off} / k_{on}$ and have been appropriately rounded. Double-occupancy was estimated using the calculated K_D values as per mass-action law (see section 2.10.6).

	p_b (%)	k_{on}^{app} (s^{-1})	k_{on} x 10^4 ($M^{-1}s^{-1}$)	K_{off} (s^{-1})	K_D (mM)	Residues used for fitting
$PRD_{703-800}^{Strep}$ + TSG101-UEV (1:1 complex)						
Site 1	34 ± 3	344 ± 10	76± 2	489 ± 11	0.6 ± 0.02	706, 713, 714, 716, 724
Site 2	7± 2	263 ± 42	58 ± 9	1941 ± 93	3.3 ± 0.6	770, 775, 778
Site 3	3 ± 3	206 ± 105	45 ± 3	3281 ± 313	7.2 ± 3.7	787, 797
$PRD_{703-800}^{Strep}$ + TSG101-UEV (1:2 complex)						
Site 1 + 2	5 ± 2					
Site 1 + 3	2 ± 2					

2.7 Amyloids and gels of CPRD

In contrast to $PRD^{Strep}_{703\text{-}800}$, which exhibited high solubility (soluble up to ~2 mM), the C-terminal portion, $PRD_{800\text{-}868}$, was poorly soluble under aqueous conditions (<30 μM; pH 4.5 to 7). The presence of an N-terminal GB1 fusion tag, often employed to overcome protein solubility and stability issues (55, 56), greatly improved the solubility of $PRD_{800\text{-}868}$ (soluble up to ~0.5 mM). Due to its favorable properties, including small size, high solubility, and extreme thermal stability, and because it usually does not influence structural characteristics of the tagged partner, the GB1 tag is often considered to be an ideal solubility-enhancement tag. The use of GB1 fusion construct allowed us to collect highly reproducible data and characterize aggregation properties of $PRD_{800\text{-}868}$ (a serendipitous observation during purification of recombinant $PRD_{800\text{-}868}$ revealed its aggregation-prone behavior). Spectral-shift assays were carried out using an amyloid-specific dye, CR, to explore the possibility that GB1-$PRD_{800\text{-}868}$ aggregates were amyloidogenic (57). Clear shifts toward 540 nm were observed for aggregates of GB1-$PRD_{800\text{-}868}$ in contrast to its N-terminal soluble counterpart, GB1-$PRD^{Strep}_{703\text{-}800}$, indicating the presence of amyloid structures for GB1-$PRD_{800\text{-}868}$ aggregates (Fig. 2.7 A). Emission assays carried out using ThT (58), another amyloid-specific dye that is thought to form ordered arrays along the lengths of fibrils, leading to increase in its fluorescence, indicated the presence of cross-β-sheet conformations (59) for GB1-$PRD_{800\text{-}868}$ aggregates, corroborating their amyloidogenic nature (Fig. 2.7 B). Analysis of GB1-$PRD_{800\text{-}868}$ aggregates by negative-stain EM elucidated that these aggregates consist of unbranched filaments, characteristic of amyloid fibrils (Fig. 2.7 C and D). After ~3 d at room temperature under non-agitated (quiescent) conditions, GB1-$PRD_{800\text{-}868}$ aggregates coalesced to form a dense gel. Upon inverting the tube, the GB1-$PRD_{800\text{-}868}$ solution remained at the bottom of the tube instead of falling into the cap, indicating a significant increase in viscosity (Fig. 2.7 E). Analysis of GB1-$PRD_{800\text{-}868}$

gel by negative-stain EM revealed a dense network of intertwined fibrils (Fig. 2.7 F). Note that the gel-forming behavior of GB1-PRD$_{800\text{-}868}$ is consistent with a wide variety of amyloid-forming polypeptides that have been shown to form hydrogels (60).

To validate and gain a mechanistic understanding of GB1-PRD$_{800\text{-}868}$ amyloid formation, we monitored aggregation kinetics using ThT fluorescence. The effects of the following experimental conditions on aggregation kinetics were monitored (one at a time): pH, ionic strength, protein concentration, and temperature (Fig. 2.7.1). GB1-PRD$_{800\text{-}868}$ exhibited sigmoidal aggregation profiles, ThT signal against time, a hallmark of amyloid formation (61). Most profiles displayed an initial dip in ThT signals, followed by a small lag phase, a robust growth phase, and a final plateau. High-quality data were obtained with continuous linear shaking with essentially no variations between replicates (raw data of three replicates from one plate are shown, n = 3; Fig. 2.7.1 A-D). To rule out the possible contributions from the GB1 fusion tag in PRD$_{800\text{-}868}$ aggregation, identical experiments were performed on GB1-PRD$^{\text{Strep}}_{703\text{-}800}$ and on the GB1 tag itself, which showed no obvious ThT signals (Fig. 2.7.1 A). ThT signals of GB1-PRD$_{800\text{-}868}$ samples at zero time point (t0) were considerably higher than the corresponding controls, indicating the presence of substantial GB1-PRD$_{800\text{-}868}$ aggregates at t0. The lyophilized GB1-PRD$_{800\text{-}868}$ samples were treated with ammonium hydroxide to produce an aggregate-free solution (62); however, this method was not fully effective and did not result in complete solubilization and disaggregation of GB1-PRD$_{800\text{-}868}$ samples. Faster aggregation was observed at pH 7.0 versus pH 6.5, 7.5 and 8.0 (Fig. 2.7.1 A) and with 0 mM NaCl versus 250 and 500 mM NaCl (Fig. 2.7.1 B). Changes in the concentration of GB1-PRD$_{800\text{-}868}$ did not affect its aggregation rates (Fig. 2.7.1 C; also see Fig. 2.7.2 for measurements carried out under quiescent conditions, which show a similar trend). A significant increase in rates was observed upon an increase in temperature (Fig. 2.7.1 D). At 40

°C, a half-maximal signal was reached within ∼1 h ($t_{1/2}$ = 1 h), whereas the corresponding $t_{1/2}$ values for 25, 30, and 35 °C were ∼11, ∼4, and ∼2 h, respectively. To further assess the impact of temperature on aggregation, ThT emission spectra were recorded (Fig. 2.7.1 E; n = 3). GB1-$PRD_{800-868}$ samples were incubated at 40 °C until the maximum ThT signal was reached (∼2 h), whereupon the temperature was reduced to 4 °C. Surprisingly, ThT signals of GB1-$PRD_{800-868}$ amyloid fibrils decreased as a function of time at 4 °C (incubation time: ∼4 h), indicating that $PRD_{800-868}$ forms reversible amyloids. Similar measurements carried out at 2, 6, 8, and 10 °C showed a slightly faster dissolution rate at 2 °C compared with 4 °C (incubation time: ∼3 h) and essentially no decrease in ThT signals at 8 and 10 °C, indicating that the $PRD_{800-868}$ filaments are stable at and above 8 °C (Fig. 2.7.3). A similar behavior was seen with GB1-$PRD_{800-868}$ gel, which became fragile and liquid-like at 4 °C (Fig. 2.7.1 E, Lower). ThT measurements were also carried out on $PRD_{800-868}$ (without the GB1 tag), which displayed characteristic sigmoidal profiles (Fig. 2.7.1 F). Poor solubility of $PRD_{800-868}$ resulted in significant variations between replicates and, therefore, precluded us from carrying out a thorough kinetic analysis.

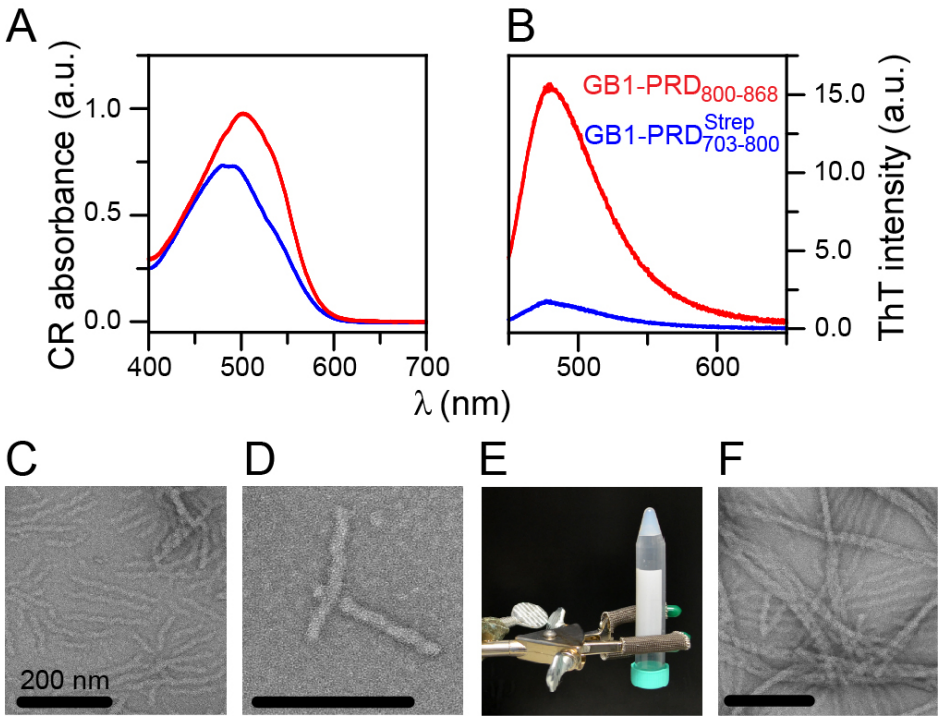

Figure 2.7: Amyloid fibrils and gel formed by GB1-PRD$_{800-868}$

(A and B) Absorbance spectra of CR **(A)** and emission spectra of ThT **(B)** for aggregates formed by GB1-PRD$_{800-868}$ (red). GB1-PRD$^{Strep}_{703-800}$ samples (blue) were used as controls. Raw data of three replicates (n = 3) are plotted against wavelength (nm). **(C and D)** Negatively stained EM images of GB1-PRD$_{800-868}$ amyloid fibrils. (Scale bars, 200 nm.) **(E)** Formation of a gel by GB1-PRD$_{800-868}$. To initiate the gel formation, a 0.1 mM GB1-PRD$_{800-868}$ sample was kept at room temperature under quiescent conditions for ~3 d. **(F)** EM images of GB1-PRD$_{800-868}$ gel.

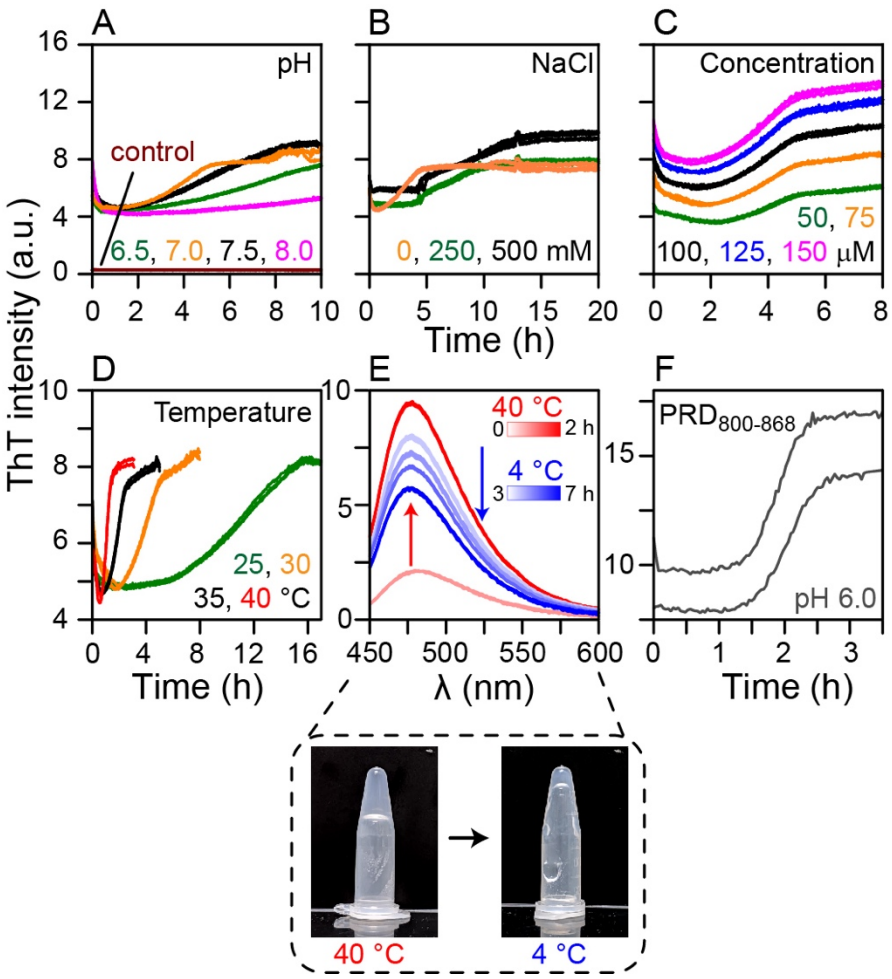

Figure 2.7.1: Formation and dissolution of GB1-PRD$_{800\text{-}868}$ amyloid fibrils

(A-D) ThT fluorescence was monitored to determine the effects of pH **(A)**, ionic strength **(B)**, concentration **(C)**, and temperature **(D)** on the aggregation kinetics of GB1-PRD$_{800\text{-}868}$ (raw data of three replicates [n = 3] are plotted against time). Control curves (dark red) **(A)** are collected using GB1-PRD$^{\text{Strep}}_{703\text{-}800}$. Control experiments were also carried out on GB1 fusion tag and showed no ThT signal. For A-C, the measurements were carried out at 30 °C. **(E)** Dissolution of GB1-PRD$_{800\text{-}868}$ amyloid fibrils at 4 °C. ThT emission spectra of GB1-PRD$_{800\text{-}868}$ (n = 3). Samples were incubated at 40 °C for ~2 h (0 and 2-h time points are shown in light and dark red, respectively). Temperature was dropped to 4 °C, and fluorescence was measured until the reading was stabilized (3 to 7 h; light-to-dark blue gradient). The blue and red gradient color bars denote incubation time at 4 and 40 °C, respectively. The gel formed by GB1-PRD$_{800\text{-}868}$ at 40 °C became fragile at 4 °C **(E, Lower)**. ThT assays were also carried out on PRD$_{800\text{-}868}$. Poor solubility of PRD$_{800\text{-}868}$ resulted in large variations in kinetic curves (n = 2) **(F)**. a.u., arbitrary units.

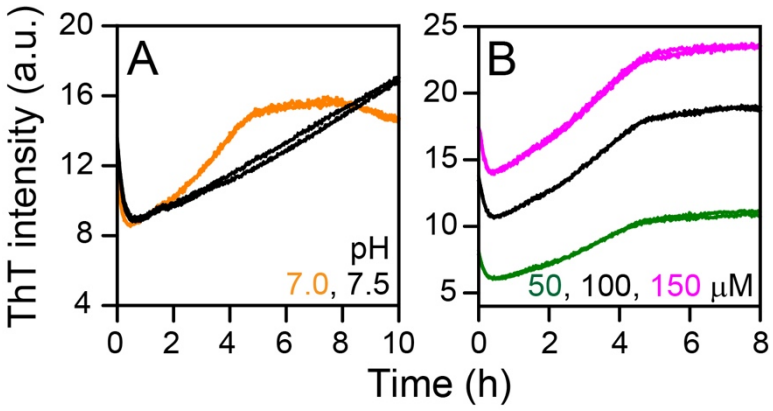

Figure 2.7.2: Aggregation kinetics of GB1-PRD$_{800-868}$ under quiescent conditions

ThT fluorescence were monitored under quiescent conditions to determine the effects of **(A)** pH and **(B)** concentration on the aggregation kinetics of GB1-PRD$_{800-868}$ (raw data of two replicates, $n = 2$, are plotted against time). Experiment and buffer conditions were as follows: (A) pH 7.0 (50 mM sodium phosphate), 7.5 (50 mM Tris) at [GB1-PRD$_{800-868}$] = 0.075 mM, 30 ºC. In addition, each buffer contained 1 mM DTT and 1mM EDTA. **(B)** 50 mM sodium phosphate, pH 7.0, 1 mM DTT and 1mM EDTA at 30 ºC.

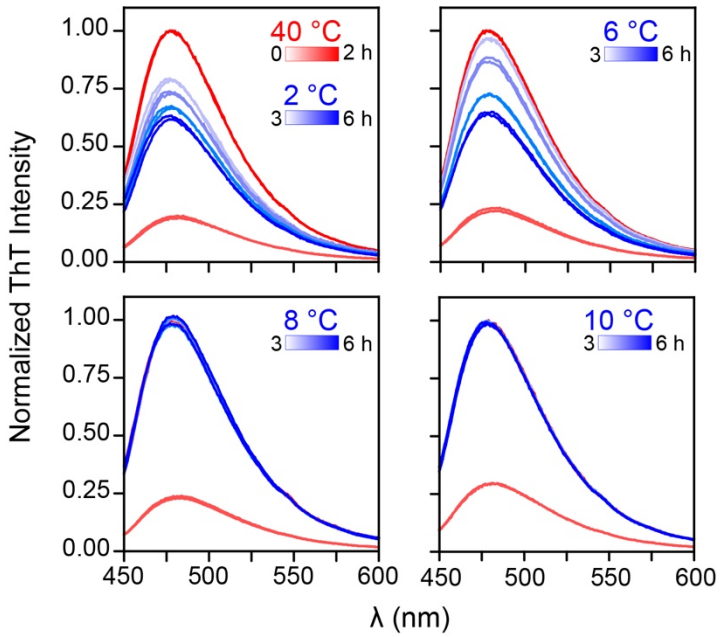

Figure 2.7.3: Effect of temperature on aggregation kinetics of GB1-PRD$_{800-868}$

ThT fluorescence of GB1-PRD$_{800-868}$ were monitored by fluorescence spectroscopy (plot shows raw data of two replicates, $n = 2$). Samples were incubated at 40 °C for ~2 h (0 and 2 h time points are shown in light and dark red, respectively). Temperature was dropped to a desired temperature (2, 6 and 8 °C, one at a time) and fluorescence were measured until the reading was stabilized (light to dark blue gradient). Buffer conditions were as follows: 50 mM sodium phosphate, pH 7.0, 1 mM DTT and 1mM EDTA at 30 ºC.

2.8 Src-mediated dissolution of GB1-PRD$_{800-868}$ amyloid fibrils

Src kinase was shown to hyperphosphorylate ALIX-PRD, culminating in a cellular redistribution of ALIX and initiating the formation of ESCRT-mediated intraluminal vesicles (26, 63). To study Src-PRD interactions, we carried out in vitro phosphorylation reactions using full-length Src. Recombinant full-length Src activity was measured using ADP-Glo assays (Fig. 2.8) and was found to be consistent with previous reports (64). PRD constructs, namely PRD$^{Strep}_{703-800}$ and PRD$_{800-868}$, were incubated with Src in the presence of adenosine triphosphate (ATP) (30 °C; incubation time: 5 h), and the products were monitored using Phos-tag SDS-PAGE (65). The latter is a modified version of SDS-PAGE that carries a phosphate-binding tag, which attenuates the migration of phosphorylated proteins, leading to a distinct separation of nonphosphorylated and phosphorylated species. Mobility shifts of phosphorylated PRD$_{800-868}$ products were readily visible (Fig. 2.8.1 A). No such shifts were observed for PRD$^{Strep}_{703-800}$, implying lack of phosphorylation (PRD$^{Strep}_{703-800}$ and PRD$_{800-868}$ contain 1 versus 14 tyrosines, respectively; cf., Fig. 2.1 A and D). To circumvent the poor solubility of PRD$_{800-868}$, a kinase reaction was carried out on GB1-PRD$_{800-868}$, and the corresponding mobility shifts indicated its phosphorylation. However, a control reaction carried out on the GB1 fusion tag revealed that the tag itself, comprising four tyrosines, undergoes residual phosphorylation in the presence of Src (Fig. 2.8.1 A and Table 2.2). Src-mediated phosphorylation of PRD$_{800-868}$ and the lack of phosphorylation of PRD$^{Strep}_{703-800}$ were unambiguously confirmed by Western blotting and MS (Fig. 2.8.1 B-D, respectively). LC-ESI-TOFMS analyses of in vitro kinase reactions revealed the formation of hyperphosphorylated PRD$_{800-868}$, elucidating phosphorylation of 9 (out of 18) and 4 (out of 14) tyrosine residues of GB1-PRD$_{800-868}$ and PRD$_{800-868}$, respectively (Fig. 2.8.1 C and D and Table 2.2). LC-tandem MS (LC-MS/MS) sequencing of chymotrypsin-digested GB1-PRD$_{800-868}$ revealed phosphorylation of the following PRD$_{800-868}$

tyrosine residues upon Src treatment: 803, 806, 829, 833, and 837 (Fig. 2.8.1 C, Upper; also see Fig. 2.8.2). Finally, we note that nothing definitive can be said about the phosphorylation status of remaining tyrosine residues of $PRD_{800\text{-}868}$, namely 809, 812, 821, 824, 826, 846, 854, 864, and 865, because of sequencing coverage gaps arising from problems associated with proteolytic digestion of $PRD_{800\text{-}868}$, which carries no native lysine and arginine residues (cf., Fig. 2.1 D) and, thus, is not amenable to traditional trypsin-based proteomics (66).

A previous report suggested direct interactions between the SH3 domain of Src and the ^{752}PQPPAR^{757} motif of ALIX-PRD (26). To investigate $PRD^{Strep}_{703\text{-}800}$ + Src interactions, NMR-titration experiments were carried out using NMR-visible $PRD^{Strep}_{703\text{-}800}$ and unlabeled Src (Fig. 2.8.3). With a minor exception of residues P754 and P759 ($^{13}C'/^{15}N$ cross-peak intensity ratios of ~0.55 and ~0.63, respectively), no discernible $^{1}H_N/^{15}N$ and $^{13}C'/^{15}N$ cross-peak intensity changes and chemical-shift perturbations were observed for $PRD^{Strep}_{703\text{-}800}$ on the addition of 3 molar equivalents of Src, indicating that full-length Src did not interact with $PRD^{Strep}_{703\text{-}800}$. The apparent discrepancy between these two results can be attributed to the use of full-length Src (this work) versus the isolated SH3 domain of Src (26). Recombinant Src is phosphorylated at multiple sites (Fig. 2.2.1 C) and, thus, likely exists in a clamped autoinhibited state (67). This closed conformation is expected to limit the access of the SH3 domain of Src to $PRD^{Strep}_{703\text{-}800}$, leading to no noticeable in vitro interactions between the two proteins. In line with these observations, the study mentioned above demonstrated that a constitutively active form of full-length Src that exists in an open conformation could interact with ALIX in Src-/-/Yes-/-/ Fyn-/- (SYF) mouse embryo fibroblasts (26). Our results are in agreement with a recently proposed model of Src-ALIX interactions in exosomes (63), in which active Src associated with ALIXPRD via its SH3 domain and these interactions were precluded by the clamped conformation of autoinhibited Src.

The impact of phosphorylation on the aggregation of GB1-PRD$_{800-868}$ was assessed using fluorescence and NMR spectroscopy. For ThT assays (Fig. 2.8 E), 150 μM GB1-PRD$_{800-868}$ samples were incubated with varying amounts of Src (1.5, 3, and 15 μM) and 2 mMATP (pH 7.5). As seen above (cf., Fig. 2.7.1 A-D), ThT signals at t0 were considerably higher than the baseline levels, likely due to the presence of preexisting GB1-PRD$_{800-868}$ aggregates. However, a complete loss of ThT signals was observed as phosphorylation proceeded in real time. The dissolution rates were proportional to the amount of Src and, therefore, to the rate of phosphorylation. Half-lives of GB1-PRD$_{800-868}$ aggregates were as follows: ∼1.5, ∼1.0, and ∼0.6 h at 30 °C for samples containing 1.5, 3, and 15 μMSrc, respectively. Corresponding control experiments carried out on GB1-PRD$_{800-868}$ + Src samples (without ATP) displayed characteristic sigmoidal profiles, indicating that the presence of Src per se does not hinder GB1-PRD$_{800-868}$ aggregation. In a separate experiment, 3 μM Src + 2 mM ATP was added to 150 μM GB1-PRD$_{800-868}$ samples upon reaching a stationary phase, which resulted in a significant loss of ThT signal with the corresponding half-life of ∼1 h (Fig. 2.8.1 F). These observations indicate that both preformed GB1-PRD$_{800-868}$ aggregates at t0 as well as aggregates formed in the plateau phase are susceptible to Src-mediated dissolution and establish that Src-mediated phosphorylation results in the dissolution of GB1-PRD$_{800-868}$ fibrils.

Src-mediated dissolution of GB1-PRD$_{800-868}$ assemblies was further validated by NMR spectroscopy (Fig. 2.8.1 G). Two ^{15}N-^{1}H TROSY-HSQC spectra were recorded on ^{15}N-labeled GB1-PRD$_{800-868}$ in the presence of Src and ATP. The spectrum recorded at t_0 exhibited spectroscopic signs of aggregation, i.e., resonances were broadened beyond the limits of detection (Fig. 2.8.1 G, Inset), confirming the presence of very high-molecular-weight GB1-PRD$_{800-868}$ aggregates at t0. The reaction was allowed to proceed for 5 h, whereupon the same sample yielded

a well-dispersed, high-quality spectrum (Fig. 2.8.1 G). These observations established that phosphorylation dissolves GB1-$PRD_{800-868}$ amyloids into NMR-amenable species that are likely monomeric. Control experiments were carried out on the GB1 fusion tag in the presence of Src and ATP under identical conditions. A near-perfect superimposition of spectra of these two proteins, phosphorylated GB1-$PRD_{800-868}$ against phosphorylated GB1 tag, allowed a ready identification of $PRD_{800-868}$ resonances. A narrow backbone amide proton dispersion of $PRD_{800-868}$ cross-peaks, ~7.3 to ~8.7 ppm, revealed that (phosphorylated) $PRD_{800-868}$, like its N-terminal counterpart, $PRD^{Strep}_{703-800}$, is also disordered in solution. Taken together, the above observations corroborate and confirm that GB1-$PRD_{800-868}$ forms reversible amyloid fibrils.

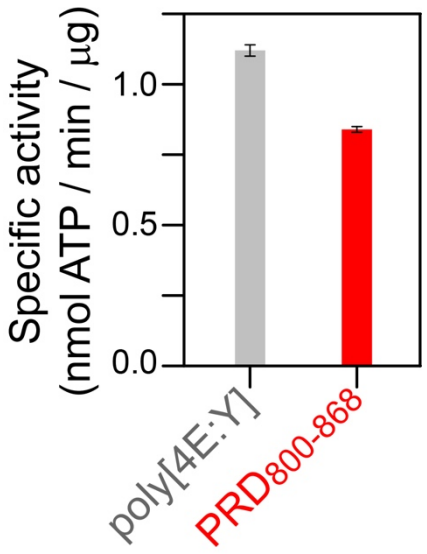

Figure 2.8: Quantification of recombinant Src kinase activity

Activity of recombinant Src was measured using ADP-Glo assay. Data are expressed as means ± s.e.m. of three replicates. These results, especially specific activity against poly[4E:Y] kinase substrate, are consistent with previous reports (64). Buffer and experimental conditions were as follows: 50 mM Tris, pH 7.5, 1 mM ATP, 5 mM $MgCl_2$, 0.5 mM EDTA, 2 mM DTT, and 25 °C.

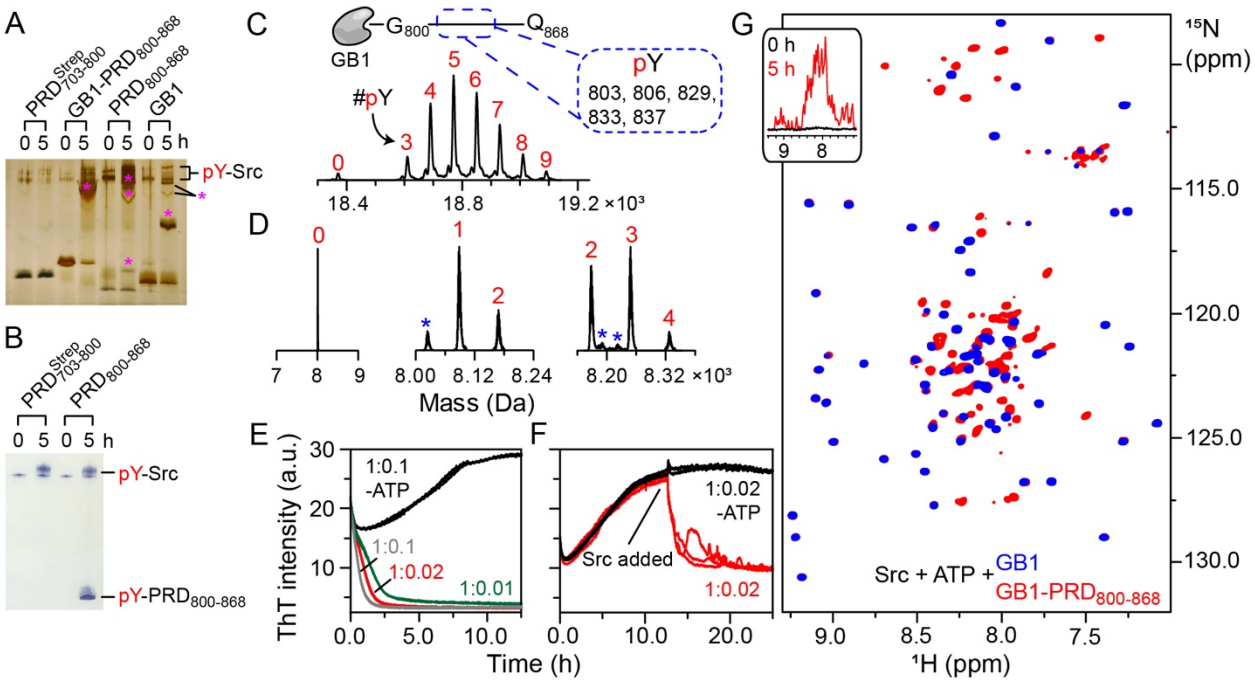

Figure 2.8.1: Dissolution of GB1-PRD$_{800-868}$ amyloids upon Src-mediated tyrosine hyperphosphorylation

(A-D) Characterization of in vitro phosphorylation of PRD constructs using Phos-tag SDS-PAGE **(A)**, Western blotting **(B)**, and MS **(C and D)**. For Phos-tag gel, the following constructs, namely PRD$^{Strep}_{703-800}$, GB1-PRD$_{800-868}$, PRD$_{800-868}$, and the GB1 tag, were incubated with Src (substrate to kinase molar ratio: 1:0.01). Phosphorylated products were visualized by silver staining and are marked by pink asterisks. **(B)** In vitro phosphorylation of PRD$^{Strep}_{703-800}$ and PRD$_{800-868}$ by Western blotting. **(C and D)** LC-ESI-TOFMS and LC-MS/MS analyses of in vitro phosphorylation reactions revealed hyperphosphorylated states of GB1-PRD$_{800-868}$ **(C)** and PRD$_{800-868}$ **(D)**. A schematic representation of GB1-PRD$_{800-868}$ along with phosphorylated tyrosines (dashed rectangle) are shown above the graph in **(C)**. The numbers in red represent the number of phosphorylated tyrosines, labeled as pY (peaks marked with blue asterisks represent sodium/iron adducts; Table 2.2). **(E-G)** The impact of tyrosine phosphorylation on aggregation kinetics of GB1-PRD$_{800-868}$ was assessed using ThT assays **(E and F)** and NMR spectroscopy **(G)**. For ThT assays (n = 3) **(E)**, 150 µM GB1-PRD$_{800-868}$ samples were incubated at 30 °C with 2 mM ATP and varying concentrations of Src (molar ratios: 1:0.1 [gray], 1:0.02 [red], and 1:0.01 [green]). a.u., arbitrary units. Control experiments were carried out on a GB1-PRD$_{800-868}$ + Src mixture in the absence of ATP (black; molar ratio: 1:0.1). **(F)** Samples of 150 µM GB1-PRD$_{800-868}$ were incubated at 30 °C without Src (n = 5) for ~11 h. Src + ATP were then added to three samples (red), whereas the remaining two (black) received only Src. G shows the overlay of expanded regions of the ^{1}H-^{15}N TROSY-HSQC spectra of phosphorylated GB1-PRD$_{800-868}$ (red) and the phosphorylated GB1 tag (blue). Both were incubated with Src (molar ratio: 1:0.1) in the presence of 2mMATP for 5 h at 30 °C. **(G, Inset)** Corresponding one-dimensional profiles of ^{15}N-labeled GB1-PRD$_{800-868}$ recorded at 0 and 5 h (black and red, respectively) after addition of unlabeled Src and ATP.

Table 2.2: LC-ESI-TOFMS analysis of Src-mediated phosphorylation of GB1-PRD$_{800-868}$ and PRD$_{800-868}$ constructs

All masses are in Daltons. GB1-PRD$_{800-868}$ and PRD$_{800-868}$ contain 18 and 14 tyrosine residues, respectively. GB1-PRD$_{800-868}$ and PRD$_{800-868}$ samples were incubated with recombinant Src (molar ratio 5:1) at 30 °C for 1 h. Reactions were quenched by heat-shock (90 °C) and the resultant mixtures were subjected to LC-ESI-TOFMS analysis. Buffer conditions were as follows: 50 mM Tris, pH 7.5, 50 mM NaCl, 0.5 mM EDTA, 5 mM $MgCl_2$, and 16 ng/µL of bovine serum albumin (BSA). Interactions between cleaved N-terminal fusion tag, GB1-6xHis-TEV, and Src were also analyzed by LC-ESI-TOFMS and revealed formation of 2 phosphorylated adducts (note that GB1-6xHis-TEV contains 4 tyrosine residues). In addition to non- and phosphorylated products, the following adducts were observed for PRD$_{800-868}$ sample (marked with blue asterisks in Fig. 2.7 D) - 8024 Da, 8190 Da and 8222 Da. These are most likely due to hydroxylation, and in the latter two cases, Na and Fe-adducts, respectively. Poor signal of PRD$_{800-868}$ sample might also mean that these are artifacts of electrospray ionization.

# pY	Experimental	GB1-PRD$_{800-868}$ calculated	Difference	Experimental	PRD$_{800-868}$ calculated	Difference
0	18,370	18,370	0	8,009	8,009	0
1	-	18,450	NA	8,088	8,089	-1
2	-	18,530	NA	8,168	8,169	-1
3	18,610	18,610	0	8,248	8,249	-1
4	18,690	18,690	0	8,327	8,329	-2
5	18,770	18,770	0	-	-	NA
6	18,850	18,850	0	-	-	NA
7	18,930	18,930	0	-	-	NA
8	19,010	19,010	0	-	-	NA
9	19,092	19,090	+2	-	-	NA

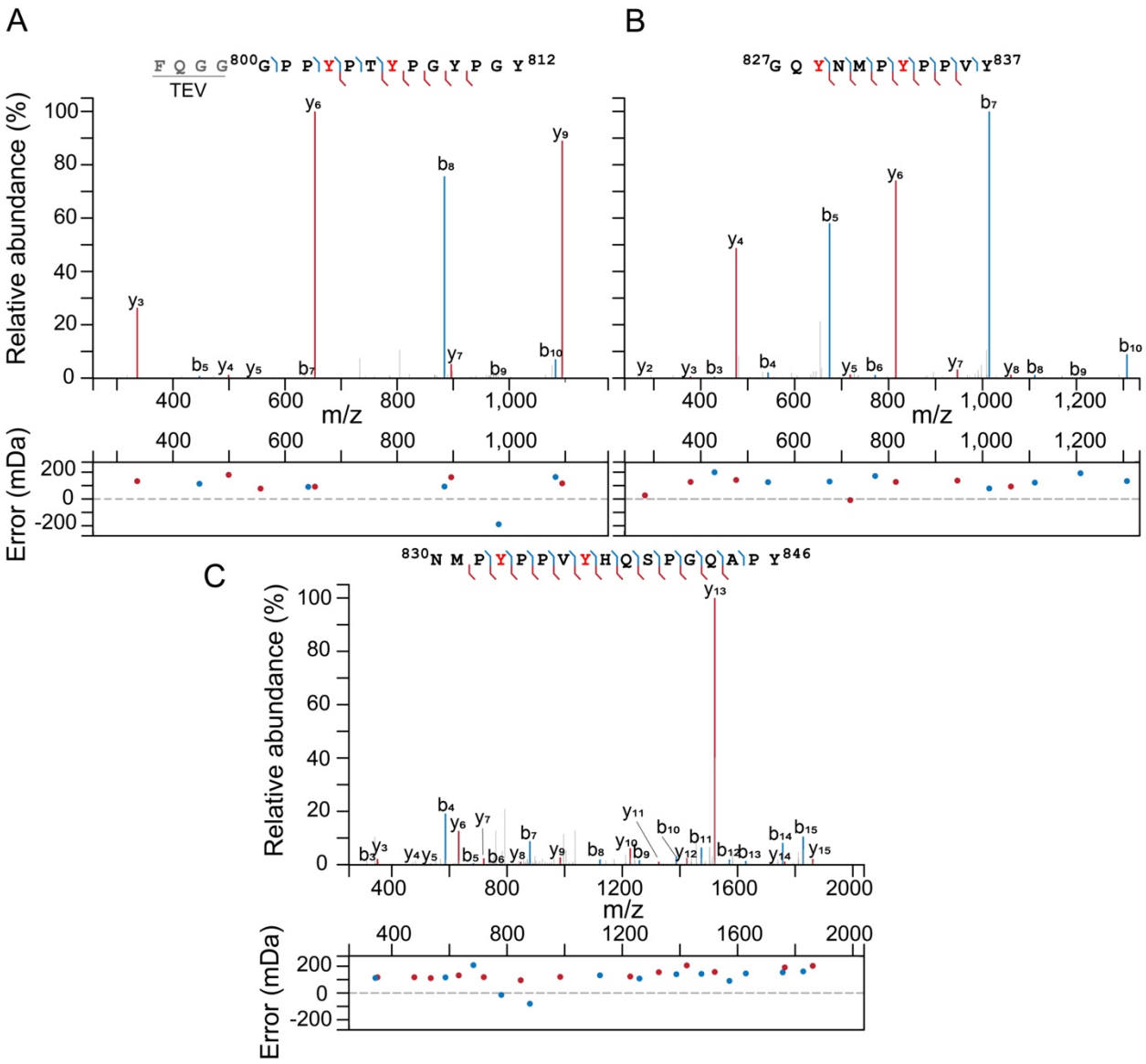

Figure 2.8.2: LC-MS/MS analyses of Src-mediated phosphorylation of GB1-PRD$_{800\text{-}868}$

(A - C) Panels show assignment of collision-induced dissociation (CID) fragment ions to the peptide primary sequence according to the standard nomenclature (97). The phosphorylated tyrosine residues are denoted in red. The b_n and y_n ions are denoted by the blue and red brackets, respectively. Residuals (observed spectral position minus calculated m/z) for each fragment ion peak are plotted below the panels. Figure was formatted using IPSA (98).

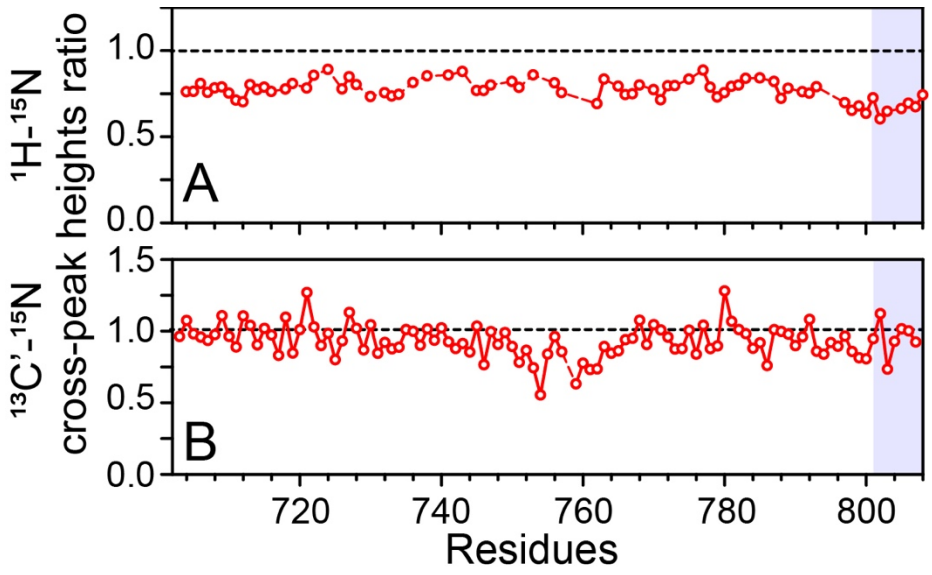

Figure 2.8.3: NMR analysis of $PRD^{Strep}_{703-800}$ + Src kinase interactions

Changes in **(A)** $^{1}H/^{15}N$ and **(B)** $^{13}C'/^{15}N$ cross-peak intensities upon addition of molar excess of Src to $PRD^{Strep}_{703-800}$ sample. 2D ^{1}H-^{15}N TROSY-HSQC and ^{13}C-^{15}N CON experiments were recorded on uniformly ^{15}N and $^{15}N/^{13}C$-labeled $PRD^{Strep}_{703-800}$ sample (in the absence and the presence of molar excess of non-labeled Src kinase). Note that ^{13}C-^{15}N CON correlates the amide nitrogen with the carbonyl carbon of the preceding residue and thus is the experiment of choice to analyze proline-rich IDPs (18). Negligible changes in ratios of cross-peak intensities (except residues P754 and P759; $^{13}C'/^{15}N$ cross-peak intensity ratios of ~ 0.55 and ~ 0.63, respectively), as well as chemical shifts (≤ 0.03 ppm) between the two proteins, indicate a lack of association between full-length Src and $PRD^{Strep}_{703-800}$. Buffer and experimental conditions were as follows: 20 mM sodium phosphate, pH 6.5, 50 mM NaCl, 2 mM EDTA, 1 mM TCEP, and 30 °C. The concentration of isotopically labeled $PRD^{Strep}_{703-800}$ was 25 μM, while concentration of non-labeled Src was 75 μM. Errors are given by $\{\text{ratio} \times ((\text{noise}_1/\text{height}_1)^2 + (\text{noise}_2/\text{height}_2)^2)^{1/2}\}$.

2.9 Concluding remarks

In summary, we made use of two recombinant constructs ($PRD^{Strep}_{703\text{-}800}$ and $PRD_{800\text{-}868}$) to carry out a thorough characterization of ALIX-PRD in solution (Fig. 2.1). We performed a detailed NMR characterization of the conformational plasticity of $PRD^{Strep}_{703\text{-}800}$ (a 98-residue polypeptide representing the N-terminal portion of ALIX-PRD) and carried out quantitative analyses of its interactions with TS˙G101-UEV. In addition, we uncovered remarkable aggregation properties of $PRD_{800\text{-}868}$ (a 69-residue polypeptide representing the tyrosine-rich C-terminal portion of ALIX-PRD), which forms amyloids under near physiological conditions that dissolve upon posttranslational modifications (Src-mediated tyrosine phosphorylation) or at low temperatures (2 to 6 °C).

2.9.1 Interactions between ALIX-PRD and TSG101-UEV

NMR-backbone chemical shifts, 3JHNHα couplings, and ^{15}N-relaxation rates indicate that $PRD^{Strep}_{703\text{-}800}$ is disordered in solution with no indication of any significant secondary-structure propensity (Fig. 2.3.1). NMR-titration experiments demonstrate that $PRD^{Strep}_{703\text{-}800}$ contains three PTAP-like motifs, namely ^{717}PSAP^{720}, ^{769}PSAT^{772}, and ^{790}PGSAP^{794}, which compete for a single binding site on TSG101-UEV (Figs. 2.3, Fig. 2.5 and Fig. 2.4). ^{15}N-relaxation measurements carried out on $PRD^{Strep}_{703\text{-}800}$ in the presence of TSG101-UEV show a lack of global ordering upon complex formation but point to local ordering around the interaction sites of $PRD^{Strep}_{703\text{-}800}$ (Fig. 2.4.1). Quantitative analyses of ^{15}N-CPMG dispersion data (Fig. 2.6) indicate low-affinity interactions for each of the three PTAP-like motifs (~0.6 to ~7 mM) and elucidate that the N-terminal ^{717}PSAP^{720} motif is the primary site of interaction, whereas the other two sites, ^{769}PSAT^{772} and ^{790}PGSAP^{794}, are secondary. These observations are in excellent agreement with a previous in vivo study (30), which indicated that mutations in the ^{717}PSAP^{720} motif did not abolish ALIX-

TSG101 interactions. They are also consistent with the fact that among the three PTAP-like motifs of ALIX-PRD, the ^{717}PSAP^{720} motif is completely conserved among vertebrates (Fig. 2.1.1). The analyses of CPMG dispersions allowed us to quantitate the amount of complex formed between each of the three PTAP-like motifs in the context of $PRD^{Strep}_{703\text{-}800}$ and TSG101-UEV, as well as populations of higher-order complexes in which two PTAP-like motifs are simultaneously occupied by two TSG101-UEV molecules (steric hindrance between ^{769}PSAT^{772} and ^{790}PGSAP^{794} motifs is likely to prevent a 1:3 stoichiometry between $PRD^{Strep}_{703\text{-}800}$ and TSG101-UEV). We hypothesize that the conformational plasticity of disordered $PRD^{Strep}_{703\text{-}800}$ will provide plausible opportunities for its unbound PTAP-like motifs to (re)bind before they diffuse out of proximity of TSG101-UEV. Since the C-terminal PRD forms amyloidogenic aggregates, in the event of PRD-mediated oligomerization of ALIX, we predict that ALIX oligomers will exhibit a markedly increased binding affinity to TSG101-UEV. These observations agree with a prior in vivo study (30), which showed that the multimerization-deficient ALIX constructs carrying the C-terminal PRD deletions and mutations were unable to interact with TSG101 despite comprising all three PTAP-like motifs mentioned above. Moreover, restoration of ALIX multimerization via a chimeric attachment of a GCN4 leucine zipper was shown to reinstate binding to TSG101. The lack of in vivo interactions between monomeric ALIX and TSG101 confirms the ultraweak nature of these interactions. The additive effect of multivalency is likely responsible for generating detectable in vivo interactions between the two proteins upon ALIX oligomerization. In addition to the UEV domain, full-length TSG101 comprises a coiled-coil domain that is shown to form tetrameric assemblies in solution (68). Based on these observations, we predict a dramatic increase in avidity for interactions between ALIX oligomers and TSG101 tetramers in vivo.

2.9.2 Amyloid fibrils of ALIX-PRD

The amyloid fibrils and gel of $PRD_{800-868}$, visualized by negative-stain EM, revealed rope-like unbranched assemblies and a dense phase comprising an intertwined fibrous network, respectively (Fig. 2.7). In addition, fibril formation yielded a characteristic ThT-fluorescence enhancement (Fig. 2.7.1). Aggregation kinetics of $PRD_{800-868}$, monitored by ThT fluorescence, show that aggregation is influenced by pH and ionic strength (faster aggregation at pH 7.0 and zero ionic strength) as well as by temperature, with high temperatures promoting aggregation (∼10-fold increase in aggregation at 40 versus 25 °C) and low temperatures (2 to 6 °C), promoting dissolution of amyloid fibrils. The discovery that temperature affects aggregation kinetics highlights the potential role of the hydrophobic effect in the formation of $PRD_{800-868}$ fibrils. It is well known that the clustering of hydrophobic groups in polar solvents gives rise to a temperature-dependent hydrophobic effect that peaks between 30 and 80 °C and becomes weaker at lower and higher temperatures (69). Since the initial protein concentration did not affect the aggregation rates (Fig. 2.7.1 C), we hypothesize that aggregation of $PRD_{800-868}$ is primarily governed by a monomer-independent secondary-nucleation step in the form of fibril fragmentation (61). Further, we speculate that the presence of ∼20% tyrosines in $PRD_{800-868}$ (Fig. 2.1 D) drives its fibril formation through extensive stacking of aromatic rings of tyrosine residues accompanied by hydrophobic CH/π tyrosine-proline interactions (70). The remarkable conservation of $PRD_{800-868}$ among vertebrates, with a near-complete conservation of tyrosine and proline residues (Fig. 2.1.1), supports this hypothesis. It is further supported by the phosphorylation-mediated dissolution of amyloid fibrils (Fig. 2.8.1), where the introduction of negatively charged phosphate groups creates charge repulsion. Surprisingly, aggregates formed at the stationary phase are also susceptible to phosphorylation-mediated dissolution (Fig. 2.8.1 F), which provides important clues about their

structure. We hypothesize that a few tyrosine residues are solvent-exposed in $PRD_{800-868}$ aggregates and, therefore, accessible for Src-mediated phosphorylation. Charge-repulsion created by phosphorylation of these tyrosine residues will likely initiate the disassembly. We hypothesize that both soluble and insoluble aggregates are present at the stationary phase and that the soluble aggregates are amenable to Src-mediated dissolution, whereas insoluble fibrils are inaccessible to Src. This hypothesis is supported by the fact that the addition of an Src + ATP mixture to $PRD_{800-868}$ samples at the stationary phase does not culminate in a complete loss of ThT signal, indicating the presence of residual fibrils in the $PRD_{800-868}$ samples.

2.9.3 ALIX-PRD polymerization and ALIX function

The ESCRT-III proteins, CHMPs, polymerize into filamentous structures and are the main drivers of ESCRT-mediated membrane remodeling (19, 20). Note that the CHMP4 paralogues (CHMP4A and -B; Snf7 in yeast) are the most abundant components of ESCRT-III. The CHMP4 proteins exist as soluble monomers in solution and, therefore, need to be activated. This is achieved by nucleation factors, which trigger the polymerization of CHMP4. ALIX is a well-known nucleator factor of CHMP4 proteins (71). The N-terminal Bro1 domain of ALIX directly binds to and nucleates CHMP4 (72). The Bro1 domain interacts with lysobisphosphatidic acid, a phospholipid found in late endosomes, which allows ALIX to mediate the highly selective recruitment of CHMP4 paralogs to late endosomes (73). Based on our results, we predict that the oligomerization of ALIX mediated by the amyloidogenic assemblies of the C-terminal PRD will likely result in a multiplicative increase in binding affinity between the Bro1 domain and CHMP4 proteins, resulting in nucleation and polymerization of CHMP4. ALIX colocalizes with active Src in endosomal membranes (63). This ultimately drives the relocation of ALIX to the cytoplasm and reduces its association with its binding partners (26). Our results are in excellent agreement with

this in vivo study as we show that hyperphosphorylation of $PRD_{800-868}$ by Src shifts the equilibrium toward soluble monomeric species. Finally, we note that the N-terminal portion of ALIX-PRD is implicated in interdomain interactions with the N-terminal Bro1 domain, resulting in a closed conformation of ALIX (29). The preliminary NMR-titration experiments carried out using NMR-visible $PRD^{Strep}_{703-800}$ and unlabeled recombinant Bro1 domain did not yield any noticeable in vitro interactions between these two domains. Therefore, we cannot say anything definitive about these interdomain interactions of ALIX.

PRDs are often viewed as a collection of proline-rich motifs that serve as points of interactions for their signaling partners. Data presented here provide detailed quantitative analyses of interactions of a PRD with its binding partner. Our data also show that a PRD can form reversible amyloids and viscous gels. An array of "functional" amyloids that play physiological roles in humans have recently been identified, and a few of them have been shown to dissolve under physiological conditions (74). Further investigation is needed to determine whether amyloid formation of ALIX occurs in vivo and to uncover the exact cellular function(s) of these aggregates. From an application perspective, however, a reversible amyloid is of great significance for the development of novel biopolymers (75) that can be used for targeted drug delivery, tissue engineering, development of biosensors, and others.

2.10 Experimental procedures

2.10.1 Data availability

The ALIX-PRD plasmids, namely $PRD^{Strep}_{703-800}$and $PRD_{800-868}$, have been deposited in the Addgene Repository, https://www.addgene.org/ (accession nos. 141344 [$PRD^{Strep}_{703-800}$] and 141345 [$PRD_{800-868}$]). The chemical-shift assignments of $PRD^{Strep}_{703-800}$ have been deposited in the Biological

Magnetic Resonance Bank, http://www.bmrb.wisc.edu/ (accession no. 28111) (76). The coordinates of the docking model have been deposited in the Protein Model DataBase, http://srv00.recas.ba.infn.it/PMDB/ (accession no. PM0083242) (77).

2.10.2 Materials

Isopropyl β-d-1-thiogalactopyranoside (IPTG) and arabinose were purchased from Sigma-Aldrich (catalog no. 420322 and A3256, respectively). Thioflavin T (ThT) was purchased from Thermo Fisher Scientific (catalog no. AC211760050) and was dissolved in MilliQ water (MilliQ IQ 7000 purification system, Millipore-Sigma) at the concentration of 1 mM. Congo red (CR) was purchased from Sigma-Aldrich (catalog no. C6277) and was dissolved in MilliQ water at the concentration of 0.2% wt/vol. Adenosine 5'-triphosphate (ATP) was purchased as a 100 mM buffered solution, pH 7.5, from Thermo Fisher Scientific (catalog no. R1441) and was used without further modifications. Precast Phos-tag SDS-PAGE gels were purchased from VWR (catalog no. 103258-494). Phospho-tyrosine mouse monoclonal antibody was obtained from Cell Signaling Technology (catalog no. 9411). Secondary antibody, goat anti-mouse IgG, was obtained from Thermo Fisher Scientific (catalog no. G-21040). Pierce silver stain and ADP-Glo kinase assay kits were purchased from Thermo Fisher Scientific (catalog no. 24612) and Promega corporation (catalog no. V6930), respectively and were used according to the manufacturers' protocols. Chymotrypsin was purchased from Sigma-Aldrich (catalog no. C4129) and dissolved in a buffer containing 1 mM HCl and 2 mM $CaCl_2$, at the concentration of 2 mg/mL. Peptide substrate for Src kinase was obtained from Sigma-Aldrich (catalog no. P7244). Reagents for NMR isotopic enrichment were obtained from Cambridge Isotopes Laboratories (CIL) and Sigma-Aldrich.

2.10.3 Recombinant Protein Expression and Purification

Codon-optimized ALIX-PRD constructs (Uniprot accession no. Q8WUM4), namely GB1-$PRD^{Strep}_{703-868}$, GB1-$PRD^{Strep}_{703-815}$, GB1-$PRD^{Strep}_{703-800}$ and GB1-$PRD_{800-868}$ were subcloned in pET11a (Novagen, EMD Millipore) and were expressed in BL21(DE3) competent cells (Agilent, catalog no. 200131). Note that GB1 implies the B1 domain of protein G (35), used to enhance the expression levels, followed by a polyhistidine (6xHis) affinity tag, and a tobacco etch virus (TEV) protease cleavage site. Wild-type full-length human Src kinase construct, pEX-Src-C-His; Uniprot accession no. P12931, was a generous gift from the van der Vliet Group (University of Vermont) and was used without further modifications. Src kinase was expressed in BL21-AI cells (Thermo Fisher Scientific, catalog no. C607003). TEV protease construct was a generous gift from David S. Waugh (National Cancer Institute, National Institutes of Health). Construct expressing UEV domain of TSG101 (Uniprot accession no. Q99816), hereafter referred to as TSG101-UEV, was a generous gift from the Tjandra Group (National Heart, Lung and Blood Institute, National Institutes of Health).

GB1-$PRD^{Strep}_{703-800}$ was expressed at 16 °C, whereas GB1-$PRD_{800-868}$ was expressed at 37 °C. Briefly, cells were grown at 37 °C in 1 L Luria-Bertani (LB) medium (MP Biomedicals, catalog no. 3002-036) at natural isotopic abundance or minimal M9 medium for isotopic labeling. The latter contained 1 g/L $^{15}NH_4Cl$ (CIL) and/or 3 g/L $^{13}C_6$-d-glucose (CIL) for ^{15}N and $^{15}N/^{13}C$ labeling, respectively. For GB1-$PRD^{Strep}_{703-800}$, ~30 min prior to induction, the temperature of cell culture was reduced to 16 °C. Cells were induced with 1 mM IPTG at an optical density of A_{600} ~0.8. For GB1-$PRD_{800-868}$, cells were harvested ~4 h after induction, whereas for GB1-$PRD^{Strep}_{703-800}$, cells were harvested after ~48 h. Full-length human Src kinase was expressed as described

previously (64). Briefly, cells were grown at 37 °C in 1 L Terrific Broth (TB) medium (Thermo Fisher Scientific, catalog no. BP9728) at natural isotopic abundance. About 30 min prior to induction, the temperature of cell culture was reduced to 16 °C. Cells were induced with 0.2 % wt/vol arabinose and 1 mM IPTG at an optical density of A_{600} ~0.8 and were harvested ~24 h after induction. For TEV protease, cells were grown at 37 °C in 1 L LB medium and harvested ~3 h after induction with 1 mM IPTG. For TSG101-UEV, cells were grown at 37 °C in 1 L LB at natural isotopic abundance or M9 medium for isotopic labeling. The latter contained 0.3 g/L $^{2}H/^{15}N/^{13}C$ Isogro (Sigma-Aldrich), 99.9% (vol/vol) D_2O (CIL), 1 g/L $^{15}NH_4Cl$ (CIL), and 3 g/L $^{2}H_7$, $^{13}C_6$-d-glucose (Sigma-Aldrich) for $^{2}H/^{15}N/^{13}C$ labeling and 0.3 g/L $^{2}H/^{15}N$ Isogro (Sigma-Aldrich), 99.9% (vol/vol) D_2O, 1g/L $^{15}NH_4Cl$ (CIL), and 3g/L $^{2}H_7$,$^{12}C_6$-d-glucose (CIL) for $^{2}H/^{15}N$ labeling.

Both PRD constructs, namely GB1-$PRD^{Strep}_{703\text{-}800}$ and GB1-$PRD_{800\text{-}868}$, were purified using a combination of affinity chromatography (ÄKTA Pure protein purification system, GE Healthcare) and reverse-phase HPLC (1260 Infinity II liquid chromatography system, Agilent Technologies). The cells were resuspended in a lysis buffer containing 50 mM Tris, pH 8.0, and 250 mM NaCl. For both constructs, cells were lysed by heat-shock (80 °C, ~5 minutes) and cleared by centrifugation (48,380 × g, 25 minutes). In the case of GB1-$PRD^{Strep}_{703\text{-}800}$, lysis buffer also contained 2 mM Ethylenediaminetetraacetic acid (EDTA). For GB1-$PRD^{Strep}_{703\text{-}800}$, the cell lysate was loaded onto a Streptactin Sepharose column (GE Healthcare) and eluted in the same buffer containing 2.5 mM d-desthiobiotin (Sigma-Aldrich). The eluted GB1-$PRD^{Strep}_{703\text{-}800}$ protein was mixed with recombinant TEV protease (molar ratio 50:1) in the presence of 1 mM dithiothreitol (DTT; Sigma-Aldrich) to hydrolyze the N-terminal GB1 solubility tag. Proteolysis was allowed to proceed at room temperature for ~12 h and was assessed for completion by SDS-PAGE (NuPAGE 4-12% Bis-Tris gel; Thermo Fisher Scientific). Hydrolyzed product, $PRD^{Strep}_{703\text{-}800}$, was further purified

using reverse-phase HPLC (Jupiter 10 μm C18 300 Å column; Phenomenex, catalog no. 00G-4055-N0) with 5-55% acetonitrile gradient comprising 0.05% trifluoroacetic acid (TFA, Sigma-Aldrich). The eluted protein was freeze-dried (Labconco -84 °C Benchtop Freeze Dryer) and was stored at -80 °C before use. For GB1-$PRD_{800-868}$, the cell lysate was loaded onto a HisTrap column (GE Healthcare) with a 0-1 M imidazole gradient containing 50 mM Tris, pH 8.0, and 250 mM NaCl. The eluted protein was further purified using reverse phase HPLC (Jupiter 10 μm C18 300 Å column) and was freeze-dried. The freeze-dried fraction was reconstituted in an aqueous buffer containing 50 mM Tris, pH 8.0, 250 mM NaCl and 1 mM DTT. The resultant solution was mixed with TEV protease (molar ratio 10:1). The proteolysis reaction was carried out at room temperature (~12 h) and produced a poorly soluble hydrolyzed product, $PRD_{800-868}$. The corresponding $PRD_{800-868}$ precipitate was cleared by addition of 6 M guanidine hydrochloride to the reaction mixture. Reaction products were further purified using reverse phase HPLC (Jupiter 10 μm C18 300 Å column). The eluted $PRD_{800-868}$ fractions were pooled, lyophilized, and stored at -80 °C. Lyophilized GB1-$PRD_{800-868}$ and $PRD_{800-868}$ samples were treated with ammonium hydroxide to break up amyloid aggregates (62). Briefly, lyophilized peptides were dissolved in 10% wt/vol ammonium hydroxide (Sigma-Aldrich) at the concentration of ~1 mg/mL. Samples were incubated at room temperature for ~5 minutes, followed by sonication (~5 minutes; Elmasonic P ultrasonic bath) and lyophilization. The freeze-dried salt-free fractions were reconstituted in an aqueous buffer containing 50 mM Tris, pH 7.5, 0.5 mM EDTA and 2 mM DTT. Purification of GB1-$PRD^{Strep}_{703-868}$ and GB1-$PRD^{Strep}_{703-815}$ constructs revealed ribosomal stalling induced by polyproline stretches. We identified 4 problematic regions that resulted in production of truncated fragments (see Fig. 2.1.2). We were, therefore, unable to purify these two constructs, namely GB1-$PRD^{Strep}_{703-868}$ and GB1-$PRD^{Strep}_{703-815}$.

For Src kinase, the cells were resuspended in a lysis buffer containing 50 mM Tris, pH 8.0, and 250 mM NaCl. Cells were lysed using a homogenizer, EmulsiFlex-C3 (Avestin), and cleared by centrifugation. Cell lysate was loaded onto a HisTrap column (GE Healthcare) with a 0-1 M imidazole gradient containing 50 mM Tris, pH 8.0, and 250 mM NaCl. The eluted protein was loaded onto a Q Sepharose HP column (GE Healthcare) with a 0-1 M NaCl gradient in a buffer containing 50 mM Tris, pH 8.0, and 5 mM β-mercaptoethanol (BME). The eluted fractions were pooled, concentrated (Amicon ultra-15, 30-kDa cutoff) and were loaded onto a HiLoad 26/600 Superdex 75 pg column (GE Healthcare) pre-equilibrated with 50 mM Tris, pH 7.5, 250 mM NaCl, and 5 mM BME. Relevant fractions were pooled and concentrated to ~1 mg/mL (Amicon ultra-15, 30-kDa cutoff). Samples were aliquoted and flash-frozen and were stored at -80 °C.

For TEV protease, the cells were resuspended in a lysis buffer containing 50 mM Tris, pH 8.0, and 250 mM NaCl. Cells were lysed using EmulsiFlex-C3 and cleared by centrifugation. Cell lysate was loaded onto a HisTrap column (GE Healthcare) with a 0-1 M imidazole gradient containing 50 mM Tris, pH 8.0, and 250 mM NaCl. The eluted protein was concentrated (Amicon ultra-15, 10-kDa cutoff) and loaded onto a HiLoad 26/600 Superdex 75 pg column (GE Healthcare) pre-equilibrated with 50 mM Tris, pH 8, 250 mM NaCl and 1 mM DTT. Relevant fractions were pooled and concentrated to ~1 mg/mL (Amicon ultra-15, 10-kDa cutoff). TEV samples were aliquoted and flash-frozen and were stored at -80 °C.

In the case of TSG101-UEV, the cells were resuspended in a lysis buffer containing 50 mM Tris, pH 8.0, and 250 mM NaCl. Cells were lysed using EmulsiFlex-C3 and cleared by centrifugation. Cell lysate was loaded onto a HisTrap column (GE Healthcare) with a 0-1 M imidazole gradient containing 50 mM Tris, pH 8.0, and 250 mM NaCl. The eluted protein was concentrated (Amicon ultra-15, 10-kDa cutoff) and loaded onto a HiLoad 26/600 Superdex 75 pg

column (GE Healthcare) pre-equilibrated with 50 mM Tris, pH 8, 250 mM NaCl and 1 mM DTT. Relevant fractions were pooled and mixed with recombinant TEV protease to cleave off the N-terminal 6xHis tag (molar ratio 50:1). Reaction was carried out at room temperature (~12 h) and was assessed for completion using SDS-PAGE. Reaction mixture was loaded back onto HisTrap column (GE Healthcare). The resultant flow-through fractions were pooled, concentrated, and further purified by size exclusion chromatography (HiLoad 26/600 Superdex 75 pg column; GE healthcare). Relevant fractions were concentrated (~10 mg/mL; Amicon ultra-15, 10-kDa cutoff) and flash-frozen and were stored at -80 °C.

The above-mentioned purification schemes resulted in ≥ 99% pure proteins with the following yields: $PRD^{Strep}_{703\text{-}800}$ (~40 mg / L), $PRD_{800\text{-}868}$ (~15 mg / L), Src kinase (~5 mg / L) and TSG101-UEV (~10 mg / L); extreme care, however, is required while handling PRD constructs owing to their disordered nature and their susceptibility to proteolysis.

All protein constructs were verified by MS. Briefly, an Agilent 6230 time-of-flight mass spectrometer (TOFMS) with Jet Stream electrospray ionization source (ESI) was used for liquid chromatography (LC)-ESI-TOFMS analysis. The Jet Stream ESI source was operated under positive ion mode with the following parameters: V_{Cap} = 3500 V, fragmentor voltage = 175 V, drying gas temperature = 325 °C, sheath gas temperature = 325 °C, drying gas flow rate = 10 L / min, sheath gas flow rate = 10 L / min, nebulizer pressure = 40 psi. The chromatographic separation was performed at room temperature on a Phenomenex Aeris Widepore XB-C18 column (2.1 mm ID x 50 mm length, 3.6 µm particle size). HPLC-grade water and acetonitrile were used as mobile phases A and B, respectively. Each phase also carried 0.1% TFA. Agilent MassHunter software was used for data acquisition and analysis and MagTran software was used for mass spectrum deconvolution (78).

2.10.4 NMR sample preparation

All heteronuclear NMR experiments were carried out on uniformly ^{15}N- or $^{15}N/^{13}C$ -labeled PRD samples (unless stated otherwise). $PRD^{Strep}_{703-800}$ samples were reconstituted in a buffer containing 20 mM sodium phosphate, pH 6.5, 50 mM NaCl, 1 mM EDTA and 1 mM tris(2-carboxyethyl) phosphine (TCEP; Sigma-Aldrich). In the case of GB1-$PRD_{800-868}$ and $PRD_{800-868}$, lyophilized samples were initially treated with ammonium hydroxide to break up large amyloid aggregates (see above) and were reconstituted in a buffer containing 50 mM Tris, pH 7.5, 0.5 mM EDTA, and 2 mM DTT. Uniformly $^{15}N/^{2}H$- or $^{15}N/^{13}C/^{2}H$-labeled TSG101-UEV samples were prepared in a buffer containing 20 mM sodium phosphate, pH 6.5, 50 mM NaCl, 1 mM EDTA and 1 mM TCEP. Aligned TSG101-UEV samples (0.2 mM) were prepared using 5% PEG-hexanol (79). All NMR samples contained 7% vol/vol D_2O.

2.10.5 NMR Spectroscopy

All heteronuclear NMR experiments were carried out on uniformly ^{15}N- or $^{15}N/^{13}C$-labeled PRD samples (unless stated otherwise). $PRD^{Strep}_{703-800}$ samples were reconstituted in a buffer containing 20 mM sodium phosphate, pH 6.5, 50 mM NaCl, 1 mM EDTA and 1 mM tris(2-carboxyethyl) phosphine (TCEP; Sigma-Aldrich). In the case of GB1-$PRD_{800-868}$ and $PRD_{800-868}$, lyophilized samples were initially treated with ammonium hydroxide to break up large amyloid aggregates (see above) and were reconstituted in a buffer containing 50 mM Tris, pH 7.5, 0.5 mM EDTA, and 2 mM DTT. Uniformly $^{15}N/^{2}H$- or $^{15}N/^{13}C/^{2}H$-labeled TSG101-UEV samples were prepared in a buffer containing 20 mM sodium phosphate, pH 6.5, 50 mM NaCl, 1 mM EDTA and

1 mM TCEP. Aligned TSG101-UEV samples (0.2 mM) were prepared using 5% PEG-hexanol (79). All NMR samples contained 7% vol/vol D_2O.

NMR Spectroscopy. All heteronuclear NMR experiments were carried out at 30 °C on Bruker 600- and 800-MHz spectrometers equipped with z-gradient triple resonance cryoprobes. Spectra were processed using NMRPipe (80) and analyzed using the CCPN software suite (81). Sequential ^{1}H, ^{15}N, and ^{13}C backbone resonance assignments of TSG101-UEV and $PRD^{Strep}_{703-800}$ were carried out using conventional transverse relaxation optimized (TROSY)-based through-bond three-dimensional (3D) triple resonance experiments (82). For $PRD^{Strep}_{703-800}$, unambiguous assignments were made possible through a use of 3D (HACA)N(CA)CON experiment (18), which correlates the carbonyl carbon and amide-nitrogen of each residue with the amide-nitrogen of preceding residue and is, therefore, an optimal experiment to study proline-rich sequences. Apart from 3 residues (D703, S729 and H735), the entire backbone could be readily assigned using this strategy (~97% completion). NMR chemical shift perturbation experiments were carried out using 0.1 mM ^{15}N-labeled $PRD^{Strep}_{703-800}$ and non-labeled TSG101-UEV (0.025 mM - 0.5 mM). Identical experiments were carried out using 0.1 mM $^{15}N/^{13}C$-labeled $PRD^{Strep}_{703-800}$ and 0.3 mM TSG101-UEV with the help of 2D ^{13}C-^{15}N CON correlation experiment (18). Chemical shift perturbation experiments were also carried out between 0.1 mM $^{2}H/^{15}N$-labeled TSG101-UEV and 0.4 mM non-labeled $PRD^{Strep}_{703-800}$. $^{3}J_{HNH\alpha}$ couplings were measured on uniformly ^{15}N-labeled 0.5 mM $PRD^{Strep}_{703-800}$ sample with the help of a newly developed WATERGATE-optimized 2D TROSY pulse sequence (83). ^{15}N-R_1 and $R_1\rho$ measurements (84) were carried out on uniformly ^{15}N-labeled 0.1 mM $PRD^{Strep}_{703-800}$ samples (in the absence and presence of TSG101-UEV; 0.05, 0.1, 0.15, 0.2, 0.3 and 0.5 mM). ^{15}N-Carr-Purcell-Meiboom-Gill (CPMG) relaxation dispersions were recorded

on 0.1 mM $PRD^{Strep}_{703-800}$ samples (in the absence and presence of non-labeled TSG101-UEV; 0.2, 0.3 and 0.5 mM; one at a time) at two static spectrometer fields (600 and 800 MHz) with a constant-time period of 120 ms using a pulse scheme with amide proton decoupling that monitors the rates of in-phase ^{15}N coherences (85). Backbone amide ($^1D_{NH}$) RDCs were measured on 0.2 mM $^2H/^{15}N$-labeled TSG101-UEV using the TROSY-based ARTSY technique (86) and analyzed using Xplor-NIH (59). Effect of tyrosine phosphorylation on the aggregation state of $GB1\text{-}PRD_{800-868}$ was monitored using $^1H\text{-}^{15}N$ TROSY-HSQC spectra recorded at two time points (0 h and 5 h after mixing with Src and ATP). Corresponding spectrum of the fusion tag (GB1-6xHis-TEV) in the presence of Src was recorded under identical experimental conditions.

2.10.6 Analysis of ^{15}N CPMG relaxation dispersions

Note that three tandem proline-rich motifs of $PRD^{Strep}_{703-800}$ interact with one binding site on TSG101-UEV. As a result, ^{15}N CPMG relaxation dispersion profiles for each interacting site were fit independently. For each site, dispersion data, collected as a function of increasing TSG101-UEV concentration (cf. section 2.10.5), were fit globally to a two-state exchange model ($A \leftrightarrow B$) using an in-house MATLAB script (MathWorks Inc.) that is based on our previously published reports (51, 52), by numerically solving the McConnell equations (53); see the text below.

Briefly, for each interacting PRD site, dispersion data collected using increasing concentration of TSG101-UEV were fit simultaneously by minimizing the following sum of squared differences between the observed ('obs') and calculated ('calc') values of the experimental observables, using an in-house MATLAB script (MathWorks Inc.) –

$$F_{\text{PRD-site \#}} = \alpha_1 \sum_i \sum_k \sum_j^2 \left(\frac{R^{\text{obs, i, k, j}}_{2,\ \text{PRD-Site \#+TSG101-UEV}} - R^{\text{calc, i, k, j}}_{2,\ \text{PRD-Site \#+TSG101-UEV}}}{\sigma^{\text{obs, i,j,k}}_{R_{2,\text{PRD-Site \#+TSG101-UEV}}}} \right) \quad \textbf{(S1)}$$

where $R_{2,n}$ denotes the R_2^A of sample *n*; the subscript *i* refers to residue numbers of $PRD^{Strep}_{703\text{-}800}$-Site # (where Site # = Site 1 / 2 / 3), the subscript *k* refers to CPMG RF field strengths used for $PRD^{Strep}_{703\text{-}800}$-Site #, and the subscripts *j* refers to ^{1}H spectrometer frequency (600 and 800 MHz). The space of residue-specific fitted parameters describing $PRD^{Strep}_{703\text{-}800}$-Site # and TSG101-UEV interactions (Eq. S**1**) comprised: $\{R^{800}_{2;\text{PRD-Site \#}}; R^{600}_{2;\text{PRD-Site \#}}; \Delta\varpi^B\}$ where R_2 denotes the intrinsic transverse relaxation rate of the state **A** and 800 and 600 denote ^{1}H spectrometer fields; and $\Delta\varpi^B$ is the difference in chemical shifts between the bound and free $PRD^{Strep}_{703\text{-}800}$-Site #. The set of global parameters included: $\{k_{AB}; k_{BA}\}$. The dissociation rate constant, k_{BA}, was dynamically 'shared' for all dispersion data collected as a function of increasing TSG101-UEV concentration. The uncertainties in the values of the optimized parameters, corresponding to confidence intervals of ± 1 standard deviation were determined from the Jacobian matrix of the non-linear fit. Convergence of the solution was confirmed by varying initial values for all parameters and obtaining the same solution within reported uncertainties.

According to NMR titration data (cf. Fig. 2.3 C), sites 1 and 2 of $PRD^{Strep}_{703\text{-}800}$ are ~40 residue apart and can thus likely be occupied by two TSG101-UEV molecules at any given time (1:2 complex). Similarly, sites 1 and 3 are ~50 residues apart and can thus form a 1:2 complex. Sites 2 and 3, however, are separated by only a few residues and therefore, cannot simultaneously interact with two TSG101-UEV molecules due to steric hindrance (see Figure 2.6 D).

The total amount of free TSG101-UEV under the conditions of the experiment (100 μM $PRD^{Strep}_{703\text{-}800}$ and 500 μM TSG101-UEV) was estimated as follows. To simplify the calculation, we assumed formation of 1:1 complex. For a 1:1 complex, the total amount of Free $PRD^{Strep}_{703\text{-}800}$ can be calculated using the relationship S**2**:

$$\text{Unbound } PRD^{Strep}_{703\text{-}800} = \frac{1}{1+\left(\frac{k_{on}^{app}}{k_{off}}\right)^{site\ 1}+\left(\frac{k_{on}^{app}}{k_{off}}\right)^{site\ 2}+\left(\frac{k_{on}^{app}}{k_{off}}\right)^{site\ 3}} \quad \textbf{(S2)}$$

Note that S**2** is derived using the following two relationships:

$$\text{Unbound } PRD^{Strep}_{703\text{-}868}+Site1^{Bound}+Site2^{Bound}+Site3^{Bound}=1 \quad \textbf{(S3)}$$

$$Site\#^{Bound}=\left(\frac{k_{on}^{app}}{k_{off}}\right)^{Site\#} \times \text{Unbound } PRD^{Strep}_{800\text{-}868} \quad \textbf{(S4)}$$

where Site # = Site 1 / 2 / 3.

By substituting the appropriate rate constants in S**2**, the amount of unbound $PRD^{Strep}_{703\text{-}800}$, in the context of 1:1 complex, was calculated to be ~53%. The total amount of bound $PRD^{Strep}_{703\text{-}800}$ was, therefore, ~47%, where Unbound $PRD^{Strep}_{703\text{-}800}$ + Bound $PRD^{Strep}_{703\text{-}800}$ = 1. Under the conditions of the experiment (100 μM $PRD^{Strep}_{703\text{-}800}$ and 500 μM TSG101-UEV), the total amount of free TSG101-UEV, therefore, is 453 μM. Note that the above calculations do not take into account 1:2 complex whereupon both sites 1 and 2 or sites 1 and 3 of $PRD^{Strep}_{703\text{-}800}$ are simultaneously occupied by two TSG101-UEV molecules. However, the total amount of free TSG101-UEV can be

accurately calculated using the above method. This is because, the presence of 1:2 complex will alter the total amount of free $PRD^{Strep}_{703\text{-}800}$ but will not change the total amount of free TSG101-UEV as one will need to take into account and correct for the formation of 1:2 complex.

Using above information, the values of second-order association rate constant (k_{on}) were readily computed to be 76 ± 2, 58 ± 9 and 45 ± 23 (× 104 $M^{-1}\cdot s^{-1}$) for sites 1, 2 and 3, respectively; where $k_{on}=k_{on}^{app}$ / [free TSG101-UEV], where [free TSG101-UEV] is the concentration of free TSG101-UEV (453 μM). The resultant equilibrium dissociation constant, $K_D=\frac{k_{off}}{k_{on}}$, values were 0.64 ± 0.02 mM (site 1), 3.34 ± 0.56 mM (site 2) and 7.23 ± 3.74 mM (site 3).

The percent occupancy of each $PRD^{Strep}_{703\text{-}800}$ site (Site 1, 2 and 3) was calculated using the equilibrium dissociation constants (Figure 2.6 B). As sites 2 and 3 are mutually exclusive - i.e., cannot be occupied by two TSG101-UEV molecules at the same time (scheme above) - we calculated the cumulative dissociation constant for sites 2 and 3 to be 2285 μM by using the relationship:

$$\text{Cumulative } K_D^{\text{Site 2+Site 3}}=\left(\frac{K_D^{\text{Site 2}}\times K_D^{\text{Site 3}}}{K_D^{\text{Site 2}}+K_D^{\text{Site 3}}}\right) \qquad \textbf{(S5)}$$

Using mass-action law and $K_D^{\text{Site 1}}$ = 643 μM; Cumulative $K_D^{\text{Site 2+Site 3}}$ = 2285 μM, the percent occupancy of each site can be calculated as follows:

$$\text{Site 1}^{\text{Bound}}=34\%;\ \text{Site 2/3}^{\text{Bound}}=10\%;(\text{Site 1+Site 2/3})^{\text{Bound}}=7\% \qquad \textbf{(S6)}$$

Using the ratios of individual dissociation constants for sites 2 and 3, we deconvolute the percent occupancy of 1:1 complex to be 7 % (site 2) and 3 % (site 3). Similarly, for 1:2 complex, percent occupancy of sites 1 and 2 is 5 % and the corresponding occupancy for sites 1 and 3 is 2 % (Figure 2.6 C).

2.10.7 Sedimentation velocity analytical ultracentrifugation

Sedimentation velocity experiments were carried out at 50,000 rpm and 20 °C on a Beckman Coulter ProteomeLab XL-I analytical ultracentrifuge and An50-Ti rotor following standard protocols (87). Stock solutions of $PRD^{Strep}_{703\text{-}800}$ and TSG101-UEV, dialyzed into buffer containing 20 mM sodium phosphate, pH 6.5, 50 mM NaCl, 1 mM TCEP, and 2 mM EDTA, were diluted to 66 μM and 22 μM, respectively, and loaded in 12 mm two-channel centerpiece cells. Sedimentation data were collected using the absorbance (280 nm) and interference (655 nm) optical detection systems. Time corrected (88) data were analyzed in SEDFIT 16.2b (89) in terms of a continuous c(*s*) distribution of sedimenting species with a maximum entropy regularization confidence interval of 0.68. The solution density, solution viscosity, and protein partial specific volume were calculated based on their composition in SEDNTERP (90). Sedimentation coefficients were corrected to standard conditions in water at 20 °C, $s_{20,w}$.

2.10.8 Sedimentation equilibrium analytical ultracentrifugation

Sedimentation equilibrium experiments were carried out at 30 °C and 12,000, 22,000, and 42,000 rpm on a Beckman Optima XL-A analytical ultracentrifuge and An50-Ti rotor following standard protocols (87). Stock solutions of $PRD^{Strep}_{703\text{-}800}$ and TSG101-UEV, dialyzed into a buffer containing 20 mM sodium phosphate, pH 6.5, 50 mM NaCl, 1 mM TCEP, and 2 mM EDTA, were

diluted and loaded in two-channel centerpiece cells, and sedimentation data were collected using the absorbance (280 nm and 250 nm) optical detection system. Low concentration experiments were carried using 70 μM $PRD^{Strep}_{703\text{-}800}$ and 22 μM TSG101-UEV loaded in 12 mm two-channel centerpiece cells. Data were analyzed globally in terms of a non-interacting single species with implicit mass conservation in SEDPHAT 15.2c essentially as described (91). The buffer solution density and protein partial specific volume were calculated based on the composition using SEDNTERP (21). High concentration experiments were carried out in a similar manner. Solutions of 360 μM, 180 μM, and 90 μM $PRD^{Strep}_{703\text{-}800}$ were loaded in 3 mm, 3 mm, and 12 mm pathlength cells, respectively. Samples of 380 μM, 190 μM, and 95 μM TSG101-UEV were loaded in 1.5 mm (titanium centerpiece, Nanolytics GmBH), 3 mm, and 3 mm pathlength cells, respectively. Each dataset was analyzed globally in terms of a non-interacting single species with implicit mass conservation, as above.

2.10.9 Docking calculations

Docking calculations were performed in Xplor-NIH (59). Interfacial residues of TSG101-UEV were identified from NMR titration experiments, namely residues 32-34, 58-69, 87-103, 110-111, and 134-144. Using PosDiffPot of Xplor-NIH, the backbone heavy atom coordinates of these regions were restrained to lie within 0.1 Å rmsd of the reference X-ray structure of TSG101-UEV in complex with HIV-1 p6 analog (PDB ID 3OBU) (44). Atoms missing from the X-ray structure were added in with correct covalent geometry. Ambiguous distance restraints were applied between $PRD_{711\text{-}730}$ and interacting regions of TSG101-UEV. For each Cα atom of $PRD_{711\text{-}730}$, a distance restraint was added specifying a distance of 2 - 5 Å to any atom in an interacting region of TSG101-UEV. Similar distance restraints were applied between each Cα of interacting regions

of TSG101-UEV to any $PRD_{711-730}$ atoms. The PosDiffPot and distance restraints were applied along with the following Xplor-NIH energy terms: the TorsionDB potential of mean force, the HBPot hydrogen bond geometry term (92) and the RepelPot term (to prevent atomic overlap). Bond, bond angle, and improper angle terms were also included. During structure calculations, non-interacting regions of TSG101-UEV were held fixed in space. For initial high-temperature molecular dynamics and subsequent simulated annealing, calculations were performed using the torsion angle degrees of freedom of the interfacial regions of TSG101-UEV and $PRD_{711-730}$. For each of the 10 structures computed, the active torsion angles were first randomized and high temperature molecular dynamics run with randomized initial velocities appropriate to 3500 °K for 1000 steps. Simulated annealing was then performed using an initial temperature of 3500 °K, a final temperature of 25 °K, and temperature increment of 12.5 °K. At each temperature, molecular dynamics were run for the shorter of 100 steps or 0.2 ps. After simulated annealing, gradient minimization was performed in the Cartesian space of the atoms not held fixed in space. The lowest energy resulting structure was selected.

2.10.10 Tyrosine phosphorylation

Src-mediated in vitro tyrosine phosphorylation of $PRD^{Strep}_{703-800}$ and GB1-$PRD_{800-868}$, as well as $PRD_{800-868}$ and the fusion tag, GB1-6xHis-TEV, were monitored using Phos-tag electrophoresis, western blotting, LC-ESI-TOFMS, LC-MS/MS, and NMR (cf. section 2.10.5). For Phos-tag SDS-PAGE gels, proteins were visualized by silver staining. For western blotting, reaction mixtures separated using electrophoresis were transferred onto a PVDF membrane (Thermo Fisher Scientific, catalog no. LC2005) using a wet-transfer Mini Blot Module (Thermo Fisher Scientific, catalog no. B1000). For subsequent blocking and antibody incubation, an iBind automated western

system (Thermo Fisher Scientific, catalog no. SLF1000) was used. The following primary and secondary antibodies were used for detection, phospho-tyrosine mouse, and goat anti-mouse HRP antibody. Phosphorylated products were visualized using 1-Step Ultra TMB-Blotting Solution (Thermo Fisher Scientific, catalog no. 37574). Src activity was measured using ADP-Glo kinase assay.

For LC-MS/MS analysis, phosphorylated GB1-PRD$_{800-868}$ was digested using chymotrypsin (GB1-PRD$_{800-868}$ to chymotrypsin molar ration 50:1; total incubation time: ~90 min at room temperature). LC-MS/MS analysis was carried out by nanoLC-Orbitrap XL spectrometer. A fused silica capillary LC column (pulled to a tip with a Sutter P-2000 laser capillary puller) was packed with Agilent Zorbax resin (C18, particle size 5 μm). The inner diameter (ID) of capillary was 100 μm and the stationary phase was packed with a pressure device to a length of 80 mm. The column was equilibrated using Agilent 1100 HPLC pump, solvent A = 100% HPLC-grade water with 0.1% formic acid and solvent B = 100% acetonitrile with several 10-90% solvent B step gradients. The chymotrypsin-digested sample of phosphorylated GB1-PRD$_{800-868}$ was loaded on the column by a pressure device (2.4 μl of a 5 μM solution in 1% acetonitrile and 0.1% formic acid). The LC gradient program was 1- 34% solvent B in 66 minutes, followed by 6 minutes of 90% B, followed by 1% B at 95 minutes. Data acquisition method parameters were as follows: the capillary LC was positioned in the Thermo nanoelectrospray interface (NSI) with settings of 1.55 kV source voltage, 40 V capillary voltage, 140 V tube lens, and 165 °C capillary temperature. For the ion trap, 3 micro scans and the Fourier transform (FT) spectra, 2 micro scans were averaged. There were seven scan events per cycle (6.5 s), one FT scan (resolution 30,000) from 200-1600 m/z, followed by six ion trap, data dependent collision induced dissociation (CID) MS/MS scans. Dynamic exclusion was enabled with duration 40 s and repeat count of 2. The ion trap CID scans

had isolation width of 2.0 m/z and normalized collision energy of 35. Data analysis method parameters peptide sequence matches (PSM) were found using the OpenMS workflow (93) with the MS-GF + PSM search algorithm (26). The false discovery rate was set to 5%. Up to two post-translational modifications (PTM) per peptide were allowed for the search. Phosphorylation of tyrosine was the most prevalent PTM observed.

2.10.11 Congo Red (CR) assay

CR was dissolved in MilliQ water (0.2% wt/vol stock solution). The stock was filtered through 0.22 μm filter and used immediately. GB1-$PRD^{Strep}_{703-800}$ and GB1-$PRD_{800-868}$ samples, 100 μM each, were incubated overnight at room temperature and were mixed with CR stock solution in the morning (100:1 dilution, protein vs. CR). The mixtures were incubated at room temperature for ~45 min. Absorption spectra were measured using an Agilent Cary 50 Bio UV-Vis spectrophotometer (1-cm quartz cuvette).

2.10.12 Fibril Formation and Dissolution Kinetics

Aggregation and dissolution experiments were performed on GB1-$PRD_{800-868}$ samples in sealed 96-well flat bottom plates (Corning, catalog no. 3370) containing 100 μL sample per well (three replicates of each sample, $n = 3$, were placed in separate wells and ThT fluorescence was measured through the top and bottom of the plate). Measurements were carried out with continuous linear shaking (3.5 mm, 411.3 rpm) using a microplate reader (Infinite M Plex, Tecan). ThT (10 μM) fluorescence was recorded as a function of time; excitation and emission wavelengths were 415 and 480 nm, respectively. For aggregation experiments, the following conditions were varied (one at a time): pH 6.5 (50 mM sodium phosphate), 7.0 (50 mM sodium phosphate), 7.5 (50 mM

Tris) and 8 (50 mM Tris) at [GB1-PRD$_{800-868}$] = 0.075 mM and 0 mM NaCl; ionic strength (0, 250, and 500 mM NaCl; 50 mM sodium phosphate, pH = 7.0, temperature = 30 °C, [GB1-PRD$_{800-868}$] = 0.075 mM), concentration (0.05, 0.075, 0.1, 0.125, and 0.15 mM, 50 mM sodium phosphate, pH = 7.0, 0 mM NaCl, temperature = 30 °C) and temperature (25, 30, 35, and 40 °C; 50 mM sodium phosphate, pH = 7.0, 0 mM NaCl and [GB1-PRD$_{800-868}$] = 0.075 mM). Each buffer also contained 1 mM DTT and 1 mM EDTA. GB1-PRD$_{800-868}$ was poorly soluble below pH 6.5 (theoretical isoelectric point = 5.96). The effect of lower temperatures (2 - 10 °C) on aggregation was assessed using Agilent Cary Eclipse Fluorescence spectrophotometer. 3×150 µL of 0.1 mM GB1-PRD$_{800-868}$, samples were incubated at 40 °C for ~2 h (50 mM sodium phosphate, pH 7.0, 1 mM DTT and 1 mM EDTA; micro quartz cuvettes). During incubation, ThT fluorescence readings were measured every 30 minutes. Upon reaching a maximum signal, temperature was dropped from 40 °C to a desired temperature point (2, 4, 6, 8 and 10 °C; one at a time). ThT signals were measured every 30 minutes until a stable reading was reached.

2.10.13 Transmission electron microscopy (TEM)

Aggregated GB1-PRD$_{800-868}$ and PRD$_{800-868}$ samples, ~2 mg/mL in 50 mM sodium phosphate, pH 7, 1 mM EDTA and 1 mM DTT, were applied to the TEM grids (400-mesh formvar and carbon coated copper, Electron Microscopy Sciences, catalog no. FCF400-Cu). 1 min after deposition, the sample solution was wicked with filter paper, followed by a quick wash with 3 µL of water and addition of 3-5 drops of 2% wt/vol aqueous uranyl acetate solution. The uranyl acetate was wicked immediately with a filter paper and grids were air dried at room temperature. TEM was carried out using a FEI Tecnai F-20 microscope operated at 200 kV and images were recorded on a 4k x 4k TVIPS camera.

2.11 Acknowledgements

We thank V. Tugarinov, Z. Jiang, A. Szabo, D. H. Appella, M. Wälti, A. Ceccon, Y. Shen, J. Ying, P. A. Jennings, B. Ramaraju, A. Shihora, I. Budin, and J. A. McCammon for useful discussions and X. Huang (University of California, San Diego [UCSD] Biomolecular NMR Facility), J. Yu (NMR Facility, Sanford Burnham Prebys Medical Discovery Institute), and L. Gross and Y. Su (UCSD Molecular Mass Spectrometry Facility) for technical support. We thank A. van der Vliet (University of Vermont), D. S. Waugh (National Cancer Institute, NIH), and N. Tjandra (National Heart, Lung and Blood Institute, NIH) for Src kinase, TEV protease, and TSG101-UEV constructs, respectively. This work was funded, in part, by a 2018 Development Award from the San Diego Center for AIDS Research (an NIH-funded program; NIH Grant P30 AI036214) (to L.D.); by Collaborative Development Awards from the Cellular Host Elements in Egress, Trafficking, and Assembly of HIV Center (University of Utah; an NIH-funded program; Grant P50 AI150464) and the HIV Interactions in Viral Evolution (HIVE) Center (The Scripps Research Institute; an NIH-funded program; NIH Grant U54 AI150472) (to L.D.); NSF Graduate Research Fellowship Grant DGE-1650112 (to R.D.E.); and NIH Grant R01 GM031749 (to W.M.). V.S.R. was supported by HIVE Center Grant U54 AI150472. C.D.S. was supported by the Center for Information Technology Intramural Research Program at the NIH. R.G. was supported by the National Institute of Diabetes and Digestive and Kidney Diseases Intramural Research Program at the NIH

Chapter 2, in full, is a reprint of the material as it appears in: Elias, R. D., Ma, W., Ghirlando, R., Schwieters, C. D., Reddy, V. S., and Deshmukh, L. (2020) Proline-rich domain of human ALIX contains multiple TSG101-UEV interaction sites and forms phosphorylation-

mediated reversible amyloids. Proc Natl Acad Sci U S A, 117 (39), 24274-24284. The dissertation author was the primary investigator and author of this paper.

2.12 References

1. MacArthur, M. W., and Thornton, J. M. (1991) Influence of proline residues on protein conformation. J Mol Biol 218, 397-412

2. Williamson, M. P. (1994) The structure and function of proline-rich regions in proteins. Biochem J 297 (Pt 2), 249-260

3. Rubin, G. M., Yandell, M. D., Wortman, J. R., Gabor Miklos, G. L., Nelson, C. R., Hariharan, I. K., Fortini, M. E., Li, P. W., Apweiler, R., Fleischmann, W., Cherry, J. M., Henikoff, S., Skupski, M. P., Misra, S., Ashburner, M., Birney, E., Boguski, M. S., Brody, T., Brokstein, P., Celniker, S. E., Chervitz, S. A., Coates, D., Cravchik, A., Gabrielian, A., Galle, R. F., Gelbart, W. M., George, R. A., Goldstein, L. S., Gong, F., Guan, P., Harris, N. L., Hay, B. A., Hoskins, R. A., Li, J., Li, Z., Hynes, R. O., Jones, S. J., Kuehl, P. M., Lemaitre, B., Littleton, J. T., Morrison, D. K., Mungall, C., O'Farrell, P. H., Pickeral, O. K., Shue, C., Vosshall, L. B., Zhang, J., Zhao, Q., Zheng, X. H., and Lewis, S. (2000) Comparative genomics of the eukaryotes. Science 287, 2204-2215

4. Morgan, A. A., and Rubenstein, E. (2013) Proline: The distribution, frequency, positioning, and common functional roles of proline and polyproline sequences in the human proteome. PLOS ONE 8, e53785

5. Theillet, F. X., Kalmar, L., Tompa, P., Han, K. H., Selenko, P., Dunker, A. K., Daughdrill, G. W., and Uversky, V. N. (2013) The alphabet of intrinsic disorder: I. Act like a Pro: On the abundance and roles of proline residues in intrinsically disordered proteins. Intrinsically Disord Proteins 1, e24360

6. Wright, P. E., and Dyson, H. J. (2015) Intrinsically disordered proteins in cellular signalling and regulation. Nat Rev Mol Cell Biol 16, 18-29

7. Adzhubei, A. A., Sternberg, M. J. E., and Makarov, A. A. (2013) Polyproline-II Helix in Proteins: Structure and Function. Journal of Molecular Biology 425, 2100-2132

8. Tossavainen, H., Aitio, O., Hellman, M., Saksela, K., and Permi, P. (2016) Structural basis of the high affinity interaction between the alphavirus nonstructural protein-3 (nsP3) and the SH3 domain of Amphiphysin-2. J Biol Chem 291, 16307-16317

9. Liao, T.-J., Jang, H., Nussinov, R., and Fushman, D. (2020) High-affinity interactions of the nSH3/cSH3 domains of Grb2 with the C-terminal proline-rich domain of SOS1. Journal of the American Chemical Society 142, 3401-3411

10. Linding, R., Russell, R. B., Neduva, V., and Gibson, T. J. (2003) GlobPlot: Exploring protein sequences for globularity and disorder. Nucleic Acids Res 31, 3701-3708

11. van der Lee, R., Buljan, M., Lang, B., Weatheritt, R. J., Daughdrill, G. W., Dunker, A. K., Fuxreiter, M., Gough, J., Gsponer, J., Jones, D. T., Kim, P. M., Kriwacki, R. W., Oldfield, C. J., Pappu, R. V., Tompa, P., Uversky, V. N., Wright, P. E., and Babu, M. M. (2014) Classification of intrinsically disordered regions and proteins. Chem Rev 114, 6589-6631

12. Li, P., Banjade, S., Cheng, H. C., Kim, S., Chen, B., Guo, L., Llaguno, M., Hollingsworth, J. V., King, D. S., Banani, S. F., Russo, P. S., Jiang, Q. X., Nixon, B. T., and Rosen, M. K. (2012) Phase transitions in the assembly of multivalent signalling proteins. Nature 483, 336-340

13. Lee, Y. C., and Lee, R. T. (1995) Carbohydrate-protein Interactions: Basis of glycobiology. Accounts of Chemical Research 28, 321-327

14. Mammen, M., Choi, S. K., and Whitesides, G. M. (1998) Polyvalent interactions in biological systems: Implications for design and use of multivalent ligands and inhibitors. Angew Chem Int Ed Engl 37, 2754-2794

15. Kiessling, L. L., and Lamanna, A. C. (2003) Multivalency in biological systems. Springer Netherlands, Dordrecht

16. Kay, B. K., Williamson, M. P., and Sudol, M. (2000) The importance of being proline: the interaction of proline-rich motifs in signaling proteins with their cognate domains. The FASEB Journal 14, 231-241

17. Zarrinpar, A., Bhattacharyya, R. P., and Lim, W. A. (2003) The Structure and function of proline recognition domains. Science's STKE 2003, re8-re8

18. Bastidas, M., Gibbs, E. B., Sahu, D., and Showalter, S. A. (2015) A primer for carbon-detected NMR applications to intrinsically disordered proteins in solution. Concepts in Magnetic Resonance Part A 44, 54-66

19. Schöneberg, J., Lee, I.-H., Iwasa, J. H., and Hurley, J. H. (2017) Reverse-topology membrane scission by the ESCRT proteins. Nature Reviews Molecular Cell Biology 18, 5-17

20. Vietri, M., Radulovic, M., and Stenmark, H. (2020) The many functions of ESCRTs. Nature Reviews Molecular Cell Biology 21, 25-42

21. Ren, X., and Hurley, J. H. (2011) Proline-rich regions and motifs in trafficking: from ESCRT interaction to viral exploitation. Traffic 12, 1282-1290

22. Fisher, R. D., Chung, H. Y., Zhai, Q., Robinson, H., Sundquist, W. I., and Hill, C. P. (2007) Structural and biochemical studies of ALIX/AIP1 and its role in retrovirus budding. Cell 128, 841-852

23. Zhai, Q., Fisher, R. D., Chung, H. Y., Myszka, D. G., Sundquist, W. I., and Hill, C. P. (2008) Structural and functional studies of ALIX interactions with YPX(n)L late domains of HIV-1 and EIAV. Nat Struct Mol Biol 15, 43-49

24. Strack, B., Calistri, A., Craig, S., Popova, E., and Gottlinger, H. G. (2003) AIP1/ALIX is a binding partner for HIV-1 p6 and EIAV p9 functioning in virus budding. Cell 114, 689-699

25. von Schwedler, U. K., Stuchell, M., Muller, B., Ward, D. M., Chung, H. Y., Morita, E., Wang, H. E., Davis, T., He, G. P., Cimbora, D. M., Scott, A., Krausslich, H. G., Kaplan, J., Morham, S. G., and Sundquist, W. I. (2003) The protein network of HIV budding. Cell 114, 701-713

26. Schmidt, M. H. H., Dikic, I., and Bogler, O. (2005) Src phosphorylation of Alix/AIP1 modulates its interaction with binding partners and antagonizes its activities. J Biol Chem 280, 3414-3425

27. Shi, X., Opi, S., Lugari, A., Restouin, A., Coursindel, T., Parrot, I., Perez, J., Madore, E., Zimmermann, P., Corbeil, J., Huang, M., Arold, S. T., Collette, Y., and Morelli, X. (2010) Identification and biophysical assessment of the molecular recognition mechanisms between the human haemopoietic cell kinase Src homology domain 3 and ALG-2-interacting protein X. Biochem J 431, 93-102

28. Chatellard-Causse, C., Blot, B., Cristina, N., Torch, S., Missotten, M., and Sadoul, R. (2002) Alix (ALG-2-interacting protein X), a protein involved in apoptosis, binds to endophilins and induces cytoplasmic vacuolization. J Biol Chem 277, 29108-29115

29. Zhou, X., Si, J., Corvera, J., Gallick, G. E., and Kuang, J. (2010) Decoding the intrinsic mechanism that prohibits ALIX interaction with ESCRT and viral proteins. Biochem J 432, 525-534

30. Carlton, J. G., Agromayor, M., and Martin-Serrano, J. (2008) Differential requirements for Alix and ESCRT-III in cytokinesis and HIV-1 release. Proc Natl Acad Sci U S A 105, 10541-10546

31. Zhai, Q., Landesman, M. B., Chung, H.-Y., Dierkers, A., Jeffries, C. M., Trewhella, J., Hill, C. P., and Sundquist, W. I. (2011) Activation of the retroviral budding factor ALIX. J. Virol. 85, 9222-9226

32. Doerfel, L. K., Wohlgemuth, I., Kothe, C., Peske, F., Urlaub, H., and Rodnina, M. V. (2013) EF-P is essential for rapid synthesis of proteins containing consecutive proline residues. Science 339, 85-88

33. Ude, S., Lassak, J., Starosta, A. L., Kraxenberger, T., Wilson, D. N., and Jung, K. (2013) Translation elongation factor EF-P alleviates ribosome stalling at polyproline stretches. Science 339, 82-85

34. Woolstenhulme, C. J., Parajuli, S., Healey, D. W., Valverde, D. P., Petersen, E. N., Starosta, A. L., Guydosh, N. R., Johnson, W. E., Wilson, D. N., and Buskirk, A. R. (2013) Nascent peptides that block protein synthesis in bacteria. Proc Natl Acad Sci U S A 110, E878-887

35. Huth, J. R., Bewley, C. A., Jackson, B. M., Hinnebusch, A. G., Clore, G. M., and Gronenborn, A. M. (1997) Design of an expression system for detecting folded protein domains and mapping macromolecular interactions by NMR. Protein Sci 6, 2359-2364

36. Schmidt, T. G., and Skerra, A. (2007) The Strep-tag system for one-step purification and high-affinity detection or capturing of proteins. Nat Protoc 2, 1528-1535

37. Gill, S. C., and von Hippel, P. H. (1989) Calculation of protein extinction coefficients from amino acid sequence data. Anal Biochem 182, 319-326

38. Kjaergaard, M., Brander, S., and Poulsen, F. M. (2011) Random coil chemical shift for intrinsically disordered proteins: effects of temperature and pH. J Biomol NMR 49, 139-149

39. Kjaergaard, M., and Poulsen, F. M. (2011) Sequence correction of random coil chemical shifts: correlation between neighbor correction factors and changes in the Ramachandran distribution. J Biomol NMR 50, 157-165

40. Camilloni, C., De Simone, A., Vranken, W. F., and Vendruscolo, M. (2012) Determination of secondary structure populations in disordered states of proteins using nuclear magnetic resonance chemical shifts. Biochemistry 51, 2224-2231

41. Nielsen, J. T., and Mulder, F. A. A. (2019) Quality and bias of protein disorder predictors. Scientific Reports 9, 5137

42. Shen, Y., Roche, J., Grishaev, A., and Bax, A. (2018) Prediction of nearest neighbor effects on backbone torsion angles and NMR scalar coupling constants in disordered proteins. Protein Sci 27, 146-158

43. Pornillos, O., Alam, S. L., Davis, D. R., and Sundquist, W. I. (2002) Structure of the Tsg101 UEV domain in complex with the PTAP motif of the HIV-1 p6 protein. Nature Structural Biology 9, 812-817

44. Im, Y. J., Kuo, L., Ren, X., Burgos, P. V., Zhao, X. Z., Liu, F., Burke, T. R., Jr., Bonifacino, J. S., Freed, E. O., and Hurley, J. H. (2010) Crystallographic and functional analysis of the ESCRT-I /HIV-1 Gag PTAP interaction. Structure 18, 1536-1547

45. Bax, A., and Grishaev, A. (2005) Weak alignment NMR: a hawk-eyed view of biomolecular structure. Curr Opin Struct Biol 15, 563-570

46. Deshmukh, L., Schwieters, C. D., Grishaev, A., Ghirlando, R., Baber, J. L., and Clore, G. M. (2013) Structure and dynamics of full-length HIV-1 capsid protein in solution. J Am Chem Soc 135, 16133-16147

47. Deshmukh, L., Ghirlando, R., and Clore, G. M. (2015) Conformation and dynamics of the Gag polyprotein of the human immunodeficiency virus 1 studied by NMR spectroscopy. Proc Natl Acad Sci U S A 112, 3374-3379

48. Rückert, M., and Otting, G. (2000) Alignment of biological macromolecules in novel nonionic liquid crystalline media for NMR experiments. Journal of the American Chemical Society 122, 7793-7797

59. Schwieters, C. D., Kuszewski, J. J., Tjandra, N., and Clore, G. M. (2003) The Xplor-NIH NMR molecular structure determination package. J Magn Reson 160, 65-73

50. Palmer, A. G. (2014) Chemical exchange in biomacromolecules: Past, present, and future. Journal of Magnetic Resonance 241, 3-17

51. Deshmukh, L., Tugarinov, V., Louis, J. M., and Clore, G. M. (2017) Binding kinetics and substrate selectivity in HIV-1 protease-Gag interactions probed at atomic resolution by chemical exchange NMR. Proc Natl Acad Sci U S A 114, E9855-E9862

52. Deshmukh, L., Tugarinov, V., Appella, D. H., and Clore, G. M. (2018) Targeting a dark excited state of HIV-1 nucleocapsid by antiretroviral thioesters revealed by NMR spectroscopy. Angew Chem Int Ed Engl 57, 2687-2691

53. McConnell, H. M. (1958) Reaction rates by Nuclear Magnetic Resonance. The Journal of Chemical Physics 28, 430-431

54. Deshmukh, L., Louis, J. M., Ghirlando, R., and Clore, G. M. (2016) Transient HIV-1 Gag-protease interactions revealed by paramagnetic NMR suggest origins of compensatory drug resistance mutations. Proc Natl Acad Sci U S A 113, 12456-12461

55. Cheng, Y., and Patel, D. J. (2004) An efficient system for small protein expression and refolding. Biochemical and Biophysical Research Communications 317, 401-405

56. Zhou, P., and Wagner, G. (2010) Overcoming the solubility limit with solubility-enhancement tags: successful applications in biomolecular NMR studies. J Biomol NMR 46, 23-31

57. Klunk, W. E., Jacob, R. F., and Mason, R. P. (1999) [19] Quantifying amyloid by congo red spectral shift assay. in Methods in Enzymology, Academic Press. pp 285-305

58. Aliyan, A., Cook, N. P., and Martí, A. A. (2019) Interrogating Amyloid Aggregates using Fluorescent Probes. Chemical Reviews 119, 11819-11856

59. Tycko, R. (2015) Amyloid polymorphism: Structural basis and neurobiological relevance. Neuron 86, 632-645

60. Jean, L., Foley, A. C., and Vaux, D. J. T. (2017) The physiological and pathological implications of the formation of hydrogels, with a specific focus on amyloid polypeptides. Biomolecules 7

61. Michaels, T. C. T., Šarić, A., Habchi, J., Chia, S., Meisl, G., Vendruscolo, M., Dobson, C. M., and Knowles, T. P. J. (2018) Chemical kinetics for bridging molecular mechanisms and macroscopic measurements of amyloid fibril formation. Annual Review of Physical Chemistry 69, 273-298

62. Ryan, T. M., Caine, J., Mertens, H. D., Kirby, N., Nigro, J., Breheney, K., Waddington, L. J., Streltsov, V. A., Curtain, C., Masters, C. L., and Roberts, B. R. (2013) Ammonium hydroxide treatment of Abeta produces an aggregate free solution suitable for biophysical and cell culture characterization. PeerJ 1, e73

63. Hikita, T., Kuwahara, A., Watanabe, R., Miyata, M., and Oneyama, C. (2019) Src in endosomal membranes promotes exosome secretion and tumor progression. Scientific Reports 9, 3265

64. Heppner, D. E., Dustin, C. M., Liao, C., Hristova, M., Veith, C., Little, A. C., Ahlers, B. A., White, S. L., Deng, B., Lam, Y.-W., Li, J., and van der Vliet, A. (2018) Direct cysteine sulfenylation drives activation of the Src kinase. Nature Communications 9, 4522

65. Kinoshita, E., Kinoshita-Kikuta, E., and Koike, T. (2009) Separation and detection of large phosphoproteins using Phos-tag SDS-PAGE. Nature Protocols 4, 1513-1521

66. Tsiatsiani, L., and Heck, A. J. (2015) Proteomics beyond trypsin. FEBS J 282, 2612-2626

67. Boggon, T. J., and Eck, M. J. (2004) Structure and regulation of Src family kinases. Oncogene 23, 7918-7927

68. White, J. T., Toptygin, D., Cohen, R., Murphy, N., and Hilser, V. J. (2017) Structural stability of the coiled-coil domain of Tumor Susceptibility Gene (TSG)-101. Biochemistry 56, 4646-4655

69. Huang, D. M., and Chandler, D. (2000) Temperature and length scale dependence of hydrophobic effects and their possible implications for protein folding. Proc Natl Acad Sci U S A 97, 8324-8327

70. Zondlo, N. J. (2013) Aromatic-proline interactions: electronically tunable CH/pi interactions. Acc Chem Res 46, 1039-1049

71. Christ, L., Wenzel, E. M., Liestøl, K., Raiborg, C., Campsteijn, C., and Stenmark, H. (2016) ALIX and ESCRT-I/II function as parallel ESCRT-III recruiters in cytokinetic abscission. Journal of Cell Biology 212, 499-513

72. McCullough, J., Fisher, R. D., Whitby, F. G., Sundquist, W. I., and Hill, C. P. (2008) ALIX-CHMP4 interactions in the human ESCRT pathway. Proceedings of the National Academy of Sciences 105, 7687-7691

73. Larios, J., Mercier, V., Roux, A., and Gruenberg, J. (2020) ALIX- and ESCRT-III–dependent sorting of tetraspanins to exosomes. Journal of Cell Biology 219

74. Jackson, M. P., and Hewitt, E. W. (2017) Why are functional amyloids non-toxic in humans? Biomolecules 7

75. Mankar, S., Anoop, A., Sen, S., and Maji, S. K. (2011) Nanomaterials: amyloids reflect their brighter side. Nano Rev 2

76. Elias, R. D., Deshmukh, L., Backbone ^{1}H ^{13}C and ^{15}N chemical shift assignments of the N-terminal portion of ALIX-PRD. Biological Magnetic Resonance Data Bank. http://www.bmrb.wisc.edu/data_library/summary/index.php?bmrbId=28111. Deposited 27 March 2020

77. Elias, R. D., Deshmukh, L., Docking model of the complex between ALIX-PRD and TSG101-UEV. Protein Model Database, ID PM0083242. http://srv00.recas.ba.infn.it/PMDB/. Deposited 26 June 2020

78. Zhang, Z., and Marshal, A. G. (1998) A universal algorithm for fast and automated charge state deconvolution of electrospray mass-to-charge ratio spectra. J Am Soc Mass Spectrom 9(3):225-233.

79. Rückert, M., and Otting, G. (2000) Alignment of bological macromolecules in novel nonionic liquid crystalline media for NMR experiments. Journal of the American Chemical Society 122(32):7793-7797.

80. Delaglio, F., Grzesiek, S., Vuister, G. W., Zhu, G., and Bax, A. (1995) NMRPipe: a multidimensional spectral processing system based on UNIX pipes. J Biomol NMR 6(3):277-293.

81. Vranken, W. F., Boucher, W., Stevens, T. J., Fogh, R. H., Pajon, A., Llinas, M., Ulrich, E. L., Markley, J. L., Ionides, J., and Laue, E. D. (2005) The CCPN data model for NMR spectroscopy: development of a software pipeline. Proteins 59(4):687-696.

82. Clore, G. M., and Gronenborn, A. M. (1998) Determining the structures of large proteins and protein complexes by NMR. Trends Biotechnol 16(1):22-34.

83. Roche, J., Ying, J., and Bax, A. (2016) Accurate measurement of 3JHNHα couplings in small or disordered proteins from WATERGATE-optimized TROSY spectra. J Biomol NMR 64(1):1-7.

84. Lakomek, N. A., Ying, J., and Bax, A. (2012) Measurement of ^{15}N relaxation rates in perdeuterated proteins by TROSY-based methods. J Biomol NMR 53(3):209-221.

85. Hansen, D. F., Vallurupalli, P., and Kay, L. E. (2008) An improved ^{15}N relaxation dispersion experiment for the measurement of millisecond time-scale dynamics in proteins. The Journal of Physical Chemistry B 112(19):5898-5904.

86. Fitzkee, N. C., and Bax, A. (2010) Facile measurement of ^{1}H-^{15}N residual dipolar couplings in larger perdeuterated proteins. J Biomol NMR 48(2):65-70.

87. Zhao, H., Brautigam, C. A., Ghirlando, R., and Schuck, P. (2013) Overview of current methods in sedimentation velocity and sedimentation equilibrium analytical ultracentrifugation. Curr Protoc Protein Sci Chapter 20:Unit20 12.

88. Zhao, H., Ghirlando, R., Piszczek, G., Curth, U., Brautigam, C. A., and Schuck, P. (2013) Recorded scan times can limit the accuracy of sedimentation coefficients in analytical ultracentrifugation. Anal Biochem 437(1):104-108.

89. Schuck, P. (2000) Size-distribution analysis of macromolecules by sedimentation velocity ultracentrifugation and Lamm equation modeling. Biophys J 78(3):1606-1619.

90. Cole, J. L., Lary, J. W., Moody, T., and Laue, T. M. (2008) Analytical ultracentrifugation: sedimentation velocity and sedimentation equilibrium. Methods Cell Biol 84:143-179.

91. Ghirlando, R. (2011) The analysis of macromolecular interactions by sedimentation equilibrium. Methods 54(1):145-156.

92. Schwieters, C. D., Bermejo, G. A., and Clore, G. M. (2020) A three-dimensional potential of mean force to improve backbone and sidechain hydrogen bond geometry in Xplor-NIH protein structure determination. Protein Sci 29(1):100-110.

93. Röst, H. L., Sachsenberg, T., Aiche, S., Bielow, C., Weisser, H., Aicheler, F.,Andreotti, S., Ehrlich, H. C., Gutenbrunner, P., Kenar, E., Liang, X., Nahnsen, S., Nilse, L., Pfeuffer, J., Rosenberger, G., Rurik, M., Schmitt, U., Veit, J., Walzer, M., Wojnar, D.,Wolski, W. E., Schilling, O., Choudhary, J. S., Malmström, L., Aebersold, R., Reinert, K., Kohlbacher, O. (2016) OpenMS: a flexible open-source software platform for mass spectrometry data analysis. Nat Methods 13(9):741-748.

94. Kim, S., and Pevzner, P. A. (2014) MS-GF+ makes progress towards a universal database search tool for proteomics. Nature Communications 5(1):5277.

95. Nielsen, J. T., and Mulder, F. A. A. (2016) There is diversity in disorder-"in all chaos there is a cosmos, in all disorder a secret order". Front Mol Biosci 3:4.

96. Clore, G. M. and Garrett, D. S. (1999) R-factor, free R, and complete cross-validation for dipolar coupling refinement of NMR structures. Journal of the American Chemical Society 121(39):9008-9012.

97. Roepstorff, P., and Fohlman, J. (1984) Proposal for a common nomenclature for sequence ions in mass spectra of peptides. Biomed Mass Spectrom 11(11):601.

98. Brademan, D. R., Riley, N. M., Kwiecien, N. W., and Coon, J. J. (2019) Interactive peptide spectral annotator: a versatile web-based tool for proteomic applications. Mol Cell Proteomics 18(8 suppl 1):S193-S201.

Chapter 3: Mechanistic roles of tyrosine phosphorylation in reversible amyloids, autoinhibition, and endosomal membrane association of ALIX

3.1 Introduction

Human apoptosis-linked gene-2 interacting protein X (ALIX) is a conserved adapter protein involved in essential cellular processes, including endosomal protein sorting, apoptosis, exosome biogenesis, and many others (1–4). ALIX also regulates budding of diverse enveloped viruses, such as HIV (5, 6) and Ebola (7). It comprises an amino (N)-terminal Bro1 domain (residues 1–359), a central coiled-coil domain termed V (residues 360–702), and a carboxy (C)-terminal proline-rich domain (PRD; residues 703–868) (Fig. 3.1 A). ALIX, also known as programmed cell death 6 interacting protein (PDCD6IP), undergoes tyrosine phosphorylation at multiple sites, which regulates its cellular functions; it comprises 28 conserved tyrosine residues (8), among which 11 are localized in the C-terminal portion of PRD, residues 803 to 846. ALIX interacts with and is phosphorylated by Src kinase at late endosomal membranes (8, 9); ALIX–endosomal membrane interactions are governed by its Bro1 domain, which binds to negatively charged 2,2' lysobisphosphatidic acid (2,2' LBPA; referred to as LBPA), a phospholipid found in late endosomes (10–12). ALIX–Src interactions result in phosphorylation of the Bro1 domain and hyperphosphorylation of the tyrosine-rich portion of PRD (8, 9). These interactions promote exosome secretion and cause ALIX to relocate from a membrane-bound active conformation to a cytosolic inactive state. Interdomain interactions between PRD and the upstream globular domains, Bro1 and V, are suggested to cause ALIX autoinhibition in the cytosol (13, 14). Structural details of these interactions are unclear because of the unavailability of recombinant full-length ALIX, owing to difficulties in expressing ALIX-PRD in bacteria and its disordered nature. Intact ALIX was, however, successfully produced using a baculovirus–insect cell

expression system (14). ALIX-PRD encodes binding epitopes of numerous cellular proteins (15), and its hyperphosphorylation by Src affects its cellular interactions (8). We recently discovered that the N-terminal portion of ALIX-PRD (residues 703–800) is disordered, whereas its C-terminal tyrosine-rich portion (residues 800–868) forms amyloid fibrils that disassemble on Src-mediated hyperphosphorylation (16). However, the mechanistic effects of tyrosine phosphorylation on cellular redistribution and functions of ALIX are unclear.

Using recombinant ALIX domains and a range of biophysical methods, including NMR, fluorescence, and circular dichroism (CD) spectroscopy, mass spectrometry (MS), transmission electron microscopy (TEM), and dynamic light scattering (DLS), we elucidate how tyrosine phosphorylation affects the interplay between ALIX conformation, assembly, and function (poor bacterial expression and the overall size, ~96 kDa, do not allow for a similar study in the context of full-length ALIX). Codon optimization coupled with a single-point mutation permitted expression of full-length ALIX-PRD in Escherichia coli (E. coli). We show that PRD forms reversible β-sheet rich fibrils modulated by posttranslational modifications (PTMs), Src-mediated phosphorylation and human protein-tyrosine phosphatase 1B (PTP1B)-mediated dephosphorylation of its conserved tyrosine residues. We establish that Bro1 binds to hyperphosphorylated PRD and to analogs of late endosomal membranes. The close correlation between the regions of Bro1 that associate with hyperphosphorylated PRD and with anionic phospholipids elucidates the underlying mechanism of PRD-mediated autoinhibition of ALIX – membrane interactions and how tyrosine phosphorylation causes redistribution of ALIX away from late endosomal membranes into the cytosol.

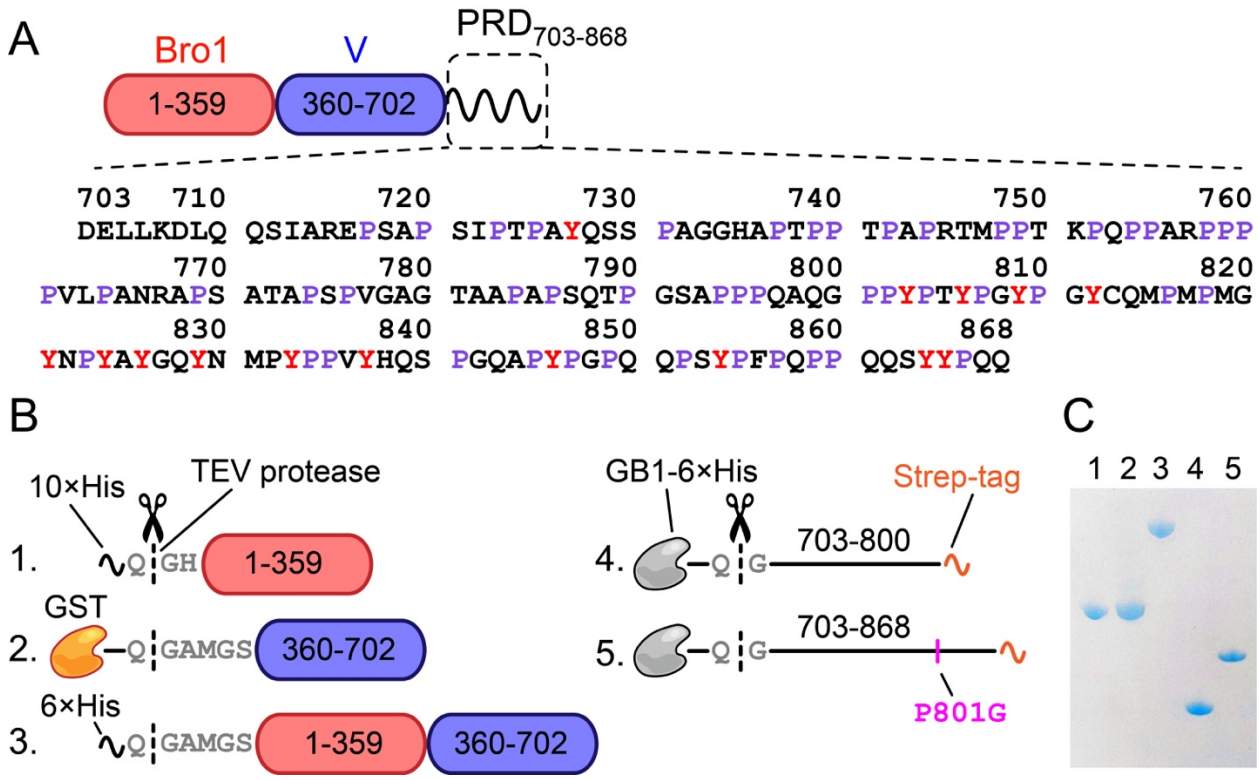

Figure 3.1: ALIX domain organization and summary of recombinant ALIX constructs used in the current work

(A) Schematic of ALIX organization. Primary sequence of the PRD is shown. **(B)** Recombinant ALIX constructs used in the current work. Constructs 1 – 3 were obtained from Addgene; accession no. 80641 (47), 17639 (48), and 42577 (49), respectively. Construct 4 is described in our previous work (16); Addgene accession no. 141344. The positions of purification tags are marked. TEV protease cutting sites are shown. The point mutation, P801G, of $PRD^{Strep}_{703-868}$ is marked. (**C**) SDS-PAGE analysis of TEV-cleaved ALIX constructs; the order of the constructs is the same as the one depicted in (**B**).

3.2 Recombinant constructs

The current work made use of five recombinant ALIX constructs (Fig. 3.1 B-C). These include constructs representing the individual Bro1 and V domains (residues 1–359 and 360–702, respectively), a construct comprising both the Bro1 and V domains (residues 1–702; referred to as Bro1-V), and two constructs representing the N-terminal portion of PRD, $PRD^{Strep}_{703\text{-}800}$ (residues 703–800), and the entire PRD, $PRD^{Strep}_{703\text{-}868}$ (residues 703–868); "Strep" denotes a noncleavable C-terminal strep-affinity tag (17) that facilitated purification of intact PRD constructs from their truncated fragments using affinity chromatography. The latter are generated during heterologous expression of ALIX-PRD in E. coli due to translational arrest induced by its 5 polyproline motifs. $PRD^{Strep}_{703\text{-}868}$ carries a P801G point mutation to resolve issues with protein expression in E. coli. We previously established that the ^{800}GPPYP^{804} segment of ALIX-PRD is responsible for ribosomal stalling in E. coli, resulting in essentially no expression of wild-type PRD beyond residue 801 (16). Note that the effects of the P801G mutation on the cellular functions of ALIX are currently not known. For paramagnetic NMR, three cysteine variants of $PRD^{Strep}_{703\text{-}868}$ were engineered (see below). We also made use of full-length Src kinase and the catalytic domain of PTP1B; see Fig. 3.2 for liquid chromatography–electrospray ionization–time-of-flight MS (LCESI- TOFMS) analyses of constructs used in current study.

ss

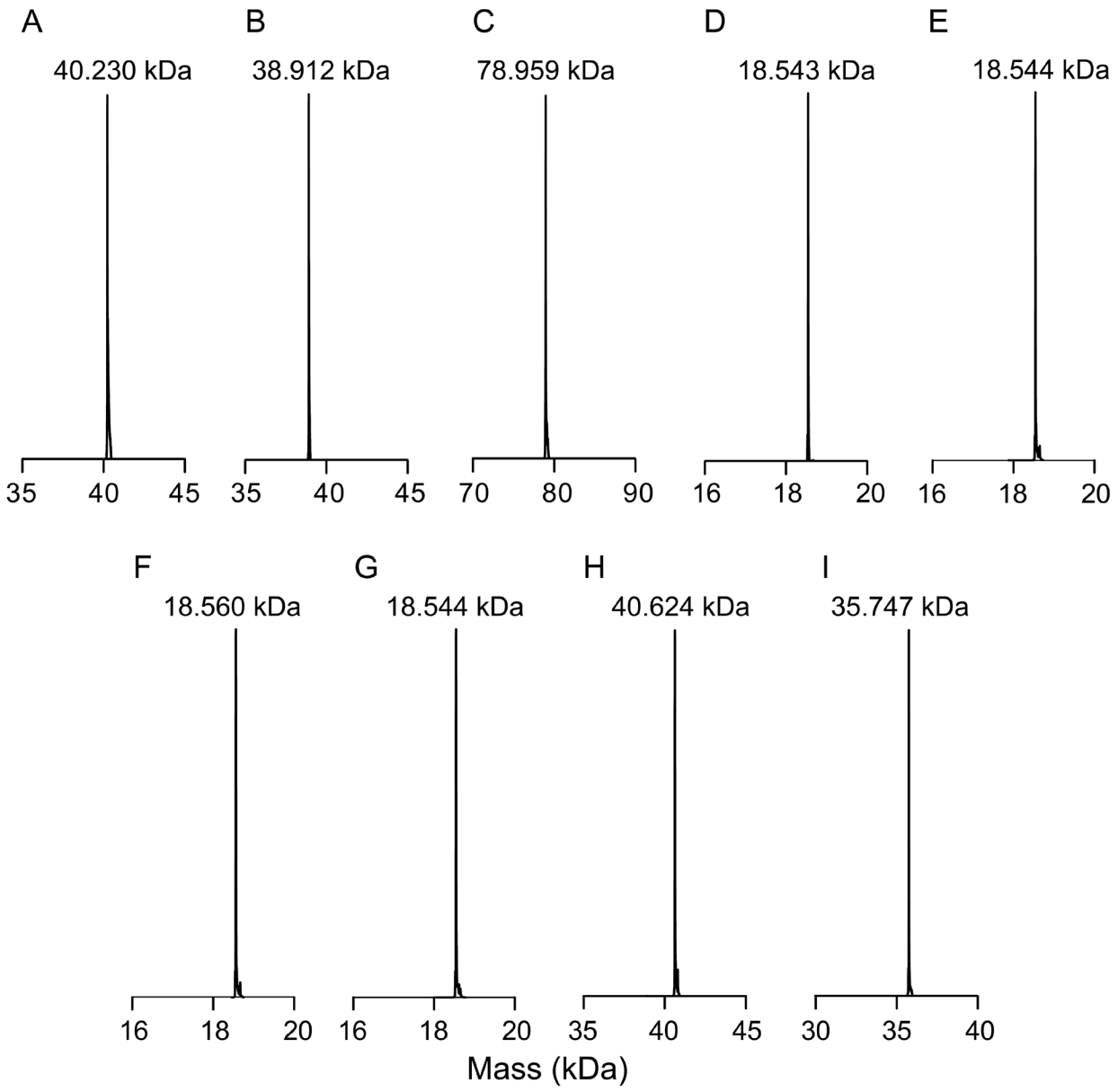

Figure 3.2: LC-ESI-TOFMS analysis of recombinant protein constructs used in current study

(A) Bro1, calculated mass: 40.231 kDa; **(B)** V, calculated mass: 38.912 kDa; **(C)** Bro1-V, calculated mass: 78.957 kDa; **(D)** $PRD^{Strep}_{703-868}$, calculated mass: 18.544 kDa; **(E)** $PRD^{Strep}_{703-868}$-S712C,C813S, calculated mass: 18.544 kDa; **(F)** $PRD^{Strep}_{703-868}$-A756C,C813S, calculated mass: 18.560 kDa; **(G)** $PRD^{Strep}_{703-868}$-S863C,C813S, calculated mass: 18.544 kDa; **(H)** MBP-E38C, calculated mass: 40.624 kDa; **(I)** catalytic domain of PTP1B, calculated mass: 35.747 kDa. The masses of the following two constructs, and full-length Src, are reported in our previous work (16).

3.3 Reversible amyloid fibrils of PRD

Using dye-binding assays with amyloid-specific probes, thioflavin T (ThT) and congo red (CR), and TEM, we previously established that the C-terminal tyrosine-rich fragment of ALIX-PRD ($PRD_{800-868}$) forms rope-like fibrils that dissolve into monomeric units on Src-mediated hyperphosphorylation (16). Because of the poor solubility of $PRD_{800-868}$ (<30 μM; pH 4.5 to 7), the data reported in our prior study were collected on a fusion protein with an N-terminal solubility enhancement tag comprising the B1 domain of protein G (GB1) (18). In contrast to $PRD_{800-868}$, $PRD^{Strep}_{703-868}$ was more soluble (~300 μM; pH 4.5 to 8), which allowed us to characterize its aggregation properties and its interactions with Src in the absence of a GB1 tag. LC-ESI-TOFMS analyses of Src-mediated phosphorylation revealed the formation of hyperphosphorylated $PRD^{Strep}_{703-868}$ with phosphorylation of 6 to 10 (out of 15) tyrosine residues (Fig. 3.3 A and Table 3.1). ThT emission assays confirmed the presence of β-sheet rich conformations for $PRD^{Strep}_{703-868}$ aggregates (Fig. 3.3 B). Spectral-shift assays carried out using CR demonstrated clear shifts toward 540 nm, further validating their amyloidogenic nature (Fig. 3.3 C). For these assays, the soluble N-terminal fragment, $PRD^{Strep}_{703-800}$ (16), and hyperphosphorylated $PRD^{Strep}_{703-868}$ served as negative controls. NMR analysis revealed a near-perfect superimposition of ^{1}H-^{15}N TROSYHSQC spectra of these two proteins, establishing Src-mediated dissolution of $PRD^{Strep}_{703-868}$ aggregates into NMR-amenable soluble monomers and the complete lack of interactions between the N- and C-terminal portions of PRD (Fig. 3.3.1). Backbone resonance assignments of hyperphosphorylated $PRD^{Strep}_{703-868}$ were not feasible owing to the complexity and the heterogeneity of its phosphorylation pattern. However, a narrow chemical shift dispersion (~7.7–8.7 ppm) suggested that the hyperphosphorylated $PRD^{Strep}_{703-868}$ is disordered in solution. TEM analyses revealed the presence of

rope-like unbranched $PRD^{Strep}_{703\text{-}868}$ filaments, characteristic of amyloid fibrils (Fig. 3.3 D). CD spectroscopic data confirmed the presence of β-sheet conformations in these fibrils (Fig. 3.3 E), corroborating the presence of amyloid structure. The corresponding CD spectrum of hyperphosphorylated $PRD^{Strep}_{703\text{-}868}$ validated its random-coil conformation.

To identify the fibril core resistant to protease treatment, a limited digestion of $PRD^{Strep}_{703\text{-}868}$ fibrils was carried out using proteinase K (PK), Figs 3.3 F-G. Based on band intensities of the reaction mixture comprising intact protein and the proteolyzed products monitored using SDS-PAGE (Fig. 3.3 F), we conclude that $PRD^{Strep}_{703\text{-}868}$ fibrils are resistant to PK digestion as the band for $PRD^{Strep}_{703\text{-}868}$ persisted after ~60 min of incubation with PK, albeit at a lower intensity than the corresponding band at time 0. In contrast, the soluble $PRD^{Strep}_{703\text{-}800}$ was completely hydrolyzed by PK within ~5 min of the reaction. LC-tandem MS (LC-MS/MS) analysis of PK-digestion of $PRD^{Strep}_{703\text{-}868}$ fibrils revealed that the two most abundant fragments were localized in the C-terminal region, residues 800–813 and 840–863 (Fig. 3.3 G and Fig. 3.3.2), indicating that these motifs likely participate in the formation of the fibril core. A limited PK digestion (incubation time ~5 min) was also performed on hyperphosphorylated $PRD^{Strep}_{703\text{-}868}$ and the corresponding cleavage products were identified using LC-MS/MS, which permitted identification of phosphorylated tyrosine residues, namely 803, 806, 809, 812, 829, 833, 837, 846, and 854 (Fig. 3.3.3). Nothing definitive can be said about the phosphorylation status of the remaining tyrosine residues, because of sequencing coverage gaps arising from problems associated with proteolytic digestion of $PRD^{Strep}_{703\text{-}868}$. Note that the tyrosine-rich portion of $PRD^{Strep}_{703\text{-}868}$, residues 800–868, carries no native lysine and arginine residues (cf., Fig. 3.1 A) and, thus, cannot be probed by traditional trypsin-

based proteomics (19). PK digestion of hyperphosphorylated $PRD^{Strep}_{703-868}$ was not analyzed by SDS-PAGE due to smearing of protein bands owing to phosphorylation (20).

To assess the impact of tyrosine phosphorylation on $PRD^{Strep}_{703-868}$ polymerization, aggregation kinetics using ThT fluorescence were monitored. $PRD^{Strep}_{703-868}$ exhibited sigmoidal aggregation profiles, a hallmark of fibril formation (Fig. 3.3 H). To establish Src-mediated dissolution of $PRD^{Strep}_{703-868}$ fibrils, Src and ATP were added to $PRD^{Strep}_{703-868}$ samples upon reaching a stationary phase (at ~3 h; Fig. 3.3 H), which resulted in a significant loss of ThT signal with a corresponding half-life ($t_{1/2}$) of ~0.2 h. The remaining $PRD^{Strep}_{703-868}$ samples were mixed with either Src or ATP and displayed no drop in ThT signals, indicating that Src or ATP do not affect $PRD^{Strep}_{703-868}$ fibrils. Remarkably, judging by the rapid appearance of characteristic sigmoidal ThT profiles ($t_{1/2}$ ~0.5 h; Fig. 3.3 I), dephosphorylation of hyperphosphorylated $PRD^{Strep}_{703-868}$ by PTP1B resulted in restoration of fibrils while the hyperphosphorylated $PRD^{Strep}_{703-868}$ without PTP1B showed no sigmoidal ThT profile [activity of recombinant PTP1B was measured using the malachite green assay; Fig. 3.3.4. For Src, the activity was measured using the ADP-Glo assay, described in our previous work (16)]. Although the exact identity of the phosphatase that works in tandem with ALIX is not known, PTP1B was suggested to regulate the endosomal sorting machinery (21). These observations establish that $PRD^{Strep}_{703-868}$ forms rope-like β-sheet rich fibrils that dissolve into soluble monomers on hyperphosphorylation by Src and that the removal of phosphoryl groups via PTP1B culminates in the restoration of fibrils, making $PRD^{Strep}_{703-868}$ a completely reversible amyloid controlled by PTMs (Fig. 3.3 J). In addition to PRD, Src is suggested to phosphorylate the Bro1 domain of ALIX in vivo (8). To characterize the impact of phosphorylation on Bro1, we carried out detailed NMR analyses of non- and phosphorylated Bro1, described below.

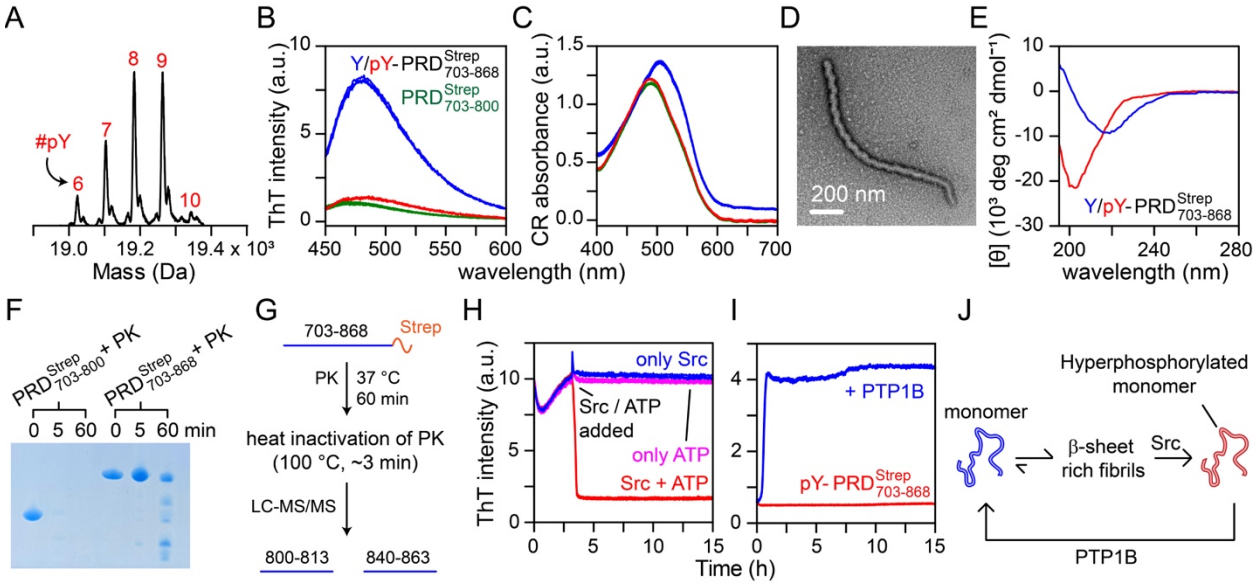

Figure 3.3: Reversible amyloids of $PRD^{Strep}_{703-868}$

(A) LC-ESI-TOFMS analysis of Src-mediated phosphorylation of $PRD^{Strep}_{703-868}$; the number of phosphorylated tyrosine residues is marked in red. Emission spectra of ThT **(B)** and absorbance spectra of CR **(C)** of $PRD^{Strep}_{703-868}$ aggregates (blue); n = 3, a.u., absorbance units. $PRD^{Strep}_{703-800}$ (green), and hyperphosphorylated $PRD^{Strep}_{703-868}$ (red) were used as controls. **(D)** Negatively stained EM images of Strep $PRD^{Strep}_{703-868}$. **(E)** CD spectra of $PRD^{Strep}_{703-868}$ fibrils (blue) and its hyperphosphorylated form (red). **(F)** SDS-PAGE analysis of limited PK digestion of $PRD^{Strep}_{703-868}$ fibrils and monomeric $PRD^{Strep}_{703-800}$. **(G)** Scheme of PK digestion and the results of LC-MS/MS analysis. **(H-I)** The impact of tyrosine phosphorylation and dephosphorylation on aggregation kinetics of $PRD^{Strep}_{703-868}$ assessed using ThT assays (30 °C; a.u., arbitrary units). **(H)** 100 µM $PRD^{Strep}_{703-868}$ was incubated without Src for ~3 h (n = 9). 10 µM Src + 1 mM ATP were added to three samples (red), whereas the remaining received either 10 µM Src (blue) or 1 mM ATP (pink). **(I)** 100 µM hyperphosphorylated $PRD^{Strep}_{703-868}$ samples (n = 3) were incubated in the absence (red) and the presence (blue) of 50 nM PTP1B. **(J)** Scheme depicting potential mode of formation and dissolution of $PRD^{Strep}_{703-868}$.

Table 3.1: LC-ESI-TOFMS analysis of Src-mediated hyperphosphorylation of $PRD^{Strep}_{703-868}$ and MTSL spin labeling of hyperphosphorylated $PRD^{Strep}_{703-868}$

All masses are in Daltons. $PRD^{Strep}_{703-868}$ contains 15 tyrosine residues (calculated mass: 18,544 Da; cf. Fig 3.2 D). Each phosphorylated residue accounts for an additional 80 daltons. $PRD^{Strep}_{703-868}$ samples were incubated with recombinant Src (molar ratio 5:1) at 30 °C for 1 h. Reactions were quenched by heat-shock (90 °C) and the resultant mixtures were subjected to LC-ESI-TOFMS analysis. Buffer conditions were as follows: 50 mM Tris, pH 7.5, 5 mM $MgCl_2$, 2 mM DTT, 1 mM ATP. Each MTSL addition accounts for an additional 184 daltons. Hyperphosphorylated samples were incubated with MTSL (protein to MTSL molar ratio: 1:10) at room temperature for ~12 h. The excess of unreacted spin label was removed using the HiPrep 26/10 Desalting column (GE Healthcare) and the resultant protein was subjected to LC-ESI-TOFMS analysis.

	Src + $PRD^{Strep}_{703-868}$			pY-$PRD^{Strep}_{703-868}$ + MSTL		
# pY	Experimental	Calculated	Difference	Experimental	Calculated	Difference
1	NA	18,624	-	NA	18,808	-
2	NA	18,704	-	NA	18,888	-
3	NA	18,784	-	NA	18,968	-
4	NA	18,864	-	NA	19,048	-
5	NA	18,944	-	19,127	19,128	-1
6	19,024	19,024	0	19,208	19,208	0
7	19,104	19,104	0	19,286	19,288	-2
8	19,184	19,184	0	19,369	19,368	1
9	19,264	19,264	0	19,488	19,488	0
10	19,344	19,344	0	NA	19,528	0

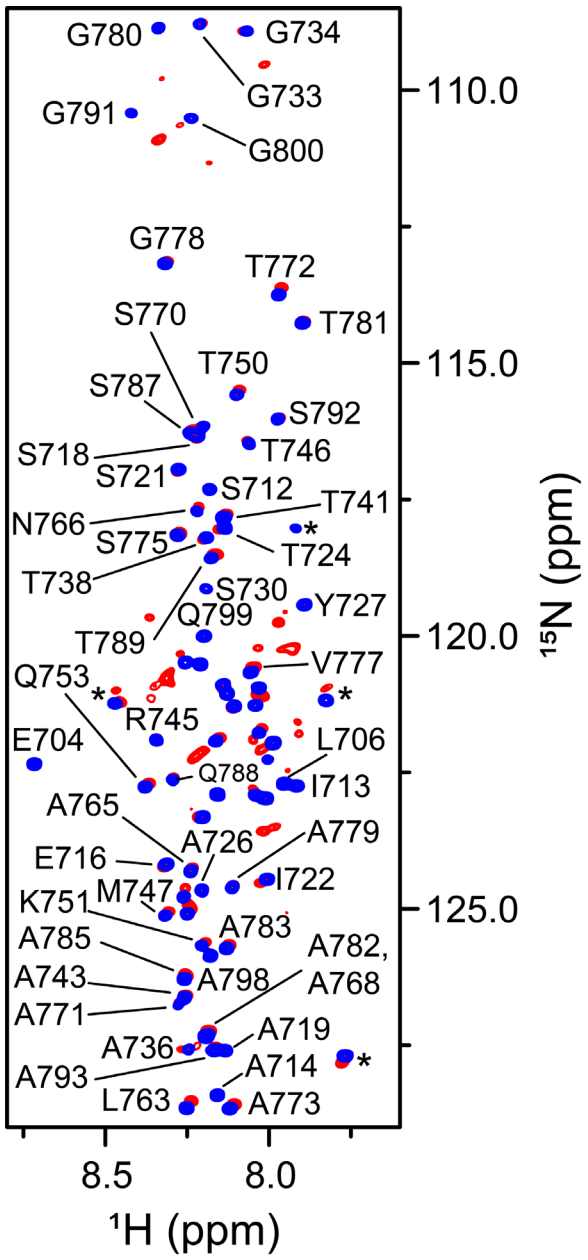

Figure 3.3.1: NMR analysis of hyperphosphorylated PRD$^{Strep}_{703-868}$

Overlay of expanded regions of the ^{1}H-^{15}N TROSY-HSQC correlation spectra of PRD$^{Strep}_{703-868}$ (blue) and hyperphosphorylated PRD$^{Strep}_{703-868}$ (red); 100 μM each. Some of the isolated cross-peaks of are labelled. The backbone resonance assignments of are taken from our previous work (16), biological magnetic resonance bank (BMRB) accession no. 28111. The cross-peaks corresponding to the C-terminal strep tag (WSHPQFEK) of are marked with asterisks. Backbone resonance assignments of hyperphosphorylated PRD$^{Strep}_{703-868}$ were not feasible owing to the complexity and the heterogeneity of its phosphorylation pattern. All data were acquired at a spectrometer ^{1}H frequency of 800 MHz at 30 °C. Buffer conditions were as follows: 20 mM sodium phosphate, pH 6.5, 50 mM NaCl, 1 mM TCEP, and 2 mM EDTA.

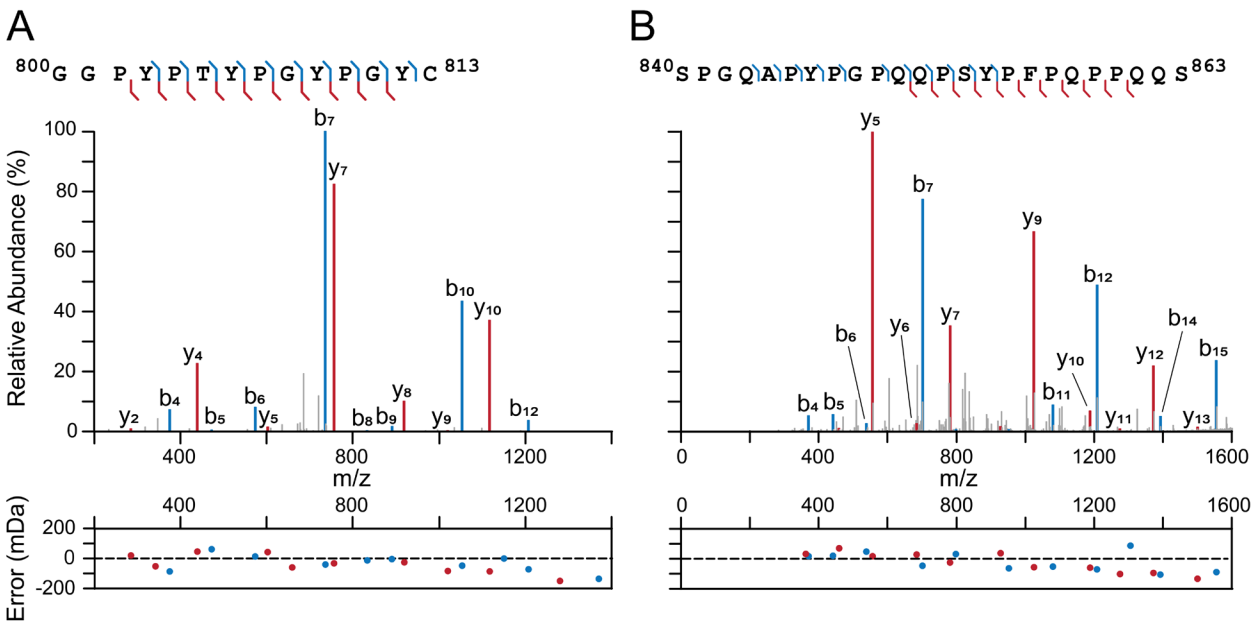

Figure 3.3.2: LC-MS/MS analysis of PK-digestion of $PRD^{Strep}_{703-868}$ fibrils

(A-B) Panels show the assignment of collision-induced dissociation (CID) fragment ions to the peptide primary sequence according to the standard nomenclature (60). The b_n and y_n ions are denoted by the blue and red brackets, respectively. Residuals (observed spectral position minus calculated m/z) for each fragment ion peak are plotted below the panels. The figure was formatted using IPSA (61). Also see Table 3.2 for the list of search parameters used for analyses and Supplementary Files for the list of all peptides that were identified. $PRD^{Strep}_{703-868}$.

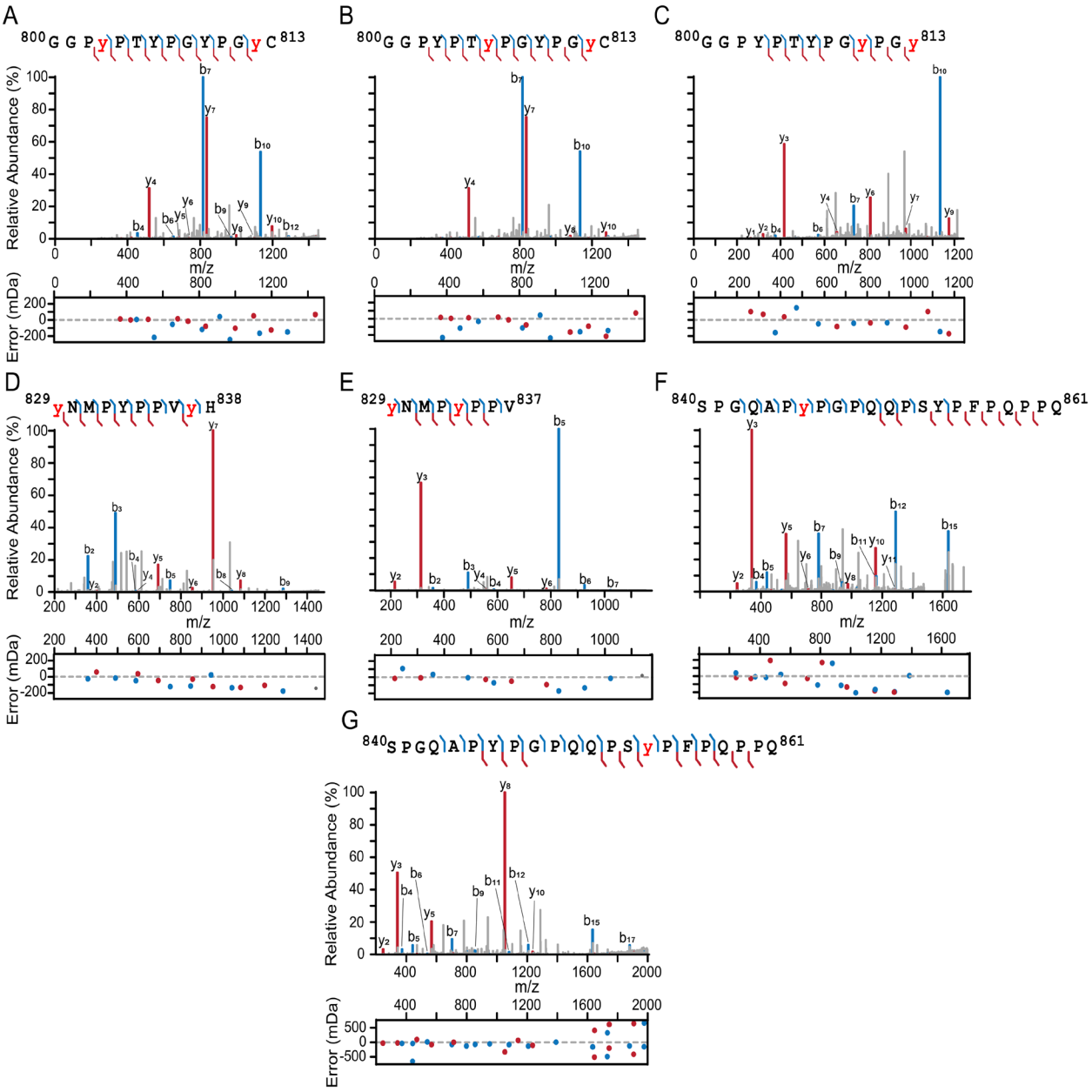

Figure 3.3.3: LC-MS/MS analysis of PK-digestion of hyperphosphorylated PRD$^{Strep}_{703-868}$

(A-G) Panels show the assignment of collision-induced dissociation (CID) fragment ions to the peptide primary sequence. The b_n and y_n ions are denoted by the blue and red brackets, respectively. Phosphorylated tyrosine residues are denoted in red. Residuals (observed spectral position minus calculated m/z) for each fragment ion peak are plotted below the panels. The figure was formatted using IPSA (61). Also see Table 3.2 for the list of search parameters used for analyses and Supplementary Files for the list of all peptides that were identified. The above results are in excellent agreement with our previous results of LC-MS/MS analysis of chymotrypsin digested hyperphosphorylated $PRD_{800-868}$ (16).

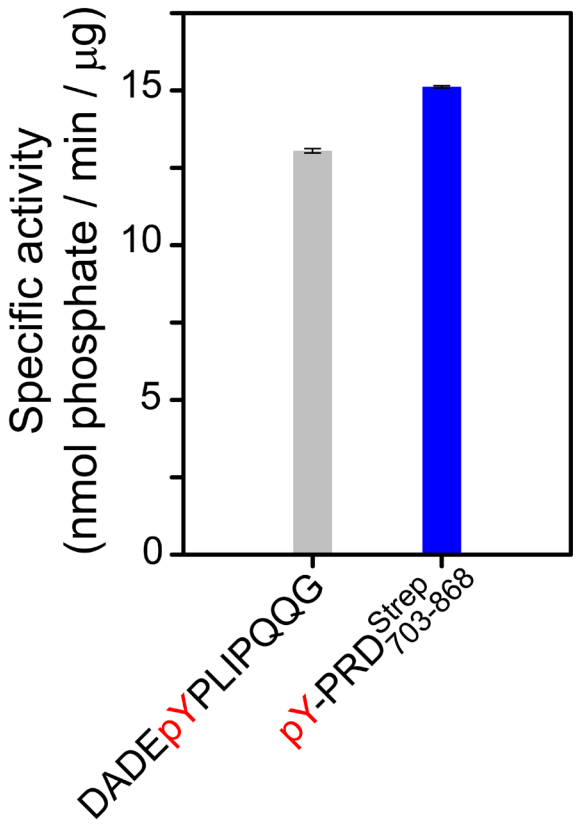

Figure 3.3.4: Quantification of PTP1B activity

The activity of the catalytic domain of recombinant PTP1B was measured using a malachite green phosphate detection assay kit (R&D systems, Inc). Data are expressed as means ± s.e.m. of three replicates. The specific activity against the control tyrosine phosphatase substrate (62); primary sequence: DADEpYPLIPQQG, where pY is phosphorylated tyrosine, is similar to the value reported by R&D systems, Inc for their commercially available PTP1B (>15 nmol/min/µg). Buffer and experimental conditions were as follows: 20 mM HEPES, pH 7.5, 1 mM DTT, 1 mM EDTA, and 30 °C.

3.4 NMR analysis of nonphosphorylated and phosphorylated Bro1

ALIX - Src interactions are suggested to proceed in a stepwise fashion in vivo, where Src first binds and phosphorylates the highly conserved region, ^{312}KKDNDFIY^{319}, of the Bro1 domain, followed by hyperphosphorylation of the tyrosine-rich portion of PRD, ultimately resulting in the relocation of ALIX from late endosomal membranes to the cytosol (8). Src-mediated phosphorylation of Bro1 was confirmed using western blotting (Fig. 3.4 A). LC-ESI-TOFMS and LC-MS/MS analyses established the formation of phosphorylated Bro1 and confirmed the phosphorylation of Y319 (Fig. 3.4 B and C, respectively). To explore the impact of tyrosine phosphorylation on Bro1 at atomic resolution, we carried out a detailed NMR investigation (Fig. 3.4.1). Although the overall size of Bro1 is relatively large for solution NMR studies (~40 kDa), excellent spectral quality was obtained by perdeuteration coupled with TROSY (Fig. 3.4.1 A), which allowed us to carry out nearly complete backbone resonance assignments of Bro1. Based on an excellent agreement between the secondary structure derived from the assigned backbone chemical shifts (^{13}Cα, ^{13}Cβ, ^{13}C′, ^{15}N, and ^{1}H$_N$) using TALOS-N (22) with that obtained from the three-dimensional crystal structure of Bro1 [Protein Data Bank (PDB) entry 5WA1 (23); Fig. 3.4.2], we conclude that recombinant Bro1 is well-folded in solution. To probe structural and conformational changes that take place in Bro1 upon Src-mediated phosphorylation of Y319, ^{1}H$_N$/^{15}N chemical shift perturbation mapping was utilized. NMR analyses of phosphorylated Bro1 revealed large ^{1}H$_N$/^{15}N chemical shift perturbations that arise from the introduction of a negatively charged phosphoryl group (Fig. 3.4.1 B). Mapping of these perturbations onto the crystal structure of Bro1 allowed identification of regions affected by tyrosine phosphorylation (Fig. 3.4.1 C). All perturbations were localized in the regions surrounding Y319, which further confirmed specific phosphorylation of Bro1 by Src. The heteronuclear ^{15}N-{^{1}H} NOE data (Fig. 3.4.3) of non- and

phosphorylated Bro1 indicated that the introduction of phosphoryl group did not affect the local internal mobility of Bro1. Collectively, the above data established that Src-mediated phosphorylation of Bro1 at Y319 induces local changes.

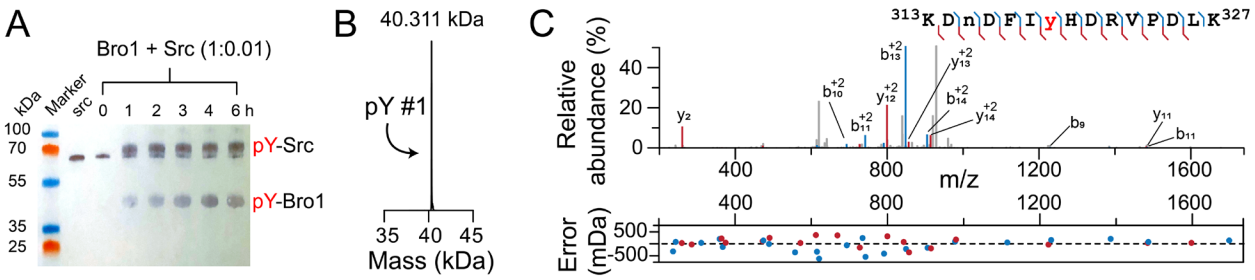

Figure 3.4: Analyses of Src-mediated in vitro phosphorylation of Bro1

(A) Time course of Src-mediated in vitro phosphorylation of Bro1 by western blotting. The concentration of Bro1 was 50 µM; the number in parenthesis represent the molar ratio of Bro1 to Src. **(B)** LC-ESI-TOFMS and **(C)** LC-MS/MS analyses of phosphorylated Bro1 revealed that Bro1 is monophosphorylated by Src at residue 319 (note that Bro1 carries 12 native tyrosine residues; cf. Fig 3C). For panel C, residuals (observed spectral position minus calculated m/z) for each fragment ion peak are plotted below the panel. The phosphorylated tyrosine residue (Y319) is denoted in red. The figure was formatted using IPSA (61). Also see Table 3.2 for the list of search parameters used for analyses and Supplementary Files for the list of all peptides that were identified. Buffer and experimental conditions were as follows: 50 mM Tris, pH 7.5, 1 mM ATP, 5 mM $MgCl_2$, 0.5 mM EDTA, 2 mM DTT, and 30 °C.

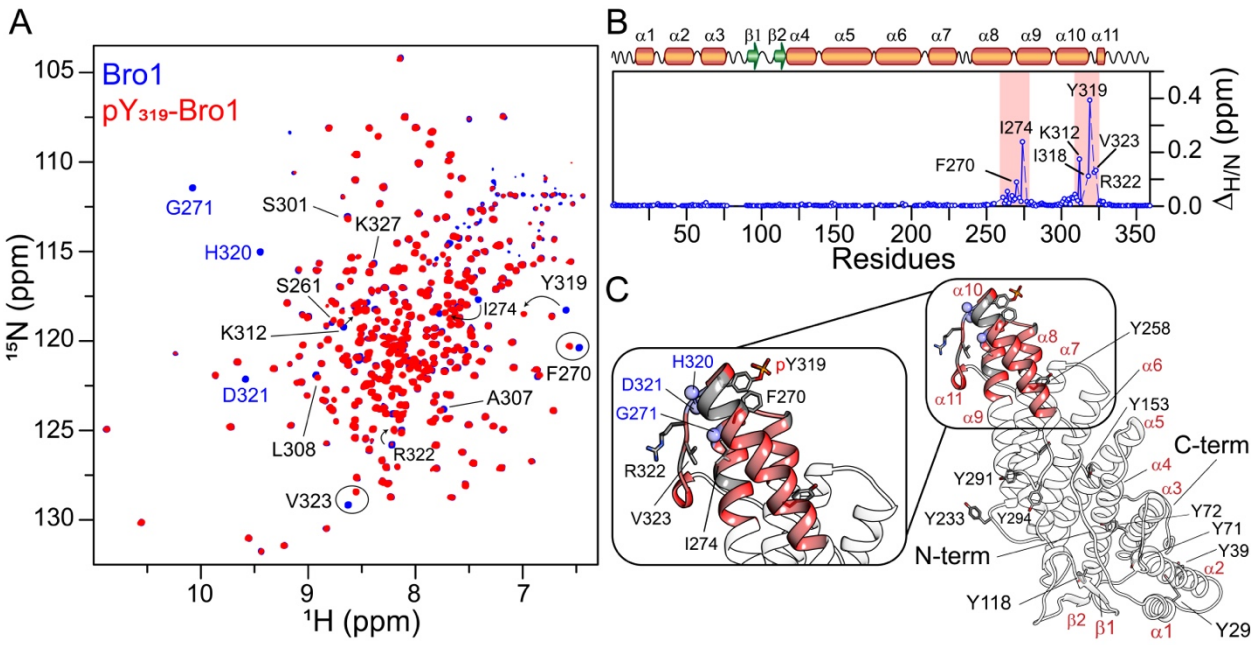

Figure 3.4.1: NMR characterization of nonphosphorylated and phosphorylated Bro1

(A) Overlay of ^{1}H–^{15}N TROSY–HSQC spectra of nonphosphorylated (blue) and phosphorylated (red) Bro1. A few of the ^{1}H–^{15}N crosspeaks that undergo chemical shift changes on phosphorylation are labeled and circled. Residues that exhibit resonance line broadening upon phosphorylation, namely G271, H320, and D321, are labeled in blue. **(B)** $^{1}H_N/^{15}N$ chemical shift perturbation profile of Bro1 upon phosphorylation. Secondary structure elements are indicated above the panel. Red rectangles indicate residues (261–280 and 300–328) that exhibit large chemical shift perturbations because of phosphorylation. **(C)** A ribbon diagram of phosphorylated Bro1 constructed using Protein Data Bank entry 5WA1 in Xplor-NIH (65); Y319 and a few of the residues that undergo large chemical shift changes upon phosphorylation are shown in stick representation. Red ribbons represent residues that are most affected because of phosphorylation. Gray ribbons indicate residues around the phosphorylation site that could not be assigned unambiguously. Residues that undergo resonance line broadening upon phosphorylation are depicted as blue spheres.

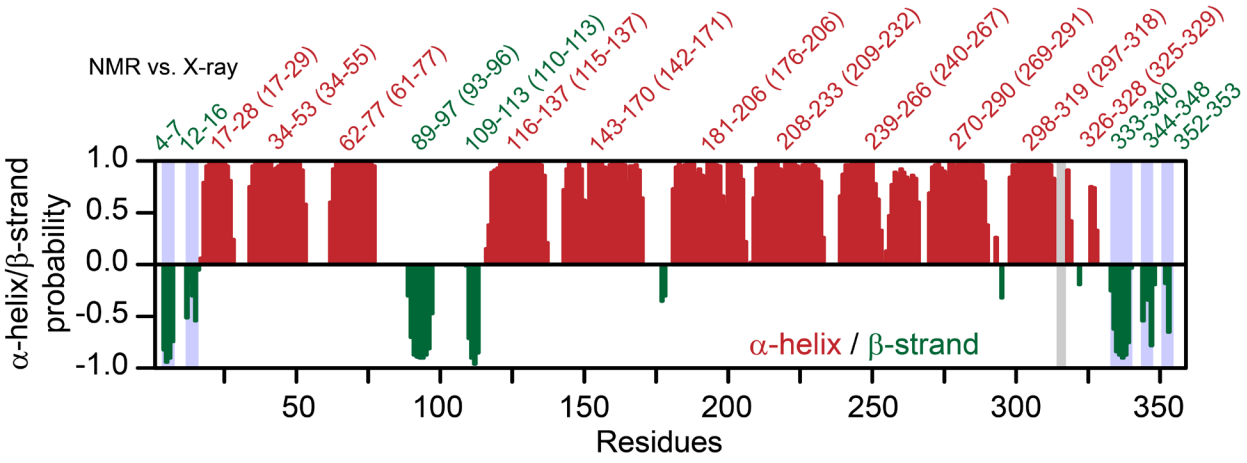

Figure 3.4.2: NMR and X-ray derived secondary structure elements of Bro1

Secondary structure probability, α helix in red and β strand in green, derived from the backbone chemical shifts (^{13}Cα, ^{13}Cβ, ^{13}C′, ^{15}N, and ^{1}H$_N$) of Bro1 using TALOS-N (22). The numbers on the top of the panel represent motifs constituting the corresponding secondary structure elements; the numbers in parenthesis are the corresponding motifs obtained from the coordinates of the X-ray structure of Bro1, Protein Data Bank (PDB) entry 5WA1 (23). Note that in contrast to X-ray, NMR chemical shifts predicted ordered strand conformations for several residues of the extreme N- and C-termini, specifically residues 4-7, 12-16, 333-340, 344-348, and 352-353 (marked in blue semi-transparent rectangles; only predictions with probability greater than 0.5 are highlighted). Semi-transparent gray rectangles mark missing predictions for residues 314-317 that could not be assigned unambiguously. Note that the low helical probability of residues 253-256 is due to the lack of availability of backbone carbon chemical shifts in that region.

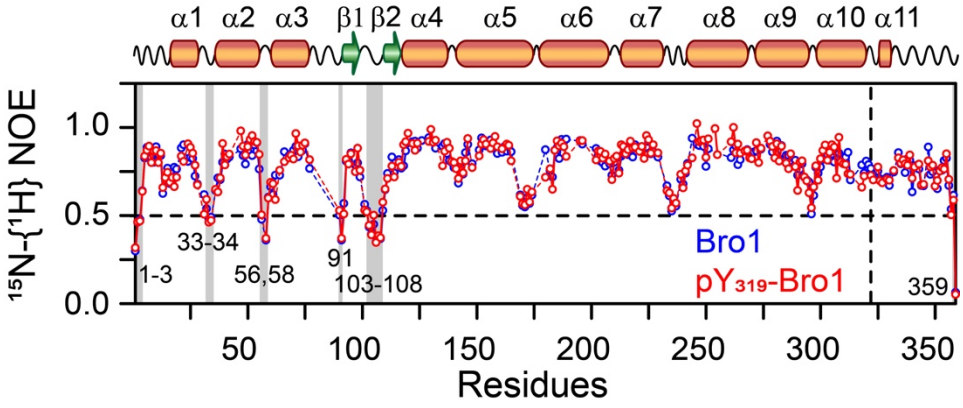

Figure 3.4.3: ^{15}N-{^{1}H} heteronuclear NOE data for nonphosphorylated and phosphorylated Bro1

Regions with high local mobility on the nanosecond time scale, ^{15}N–{^{1}H} NOE < 0.5, are labeled and marked with semi-transparent gray rectangles. The location of Y319 is indicated by a vertical dashed line. All data were acquired with 500 μM ^{2}H/^{15}N labeled proteins at a spectrometer ^{1}H frequency of 800 MHz at 30 °C.

3.5 Lack of interactions between PRD and globular ALIX domains

A prior study suggested that the N-terminal portion of PRD, specifically the ^{717}PSAP^{720} motif that interacts with the ubiquitin E2 variant domain of tumor-susceptibility gene 101 (TSG101-UEV), directly associates with the Src-binding region of Bro1 (13). PRD was also suggested to prevent the binding between the V domain and the YPX$_n$L consensus motifs (X = any residue and *n* = 1-3) found in viral proteins, although molecular details of this inhibition were not determined (14). To investigate interdomain interactions of ALIX, we carried out $^{1}H_N/^{15}N$ chemical shift perturbation mapping using $PRD^{Strep}_{703\text{-}800}$ and non- and phosphorylated Bro1 (Fig. 3.5). Negligible $^{1}H_N/^{15}N$ chemical-shift perturbations were observed for both non- and phosphorylated NMR-visible Bro1, one at a time, upon the addition of three molar equivalents of $PRD^{Strep}_{703\text{-}800}$ (Fig. 3.5 A-B, respectively), indicating that Bro1 did not bind to $PRD^{Strep}_{703\text{-}800}$. The corresponding titration experiments carried out using NMR-visible $PRD^{Strep}_{703\text{-}800}$ and unlabeled non- and phosphorylated Bro1 yielded negligible chemical-shift changes (Fig. 3.5 C), confirming the lack of Bro1 - $PRD^{Strep}_{703\text{-}800}$ interactions. To determine the involvement of the V domain, titration experiments were carried out using NMR-visible $PRD^{Strep}_{703\text{-}800}$, in the absence and presence of 3 molar equivalents of V and Bro1-V constructs (one at a time). Minimal chemical shift changes indicated that V and Bro1-V constructs did not bind to $PRD^{Strep}_{703\text{-}800}$ (Fig. 3.5 C). Experiments using NMR-visible V and Bro1-V constructs were not viable since both produced poor-quality NMR spectra, likely due to the open-close transitions of the V-domain in solution (14). Collectively, these observations indicated that Bro1 and V domains did not interact with $PRD^{Strep}_{703\text{-}800}$. These findings are consistent with the fact that unlike proline-recognition domains such as UEV (24,25), Bro1 domains have not been known to bind to proline-rich motifs, and that ALIX-PRD carries no YPX$_n$L consensus motif recognized by the V-domain. Finally, nothing definitive can be said about

the interactions of intact $PRD^{Strep}_{703\text{-}868}$ with Bro1 and V domains in solution because of its propensity to form fibrils. We, however, uncovered novel interactions between Bro1 and hyperphosphorylated $PRD^{Strep}_{703\text{-}868}$, which are described below.

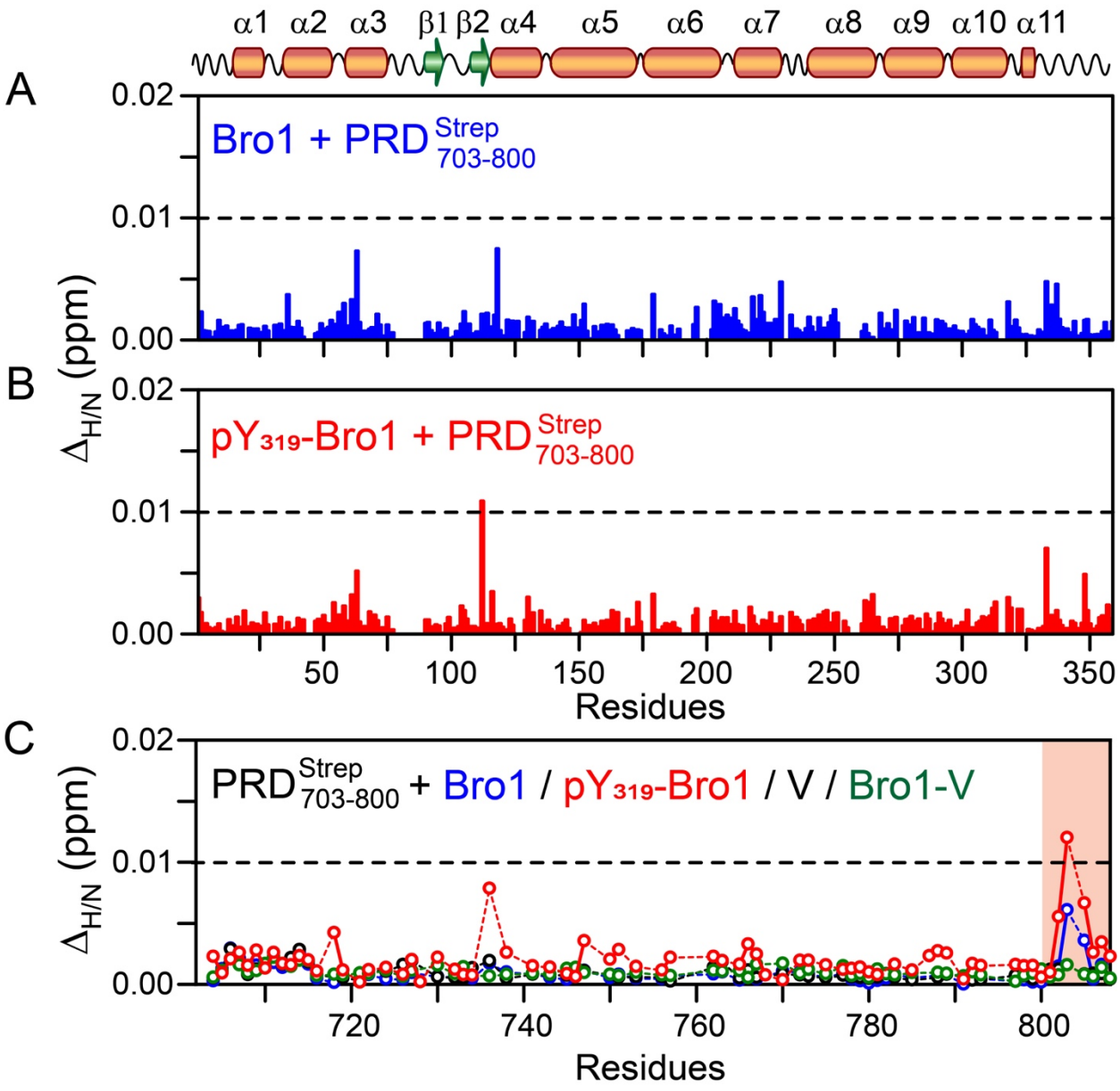

Figure 3.5: Lack of association between PRD and globular ALIX domains

$^{1}H_N/^{15}N$ chemical shift perturbation profiles of **(A)** non-phosphorylated and **(B)** phosphorylated $^{2}H/^{15}N$-labeled Bro1 on addition of three-molar equivalent of non-labeled $PRD^{Strep}_{703\text{-}800}$. **(C)** $^{1}H_N/^{15}N$ chemical shift perturbation profiles of ^{15}N-labeled $PRD^{Strep}_{703\text{-}800}$ on addition of non-labeled Bro1 (blue), phosphorylated Bro1 (red), V (black), and Bro-V (dark green); one at a time, $PRD^{Strep}_{703\text{-}800}$ to globular ALIX domains molar ratio = 1:3. Region highlighted in semitransparent orange rectangle indicates the location of the C-terminal strep purification tag (residues 801-808).

3.6 Interactions between Bro1 and hyperphosphorylated PRD

Src-mediated hyperphosphorylation of PRD relocates ALIX from late endosomal membranes to the cytosol (8), indicating a likely competition between hyperphosphorylated PRD and membranes for association with the phospholipid binding region(s) of Bro1. To test this hypothesis and identify contacts between Bro1 and hyperphosphorylated $PRD^{Strep}_{703\text{-}868}$, we made use of intermolecular paramagnetic relaxation enhancement, PRE (26). The magnitude of the PRE effect is very large owing to the large magnetic moment of the unpaired electron of the paramagnetic label and is proportional to the $<r^{-6}>$ paramagnetic label - proton distance, which enables the detection of sparsely populated (as low as 0.5-1% in favorable cases) encounter complexes between binding partners (27). The paramagnetic nitroxide spin label, (1-Oxyl-2,2,5,5-tetramethyl-Δ3-pyrroline-3-methyl) methanethiosulfonate (MTSL), was introduced at four separate sites on hyperphosphorylated $PRD^{Strep}_{703\text{-}868}$ via disulfide linkages (Fig. 3.6 A; also see Fig. 3.6 B and Table 3.1 for LC-ESI-TOFMS analysis of MTSL conjugated products). These four sites were the native cysteine residue of $PRD^{Strep}_{703\text{-}868}$, C813, and three engineered sites, S712C, A756C, and S863C (Fig. 3.6.1 A; in all cysteine variants, C813 was mutated to a serine). Site C813 lies adjacent to a cluster of tyrosine residues that are phosphorylated by Src (cf. Fig. 3.3.3). Sites S712C and A756C are located near the motif that binds to TSG101-UEV [residues 717-720; (16)] and in the highly basic region of PRD (residues 756-767; theoretical isoelectric point ~12), respectively. Site S863C is located at the extreme C-terminus of PRD and is adjacent to ^{864}YY^{865} (cf. Fig. 3.1 A); we were unable to detect the phosphorylation status of these two tyrosine residues because of sequencing coverage gaps.

Intermolecular PRE (^1H_N-Γ_2) profiles observed for NMR visible Bro1 in the presence of paramagnetically labeled hyperphosphorylated $PRD^{Strep}_{703\text{-}868}$ and its cysteine variants are shown in

Fig. 3.6.1 B. When the paramagnetic label was located at site S712C of $PRD^{Strep}_{703\text{-}868}$, two lone ≥ 25 s^{-1} PREs were observed (residues 233 and 336 of Bro1), whereas no strong PRE of ≥ 25 s^{-1} were seen when the label was conjugated to site A756C of $PRD^{Strep}_{703\text{-}868}$. These minimal intermolecular PRE effects indicate that interactions of Bro1 with sites S712C and A756C of $PRD^{Strep}_{703\text{-}868}$ are negligible. These observations validate the results of our NMR titration experiments, which demonstrated that the isolated Bro1 did not associate with the N-terminal portion of PRD and rule out transient association between the highly basic region of PRD encompassing site A756C and electronegative surface accessible regions of Bro1. When the paramagnetic label was located at site C813 of $PRD^{Strep}_{703\text{-}868}$, strong PREs (≥ 25 s^{-1}) were observed for several Bro1 residues, with residues 91, 114, 116, and 233 completely broadened out. These observations indicate that the spin label is in the close vicinity of the above Bro1 residues, possibly due to its proximity to phosphorylated tyrosine residues of $PRD^{Strep}_{703\text{-}868}$ that likely drive the interdomain electrostatic association. No strong PREs (≥ 25 s^{-1}) were observed with the paramagnetic label at site S863C of $PRD^{Strep}_{703\text{-}868}$, indicating minimal interactions with this site, perhaps because tyrosine residues located next to this site (^{864}YY^{865}) are not phosphorylated by Src. Control experiments carried out using either free water-soluble paramagnetic nitroxide label, 4-Hydroxy-2,2,6,6-tetramethylpiperidine 1-oxyl (TEMPOL), or an unrelated MTSL-conjugated protein, apo maltose-binding protein carrying a E38C point mutation (MBP-E38C), showed no significant intermolecular PRE effects (Fig. 3.6.2). These results establish that the intermolecular PREs obtained for Bro1 with label at site C813 of hyperphosphorylated $PRD^{Strep}_{703\text{-}868}$ arise from a specific association of this site with Bro1 and not from preferential binding of the paramagnetic label to Bro1.

A quantitative interpretation of the strong intermolecular PREs obtained with paramagnetic label conjugated to site C813 is not plausible owing to the disordered nature of hyperphosphorylated $PRD^{Strep}_{703\text{-}868}$ and the complexity of phosphorylation pattern (cf. Fig. 3.6 B), culminating in a highly dynamic encounter complex with Bro1. The experimental manifestation of this dynamic complex is the approximately uniform, elevated $^{1}H\text{-}\Gamma_2$ PRE background of ~10 – 15 s^{-1} (Fig. 3.6.1 B; for the other three sites of $PRD^{Strep}_{703\text{-}868}$, this background is relatively lower, ~5 – 10 s^{-1}, and stems from random collisions of these three sites with surface accessible sites of Bro1). Mapping these substantial PREs on to the crystal structure of Bro1, however, allowed us to identify the preferential mode of interactions between hyperphosphorylated $PRD^{Strep}_{703\text{-}868}$ and Bro1. Two clusters of intermolecular contacts can be discerned (Fig. 3.6.1 C), both residing on the two arms of the convex face of Bro1. For comparison, the molecular surface of Bro1 color-coded according to electrostatic potential calculated using software APBS (28) is shown in Fig. 3.6.1 D. One contact site comprises the N-terminal portion of Bro1, residues 13, 16, 17, 52, 59, 61, 91, 92, 114, 116, and 118. Because three of these residues were completely broadened out in the presence of paramagnetically labeled hyperphosphorylated $PRD^{Strep}_{703\text{-}868}$, we speculate that this cluster makes primary contact with paramagnetically labeled site C813. This cluster has a strong basic character and, therefore, can electrostatically associate with hyperphosphorylated $SPRD^{Strep}_{703\text{-}868}$, further validating that the interdomain interactions are governed by phosphorylated tyrosine residues of PRD. The other contact site comprises residues 203, 209, 229, 233, 241, 246, 248, 296, and 297, and residue 3, which lies in close vicinity of this cluster. Because of a less pronounced electropositive surface, we hypothesize that this Bro1 cluster serves as a secondary contact site with hyperphosphorylated $PRD^{Strep}_{703\text{-}868}$. Technical difficulties prevented us from measuring intermolecular PREs on phosphorylated Bro1 owing to a significant precipitation observed upon

mixing phosphorylated Bro1 with paramagnetically labeled hyperphosphorylated $PRD^{Strep}_{703\text{-}868}$. However, since Y319 of Bro1 is located away from the two Bro1 regions that interact with hyperphosphorylated $PRD^{Strep}_{703\text{-}868}$ (Fig. 3.6.1 C), we predict that Bro1 phosphorylation will have a negligible effect on the association of these two domains. Collectively, the above observations establish that site C813 of hyperphosphorylated $PRD^{Strep}_{703\text{-}868}$, which lies adjacent to a group of phosphorylated tyrosine residues, transiently interacts with two electropositive regions of Bro1.

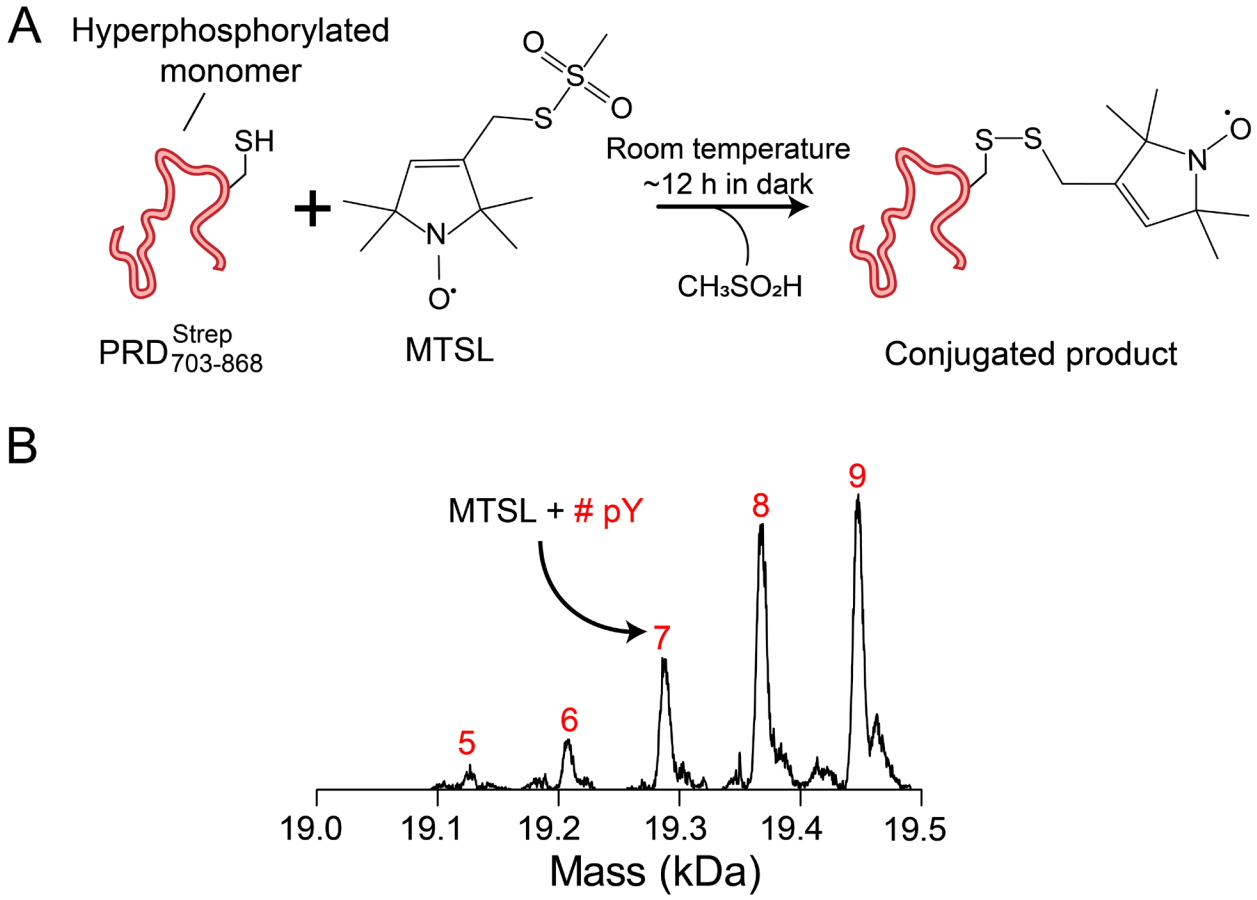

Figure 3.6: Site-specific spin labeling of hyperphosphorylated $PRD^{Strep}_{703-868}$ with MTSL

(A) Schematic of the conjugation reaction between hyperphosphorylated $PRD^{Strep}_{703-868}$ and nitroxide spin label, MTSL. **(B)** LC-ESI-TOFMS analysis of MTSL-labeled hyperphosphorylated. Each peak in the deconvoluted spectrum represents a conjugated product carrying one MTSL moiety; the numbers in red represent the number of phosphorylated tyrosine residues (see Table 3.1 for additional details).

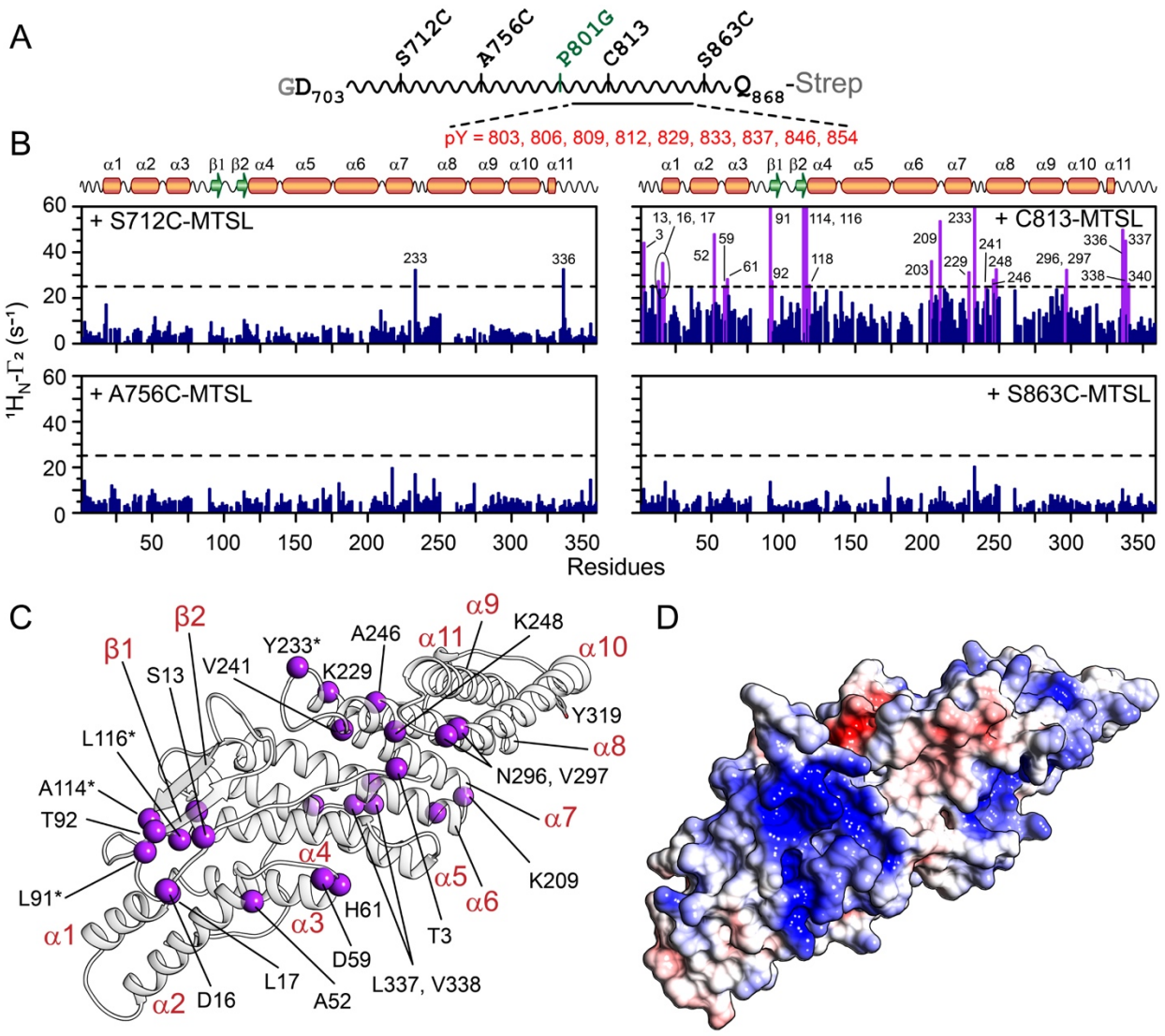

Figure 3.6.1: PRE mapping of Bro1-hyperphosphorylated PRD interactions

(A) Schematic of $PRD^{Strep}_{703-868}$; vertical lines indicate the location of the four independent conjugation sites and of the P801G mutation (green). The location of phosphorylated tyrosine residues is shown. **(B)** Intermolecular PREs observed on $^{2}H/^{15}N$-labeled Bro1 (200 μM) arising from MTSL label conjugated to hyperphosphorylated $PRD^{Strep}_{703-868}$ at four specific sites; Bro1 to $PRD^{Strep}_{703-868}$ molar ratio = 1:1. Conjugation of MTSL at site C813 produced a noticeable intermolecular PREs; residues with intermolecular PREs above the background are labeled and indicated by purple bars. PREs too large (> 60 s^{-1}) to be accurately measured are plotted as 60 s^{-1}. The remaining three conjugation sites did not generate large intermolecular PREs; a few exceptions are labeled. **(C)** Ribbon representation of Bro1; residues that exhibit large PREs (≥ 25 s^{-1}) with spin label at site C813 are depicted as purple spheres; residues that were completely broadened out are marked with asterisks. Y319 is shown in a stick representation. **(D)** Molecular surface of Bro1 (in the same orientation as C) color coded according to electrostatic potential; ± 5 kT with blue, positive; white, neutral; and red, negative.

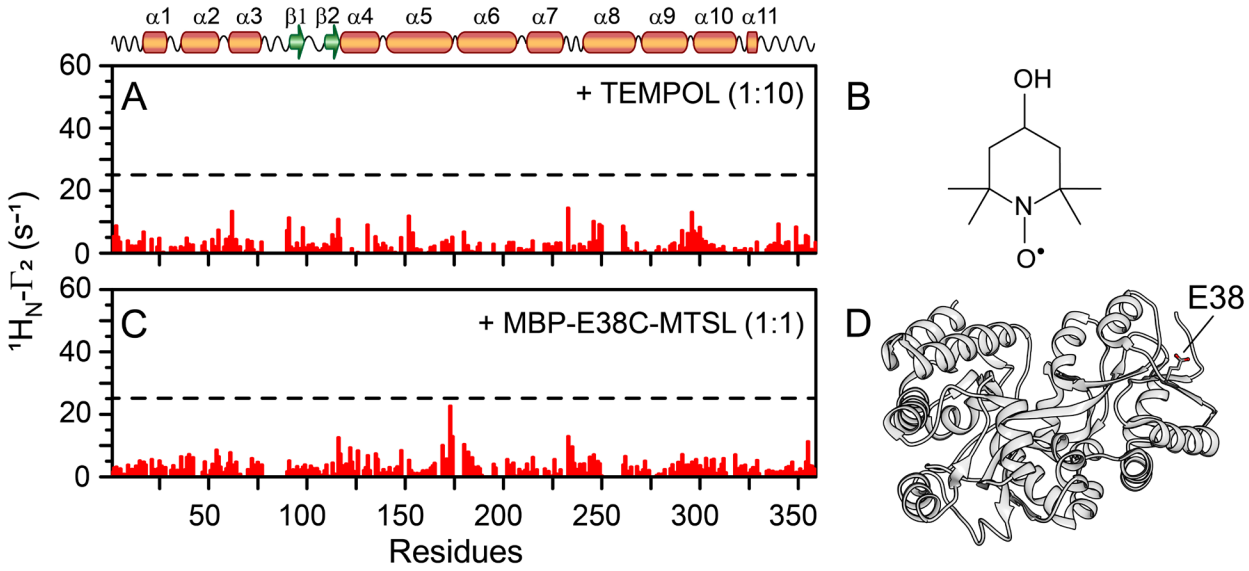

Figure 3.6.2: Intermolecular PRE controls

Negative PRE controls (red vertical bars) are provided by the intermolecular PRE profiles observed on $^{15}N/^{2}H$-labeled Bro1 upon addition of **(A)** water soluble TEMPOL; the structure of TEMPOL is shown in panel B, and **(C)** apo-maltose binding protein (MBP-E38C) conjugated to a paramagnetic MTSL probe. Secondary structure elements of Bro1 are indicated above the panels. A few small solvent PREs with ^1H_N-Γ_2 values in the range of 5–10 s^{-1} are observed with TEMPOL owing to random collisions at solvent-exposed, surface accessible sites of Bro1. All PREs observed with either TEMPOL or MBP-E38C-MTSL are much smaller than those observed with hyperphosphorylated $PRD^{Strep}_{703-868}$ labeled with MTSL at site C813 (cf. Fig. 3.6.1 B, top right). The concentration of Bro1 was 200 μM. The numbers in parenthesis represent the molar ratios of Bro1 to TEMPOL / Bro1 to MTSL-tagged MBP-E38C. Buffer conditions were as follows: 20 mM sodium phosphate, pH 6.5, 50 mM NaCl, and 2 mM EDTA. All data were acquired at a spectrometer ^1H frequency of 800 MHz at 30 °C using a two-time point method (26,27). **(D)** Ribbon representation of wild-type open form of apo MBP; Protein Data Bank (PDB) entry: 1FQA (63). Residue E38, located on the surface of MBP, is shown in stick representation.

3.7 Interactions between Bro1 and analogs of late endosomal membranes

To identify the phospholipid binding region(s) of Bro1, we made use of NMR titration experiments, where unilamellar lipid vesicles were mixed with NMR-visible Bro1. To mimic the composition of late endosomal membranes, extruded vesicles were made using 1-palmitoyl-2-oleoyl-glycero-3-phosphocholine (POPC), 1-palmitoyl-2-oleoyl-sn-glycero-3-phosphoethanolamine (POPE), and LBPA. We also made use of zwitterionic vesicles comprising POPC and POPE, and negatively charged vesicles composed of POPC, POPE, and 1-palmitoyl-2-oleoyl-sn-glycero-3-phospho-Lserine (POPS). Note that eukaryotic membranes, including those of late endosomes, are highly complex and that the vesicles used here represent an artificial system. However, the latter offer the most native-like local membrane environment and, therefore, are often considered simplified models of cellular membranes (29). The size distribution of vesicles, in the absence and presence of Bro1, was measured by DLS and was found to be homogenous with mean diameters ranging from 130 – 150 nm (Fig. 3.7). A previous study suggested that the binding of divalent calcium to Bro1 was necessary for Bro1 – membrane interactions (11). However, negligible chemical shift changes were observed for Bro1 resonances in the presence of a molar excess of calcium, which ruled out Bro1 - calcium interactions (Fig. 3.7.1).

On addition of POPC/POPE/LBPA vesicles (molar ratio 6:3:1) to 100 μM NMR visible Bro1 (protein to lipid molar ratio: 1:30), ~20-30% resonance broadening was observed for a majority of ^{1}H-^{15}N cross peaks of Bro1 (Fig. 3.7.2 A; no chemical shift perturbations and new resonances were observed upon addition of vesicles to Bro1). When LBPA concentration was increased in a stepwise fashion (10, 12.5, and 15 mol percent of LBPA; Fig. 3.7.2 A-C), cross-peaks of Bro1 were progressively attenuated. These results indicate the formation of a high-molecular weight complex between Bro1 and lipid vesicles and an increase in the vesicle-bound

population of Bro1 as a function of LBPA concentration; all NMR measurements were carried out using the same protein to lipid molar ratio of 1:30. The reductions in ^{1}H-^{15}N cross-peak volumes of Bro1 as a function of increasing LBPA concentration (Bro1 + POPC/POPE/LBPA vesicles, molar ratio 5.5:3:1.5 vs. Bro1 + POPC/POPE/LBPA vesicles, molar ratio 6:3:1) are plotted in Fig. 3.7.3 A, which permitted identification of the most affected residues that likely associate directly with LBPA-enriched particles. The solvent exposed motif, residues ^{101}KGSLFGGSVK^{110}, of the extended loop that connects the two β-strands of Bro1 was predicted to insert into LBPA-enriched membranes (11). Although reduction of cross-peak volumes was observed for residues 104-106, the other residues of this exposed motif were comparatively less affected in the presence of lipid particles, with G107 being the least affected residue (Figs. 3.7.3 A and 3.7.2). A quantitative analysis of the attenuation of ^{1}H-^{15}N cross-peak volumes of G107 as a function of increasing LBPA concentration revealed the ratios of ~1 and ~0.8 between 12.5 vs. 10 and 15 vs. 10 mol percent of LBPA, respectively (~20% attenuation; Fig. 3.7.3 B). On the other hand, the most affected Bro1 residues, S13 and G55, exhibited ~60% attenuation in their cross-peak volumes as a function of increasing LBPA concentration. These observations rule out the insertion of this exposed loop into the vesicles since in the event of such insertion, the corresponding residues would exhibit a significantly greater resonance line broadening. Mapping of the most affected Bro1 residues in the presence of LBPA enriched particles onto the crystal structure of Bro1 revealed two clusters, localized on two arms of the convex face of Bro1, which likely make direct contacts with lipid particles (Fig. 3.7.3 C-D). Cluster 1 comprised residues 10, 13, 14, 17, 54, 55, 98, 184, and 185, while residues 6, 239, 241, 250, 279, 283, 290, 301, 329, and 322 formed cluster 2. Residues 27-28 and two extreme C-terminal residues, 352-353, were outliers, likely due to non-specific association with the lipid particles. Y319 of Bro1 is located away from both clusters that interact

with lipid particles. A near-perfect match was observed with the pattern and the magnitude of attenuation of resonances of non- and phosphorylated Bro1 (one at a time) in the presence of LPBA-enriched particles, indicating that Src-mediated phosphorylation of Bro1 plays no major role in interactions with phospholipids (Fig. 3.7.4). A close agreement between the two clusters that interact with lipid vesicles and the electropositive regions of Bro1 (cf. Fig. 3.6.1 C and Fig. 3.7.3 C-D) indicated that interactions between Bro1 and lipid particles were primarily governed by the negative charge of LBPA. To confirm the electrostatic nature of these interactions, similar titration experiments were carried out using Bro1, in the absence and presence of zwitterionic and negatively charged vesicles (POPC/POPE and POPC/POPE/POPS, one at a time, Fig. 3.7.5 A and B, respectively). Negligible signal reductions were observed with zwitterionic vesicles (POPC/POPE molar ratio 7:3). These results also rule out the role of viscosity on attenuation of Bro1 resonances in the presence of vesicles. Negatively charged POPC/POPE/POPS particles (molar ratio 5.5:3:1.5) produced a very similar attenuation profile as that of Bro1 + POPC/POPE/LBPA vesicles, indicating that ionic interactions drive the association between Bro1 and lipid particles. Finally, we note that despite similarities, the magnitude of cross-peak attenuation is greater with LBPA than POPS particles (cf. Fig. 3.7.2 C and Fig. 3.7.5 B, respectively), indicating a stronger association of Bro1 with LBPA-enriched particles.

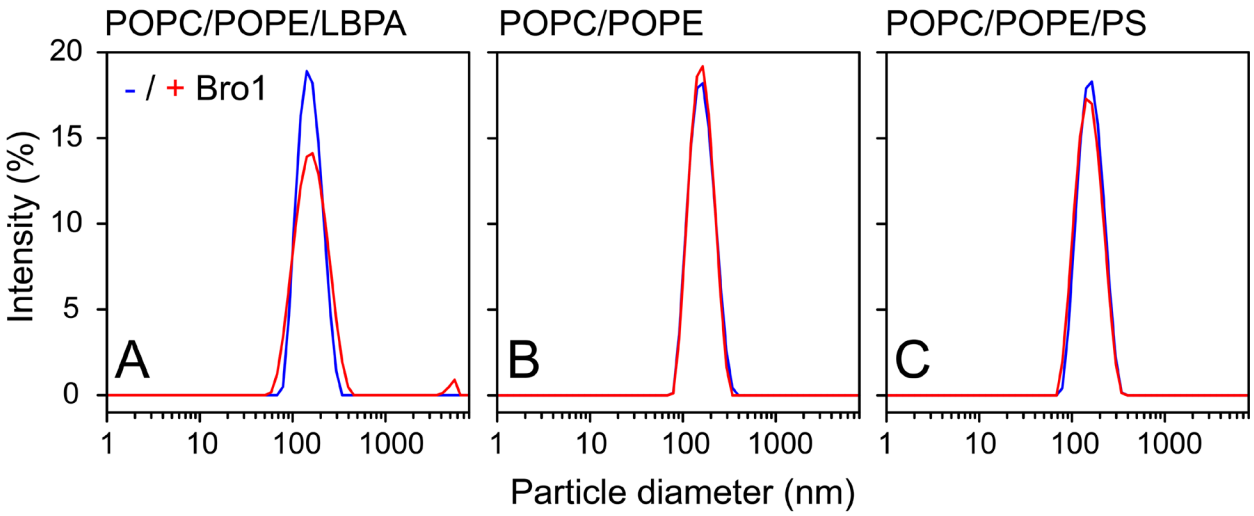

Figure 3.7: Characterization of the size distribution of lipid vesicles by DLS

The following lipid vesicle compositions were used for DLS analyses, namely **(A)** negatively charged POPC/POPE/LBPA (5.5:3:1.5); **(B)** zwitterionic POPC/POPE (7:3); and **(C)** negatively charged, POPC/POPE/POPS (5.5:3:1.5); the numbers in parenthesis represent molar ratios of phospholipids. DLS measurements were carried out on 25 μM vesicles, in the absence (blue) and the presence of Bro1 (red); protein to lipid ratio of 1:1. The mean diameters of POPC/POPE/LBPA vesicles were ~150 and ~140 nm, in the absence and presence of Bro1, respectively. Zwitterionic POPC/POPE vesicles were ~150 and ~140 nm in diameter, in the absence and presence of Bro1, respectively. POPC/POPE/POPS vesicles were ~150 and ~130 nm in diameter, in the absence and presence of Bro1, respectively. Note that the POPC/POPE/LBPA vesicles revealed the presence of a small fraction of very large aggregates (>1 μm) in the presence of Bro1, indicating a likely structural rearrangement induced by Bro1 in these vesicles resulting in the formation of larger assemblies.

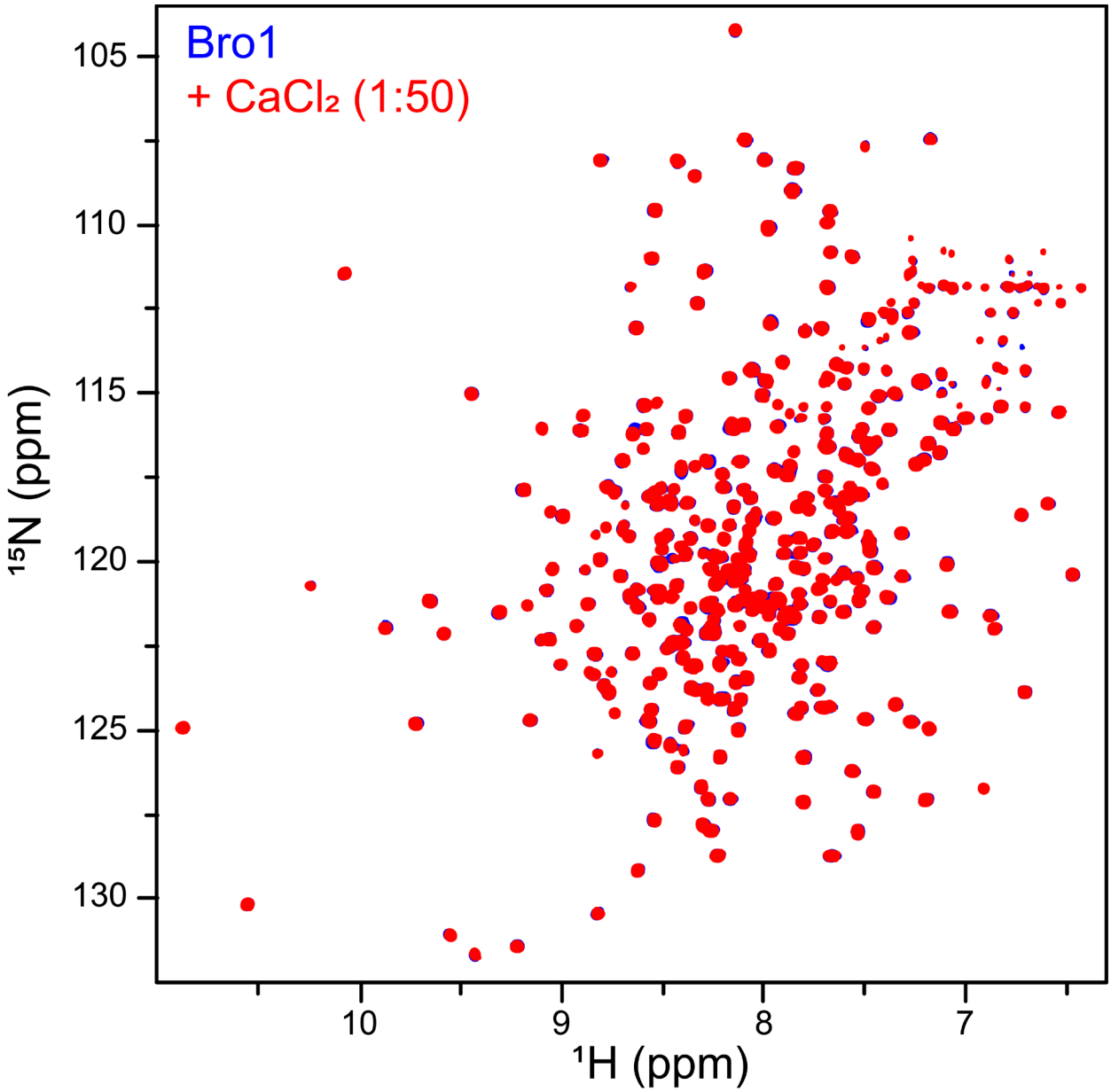

Figure 3.7.1: NMR analysis of the lack of interactions between Bro1 and calcium

Overlay of expanded regions of ^{1}H-^{15}N TROSY-HSQC spectra of Bro1, in the absence (blue) and presence of molar excess of $CaCl_2$ (red), revealed negligible chemical shift perturbations and cross-peak attenuation. Due to the incompatibility of phosphate buffer with polyvalent cations (10), experiments were carried out in the following buffer at 30 °C, 20 mM MES, pH 6.5, 50 mM NaCl, and 1mM TCEP.

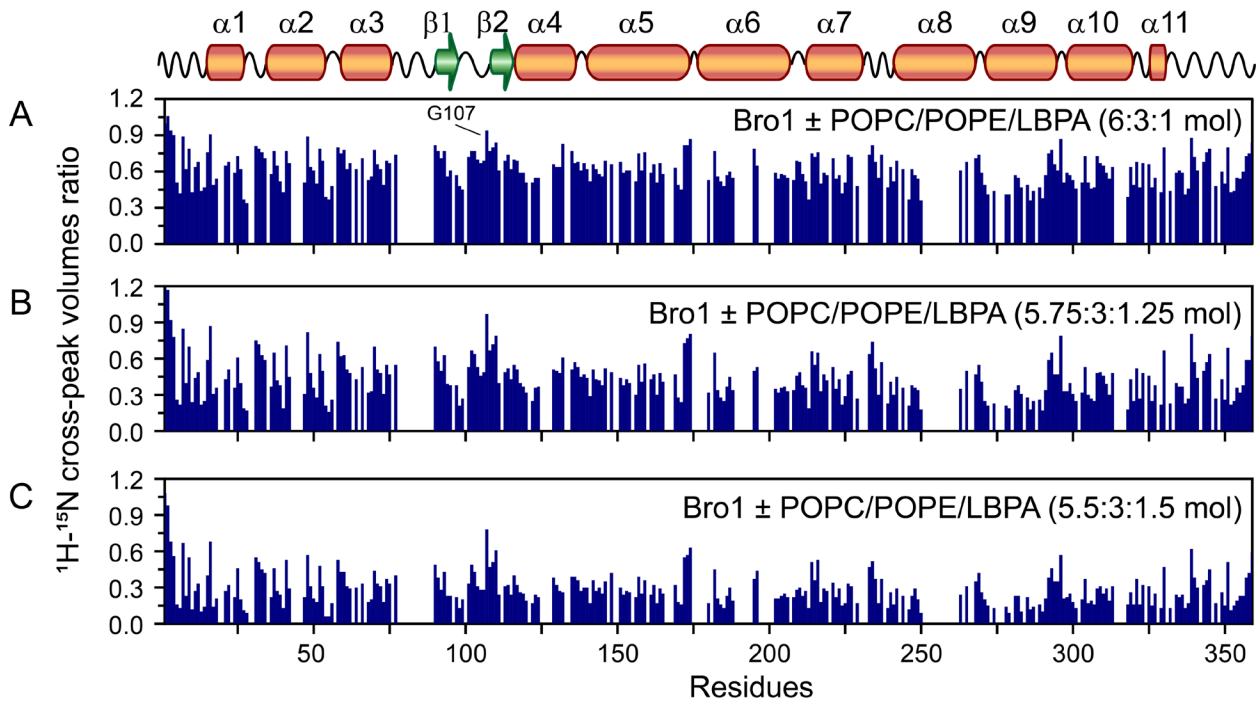

Figure 3.7.2: NMR analyses of the association of Bro1 with LBPA-enriched lipid vesicles

The panels represent ratios of ^{1}H-^{15}N cross-peak volumes of Bro1 in the presence of LBPA-enriched lipid vesicles as compared to free Bro1. The following three vesicle compositions were used: POPC/POPE/LBPA molar ratios of **(A)** 6:3:1, **(B)** 5.75:3:1.25, and **(C)** 5.5:3:1.5. G107 of the flexible extended loop that remains relatively less affected in the presence of lipid particles is marked. All data were acquired at a spectrometer ^{1}H frequency of 800 MHz at 30 °C. Buffer conditions were as follows: 20 mM sodium phosphate, pH 6.5, 50 mM NaCl, 1 mM TCEP, and 2 mM EDTA. The concentration of $^{2}H/^{15}N$ labeled Bro1 was 100 μM with a protein to lipid molar ratio of 1:30.

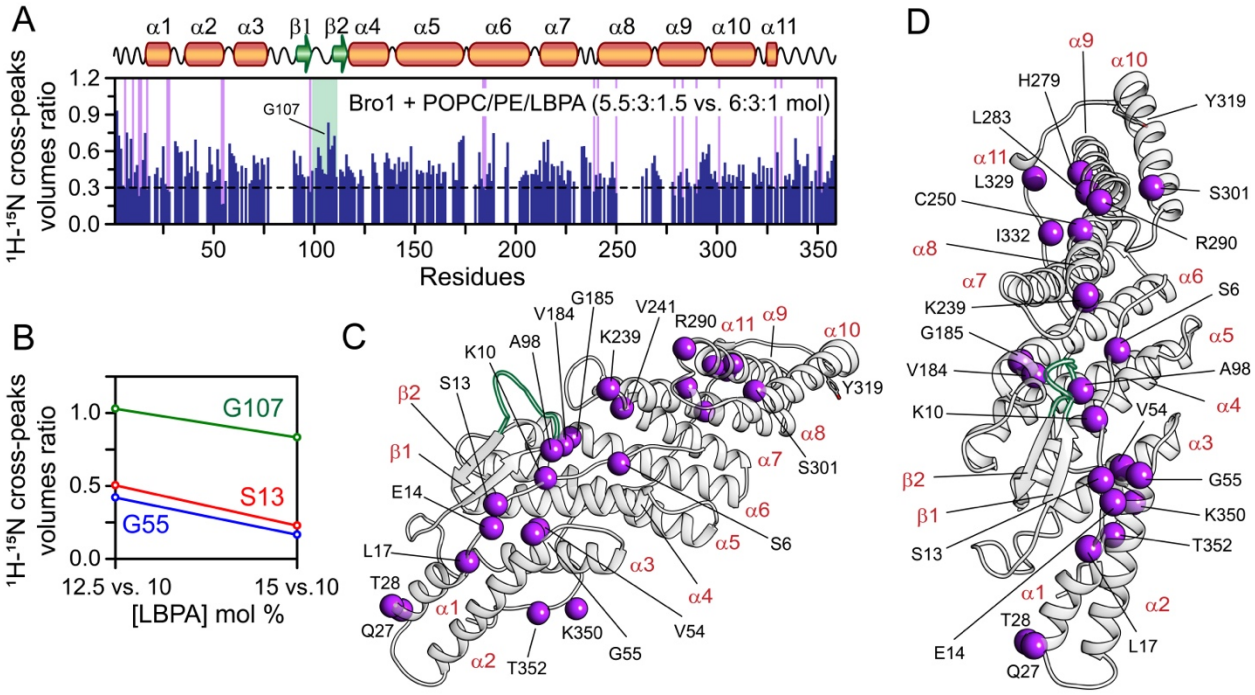

Figure 3.7.3: Interaction of Bro1 with LBPA enriched lipid vesicles

(A) Reduction in cross-peak volumes of $^{2}H/^{15}N$-labeled Bro1 (100 μM) as a function of increasing amount of LBPA; Bro1 + POPC/POPE/LBPA vesicles (5.5:3:1.5 vs. 6:3:1), the numbers in parenthesis represent the molar ratio of each phospholipid in vesicles. Bro1 to lipid molar ratio = 1:30. Semitransparent purple rectangles indicate residues that exhibit significant attenuation (≤ 0.3) in the presence of increasing concentrations of LBPA. A semitransparent green rectangle marks the location of the flexible loop connecting the two β-strands; G107 is marked. **(B)** Relative changes in cross-peak volumes of three representative residues as a function of increasing concentration of LBPA. The ratios of cross-peak volumes were obtained by recording three ^{1}H-^{15}N TROSY-HSQC spectra of Bro1 in the presence of vesicles containing increasing amounts of LBPA. The following vesicle compositions were used: POPC/POPE/LBPA molar ratios 6:3:1, 5.75:3:1.25, and 5.5:3:1.5. **(C-D)** Ribbon representation of Bro1 in two different orientations; the most affected residues upon association with LBPA-enriched vesicles are depicted as purple spheres. Y319 is shown in a stick representation. The extended loop connecting the two β- strands is marked in green.

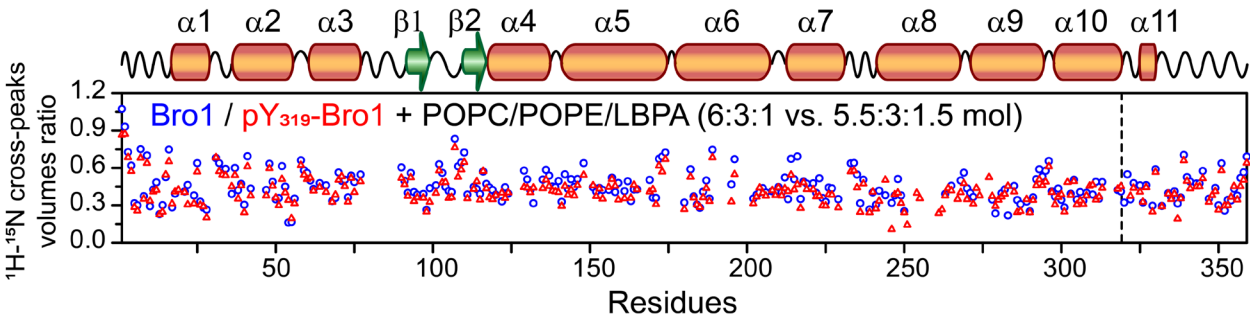

Figure 3.7.4: Comparison of the association between non- and phosphorylated Bro1 and LBPA-enriched lipid vesicles

Comparison of the reduction in ^{1}HN/^{15}N cross-peak volumes of ^{2}H/^{15}Nlabeled 100 μM non-phosphorylated (blue circles) and phosphorylated (red triangles) Bro1 in the presence of POPC/POPE/LBPA vesicles; protein to lipid molar ratio 1:30. The ratios of cross-peak volumes were obtained by recording two ^{1}H-^{15}N TROSY-HSQC correlation spectra of non- and –phosphorylated Bro1 (one at a time) in the presence of vesicles containing increasing amounts of LBPA; the following vesicle compositions were used: POPC/POPE/LBPA molar ratios of 6:3:1 and 5.5:3:1.5. The location of Y319 is indicated by a vertical dashed line. All data were acquired at a spectrometer ^{1}H frequency of 800 MHz at 30 °C. Buffer conditions were as follows: 20 mM sodium phosphate, pH 6.5, 50 mM NaCl, 1 mM TCEP, and 2 mM EDTA.

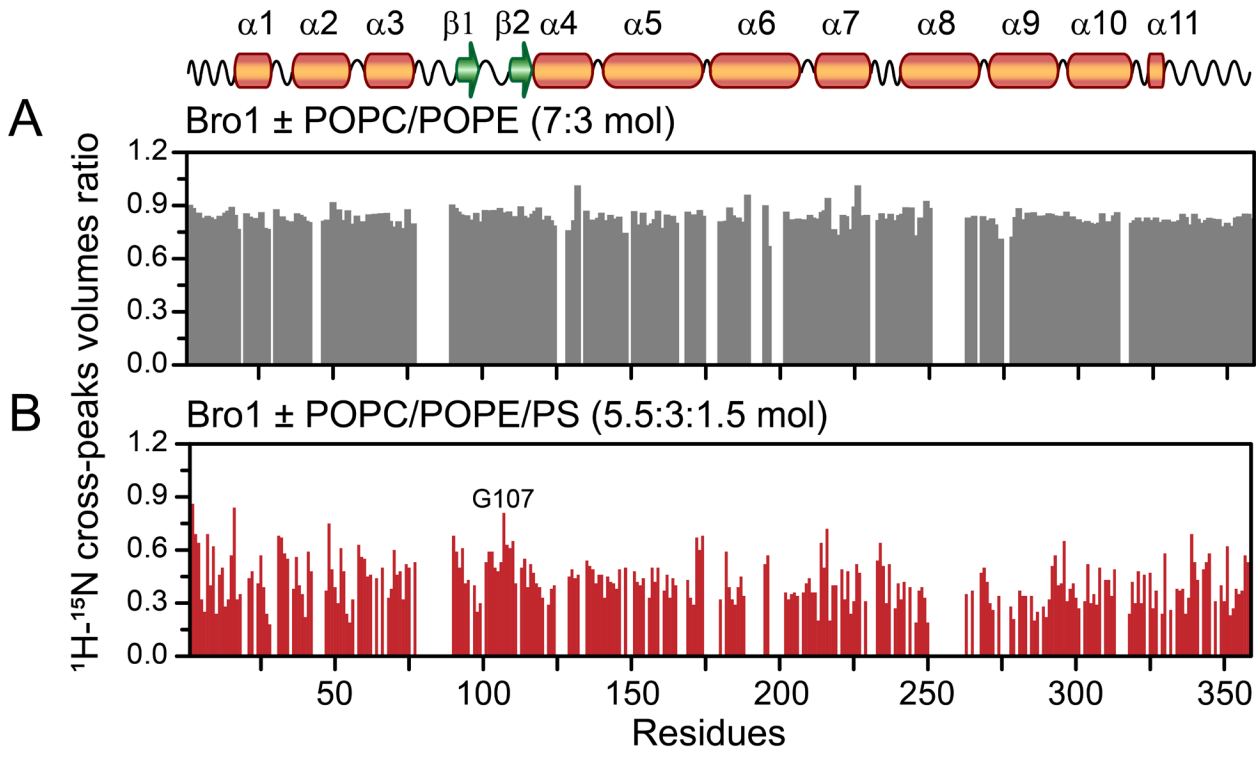

Figure 3.7.5: Changes in $^1H_N/^{15}N$ cross-peak volumes of Bro1 on addition of zwitterionic and negatively charged lipid vesicles

(A) No significant reductions were observed in cross-peak volumes of Bro1 in the presence of zwitterionic POPC/POPE (molar ratio of 7:3) vesicles, indicative of the lack of interactions between Bro1 and zwitterionic lipid particles. (B) Several regions of Bro1 showed a significant reduction in cross-peak volumes on the addition of negatively charged POPC/POPE/POPS vesicles (molar ratio of 5.5:3:1.5). All data were acquired at a spectrometer ^1H frequency of 800 MHz at 30 °C. Buffer conditions were as follows: 20 mM sodium phosphate, pH 6.5, 50 mM NaCl, 1 mM TCEP, and 2 mM EDTA. The concentration of $^2H/^{15}N$ labeled Bro1 was 100 µM with a protein to lipid molar ratio of 1:30.

3.8 Discussion

In summary, we establish that tyrosine phosphorylation of ALIX-PRD plays a critical role in its polymerization and that hyperphosphorylated PRD likely competes with anionic phospholipids for binding to the Bro1 domain. These data elucidate the underlying mechanism by which tyrosine phosphorylation triggers the cellular redistribution of ALIX and its impact on intra- and intermolecular associations that dictate the broad functional repertoire of ALIX in cell signaling.

$PRD^{Strep}_{703-868}$ exhibited remarkable aggregation properties and formed β-sheet rich amyloid fibrils that dissolved on Src kinase-mediated phosphorylation and reassembled on PTP1B-mediated dephosphorylation of its conserved tyrosine residues. LC-MS/MS analyses of PK digestion of $PRD^{Strep}_{703-868}$ fibrils revealed two protected fragments, residues 800-813 and 840-863, that likely form the fibril core. The motif encompassing residues 800-813 of PRD encodes epitopes of two binding partners, centrosomal protein of 55 kDa (CEP55), which is a mitotic phosphoprotein involved in cytokinetic abscission (30), and apoptosis linked gene-2 (ALG-2), which is a calcium-binding protein necessary for cell death (31). We speculate that the formation of ALIX fibrils provides a stringent regulatory control as the binding epitopes required for the recruitment of CEP55 and ALG-2 will be unavailable due to their involvement in fibril formation, while Src-mediated disassembly of ALIX fibrils will allow for the subsequent recruitment of CEP55 and ALG-2 by ALIX. In line with these hypotheses, a cellular study uncovered that inhibition of the focal adhesion kinase - Src signaling pathway affected the timing of CEP55 recruitment at the midbody and blocked cytokinetic abscission (32). Src-mediated hyperphosphorylation of PRD results in a heterogenous phosphorylation pattern in vitro. This complexity may provide additional regulatory control for ALIX-mediated ALG2 recruitment and

subsequent cell death. This is because the tyrosine residues of the PRD motif, residues 800-813, were shown to be critical for ALG2 association (33). The C-terminal residues of PRD (residues 832-868, especially motif ^{852}PSYP^{855}) were shown to be essential for ALIX multimerization in vivo (30). These observations are consistent with our in vitro findings that residues 840-863 of PRD are involved in fibril formation. The filament-forming components of the endosomal sorting complexes required for transport (ESCRT) pathway known as charged multivesicular body proteins (CHMPs) recruit ALIX through its Bro1 domain to endosomal membranes (34,35). Conversely, ALIX-Bro1 recruits and nucleates CHMPs (36), which are the main drivers of ESCRT-mediated membrane remodeling. We predict that the formation of PRD fibrils will likely result in a multiplicative increase in the binding affinity between Bro1 and CHMPs, culminating in nucleation and polymerization of CHMPs. These observations make a strong case for the existence of PRD-mediated ALIX assemblies in vivo and suggest a vital role of PTMs in regulating the timing of the recruitment of signaling partners of ALIX.

The structural characteristics and dynamics of the Bro1 domain were assessed using NMR spectroscopy. Conformational changes stemming from Src-mediated phosphorylation of residue Y319 of Bro1 were found to be localized around this tyrosine. NMR titration experiments ruled out the interdomain association between $PRD^{Strep}_{703\text{-}800}$ and Bro1. These results are contradictory to a previous study, which indicated that the N-terminal portion of the PRD of intact ALIX associates with the Bro1 domain and inhibits its interaction with CHMPs (13). Our results agree with a previous biophysical study that used full-length ALIX produced in insect cells and found that the presence of PRD did not influence the interactions between intact ALIX and peptide analogs of CHMPs (14). The discrepancy between these two studies was attributed to the use of pure monomeric ALIX in the biophysical investigation (14) vs. the use of crude extracts in the cellular

study (13), and the likely involvement of additional factors such as avidity effects due to ALIX and CHMP oligomerization influencing their association. Because highly sensitive PRE experiments also ruled out the association between Bro1 and the N-terminal portion of PRD at sites S712C and A756C, we argue that the cellular results of intramolecular association between the N-terminal portion of PRD and Bro1 and the corresponding prevention of Bro1 binding to CHMPs (13) could have been influenced by other adapter proteins present in crude cell extracts. Note that fibril formation was not observed in full-length ALIX made using insect cells (14), likely due to potential unaccounted PTMs such as hyperphosphorylation of PRD or because the globular domains of ALIX increase the critical concentration required for its fibrillization.

Paramagnetic NMR measurements revealed transient electrostatic interactions between Bro1 and hyperphosphorylated PRD. In intact ALIX, these interdomain interactions will likely be substantially stronger owing to their intramolecular nature. These interactions stem from a specific association between site C813 of hyperphosphorylated PRD and the basic surface of Bro1 and are governed by a patch of phosphorylated tyrosine residues encompassing residue C813. Since the same motif, residues 800-813, is likely involved in fibril formation, these intramolecular interactions will not be plausible in PRD-mediated ALIX assemblies. The biophysical study mentioned above uncovered that the presence of PRD results in inhibition of the binding of the V-domain to YPXnL motifs in monomeric full-length ALIX (14). Although NMR experiments rule out the association between the N-terminal portion of PRD and the V-domain, interdomain association between Bro1 and hyperphosphorylated PRD in full-length ALIX can likely interfere with the interactions of the V-domain with its binding partners. NMR titration experiments between Bro1 and LBPA-enriched lipid vesicles revealed that these electrostatic interactions localized on the same basic surface of Bro1 that comes into direct contact with

hyperphosphorylated PRD. Competition between intra- and intermolecular interactions are, thus, likely to redistribute ALIX away from late endosomal membranes to the cytosol. These observations are consistent with a recent in vivo study which demonstrated that deletion of PRD facilitated ALIX membrane association (37). Phosphorylation of Bro1 was found to play no major role in interactions between Bro1 and anionic lipid vesicles, nor is it likely involved in the interdomain interactions with hyperphosphorylated PRD. Even though the Src-binding motif represents the most conserved set of residues in mammalian Bro1 domains, mutation of Y319 of the yeast Bro1 ortholog had no effect on multivesicular body sorting (38). Our results are consistent with this observation and indicate that the phosphorylation of this residue is linked to other functions in mammalian cells that do not involve membrane associations.

Altogether, the above results indicate that the PTM-mediated formation and dissolution of ALIX amyloids will provide a strict spatiotemporal control on the recruitment of its binding partners involved in cytokinesis and apoptosis and will likely control nucleation of CHMPs and the corresponding endosomal membrane remodeling. ALIX – Src interactions at late endosomal membranes will result in phosphorylation of Bro1 and PRD of ALIX and shift the equilibrium towards monomeric ALIX. The hyperphosphorylated PRD will then compete against late endosomal membranes for binding to Bro1, culminating in a redistribution of ALIX back to the cytosol. Finally, we note that amyloids are commonly associated with proteinopathies, including Alzheimer's and Parkinson's diseases (39). Recent discoveries of functional amyloids have challenged this perception by elucidating the physiological roles of amyloids and their ubiquitous distribution in lower and higher-order organisms (40-43). These discoveries have led to the emergence of a new narrative, which posits that amyloidogenesis represents a functional phase transition, similar to the one found in nature between gas, liquid, and solid phases, and suggests

that cells may harness many useful characteristics of amyloids, including extreme stability, avidity, prion-like replication, and many others. Exactly how cells generate physiological amyloids without succumbing to pathology is not known. One suggested mechanism is the dissolution of amyloids, often through chaperones or changes in pH. The modulation of amyloids via PTMs described here, specifically a rapid disassembly and assembly of fibrils through tyrosine phosphorylation and dephosphorylation, respectively, represents another elegant mechanism with which cells may control the associated cytotoxicity. Given the prevalence of phosphorylation in eukaryotes (44) and that many proteins are prone to aggregation (45,46), we hypothesize that such regulatory control on amyloid production is widespread, allowing eukaryotic cells to escape the cytotoxic effects of functional amyloids.

3.9 Experimental procedures

3.9 .1 Data availability

Plasmids of full-length ALIX-PRD, $PRD^{Strep}_{703\text{-}868}$, and its cysteine variants, namely $PRD^{Strep}_{703\text{-}800}$-S712C, C813S; $PRD^{Strep}_{703\text{-}800}$-A756C,C813S; and $PRD^{Strep}_{703\text{-}800}$-S863C, C813S have been deposited in the Addgene repository, https://www. addgene.org/ (accession nos. 164444, 164445, 164446, and 164447, respectively). The chemical shift assignments of Bro1 have been deposited in the Biological Magnetic Resonance Bank, https://bmrb.io/ (accession no. 50707). LC–MS/MS data were deposited to the MassIVE data repository, https://massive.ucsd.edu/ (accession no. MSV000088057).

3.9.2 Materials

Isopropyl β-d-1-thiogalactopyranoside (IPTG) and arabinose were purchased from Sigma-Aldrich (catalog no. 420322 and A3256, respectively). ThT was purchased from Thermo Fisher

Scientific (catalog no. AC211760050). CR was purchased from Sigma-Aldrich (catalog no. C6277). Buffered ATP solution (pH 7.5) was obtained from Thermo Fisher Scientific (catalog no. R1441). Phospho-tyrosine mouse monoclonal antibody was obtained from Cell Signaling Technology (catalog no. 9411). Secondary antibody, goat anti-mouse IgG, was obtained from Thermo Fisher Scientific (catalog no. G-21040). The malachite green phosphate detection kit and PTP1B substrate were purchased from R&D systems, Inc. (catalog no. DY996 and ES006, respectively). PK solution (20 mg/mL) was purchased from Thermo Fisher Scientific (catalog no. 25530049). Reagents for NMR isotopic enrichment were obtained from Cambridge Isotopes Laboratories (CIL) and Sigma-Aldrich. Paramagnetic MTSL and its diamagnetic counterpart, (1-Acetoxy-2,2,5,5-tetramethyl-δ-3-pyrroline-3-methyl) Methanethiosulfonate, MTS, were purchased from Toronto Research Chemicals Inc. (catalog no. O875000, and A167900, respectively). TEMPOL was purchased from Sigma-Aldrich (catalog no. 176141). Phospholipids, POPC, POPE, and POPS, were purchased from Avanti Polar Lipids, Inc. (catalog no. 850457C, 850757C, 840034C, respectively). LBPA was purchased from Thermo Fisher Scientific (catalog no. 50720538).

3.9.3 Recombinant protein expression and purification

Codon-optimized (Genewiz, Inc.) ALIX-PRD constructs (Uniprot accession no. Q8WUM4), GB1-$PRD^{Strep}_{703\text{-}868}$ and GB1-$PRD^{Strep}_{703\text{-}800}$, were subcloned in pET11a (Novagen, EMD Millipore) and expressed in BL21(DE3) competent cells (Agilent, catalog no. 200131). Cysteine variants of GB1-$PRD^{Strep}_{703\text{-}868}$ used for paramagnetic NMR measurements were generated using site-directed mutagenesis. The recombinant constructs representing globular ALIX domains, namely Bro1 (residues 1-359), V (residues 359-702), and Bro1-V (residues 1-702), were obtained from Addgene, accession no. 80641 (47), 17639 (48), and 42577 (49), respectively. The human Src

kinase construct (Uniprot accession no. P12931) comprising a C-terminal TEV-cleavable polyhistidine tag, pEX-Src-C-His was a generous gift from the van der Vliet Group (University of Vermont) and was expressed in BL21-AI cells (Thermo Fisher Scientific, catalog no. C607003). The construct representing the catalytic domain of human PTP1B (residues 1-301; Uniprot accession no. P18031) was obtained from Addgene, accession no. 102719 (50), and expressed in BL21(DE3) competent cells. The TEV protease construct was a generous gift from David S. Waugh (National Cancer Institute, National Institutes of Health). The construct of MBP-E38C (Uniprot accession no. P0AEX9) was a generous gift from G. Marius Clore (National Institute of Diabetes and Digestive and Kidney Diseases, National Institutes of Health). MBP-E38C was expressed in BL21-CodonPlus (DE3)-RIPL competent cells (Agilent, catalog no. 230280).

ALIX-PRD constructs, GB1-PRD$^{\text{Strep}}_{703\text{-}868}$ and its cysteine variants, and GB1-PRD$^{\text{Strep}}_{703\text{-}800}$ were expressed at 16 °C. Briefly, cells were grown at 37 °C in 1 L Luria-Bertani (LB) medium (MP Biomedicals, catalog no. 3002-036) at natural isotopic abundance or minimal M9 medium for isotopic labeling. The latter contained 1 g/L $^{15}NH_4Cl$ (CIL) for ^{15}N labeling. About 30 min prior to induction, the temperature of cell culture was reduced to 16 °C. Cells were induced with 1 mM IPTG at an optical density of A_{600} ~0.8 and harvested after ~48 h. Src kinase was expressed according to our previous protocol (16). Briefly, cells were grown at 37 °C in 1 L Terrific Broth (TB) medium (Thermo Fisher Scientific, catalog no. BP9728) at natural isotopic abundance. About 30 min prior to induction, the temperature of cell culture was reduced to 16 °C. Cells were induced with 0.2 % wt/vol arabinose and 1 mM IPTG at an optical density of A_{600} ~0.8 and harvested ~24 h after induction. The catalytic domain of PTP1B was expressed at 16 °C. Cells were grown at 37 °C in 1 L LB medium and ~30 min prior to induction, the temperature of cell culture was reduced to 16 °C. Cells were induced with 1 mM IPTG at an optical density of A_{600} ~0.8 and harvested

~24 h after induction. For TEV protease, cells were grown at 37 °C in 1 L LB medium and harvested ~4 h after induction with 1 mM IPTG. The recombinant constructs of globular ALIX domains, namely Bro1, V, and Bro1-V, were expressed at 16 °C. Cells were grown at 37 °C in 1 L LB at natural isotopic abundance or in the case of Bro1, in M9 medium for isotopic labeling. The latter contained 0.3 g/L $^{2}H/^{15}N/^{13}C$ Isogro (Sigma-Aldrich), 99.9% (vol/vol) D_2O (CIL), 1 g/L $^{15}NH_4Cl$ (CIL), and 3 g/L $^{2}H_7,^{13}C_6$-d-glucose (Sigma-Aldrich) for $^{2}H/^{15}N/^{13}C$ labeling and 0.3 g/L $^{2}H/^{15}N$ Isogro (Sigma-Aldrich), 99.9% (vol/vol) D_2O (CIL), 1g/L $^{15}NH_4Cl$ (CIL), and 3g/L $^{2}H_7,^{12}C_6$-d-glucose (CIL) for $^{2}H/^{15}N$ labeling. About 30 min prior to induction, the temperature of cell culture was reduced to 16 °C. Cells were induced with 1 mM IPTG at an optical density of A_{600} ~0.8 and harvested after ~24 h.

PRD constructs were purified using a combination of affinity chromatography (ÄKTA Pure and Start protein purification systems, GE Healthcare) and reverse-phase HPLC (1260 Infinity II liquid chromatography system, Agilent Technologies). The purification protocol for GB1-$PRD^{Strep}_{703\text{-}800}$ is described in our previous work (16). Briefly, the cells were resuspended in a lysis buffer containing 50 mM tris(hydroxymethyl)aminomethane (Tris), pH 8.0, 2 mM Ethylenediaminetetraacetic acid (EDTA), and 250 mM NaCl. Cells were lysed by heat-shock (80 °C, ~5 minutes) and cleared by centrifugation (48,380 × g, 25 minutes). The cell lysate was loaded onto a Streptactin Sepharose column (GE Healthcare), pre-equilibrated with a running buffer containing 50 mM Tris, pH 8.0, 2 mM EDTA, and 250 mM NaCl, and eluted in the same buffer containing 2.5 mM d-desthiobiotin (Sigma-Aldrich). The eluted GB1-$PRD^{Strep}_{703\text{-}800}$ protein was mixed with recombinant TEV protease (molar ratio 50:1) in the presence of 1 mM dithiothreitol (DTT; Sigma-Aldrich) to hydrolyze the N-terminal GB1 solubility tag. Proteolysis was allowed to proceed at room temperature for ~12 h and was assessed for completion by sodium dodecyl sulfate

polyacrylamide gel electrophoresis (SDS-PAGE; Bolt 4-12% Bis-Tris gel; Thermo Fisher Scientific). The hydrolyzed product, $PRD^{Strep}_{703-800}$, was further purified using reverse-phase HPLC (Jupiter 10 μm C18 300 Å column; Phenomenex, catalog no. 00G-4055-N0) with a 5-55% acetonitrile gradient comprising 0.05% trifluoroacetic acid (TFA, Sigma-Aldrich). The eluted protein was freeze-dried (Labconco -84 °C Benchtop Freeze Dryer) and was stored at -80 °C before use. For GB1-$PRD^{Strep}_{703-868}$ and its cysteine variants, the cells were resuspended in a denaturing buffer containing 50 mM Tris, pH 8.0, and 6 M guanidine hydrochloride (Sigma-Aldrich). Cells were lysed using a homogenizer, EmulsiFlex-C3 (Avestin), and cleared by centrifugation. The cell lysate was filtered through a 0.45 μm vacuum-driven filtration device (Stericup; Sigma-Aldrich) and loaded onto a HisTrap column (GE Healthcare), pre-equilibrated with a denaturing buffer containing 50 mM Tris, pH 8.0, and 6 M guanidine hydrochloride. The bound protein was washed with 10 column volumes of refolding buffer containing 50 mM Tris, pH 8.0, and 250 mM NaCl, and eluted in the same buffer containing 0.5 M imidazole (Sigma-Aldrich). The eluted protein was loaded onto a Streptactin Sepharose column, preequilibrated with a running buffer containing 50 mM Tris, pH 8.0, 2 mM EDTA, and 250 mM NaCl, and eluted in the same buffer containing 2.5 mM d-desthiobiotin. The resultant elution was mixed with recombinant TEV protease (molar ratio 100:1) in the presence of 1 mM DTT to hydrolyze the N-terminal GB1 solubility tag. The proteolysis reaction was carried out at room temperature (~12 h) and was assessed for completion by SDS-PAGE. The hydrolyzed product, $PRD^{Strep}_{703-868}$, was further purified using reverse phase HPLC (Jupiter 10 μm C18 300 Å column) using a 25-37% acetonitrile gradient comprising 0.1% TFA. The eluted $PRD^{Strep}_{703-868}$ fractions were pooled, lyophilized, and stored at -80 °C.

The purification protocol for Src kinase is described in our previous work (16). Briefly, the cells were resuspended in a lysis buffer containing 50 mM Tris, pH 8.0, and 250 mM NaCl. Cells

were lysed using an EmulsiFlex-C3 and cleared by centrifugation. The cell lysate was loaded onto a HisTrap column (GE Healthcare) with a 0–1 M imidazole gradient containing 50 mM Tris, pH 8.0, and 250 mM NaCl. The eluted protein was loaded onto a Q Sepharose HP column (GE Healthcare) with a 0–1 M NaCl gradient in a buffer containing 50 mM Tris, pH 8.0, and 5 mM β-mercaptoethanol (BME). The eluted fractions were pooled, concentrated (Amicon ultra-15, 30-kDa cutoff), and loaded onto a HiLoad 26/600 Superdex 75 pg column (GE Healthcare) preequilibrated with 50 mM Tris, pH 7.5, 250 mM NaCl, and 5 mM BME. Relevant fractions were pooled and concentrated to ~1 mg/mL (Amicon ultra-15, 30-kDa cutoff). Samples were aliquoted, flash-frozen, and stored at -80 °C.

For the catalytic domain of PTP1B, the cells were resuspended in a lysis buffer containing 50 mM Tris, pH 8.0, and 250 mM NaCl. Cells were lysed using an EmulsiFlex-C3 and cleared by centrifugation. The cell lysate was loaded onto a HisTrap column (GE Healthcare) with a 0–1 M imidazole gradient containing 50 mM Tris, pH 8.0, and 250 mM NaCl. The eluted protein was concentrated (Amicon ultra-15, 10-kDa cutoff) and loaded onto a HiLoad 26/600 Superdex 75 pg column (GE Healthcare) pre-equilibrated with 50 mM Tris, pH 8, and 250 mM NaCl. Relevant fractions were pooled and mixed with recombinant TEV protease (molar ratio 50:1) in the presence of 1 mM DTT to hydrolyze the N-terminal polyhistidine (6xHis) affinity tag. The proteolysis reaction was carried out at room temperature (~12 h) and was assessed for completion by SDSPAGE. The reaction mixture was loaded back onto a HisTrap column (GE Healthcare). The resultant flow-through fractions of hydrolyzed PTP1B were pooled, concentrated, and further purified by size exclusion chromatography (HiLoad 26/600 Superdex 75 pg column; GE healthcare). Relevant fractions were concentrated (~3 mg/mL; Amicon ultra-15, 10-kDa cutoff), flash-frozen, and stored at -80 °C.

The purification protocol for TEV protease is described in our previous works (16,51). Briefly, the cells were resuspended in a lysis buffer containing 50 mM Tris, pH 8.0, and 250 mM NaCl. Cells were lysed using an EmulsiFlex-C3 and cleared by centrifugation. The cell lysate was loaded onto a HisTrap column (GE Healthcare) with a 0–1 M imidazole gradient containing 50 mM Tris, pH 8.0, and 250 mM NaCl. The eluted protein was concentrated (Amicon ultra-15, 10-kDa cutoff) and loaded onto a HiLoad 26/600 Superdex 75 pg column (GE Healthcare) preequilibrated with 50 mM Tris, pH 8, 250 mM NaCl and 1 mM DTT. Relevant fractions were pooled and concentrated to ~1 mg/mL (Amicon ultra-15, 10-kDa cutoff). The samples were aliquoted, flash-frozen, and stored at -80 °C.

For the Bro1 domain, the cells were resuspended in a lysis buffer containing 50 mM Tris, pH 8.0, and 250 mM NaCl. Cells were lysed using EmulsiFlex-C3 and cleared by centrifugation. The cell lysate was loaded onto a HisTrap column (GE Healthcare) with a 0–1 M imidazole gradient containing 50 mM Tris, pH 8.0, and 250 mM NaCl. The eluted protein was concentrated (Amicon ultra-15, 10-kDa cutoff) and loaded onto a HiLoad 26/600 Superdex 75 pg column (GE Healthcare) pre-equilibrated with 50 mM Tris, pH 8, 250 mM NaCl and 1 mM DTT. Relevant fractions were pooled and mixed with recombinant TEV protease to cleave off the N-terminal 10xHis affinity tag (molar ratio 5:1). Proteolysis was carried out at room temperature (~48 h) and was assessed for completion using SDS-PAGE. The reaction mixture was loaded back onto a HisTrap column (GE Healthcare). The resultant flow-through fractions of hydrolyzed Bro1 were pooled, concentrated, and further purified by size exclusion chromatography (HiLoad 26/600 Superdex 75 pg column; GE healthcare). Relevant Bro1 fractions were pooled and stored at -80 °C.

For the V domain, the cells were resuspended in a lysis buffer containing 50 mM Tris, pH 8.0, and 250 mM NaCl. Cells were lysed using an EmulsiFlex-C3 and cleared by centrifugation. Cell lysate was loaded onto a Glutathione Sepharose 4 Fast Flow column (GE Healthcare) with a 0–10 mM L-glutathione (Sigma-Aldrich) gradient containing 50 mM Tris, pH 8.0, and 250 mM NaCl. The eluted protein was concentrated (Amicon ultra-15, 10-kDa cutoff) and loaded onto a HiLoad 26/600 Superdex 75 pg column (GE Healthcare) pre-equilibrated with 50 mM Tris, pH 8, 250 mM NaCl and 1 mM DTT. Relevant fractions were pooled and mixed with recombinant TEV protease to cleave off the N-terminal GST affinity tag (molar ratio 50:1). Proteolysis was carried out at room temperature (~12 h) and was assessed for completion using SDS-PAGE. The reaction mixture was loaded back onto a Glutathione Sepharose 4 Fast Flow column (GE Healthcare). The resultant flow-through fractions were pooled, concentrated, and further purified by size exclusion chromatography (HiLoad 26/600 Superdex 75 pg column; GE healthcare). Relevant fractions were pooled, concentrated (~10 mg/mL; Amicon ultra-15, 10-kDa cutoff), and stored at -80 °C.

For the Bro1-V construct, the cells were resuspended in a lysis buffer containing 50 mM Tris, pH 8.0, and 250 mM NaCl. Cells were lysed using an EmulsiFlex-C3 and cleared by centrifugation. The cell lysate was loaded onto a HisTrap column (GE Healthcare) with a 0–1 M imidazole gradient containing 50 mM Tris, pH 8.0, and 250 mM NaCl. The eluted protein was concentrated (Amicon ultra-15, 30-kDa cutoff) and loaded onto a HiLoad 26/600 Superdex 200 pg column (GE Healthcare) pre-equilibrated with 50 mM Tris, pH 8, 250 mM NaCl and 1 mM DTT. Relevant fractions were pooled and mixed with recombinant TEV protease to cleave off the N-terminal 6xHis affinity tag (molar ratio 5:1). Proteolysis was carried out at room temperature (~48 h) and was assessed for completion using SDS-PAGE. The reaction mixture was loaded back onto the HisTrap column (GE Healthcare). The resultant flow-through fractions were pooled,

concentrated, and further purified by size exclusion chromatography (HiLoad 26/600 Superdex 200 pg column; GE healthcare). Relevant fractions were pooled and stored at -80 °C.

For apo MBP-E38C, the cells were resuspended in a lysis buffer containing 50 mM Tris, pH 8.0, and 250 mM NaCl. Cells were lysed using an EmulsiFlex-C3 and cleared by centrifugation. Cell lysate was loaded onto an Amylose resin column (New England BioLabs Inc.) with a 0–10 mM maltose gradient containing 50 mM Tris, pH 8.0, 1 mM DTT, and 250 mM NaCl. The eluted protein was concentrated (Amicon ultra-15, 30-kDa cutoff) and loaded onto a HiLoad 26/600 Superdex 75 pg column (GE Healthcare) pre-equilibrated with 50 mM Tris, pH 8, 1 mM DTT, and 250 mM NaCl. Relevant fractions were pooled and concentrated to ~10 mg/mL (Amicon ultra-15, 30-kDa cutoff). The samples were aliquoted and flash-frozen and stored at -80 °C.

The above-mentioned purification schemes resulted in ≥ 99% pure proteins with the following yields: $PRD^{Strep}_{703\text{-}800}$ (~40 mg / L), $PRD^{Strep}_{703\text{-}868}$ (~25 mg / L), Src (~5 mg / L), PTP1B (~45 mg / L), Bro1 (~50 mg / L), V (~45 mg / L), Bro1-V (~40 mg / L), and MBP-E38C (~10 mg / L).

3.9.4 MS analyses

All protein constructs, the end-products of in vitro phosphorylation, and site-specific spin labeling reactions (see below) were verified by MS using our previously published protocols (16,51). Briefly, an Agilent 6230 TOF-mass spectrometer with Jet Stream ESI was used for LC-ESI-TOFMS analysis. The Jet Stream ESI source was operated under positive ion mode with the following parameters: VCap = 3500 V, fragmentor voltage = 175 V, drying gas temperature = 325 °C, sheath gas temperature = 325 °C, drying gas flow rate = 10 L / min, sheath gas flow rate = 10 L / min, nebulizer pressure = 40 psi. The chromatographic separation was performed at room temperature on a Phenomenex Aeris Widepore XB-C18 column (2.1 mm ID x 50 mm length, 3.6

μm particle size). HPLC-grade water and acetonitrile were used as mobile phases A and B, respectively. Each phase also carried 0.1% TFA. Agilent MassHunter software was used for data acquisition and analysis and MagTran software was used for mass spectrum deconvolution (52).

3.9.5 PK digestion

Fibrils of $PRD^{Strep}_{703-868}$ and soluble $PRD^{Strep}_{703-800}$ (~40 μM each) were incubated with PK (1 μg/mL) in a buffer comprising 50 mM Tris, pH 8, 1 mM DTT, and 0.5 mM EDTA (37 °C, ~60 min). Aliquots were taken at regular intervals and heated at 100 °C for ~3 min to inactivate PK. The reactions were assessed using SDS-PAGE, visualized using PageBlue staining solution (Thermo Fisher Scientific, catalog no. 24620). Reactions were also analyzed by LC-MS/MS using our previously published protocol (16). Briefly, LC-MS/MS analysis was carried out by the nanoLC-Orbitrap XL spectrometer. A fused silica capillary LC column (pulled to a tip with a Sutter P-2000 laser capillary puller) was packed with Agilent Zorbax resin (C18, particle size 5 μm). The inner diameter (ID) of the capillary was 100 μm, and the stationary phase was packed with a pressure device to a length of 70 mm. The column was equilibrated using an Agilent 1100 HPLC pump, solvent A = 100% HPLC-grade water with 0.1% formic acid and solvent B = 100% acetonitrile with several 10-90% solvent B step gradients. The PK-digested sample of $PRD^{Strep}_{703-868}$ fibrils was diluted by a factor of 100 with 2% acetonitrile and 0.1% formic acid and loaded on the column by a pressure device (2.1 μl; ~ 2 pmol on column). The LC gradient program was 1- 34% solvent B in 66 minutes, followed by 6 minutes of 90% B, followed by 1% B at 95 minutes. Data acquisition method parameters were as follows: the capillary LC was positioned in the Thermo nanoelectrospray interface (NSI) with a 1.55 kV source voltage, 48 V capillary voltage, 85 V tube lens, and 165 °C capillary temperature. For the ion trap, 3 micro scans and the Fourier transform

(FT) spectra, 2 micro scans were averaged. There were seven scan events per cycle (6.5 s), one FT scan (resolution 30,000) from 200-1600 m/z, followed by six ion trap, data dependent collision induced dissociation (CID) MS/MS scans. Dynamic exclusion was enabled with duration of 40 s and a repeat count of 2. The ion trap CID scans had an isolation width of 2.0 m/z and a normalized collision energy of 35. The data analysis method was as follows: peptide sequence matches (PSM) were found using the OpenMS workflow (53) with the MS-GF + PSM search algorithm (54). The false discovery rate was set to 5%. The enzyme parameter was set to 'Unspecific cleavage'. The search parameters used for LC-MS/MS analyses are tabulated in Table 3.2, while Supplementary Files lists all peptides identified by these analyses.

Table 3.2: List of search parameters used for LC-MS/MS analyses (see Figs. 3.3.2, 3.3.3, and 3.4 C)

Search Parameters	Name / Entry / Value
Peaklist generating software	MSConvert Proteowizard (version 3.0.21033 64-bit)
Search engine	Knime (version 3.6.0 v201807100937) workflow manager with OpenMS-2.3.0 with MSGFplus adaptor 11/10/2017
Sequence database	Uniprot accession no. Q8WUM4; entry version 197 (02 Jun 2021)
Database entries searched	Only Uniprot accession no. Q8WUM4
Proteases used	PK (non-specific cleavage) trypsin (cleaves C-terminal to arginine or lysine except when followed by a proline)
Missed / non-specific cleavages permitted	PK: minimum peptide length 6, maximum 60 Trypsin: minimum peptide length 4, maximum 50
Fixed modifications considered	None
Variable modifications considered	PK: phosphotyrosine, deamidated(N) Trypsin: phosphotyrosine, deamidated(N), phosphoserine, phosphothreonine
Mass tolerance for precursor ions	10 parts per million of precursor ion m/z
Mass tolerance for fragment ions	1 m/z
Threshold score/Expectation value	optimized global SpecEValue score ≤ 0.01
False discovery rate	0.05; estimated from OpenMS FalseDiscoveryRate node

3.9.6 Tyrosine phosphorylation

Lyophilized $PRD^{Strep}_{703-868}$ was reconstituted in a buffer comprising 50 mM Tris, pH 7.5, 5 mM $MgCl_2$, 2 mM DTT, and 0.5 mM EDTA. The resultant $PRD^{Strep}_{703-868}$ solution (50 μM) was mixed with 1 mM ATP and ~5 μM Src. The phosphorylation reaction was allowed to proceed for ~12 h at 30 °C. Src was then removed from the reaction mixture using a HisTrap column (GE Healthcare) pre-equilibrated with 50 mM Tris, pH 8, and 250 mM NaCl. The resultant flow-through fractions of phosphorylated $PRD^{Strep}_{703-868}$ were pooled, and excess ATP/ADP were removed using a HiPrep 26/10 Desalting column (GE Healthcare) pre-equilibrated with 20 mM sodium phosphate, pH 6.5, 50 mM NaCl, 2 mM EDTA, and 1 mM TCEP (Sigma-Aldrich).

The eluted fractions of Bro1 and Src from a sizing column were mixed; Bro1 to Src molar ratio: ~5:1. The resultant mixture was concentrated to a final volume of ~7 mL (Amicon ultra-15, 30-kDa cutoff) and dialyzed against a buffer containing 50 mM Tris, pH 8, 2 mM ATP, 5 mM $MgCl_2$, 2 mM DTT, and 0.5 mM EDTA (Slide-A-Lyzer G2 dialysis cassettes; Thermo Fisher Scientific). The reaction was allowed to proceed for ~18 h at room temperature with one buffer change at ~4 h time point in the dialysis. Phosphorylated Bro1 was purified from the mixture using the procedure mentioned above. The status of phosphorylation was assessed using LC-ESI TOFMS, LC-MS/MS, and NMR. For LC-MS/MS, phosphorylated Bro1 was digested using trypsin (Bro1 to trypsin molar ratio 50:1; incubation time: ~90 min, room temperature). Hyperphosphorylated $PRD^{Strep}_{703-868}$ samples were digested using PK ($PRD^{Strep}_{703-868}$ to PK molar ratio of 1000:1; incubation time: ~5 min, 37 °C). LC-MS/MS analyses were carried out using a similar procedure as the one used to identify products of PK digestion of $PRD^{Strep}_{703-868}$ fibrils. Up to two PTMs per peptide were allowed for the search. Phosphorylation of tyrosine was the most prevalent PTM observed (also see Table 3.2 and Supplementary Files). For Bro1, phosphorylation was also

assessed using western blotting. Bro1 + Src reaction mixture separated using electrophoresis was transferred onto a 0.45 μm nitrocellulose membrane (Thermo Fisher Scientific, catalog no. LC2001) using a wet transfer Mini Blot Module (Thermo Fisher Scientific, catalog no. B1000). Procedures for blotting and subsequent product visualization are described previously (16).

3.9.7 Large unilamellar lipid vesicles

Lipid vesicles were prepared according to the protocols published by Jiang et al (55). Briefly, lipids were stored in chloroform/methanol (2:1) stock solutions at -20 °C. Lipid films were prepared by drying the appropriate amounts of stock solutions under a stream of dry nitrogen followed by vacuum desiccation (vacuum oven; VWR) at room temperature for ~2 h to remove traces of organic solvents. The resultant lipid films were hydrated using appropriate volumes of buffer containing 20 mM sodium phosphate, pH 6.5, 50 mM NaCl, 1 mM EDTA, and 1 mM TCEP and subjected to vortex mixing (~3 times, 60 s each). The multilamellar vesicle solutions were extruded through a 100 nm diameter polycarbonate membrane (Whatman, GE Healthcare) using an extrusion kit (Avanti Polar Lipids, Inc.) and used immediately for NMR and size measurements.

3.9.8 DLS

The size distribution of lipid vesicles was determined by DLS at 25 °C using 25 μM vesicles, with and without 25 μM Bro1. Measurements were performed using the Zetasizer Nano ZS (Malvern Instruments, US) instrument operating at a wavelength of 633 nm. The measurements were repeated 15 times after a 1 min temperature equilibration. A cumulant fit and a sphere model were used to obtain the average hydrodynamic radius (130-150 nm).

3.9.9 Site-specific spin labeling

MTSL and MTS were reconstituted in ethanol (Sigma-Aldrich) to a final concentration of ~100 mM and mixed with the protein of interest at a molar ratio of 10:1 (spin label vs. protein). The spin labeling reaction was allowed to proceed in the dark for ~12 h at room temperature and assessed for completion using LC-ESI-TOFMS. The excess of unreacted spin label was removed using the HiPrep 26/10 Desalting column (GE Healthcare) pre-equilibrated with 20 mM sodium phosphate, pH 6.5, 50 mM NaCl, and 2 mM EDTA. The resultant protein fractions were pooled, concentrated, and immediately used for NMR measurements.

3.9.10 NMR sample preparation

Samples of ^{15}N-labeled $PRD^{Strep}_{703-800}$, ^{15}N-labeled hyperphosphorylated $PRD^{Strep}_{703-868}$, and $^{15}N/^{2}H$- or $^{15}N/^{13}C/^{2}H$-labeled Bro1 were prepared in a buffer comprising 20 mM sodium phosphate, pH 6.5, 50 mM NaCl, 2 mM EDTA and 1 mM TCEP. For paramagnetic NMR, the samples were prepared in an identical buffer without TCEP. To assess the interactions between calcium and Bro1, samples were prepared using 20 mM MES, pH 6.5, 50 mM NaCl, 2mM EDTA, and 1mM TCEP. All NMR samples contained 7% vol/vol D_2O.

3.9.11 NMR spectroscopy

All NMR experiments were carried out at 30 °C on Bruker 600- and 800- MHz spectrometers equipped with z-gradient triple resonance cryoprobes. Spectra were processed using NMRPipe (56) and analyzed using the CCPN software suite (57). Sequential ^{1}H, ^{15}N, and ^{13}C backbone resonance assignments of non- and phosphorylated Bro1 samples were carried out using conventional TROSY-based three-dimensional triple resonance experiments (58). TROSY-based

^{15}N-{^{1}H} NOE measurements (59) were carried out on ^{2}H/^{15}N-labeled non- and phosphorylated Bro1 samples at 800 MHz. The ^{15}N-{^{1}H} NOE and reference spectra were recorded with a 6 s saturation time for the NOE measurement and an equivalent recovery time for the reference measurement in an interleaved manner, each preceded by an additional 1 s recovery time. Chemical shift perturbation experiments were carried out using ^{15}N-labeled $PRD^{Strep}_{703\text{-}800}$ and non-labeled Bro1, V, and Bro1-V (one at a time). The following protein concentrations were used: 100 μM $PRD^{Strep}_{703\text{-}800}$ and 300 μM Bro1 and V (one at a time) and $PRD^{Strep}_{703\text{-}800}$ and 75 μM Bro1-V (the latter is due to the limited solubility of Bro1-V construct). Similar measurements were carried out using uniformly ^{2}H/^{15}N-labeled 100 μM non- and phosphorylated Bro1 and non-labeled 300 μM $PRD^{Strep}_{703\text{-}800}$. Perturbations were calculated as follows: $\Delta_{H/N}=\{(\Delta\delta_{HN})^2+(0.154\times\Delta\delta_{N})^2\}^{1/2}$, where $\Delta\delta_{HN}$ and $\Delta\delta_{N}$ are the $^{1}H_N$ and ^{15}N chemical shift differences in ppm, respectively, between free and bound states. To determine the effect of calcium on Bro1, titration experiments were carried out using ^{2}H/^{15}N-labeled 100 μM nonphosphorylated Bro1, in the absence and presence of 5 mM $CaCl_2$. Intermolecular transverse $^{1}H_N$-Γ_2 PRE rates were obtained by mixing 200 μM ^{2}H/^{15}N-labeled Bro1 with 200 μM MTSL/MTS labeled hyperphosphorylated $PRD^{Strep}_{703\text{-}868}$ and its cysteine variants (note that the corresponding PRE measurements on phosphorylated Bro1 were not feasible due to the limited solubility of phosphorylated Bro1 and MTSL-tagged hyperphosphorylated $PRD^{Strep}_{703\text{-}868}$ mixture). Transverse $^{1}H_N$-Γ_2 PRE rates were measured from the differences in the transverse $^{1}H_N$-R_2 relaxation rates between the paramagnetic and diamagnetic samples as described previously (26,27). Two time points (separated by 30 ms) were used for the measurements of $^{1}H_N$-R_2 rates, and the errors in the $^{1}H_N$-Γ_2 PRE rates were calculated as described previously (26). Negative control experiments were carried out using 200 μM ^{2}H/^{15}N-labeled Bro1 and 2 mM TEMPOL, and 200 μM MTSL-labeled MBP-E38C. For these experiments, 200 μM

$^{2}H/^{15}N$-labeled non-phosphorylated Bro1 served as a diamagnetic control. NMR titration experiments between $^{2}H/^{15}N$-labeled non- and phosphorylated Bro1 and neutral and negatively charged lipid vesicles were carried out using 100 μM protein (protein to lipid molar ratio: 1:30). TROSY-HSQC correlation spectra were recorded on non- and phosphorylated Bro1 in the absence and presence of unilamellar lipid vesicles. The following vesicles compositions were used; the numbers in parenthesis represent the molar ratios of phospholipids: POPC/POPE (7:3), POPC/POPE/POPS (5.5:3:1.5), POPC/POPE/LBPA (6:3:1), POPC/POPE/LBPA (5.75:3:1.25), and POPC/POPE/ LBPA (5.5:3:1.5).

3.9.12 CR assay

CR was dissolved in MilliQ water (MilliQ IQ 7000 purification system, Millipore-Sigma). CR stock solution (0.2% wt/vol) was filtered through a 0.22 μm filter and used immediately. 100 μM solutions of non- and phosphorylated $PRD^{Strep}_{703\text{-}868}$ and $PRD^{Strep}_{703\text{-}800}$ were incubated overnight at room temperature and were mixed with CR stock solution in the morning (100:1 dilution, protein vs. CR). The mixtures were incubated at room temperature for ~45 min. Absorption spectra were measured using an Agilent Cary 50 Bio UV-Vis spectrophotometer (1- cm quartz cuvette).

3.9.13 Fibril formation and dissolution kinetics

Aggregation and dissolution experiments were performed at 30 °C on $PRD^{Strep}_{703\text{-}868}$ samples in sealed 96-well flat bottom plates (Corning, catalog no. 3370) containing 100 μL sample per well (three replicates of each sample, $n = 3$, were placed in separate wells and ThT fluorescence was measured through the top and bottom of the plate). Measurements were carried out with continuous linear shaking (3.5 mm, 411.3 rpm) using a microplate reader (Infinite M Plex, Tecan). ThT (10

μM) fluorescence was recorded as a function of time; excitation and emission wavelengths were 415 and 480 nm, respectively. For aggregation experiments, ThT signals as a function of time were recorded on 100 μM hyperphosphorylated $PRD^{Strep}_{703-868}$ samples, in the absence and presence of 50 nM PTP1B. The buffer conditions were as follows: 20 mM HEPES, pH 7.5, 1 mM DTT, 1 mM EDTA. For Src-mediated fibril dissolution experiments, lyophilized $PRD^{Strep}_{703-868}$ was reconstituted in a buffer containing 50 mM Tris, pH 7.5, 5 mM $MgCl_2$, 2 mM DTT, and 0.5 mM EDTA ($PRD^{Strep}_{703-868}$ = 100 μM). ThT signals as a function of time were recorded till the samples (n = 9) reached a stationary phase; total incubation time: ~3 h, whereupon 1 μM of recombinant Src and 1 mM ATP were added to three samples, whereas the others were mixed with either 1 μM Src or 1 mM ATP. Fibril formation of $PRD^{Strep}_{703-868}$ was also assessed using ThT emission spectra recorded on Agilent Cary Eclipse Fluorescence spectrophotometer. ThT fluorescence was recorded of 3×100 μL of 100 μM Strep $PRD^{Strep}_{703-868}$ samples at 30 °C after ~2 h incubation (20 mM HEPES, pH 7.5, 1 mM DTT, and 1 mM EDTA; micro quartz cuvettes). Similar measurements were recorded on hyperphosphorylated $PRD^{Strep}_{703-868}$ and the soluble N-terminal fragment, $PRD^{Strep}_{703-800}$, which served as negative controls.

3.9.14 TEM

$PRD^{Strep}_{703-868}$ samples, ~1.2 mg/mL, were incubated at 30 °C in 20 mM sodium phosphate, pH 7.0, 50 mM NaCl, 1 mM TCEP, and 1 mM EDTA. Aggregated samples were subjected to sonication (~10 min; Elmasonic P ultrasonic bath) and diluted to ~0.2 mg/mL immediately before application to the TEM grids (400-mesh formvar and carbon coated copper, Electron Microscopy Sciences, catalog no. FCF400-Cu). 1 min after deposition, the sample solution was wicked with

filter paper, followed by a quick wash with 3 μL of water and the addition of 3–5 drops of 2% wt/vol aqueous uranyl acetate solution. The uranyl acetate was wicked immediately with a filter paper, and the grids were air dried at room temperature. TEM images were acquired using a JEOL JEM-1400Plus transmission electron microscope (JEOL, Peabody, MA) and recorded on a Gatan OneView digital camera (Gatan, Pleasanton, CA).

3.9.15 CD spectroscopy

CD measurements (178–280 nm, 1 nm data pitch, continuous scanning with 1 nm bandwidth, 60 nm/min, and ten accumulations) with 0.1 mg/mL non- and phosphorylated $PRD^{Strep}_{703-868}$ were carried out in 2-mm-quartz cuvettes (Starna Cells Inc) using an Aviv model 215 spectrometer. The molar ellipticity was calculated using the equation: $[\theta]molar = 100*MW*\theta/cl$, where MW = molecular weight, θ = CD signal (mdeg), c = concentration (mg/mL), and l = pathlength (cm). The buffer and experimental conditions were as follows: 10 mM sodium phosphate, pH 7.0, 1 mM TCEP, 1 mM EDTA, and 25 °C.

3.9 Acknowledgments

We thank Z. Jiang, R. Ghirlando, P. A. Jennings, and I. Budin for useful discussions; X. Huang (UCSD Biomolecular NMR facility), L. Gross and Y. Su (UCSD Molecular Mass Spectrometry Facility) and G. Castillon and T. Meerloo (UCSD Cellular and Molecular Medicine Electron Microscopy Core Facility) for technical support. We thank A. van der Vliet (University of Vermont), D. S. Waugh (National Cancer Institute, National Institutes of Health, NIH), and G. Marius Clore (National Institute of Diabetes and Digestive and Kidney Diseases, NIH) for Src kinase, TEV protease, and apo-MBP-E38C constructs, respectively.

This work was funded in part by a 2018 Development Award (to L.D) from the San Diego Center for AIDS Research (SD CFAR, an NIH-funded program; P30 AI036214), and by Collaborative Development Awards (to L.D.) from the Cellular Host Elements in Egress, Trafficking, and Assembly of HIV (CHEETAH Center, University of Utah; an NIH-funded program; P50 AI150464) and HIV Interactions in Viral Evolution (HIVE Center, the Scripps research institute; an NIH-funded program; U54 AI150472), and a National Science Foundation (NSF) Graduate Research Fellowship under Grant No. DGE-1650112 (to R. D. E.). We acknowledge the use of facilities and instrumentation supported by the NSF through the UCSD Materials Research Science and Engineering Center, DMR-2011924, and by the NIH for the UCSD Cellular and Molecular Medicine EM Core Facility; S10OD023527, and the UCSD Molecular Mass Spectrometry Facility; 1S10RR25636-1A1.

Chapter 3, in full, is a reprint of the material as it appears in: Elias, R. D., Ramaraju, B., and Deshmukh, L. (2021) Mechanistic roles of tyrosine phosphorylation in reversible amyloids, autoinhibition, and endosomal membrane association of ALIX. J Biol Chem, 297 (5), 101328. The dissertation author was the primary investigator and author of this paper.

3.10 References

1. Odorizzi, G. (2006) The multiple personalities of Alix. J. Cell Sci. 119, 3025-3032

2. Sadoul, R. (2006) Do Alix and ALG-2 really control endosomes for better or for worse? Biology of the Cell 98, 69-77

3. Hurley, J. H., and Odorizzi, G. (2012) Get on the exosome bus with ALIX. Nat. Cell Biol. 14, 654-655

4. Bissig, C., and Gruenberg, J. (2014) ALIX and the multivesicular endosome: ALIX in Wonderland. Trends Cell Biol. 24, 19-25

5. Strack, B., Calistri, A., Craig, S., Popova, E., and Gottlinger, H. G. (2003) AIP1/ALIX is a binding partner for HIV-1 p6 and EIAV p9 functioning in virus budding. Cell 114, 689-699

6. von Schwedler, U. K., Stuchell, M., Muller, B., Ward, D. M., Chung, H. Y., Morita, E., Wang, H. E., Davis, T., He, G. P., Cimbora, D. M., Scott, A., Krausslich, H. G., Kaplan, J., Morham, S. G., and Sundquist, W. I. (2003) The protein network of HIV budding. Cell 114, 701-713

7. Han, Z., Madara, J. J., Liu, Y., Liu, W., Ruthel, G., Freedman, B. D., and Harty, R. N. (2015) ALIX rescues budding of a double PTAP/PPEY L-domain deletion mutant of ebola VP40: a role for ALIX in ebola virus egress. J. Infect. Dis. 212 Suppl 2, S138-S145

8. Schmidt, M. H. H., Dikic, I., and Bogler, O. (2005) Src phosphorylation of Alix/AIP1 modulates its interaction with binding partners and antagonizes its activities. J. Biol. Chem. 280, 3414-3425

9. Hikita, T., Kuwahara, A., Watanabe, R., Miyata, M., and Oneyama, C. (2019) Src in endosomal membranes promotes exosome secretion and tumor progression. Sci. Rep. 9, 3265

10. Matsuo, H., Chevallier, J., Mayran, N., Le Blanc, I., Ferguson, C., Fauré, J., Blanc, N. S., Matile, S., Dubochet, J., Sadoul, R., Parton, R. G., Vilbois, F., and Gruenberg, J. (2004) Role of LBPA and Alix in multivesicular liposome formation and endosome organization. Science 303, 531-534

11. Bissig, C., Lenoir, M., Velluz, M. C., Kufareva, I., Abagyan, R., Overduin, M., and Gruenberg, J. (2013) Viral infection controlled by a calcium-dependent lipid-binding module in ALIX. Dev. Cell 25, 364-373

12. Kobayashi, T., Stang, E., Fang, K. S., de Moerloose, P., Parton, R. G., and Gruenberg, J. (1998) A lipid associated with the antiphospholipid syndrome regulates endosome structure and function. Nature 392, 193-197

13. Zhou, X., Si, J., Corvera, J., Gallick, G. E., and Kuang, J. (2010) Decoding the intrinsic mechanism that prohibits ALIX interaction with ESCRT and viral proteins. Biochem. J. 432, 525-534

14. Zhai, Q., Landesman, M. B., Chung, H.-Y., Dierkers, A., Jeffries, C. M., Trewhella, J., Hill, C. P., and Sundquist, W. I. (2011) Activation of the retroviral budding factor ALIX. J. Virol. 85, 9222-9226

15. Ren, X., and Hurley, J. H. (2011) Proline-rich regions and motifs in trafficking: from ESCRT interaction to viral exploitation. Traffic 12, 1282-1290

16. Elias, R. D., Ma, W., Ghirlando, R., Schwieters, C. D., Reddy, V. S., and Deshmukh, L. (2020) Proline-rich domain of human ALIX contains multiple TSG101-UEV interaction

sites and forms phosphorylation-mediated reversible amyloids. Proc. Natl. Acad. Sci. U. S. A. 117, 24274-24284

17. Schmidt, T. G., and Skerra, A. (2007) The Strep-tag system for one-step purification and high-affinity detection or capturing of proteins. Nat. Protoc. 2, 1528-1535

18. Huth, J. R., Bewley, C. A., Jackson, B. M., Hinnebusch, A. G., Clore, G. M., and Gronenborn, A. M. (1997) Design of an expression system for detecting folded protein domains and mapping macromolecular interactions by NMR. Protein Sci. 6, 2359-2364

19. Tsiatsiani, L., and Heck, A. J. (2015) Proteomics beyond trypsin. FEBS J 282, 2612-2626

20. Baudier, J., and Cole, R. D. (1987) Phosphorylation of tau proteins to a state like that in Alzheimer's brain is catalyzed by a calcium/calmodulin-dependent kinase and modulated by phospholipids. J. Biol. Chem. 262, 17577-17583

21. Stuible, M., Abella, J. V., Feldhammer, M., Nossov, M., Sangwan, V., Blagoev, B., Park, M., and Tremblay, M. L. (2010) PTP1B targets the endosomal sorting machinery: dephosphorylation of regulatory sites on the endosomal sorting complex required for transport component STAM2. J. Biol. Chem. 285, 23899-23907

22. Shen, Y., and Bax, A. (2013) Protein backbone and sidechain torsion angles predicted from NMR chemical shifts using artificial neural networks. J. Biomol. NMR 56, 227-241

23. Sadler, J. B. A., Wenzel, D. M., Williams, L. K., Guindo-Martínez, M., Alam, S. L., Mercader, J. M., Torrents, D., Ullman, K. S., Sundquist, W. I., and Martin-Serrano, J. (2018) A cancer-associated polymorphism in ESCRT-III disrupts the abscission checkpoint and promotes genome instability. Proc. Natl. Acad. Sci. U. S. A. 115, E8900-E8908

24. Kay, B. K., Williamson, M. P., and Sudol, M. (2000) The importance of being proline: the interaction of proline-rich motifs in signaling proteins with their cognate domains. FASEB J. 14, 231-241

25. Zarrinpar, A., Bhattacharyya, R. P., and Lim, W. A. (2003) The structure and function of proline recognition domains. Sci. STKE 2003, re8-re8

26. Clore, G. M., and Iwahara, J. (2009) Theory, practice, and applications of paramagnetic relaxation enhancement for the characterization of transient low-population states of biological macromolecules and their complexes. Chem. Rev. 109, 4108-4139

27. Deshmukh, L., Louis, J. M., Ghirlando, R., and Clore, G. M. (2016) Transient HIV-1 Gag-protease interactions revealed by paramagnetic NMR suggest origins of compensatory drug resistance mutations. Proc. Natl. Acad. Sci. U. S. A. 113, 12456-12461

28. Baker, N. A., Sept, D., Joseph, S., Holst, M. J., and McCammon, J. A. (2001) Electrostatics of nanosystems: Application to microtubules and the ribosome. Proc. Natl. Acad. Sci. U. S. A. 98, 10037-10041

29. Rideau, E., Dimova, R., Schwille, P., Wurm, F. R., and Landfester, K. (2018) Liposomes and polymersomes: a comparative review towards cell mimicking. Chem. Soc. Rev. 47, 8572-8610

30. Carlton, J. G., Agromayor, M., and Martin-Serrano, J. (2008) Differential requirements for Alix and ESCRT-III in cytokinesis and HIV-1 release. Proc. Natl. Acad. Sci. U. S. A. 105, 10541-10546

31. Trioulier, Y., Torch, S., Blot, B., Cristina, N., Chatellard-Causse, C., Verna, J. M., and Sadoul, R. (2004) Alix, a protein regulating endosomal trafficking, is involved in neuronal death. J. Biol. Chem. 279, 2046-2052

32. Kamranvar, S. A., Gupta, D. K., Huang, Y., Gupta, R. K., and Johansson, S. (2016) Integrin signaling via FAK-Src controls cytokinetic abscission by decelerating PLK1 degradation and subsequent recruitment of CEP55 at the midbody. Oncotarget 7, 30820-30830

33. Shibata, H., Yamada, K., Mizuno, T., Yorikawa, C., Takahashi, H., Satoh, H., Kitaura, Y., and Maki, M. (2004) The penta-EF-hand protein ALG-2 interacts with a region containing PxY repeats in Alix/AIP1, which is required for the subcellular punctate distribution of the amino-terminal truncation form of Alix/AIP1. J. Biochem. 135, 117-128

34. Schöneberg, J., Lee, I.-H., Iwasa, J. H., and Hurley, J. H. (2017) Reverse-topology membrane scission by the ESCRT proteins. Nat. Rev. Mol. Cell Biol. 18, 5-17

35. Vietri, M., Radulovic, M., and Stenmark, H. (2020) The many functions of ESCRTs. Nat. Rev. Mol. Cell Biol. 21, 25-42

36. Christ, L., Wenzel, E. M., Liestøl, K., Raiborg, C., Campsteijn, C., and Stenmark, H. (2016) ALIX and ESCRT-I/II function as parallel ESCRT-III recruiters in cytokinetic abscission. J. Cell Biol. 212, 499-513

37. Larios, J., Mercier, V., Roux, A., and Gruenberg, J. (2020) ALIX- and ESCRT-III–dependent sorting of tetraspanins to exosomes. J. Cell Biol. 219

38. Kim, J., Sitaraman, S., Hierro, A., Beach, B. M., Odorizzi, G., and Hurley, J. H. (2005) Structural basis for endosomal targeting by the Bro1 domain. Dev. Cell 8, 937-947

39. Chiti, F., and Dobson, C. M. (2017) Protein misfolding, amyloid formation, and human disease: a summary of progress over the last decade. Annu. Rev. Biochem. 86, 27-68

40. Hammer, N. D., Wang, X., McGuffie, B. A., and Chapman, M. R. (2008) Amyloids: friend or foe? J. Alzheimers Dis. 13, 407-419

41. Jackson, M. P., and Hewitt, E. W. (2017) Why are functional amyloids non-toxic in humans? Biomolecules 7

42. Wang, M., Audas, T. E., and Lee, S. (2017) Disentangling a bad reputation: changing perceptions of amyloids. Trends Cell Biol. 27, 465-467

43. Otzen, D., and Riek, R. (2019) Functional amyloids. Cold Spring Harb. Perspect. Biol. 11

44. Khoury, G. A., Baliban, R. C., and Floudas, C. A. (2011) Proteome-wide post-translational modification statistics: frequency analysis and curation of the swiss-prot database. Sci. Rep. 1, 90

45. Chiti, F., and Dobson, C. M. (2006) Protein misfolding, functional amyloid, and human disease. Annu. Rev. Biochem. 75, 333-366

46. Schnabel, J. (2010) Protein folding: The dark side of proteins. Nature 464, 828-829

47. McCullough, J., Fisher, R. D., Whitby, F. G., Sundquist, W. I., and Hill, C. P. (2008) ALIX-CHMP4 interactions in the human ESCRT pathway. Proc. Natl. Acad. Sci. U. S. A. 105, 7687-7691

48. Lee, S., Joshi, A., Nagashima, K., Freed, E. O., and Hurley, J. H. (2007) Structural basis for viral late-domain binding to Alix. Nat. Struct. Mol. Biol. 14, 194-199

49. Carlson, L. A., and Hurley, J. H. (2012) In vitro reconstitution of the ordered assembly of the endosomal sorting complex required for transport at membrane-bound HIV-1 Gag clusters. Proc. Natl. Acad. Sci. U. S. A. 109, 16928-16933

50. Choy, M. S., Li, Y., Machado, L., Kunze, M. B. A., Connors, C. R., Wei, X., Lindorff-Larsen, K., Page, R., and Peti, W. (2017) Conformational rigidity and protein dynamics at distinct timescales rgulate PTP1B activity and allostery. Mol. Cell 65, 644-658.e645

51. Ramaraju, B., Nelson, S. L., Zheng, W., Ghirlando, R., and Deshmukh, L. (2021) Quantitative NMR study of insulin-degrading enzyme using amyloid-β and HIV-1 p6 elucidates its chaperone activity. Biochemistry 60, 2519-2523

52. Zhang, Z., and Marshall, A. G. (1998) A universal algorithm for fast and automated charge state deconvolution of electrospray mass-to-charge ratio spectra. J. Am. Soc. Mass Spectrom. 9, 225-233

53. Rost, H. L., Sachsenberg, T., Aiche, S., Bielow, C., Weisser, H., Aicheler, F., Andreotti, S., Ehrlich, H. C., Gutenbrunner, P., Kenar, E., Liang, X., Nahnsen, S., Nilse, L., Pfeuffer, J., Rosenberger, G., Rurik, M., Schmitt, U., Veit, J., Walzer, M., Wojnar, D., Wolski, W. E., Schilling, O., Choudhary, J. S., Malmstrom, L., Aebersold, R., Reinert, K., and Kohlbacher, O. (2016) OpenMS: a flexible open-source software platform for mass spectrometry data analysis. Nat Methods 13, 741-748

54. Kim, S., and Pevzner, P. A. (2014) MS-GF+ makes progress towards a universal database search tool for proteomics. Nature Communications 5, 5277

55. Jiang, Z., de Messieres, M., and Lee, J. C. (2013) Membrane remodeling by α-synuclein and effects on amyloid formation. J. Am. Chem. Soc. 135, 15970-15973

56. Delaglio, F., Grzesiek, S., Vuister, G. W., Zhu, G., Pfeifer, J., and Bax, A. (1995) NMRPipe: a multidimensional spectral processing system based on UNIX pipes. J. Biomol. NMR 6, 277-293

57. Vranken, W. F., Boucher, W., Stevens, T. J., Fogh, R. H., Pajon, A., Llinas, M., Ulrich, E. L., Markley, J. L., Ionides, J., and Laue, E. D. (2005) The CCPN data model for NMR spectroscopy: development of a software pipeline. Proteins 59, 687-696

58. Clore, G. M., and Gronenborn, A. M. (1998) Determining the structures of large proteins and protein complexes by NMR. Trends Biotechnol. 16, 22-34

59. Lakomek, N. A., Ying, J., and Bax, A. (2012) Measurement of ^{15}N relaxation rates in perdeuterated proteins by TROSY-based methods. J. Biomol. NMR 53, 209-221

60. Roepstorff, P., and Fohlman, J. (1984) Proposal for a common nomenclature for sequence ions in mass spectra of peptides. Biomed. Mass Spectrom. 11, 601

61. Brademan, D. R., Riley, N. M., Kwiecien, N. W., and Coon, J. J. (2019) Interactive peptide spectral annotator: a versatile web-based tool for proteomic applications. Mol. Cell. Proteomics 18, S193-S201

62. Zhang, Z. Y., Thieme-Sefler, A. M., Maclean, D., McNamara, D. J., Dobrusin, E. M., Sawyer, T. K., and Dixon, J. E. (1993) Substrate specificity of the protein tyrosine phosphatases. Proc. Natl. Acad. Sci. U. S. A. 90, 4446-4450

63. Duan, X., Hall, J. A., Nikaido, H., and Quiocho, F. A. (2001) Crystal structures of the maltodextrin/maltose-binding protein complexed with reduced oligosaccharides: flexibility of tertiary structure and ligand binding. J. Mol. Biol. 306, 1115-1126

64. Ferreira, C. M. H., Pinto, I. S. S., Soares, E. V., and Soares, H. M. V. M. (2015) (Un)suitability of the use of pH buffers in biological, biochemical and environmental studies and their interaction with metal ions – a review. RSC Adv. 5, 30989-31003

65. Schwieters, C. D., Kuszewski, J. J., Tjandra, N., and Clore, G. M. (2003) The Xplor-NIH NMR molecular structure determination package. J. Magn. Reson. 160, 65-73

Chapter 4: Reversible phase separation of ESCRT-protein ALIX through tyrosine phosphorylation

4.1 Introduction

Cytokinetic abscission, the final step of cell division, is tightly regulated and coordinated with chromosome segregation to ensure accurate distribution of genetic material (1). In animal cells, it is carried out by the endosomal sorting complex required for transport (ESCRT) machinery, which severs a membranous intercellular bridge, comprising a microtubule-rich structure called the midbody (2). Five functionally distinct ESCRT factors/complexes, namely apoptosis-linked gene-2 interacting protein X (ALIX), ESCRT-37 I, -II, -III, and ATPase vacuolar protein sorting-associated protein 4 (VPS4), are sequentially recruited to the midbody with the localization of charged multivesicular body protein 4B (CHMP4B), a late-acting ESCRT-III paralog that polymerizes into membrane-40 constricting filaments, initiating the final separation of the daughter cells (Fig. 4.1). The early-acting ESCRT components, tumor susceptibility gene 101 (TSG101; ESCRT-I) and ALIX, are initially recruited to the midbody by the microtubule-bundling centrosomal protein of 55 kDa (CEP55). ALIX (Fig. 4.1.1 A), the central regulator of abscission, performs multiple functions. ALIX binds to TSG101, thereby initiating TSG101-mediated recruitment of CHMP4B to the midbody. ALIX also facilitates an alternative CHMP4B recruitment pathway as its Bro1 domain binds to the extreme C-terminal motifs of CHMP4 paralogs (3). Moreover, ALIX promotes closed-to-open transitions of inactive cytosolic CHMP4 monomers by a yet unknown mechanism, triggering their polymerization required for abscission (4). In response to chromosome segregation defects and mitotic errors, a conserved Aurora-B kinase dependent mechanism known as the “abscission checkpoint” (NoCut pathway in yeast) arrests the abscission to prevent the accumulation of DNA damage (5-7). Unlike CHMP4B, which

is indispensable for cytokinetic membrane fission, its paralog, CHMP4C, is instrumental in maintaining the checkpoint (8). The latter depends on its interactions with ALIX, as an allele of CHMP4C (with A232T point-mutation) defective in binding to ALIX overrides the checkpoint, resulting in increased susceptibility to several cancers, including ovarian cancer (9, 10).

The abscission timing depends on the differential spatiotemporal distribution of ALIX and CHMP4 paralogs. In these regards, cytoplasmic compartments termed "abscission checkpoint bodies" (ACBs), which form during stress conditions that activate the checkpoint, were recently discovered (11). These ACBs stem from cytoplasmic structures known as mitotic interchromatin granules (MIGs), which, in turn, originate from nuclear speckles, the nuclear compartments associated with active transcription sites (12). Phase separation of biomolecules into membraneless compartments serves numerous functions, including sequestration and storage of cellular factors (13-16). Both MIGs and nuclear speckles exhibit liquid-liquid phase separation characteristics (17, 18). A prolonged abscission checkpoint induces the transition of MIGs into ACBs. The latter confine multiple abscission factors, including ALIX, CHMP4B, CHMP4C, and Aurora-B, thus delaying the localization of ALIX and, consequently, the ALIX-mediated localization of CHMP4B at the midbody (11). ALIX maintains the integrity of ACBs, as depletion of ALIX was shown to reduce their size substantially (11). Additionally, the recruitment of ALIX contributes to the biogenesis of ACBs from MIGs. However, the mechanism(s) by which ALIX maintains the integrity of ACBs and orchestrates their transformation from MIGs is unclear. Moreover, even though Src-kinase-mediated phosphorylation of ALIX regulates its cellular functions (19), Src-signaling is required for successful abscission (20), and protein-tyrosine phosphatase 1B (PTP1B) targets the ESCRT machinery (21), the interplay between reversible tyrosine phosphorylation of ALIX and the biogenesis and stability of ACBs is not known. A mechanistic understanding of

these processes will provide crucial insights into how order is achieved in the last step of cell division as well as the impact and role of posttranslational modifications (PTMs) in regulating the timing of protein compartmentalization.

Here we describe our discovery of ALIX's phase separation in vivo and in vitro. We show that condensates of recombinant ALIX readily confine CHMP4 paralogs, CHMP4B and CHMP4C. Nuclear magnetic resonance (NMR) measurements provided mechanistic insights into how ALIX triggers CHMP4 activation needed for membrane scission. The formation and dissolution of condensates of recombinant ALIX could be tuned by PTP1B and Src. Thus, we propose that phase separation of ALIX will play a vital role in the biogenesis of ACBs and in maintaining their integrity, and that upon resolution of the checkpoint, Src-mediated dissolution of ALIX assemblies will re-route ALIX from ACBs to the midbody, thereby controlling the abscission timing.

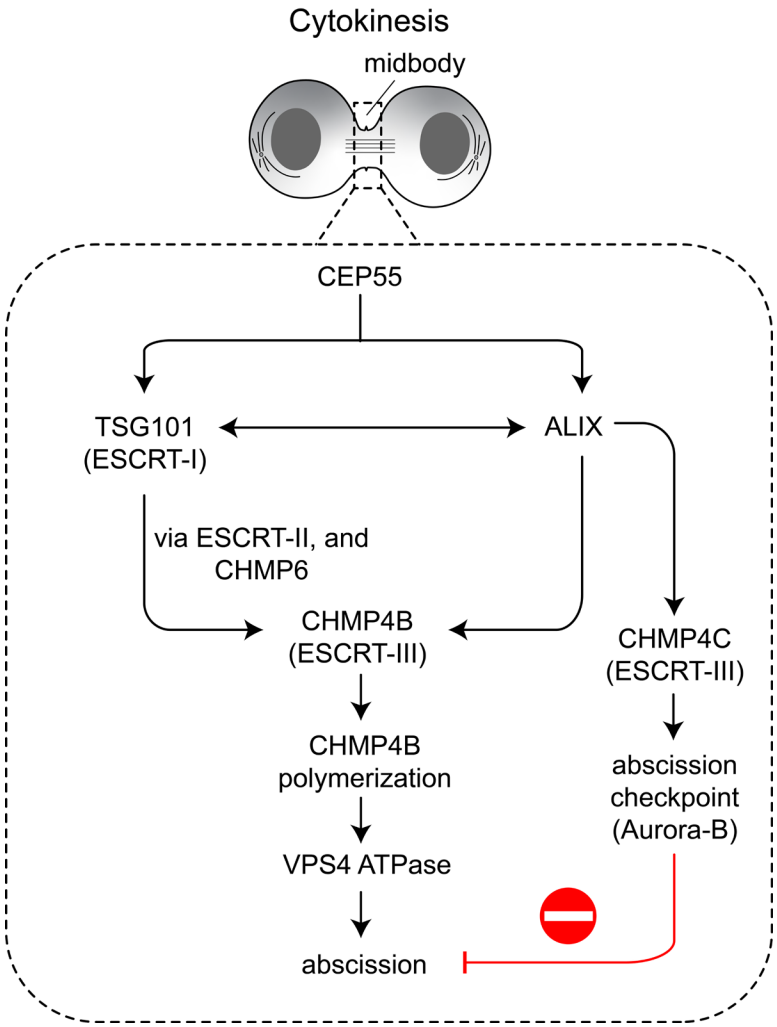

Figure 4.1: The endosomal sorting complex required for transport (ESCRT) machinery in cytokinetic abscission

Schematic of the recruitment pathways of ESCRT-factors to the midbody, derived from prior biochemical, cellular, and functional results (6, 7). ALIX and TSG101 are recruited to the midbody by CEP55. However, abscission can also proceed via CEP55-independent pathways (78, 79); not shown.

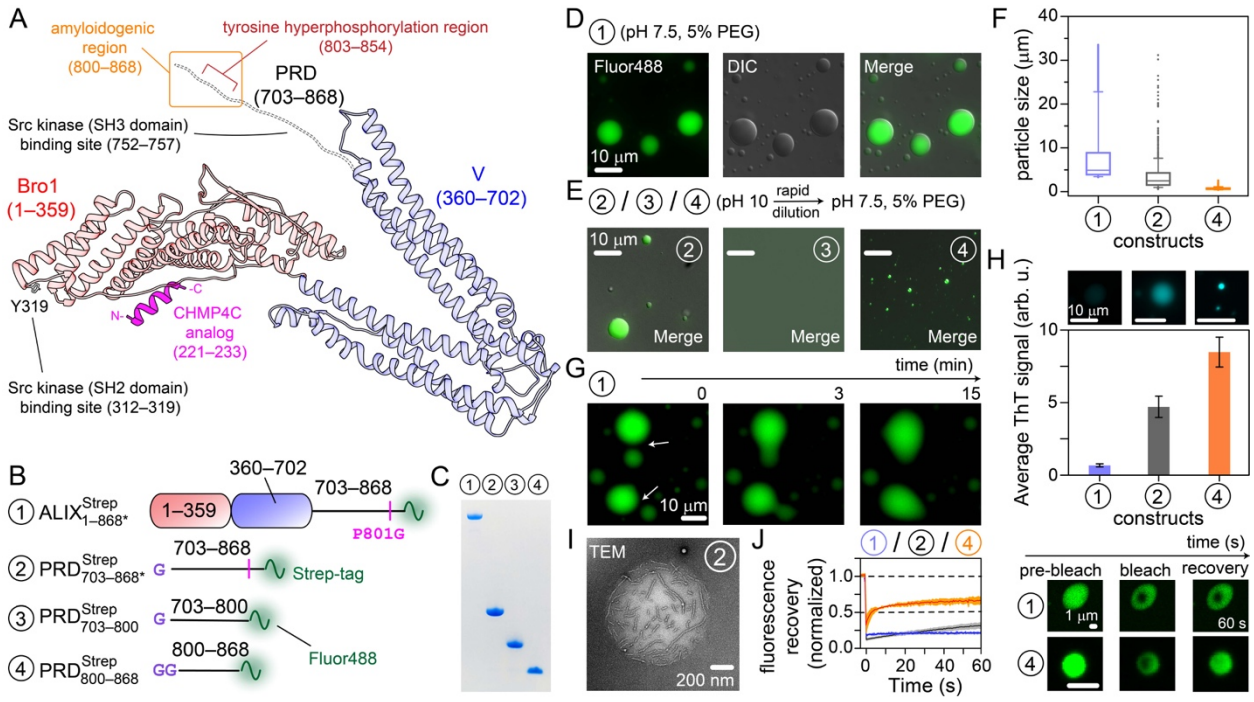

Figure 4.1.1: Phase separation of recombinant ALIX

(A) Schematic of ALIX comprising Bro1, V, and PRD (red and blue ribbons and dashed black lines, respectively), derived from the X-ray structure of Bro1-V domains (71); numbers in parentheses signify ALIX residues. The functional motifs of ALIX relevant to current study are marked and labeled (19, 22, 23). The model also depicts a CHMP4C analog (magenta ribbon) in its Bro1-bound form, obtained from the X-ray structure of Bro1–CHMP4C peptide complex (10). **(B)** ALIX constructs (Fig. 4.1.2) tested in phase separation experiments. Each construct is designated by a circled number. The positions of the strep tags, the P801G mutations, and Alexa-Fluor488 labeling sites are marked. Remnant residues of the TEV protease cleavage sites are labeled in purple. **(C)** SDS-PAGE analysis of ALIX constructs; throughout the figure, the circled numbers signify the constructs shown in panel B. **(D and E)** Microscopy images of droplets made by ALIX constructs; $PRD^{Strep}_{703\text{-}800}$ (construct 3) did not phase separate. **(F)** Box plot of the size distribution of condensates of $ALIX^{Strep}_{1\text{-}868*}$ (blue), $PRD^{Strep}_{703\text{-}868*}$ Strep (gray) and $PRD^{Strep}_{800\text{-}868}$ (orange); n ≥ 1900. **(G)** Representative montage of the slow fusion of $ALIX^{Strep}_{1\text{-}868*}$ condensates. **(H)** Quantitative analysis of the co-partitioning of 20 μM ThT dye in freshly prepared condensates (n ≥ 25) of ALIX constructs, same color scheme as panel F. Top: representative images of the corresponding condensates. **(I)** Representative TEM image of an aged $PRD^{Strep}_{703\text{-}868*}$ Strep droplet; incubation time ~2 days at room temperature. **(J)** FRAP analysis with the solid line and shaded region representing the mean and SD, respectively ($n = 3$). The right panels show the fluorescence of representative condensates of $ALIX^{Strep}_{1\text{-}868*}$ and $PRD^{Strep}_{800\text{-}868}$ at different time points. All phase-separation experiments were performed at room temperature in 20 mM HEPES, pH 7.5, 50 mM NaCl, 1 mM DTT, 1 mM EDTA, and 5% (w/v) PEG-4000, with 50 μM proteins. For ALIX-PRD constructs, lyophilized polypeptides were dissolved in a buffer containing 20 mM CAPS, pH 10, and 50 mM NaCl, followed by a rapid dilution in the above-mentioned buffer.

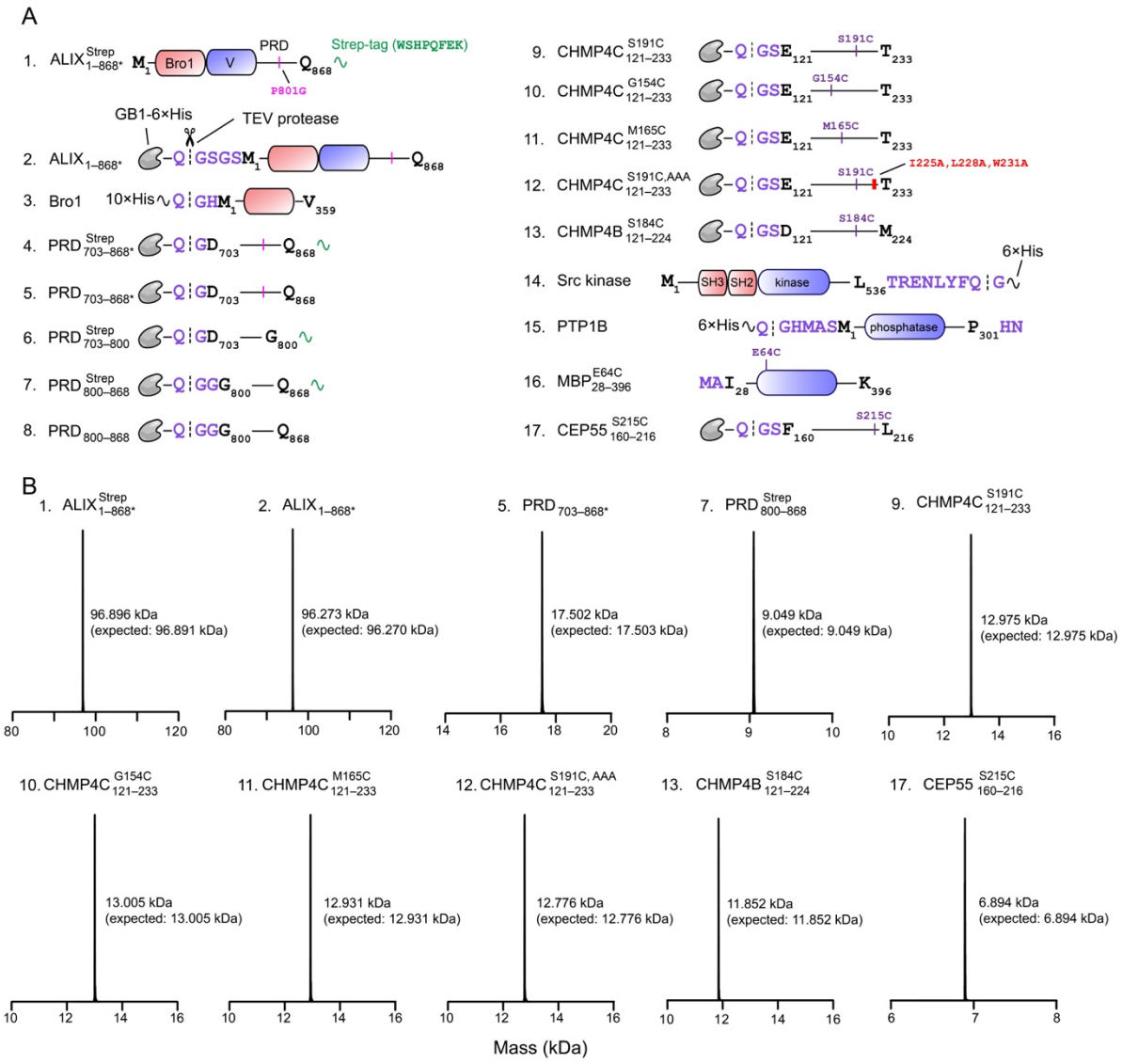

Figure 4.1.2: Constructs used in current study

(A) List of constructs used in current study. Constructs 1, 2, 4–12, and 16 were custom-synthesized from Azenta Life Sciences. Note that GB1-6xHis denotes B1 domain of protein G, GB1 (57), used to enhance protein expression levels, followed by a spacer sequence, a polyhistidine (6xHis) affinity tag, and a TEV protease cleavage site. Constructs 1–12 and 16 were subcloned in pET11a and expressed in BL21(DE3) competent cells (Agilent). Constructs 3 and 14 were obtained from the Addgene repository [accession no. 80641 (3) and 102719 (56), respectively]. Constructs 1, 2, 5, 7, 9–13, and 17 were deposited in the Addgene repository as a part of the current study (accession no. 180024, 180025, 180029, 180023, 180027, 190783, 190784, 199242, 180026, and 186793 respectively). Constructs 4, 6, and 8 were deposited in the Addgene repository as a part of our published works (22, 23) [accession no. 164444, 141344, and 141345, respectively]. Constructs 14 and 16 were generous gifts from Albert van der Vliet (University of Vermont), and G. Marius Clore (NIH). Src kinase (construct 14) was expressed in BL21-AI cells (Thermo Fisher Scientific). **(B)** Analysis of recombinant proteins using liquid chromatography–electrospray ionization–time-of-flight mass spectrometry (LC–ESI–TOFMS). Masses of constructs 3, 4, 6, 8, and 14–16 were reported in our previously published works (22, 23).

4.2 ALIX condensates and identification of its phase separation motif

We sought to determine the phase separation characteristics of recombinant ALIX because the extreme C-terminal portion of its disordered proline-rich domain (PRD; Fig. 4.1.1 A) formed β-sheet-rich amyloid fibrils (22, 23), and amyloidogenic sequences may phase separate (13, 14). Heterologous expression of ALIX in *Escherichia coli* (*E. coli*) is hampered by its PRD, which induces ribosomal stalling (22). We resolved these expression issues by introducing a point mutation, P801G, in its PRD, which enabled a high-yield expression of recombinant ALIX (~40 mg/1 L of bacterial culture). This P801G substitution likely works by altering the ^{800}GPP^{802} motif of ALIX, which is known to induce polyproline-mediated ribosomal stalling in bacteria (24). Note that we previously used this substitution to produce milligram quantities of recombinant ALIX-PRD (23). The P801G substitution resides in the CEP55-binding motif of ALIX-PRD, residues 797–808 (25). Mutated ALIX-PRD, however, retained its CEP55 binding ability (see below), likely because structurally dynamic PRDs can often tolerate combinations of various residues without compromising their functional integrity (22). The following constructs were used to test phase separation of ALIX (Fig. 4.1.1 B–C): full-length ALIX ($ALIX^{Strep}_{1\text{-}868*}$), a construct representing its PRD ($PRD^{Strep}_{703\text{-}868*}$), and two constructs representing the N-terminal soluble portion and the C-terminal amyloidogenic portion of its PRD ($PRD^{Strep}_{703\text{-}800}$ and $PRD^{Strep}_{800\text{-}868}$, respectively); the numbers signify ALIX residues, the asterisk denotes P801G mutation, and Strep indicates a C-terminal strep tag (26), which facilitated rapid protein purification using affinity chromatography and Alexa-Fluor488 labeling (Methods).

$ALIX^{Strep}_{1\text{-}868*}$ was monomeric by analytical ultracentrifugation (AUC; Fig. 4.2), consistent with a prior study that reported that ALIX made using insect cells was monomeric (27). Its

solution, however, became turbid in the presence of a molecular crowder polyethylene glycol 4000 (PEG-4000), and subsequent examination by microscopy revealed its spherical condensates (Fig. 4.1.1 D). To disaggregate fibrils, lyophilized ALIX-PRD constructs were dissolved in a basic (pH 10) buffer (28, 29). Upon rapid dilution to physiological pH conditions (pH 7.5) in the presence of PEG-4000, $PRD^{Strep}_{703\text{-}868*}$, and its truncated counterpart, $PRD^{Strep}_{800\text{-}868}$, also condensed into droplets (Fig. 4.1.1 E). Additionally, $PRD^{Strep}_{800\text{-}868}$ formed condensates without PEG-4000 (Fig. 4.2.1), suggesting that it is responsible for ALIX's phase separation. In contrast, $PRD^{Strep}_{703\text{-}800}$ did not phase separate under any conditions tested, consistent with our prior observations that this portion of ALIX-PRD is non-amyloidogenic and highly soluble (22). The median diameters of condensates of $ALIX^{Strep}_{1\text{-}868*}$, $PRD^{Strep}_{703\text{-}868*}$, and $PRD^{Strep}_{800\text{-}868}$ (50 μM each) were ~5, ~1.5, and ~0.5 μm, respectively (Fig. 4.1.1 F), establishing that ALIX condensates were larger than those of its PRD. Corresponding ALIX constructs without strep tags also formed condensates (Fig. 4.2.2), ruling out the contribution of the strep tag in ALIX's phase separation. Although we occasionally observed a fusion of freshly prepared $ALIX^{Strep}_{1\text{-}868*}$ droplets, the corresponding timescales were in minutes and resulted in the formation of uneven oblong structures (Fig. 4.1.11 G), suggesting the presence of viscous liquids in these condensates. A varying degree of co-partitioning of amyloid-sensitive dye, thioflavin T (ThT), was detected in freshly prepared condensates, with low ThT partitioning in $ALIX^{Strep}_{1\text{-}868*}$ droplets vs. a robust partitioning in condensates of ALIX-PRD constructs, $PRD^{Strep}_{703\text{-}868*}$ and $PRD^{Strep}_{800\text{-}868}$ (Fig. 4.1.1 H and Fig. 4.2.3), indicating the presence of amyloid fibrils in the latter cases. Such fibrils could be occasionally visualized in aged droplets of $PRD^{Strep}_{703\text{-}868*}$ using transmission electron microscopy (TEM; Fig. 4.1.1 I). Little to no fluorescence recoveries after photobleaching (FRAP) were observed for the freshly prepared condensates of ALIX

constructs (Fig. 4.1.1 J), which established their partially solid/gel-like character. About 40% average recovery (in 60 s) was observed for $PRD^{Strep}_{800\text{-}868}$ as opposed to ≤ _20% recoveries for $PRD^{Strep}_{703\text{-}868*}$ and $ALIX^{Strep}_{1\text{-}868*}$, indicating that the cycling between soluble and phase-separated states was relatively more hindered in larger ALIX constructs, perhaps due to their increased gelation stemming from the presence of additional intermolecular interactions. Biological condensates often exhibit such nondynamic phases, which are implicated in cellular and pathological processes (13). Note that because of the spherical morphology of condensates of ALIX constructs (cf. Fig. 4.1.1 D–E), there exists a possibility that these droplets are initially liquid-like but then rapidly transition into nondynamic phases within a few minutes of their preparation. Collectively, these results establish that recombinant ALIX phase separates under crowding conditions and the phase-separation motif likely resides in the amyloidogenic portion of its PRD.

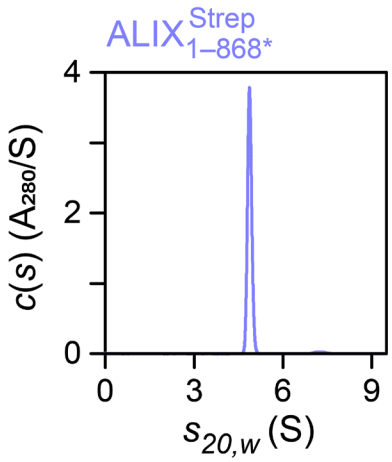

Figure 4.2: Recombinant ALIX is monomeric in solution

Absorbance sedimentation c(*s*) profile of $ALIX^{Strep}_{1\text{-}868*}$ at 30 ºC, establishing the presence of a monodispersed monomeric species.

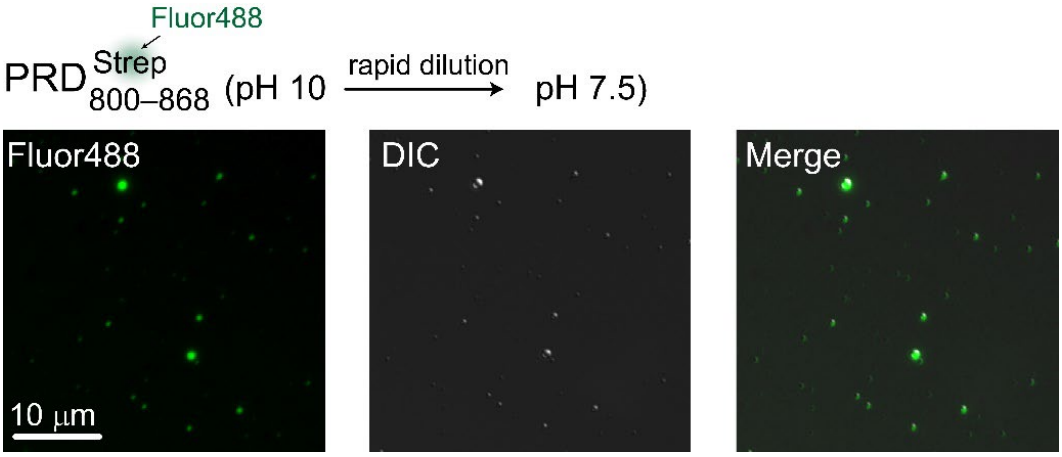

Figure 4.2.1: Phase separation of $PRD^{Strep}_{800\text{-}868}$ in the absence of PEG-4000

Representative microscopy images of Alexa-Fluor488-labeled $PRD^{Strep}_{800\text{-}868}$ droplets; DIC = differential interference contrast.

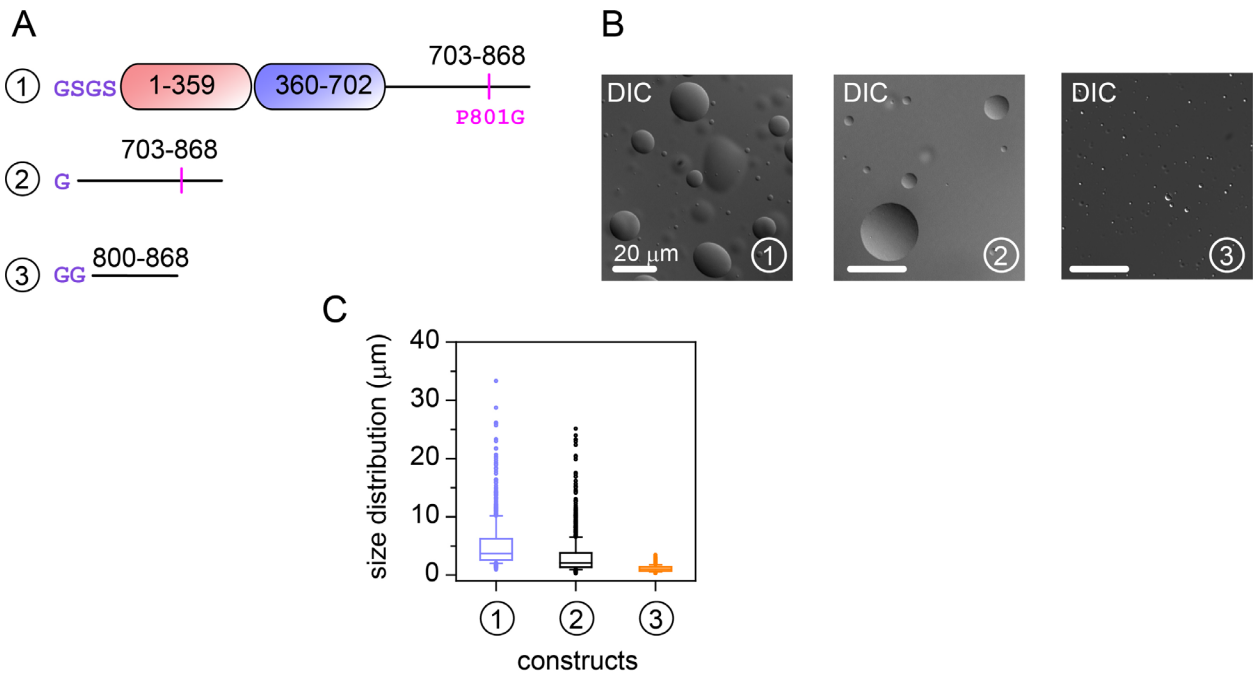

Figure 4.2.2: Phase separation of ALIX constructs in the absence of strep tags

(A) List of ALIX constructs used to rule out the contribution of the strep tag in its phase separation, namely $ALIX_{1–868*}$, $PRD_{703–868*}$, and $PRD_{800–868}$ (constructs 1, 2, and 3, respectively). Remnant non-native residues of the TEV protease cleavage sites are labeled in purple. The location of P801G mutation is marked with pink vertical line. **(B)** DIC images of droplets made by each ALIX constructs. **(C)** Box plot of the size distribution of condensates made by each construct, $n \geq 950$. Median diameters of the condensates were as follows: ~4 µm ($ALIX_{1–868*}$), ~2 µm ($PRD_{703–868*}$), and 0.5 µm ($PRD_{800–868}$).

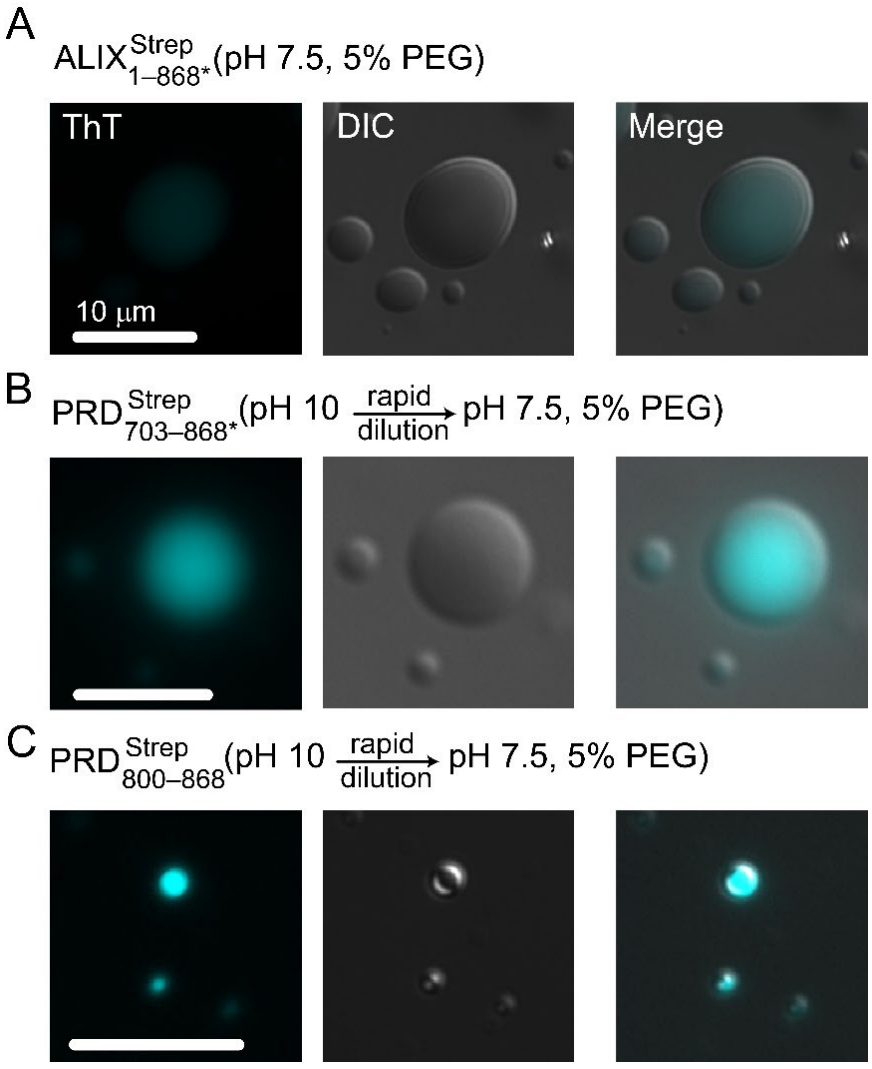

Figure 4.2.3: Differential co-localization of Thioflavin T (ThT) in ALIX condensates

Representative microscopy images depicting a varying degree of co-partitioning of amyloid-sensitive dye, ThT, in condensates made by **(A)** $ALIX^{Strep}_{1\text{-}868*}$, **(B)** $PRD^{Strep}_{703\text{-}868*}$, and **(C)** $PRD^{Strep}_{800\text{-}868}$. Experimental and buffer conditions are the same as described in Fig. 4.2 caption. The concentration of ThT was 20 μM. Images were taken immediately after the formation of condensates.

4.3 Phase separation of ALIX living cells

Next, we examined phase separation of ALIX in mammalian cells. Overexpression of $ALIX_{1–868*}$ tagged with a fluorescent protein mNeonGreen (30) [$ALIX^{mNG}_{1-868*}$, Fig. 4.3 A] in human embryonic kidney (HEK) 293T cells resulted in the formation of submicron-scale puncta, which could be visualized using live-cell fluorescence microscopy (Fig. 4.3 B and Fig. 4.3.1). Puncta were observed in ~20% of the representative imaged cells, with a median value of ~8 puncta/punctated cell (Fig. 4.3 C). To determine the impact of the P801G mutation on the phase separation of ALIX, similar experiments were performed with mNeonGreen-tagged wild-type ALIX ($ALIX^{mNG}_{1-868}$), which also exhibited puncta formation with ~7 puncta/punctated cell (Fig. 4.3 B–C), demonstrating that ALIX's phase separation is not influenced by the P801G mutation. In contrast, overexpression of mNeonGreen-tagged ALIX lacking the PRD ($ALIX^{mNG}_{1-702}$) resulted in an almost complete loss of puncta formation (Fig. 4.3 B–C), confirming that the PRD of ALIX is necessary for its phase separation. In-cell FRAP experiments carried out on $ALIX^{mNG}_{1-868*}$ puncta corroborated our in vitro results with negligible fluorescence recovery (Fig. 4.3 D), establishing their nondynamic nature. These results show that ALIX forms condensates in living cells and the PRD is required for its phase separation.

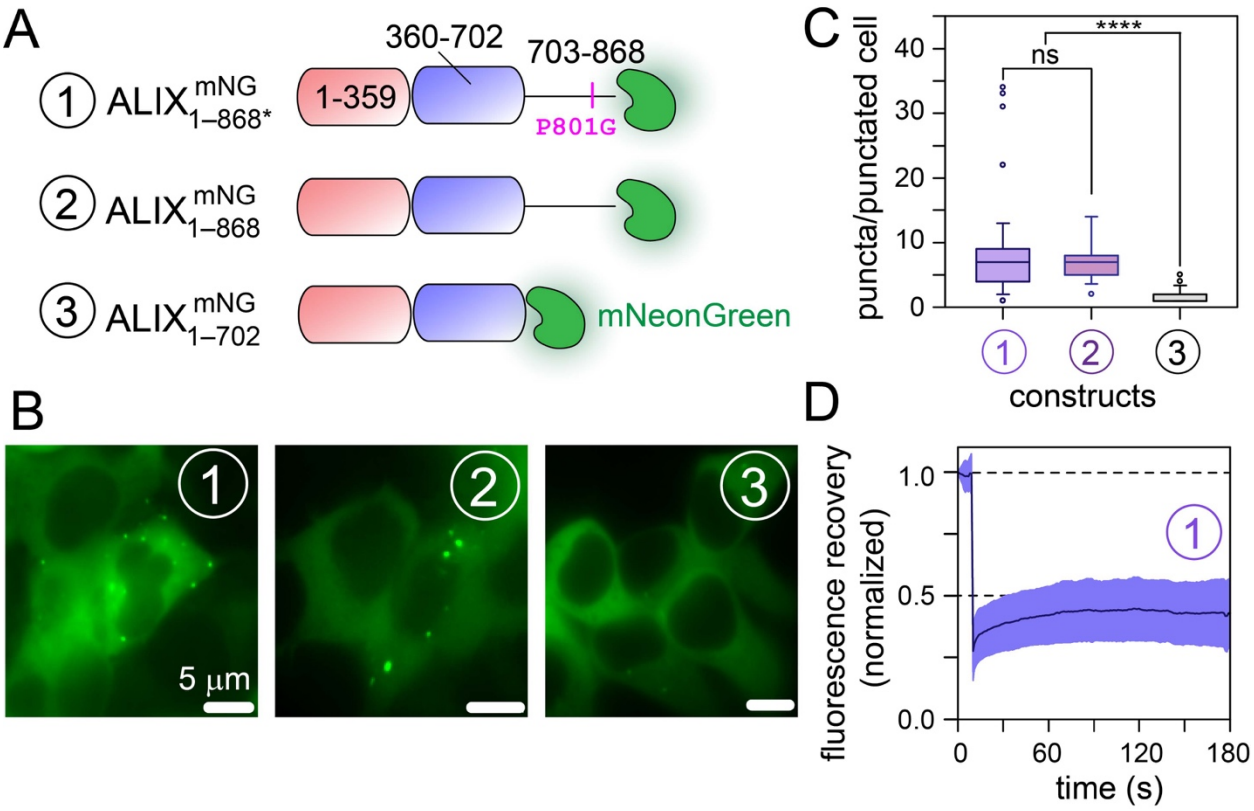

Figure 4.3: Phase separation of ALIX in HEK293T cells

(A) Schematic of ALIX constructs used for cellular experiments. Each construct is designated by a circled number and carries fluorescent protein, mNeonGreen (mNG), at the C-terminus; all constructs lack the strep tag. **(B)** Representative microscopy images of HEK293T cells overexpressing the three ALIX constructs shown in panel A (also see Fig. 4.3.1). For $ALIX^{mNG}_{1\text{-}868*}$ and $ALIX^{mNG}_{1\text{-}868}$ (constructs 1 and 2, respectively), about 20% protein population was colocalized in puncta, i.e., distinct fluorescence green spots (>300 representative cells, n = 5, for $ALIX^{mNG}_{1\text{-}868*}$, >200 cells, n = 3 for $ALIX^{mNG}_{1\text{-}868}$). For $ALIX^{mNG}_{1\text{-}702}$ lacking the PRD (construct 3), this phase separation is significantly abrogated (about 10% of representative cells with puncta, >400 cells, n = 3). **(C)** Box plot of the number of puncta observed per cell for each ALIX construct shown in panel A; only a representative population of cells containing puncta were used for analysis. **(D)** In-cell FRAP analysis of the condensates formed by $ALIX^{mNG}_{1\text{-}868*}$ (construct 1). Almost a complete lack of fluorescence recovery over time (~10% recovery in 180 s) confirms nondynamic nature of cellular ALIX condensates.

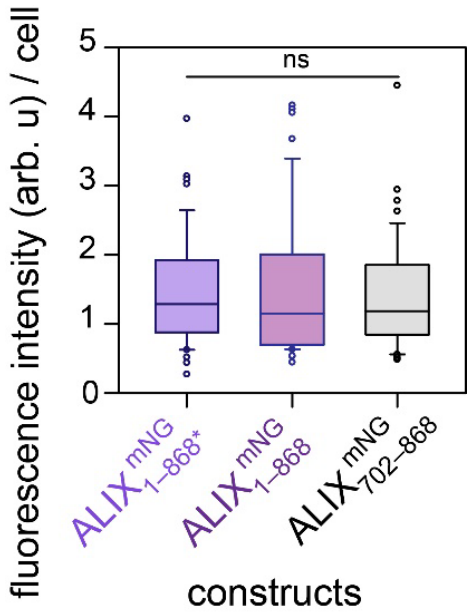

Figure 4.3.1: Expression levels of three ALIX constructs in HEK293T cells determined by fluorescence microscopy

To quantify fluorescence intensities stemming from the expression of ALIX constructs, namely $ALIX^{mNG}_{1\text{-}868*}$, $ALIX^{mNG}_{1\text{-}868}$, and $ALIX^{mNG}_{1\text{-}702}$ (see Fig. 4.3 A for construct design), the background fluorescence intensity of a cell-free region was subtracted from the emission intensities of ALIX expressing cells.

4.4 Co-partitioning of CHMP4 paralogs in ALIX condensates

Since cellular ACBs contained CHMP4C and CHMP4B (11), we used their recombinant counterparts, namely $CHMP4C^{S191C}_{121\text{-}233}$ and $CHMP4B^{S184C}_{121\text{-}224}$, to determine their co-partitioning in condensates of ALIX constructs (Fig. 4.4 A–B). Both CHMP4 constructs used here lacked their filament-forming core domains (residues 1–120) and carried a non-native cysteine residue that enabled labeling with fluorescent dyes. To assess co-partitioning of $CHMP4C^{S191C}_{121\text{-}233}$ in $ALIX^{Strep}_{1\text{-}868*}$ condensates, the two proteins were mixed, and phase-separation was induced by the addition of PEG-4000. $CHMP4C^{S191C}_{121\text{-}233}$ colocalization in these condensates was immediate and readily visible by florescence microscopy (Fig. 4.4 C and Fig. 4.4.1 A), suggesting that ALIX retained its structure in these condensates and could thus recruit its binding partners. Surprisingly, $CHMP4C^{S191C}_{121\text{-}233}$ also co-partitioned in $PRD^{Strep}_{703\text{-}868*}$ condensates (Fig. 4.4 D and Fig. 4.4.1 B), whereas no such colocalization was observed in $PRD^{Strep}_{800\text{-}868}$ droplets (Fig. 4.4 E and Fig. 4.4.1 C). Similar results, i.e., robust colocalization in $ALIX^{Strep}_{1\text{-}868*}$ and $PRD^{Strep}_{703\text{-}868*}$ condensates but no colocalization in $PRD^{Strep}_{800\text{-}868}$ droplets, were obtained using $CHMP4B^{S184C}_{121\text{-}224}$ (Fig. 4.4 F–G, and Fig. 4.4.1 A–C). These observations indicate that in addition to Bro1, ALIX harbors a second binding site for CHMP4 paralogs (see below), which likely resides in the N-terminal portion of its PRD (residues 703–800), and that the CHMP4 constructs tested here do not phase separate on their own under these experimental conditions. Experiments performed using an unrelated maltose-binding protein ($MBP^{E64C}_{28\text{-}396}$) that is not known to interact with ALIX demonstrated that it did not colocalize in condensates of ALIX constructs (Fig. 4.4 I–K), establishing that the colocalization of CHMP4 proteins in $ALIX^{Strep}_{1\text{-}868*}$ condensates stems from their specific association with ALIX. Additionally, the two CHMP4 paralogs could simultaneously co-partition inside $ALIX^{Strep}_{1\text{-}868*}$ condensates (Fig.

4.4 L). The latter showed minimal changes in respective fluorescence intensities after 2 h (Fig. 4.4 M), demonstrating that CHMP4 proteins remained confined within these condensates. Thus, we argue that ALIX's ability to phase separate and selectively recruit CHMP4 paralogs will likely be vital contributing factors to the biogenesis and stability of cellular ACBs, explaining prior in vivo observations that showed that depletion of ALIX resulted in ~50% reduction in their volume (11).

Figure 4.4: Colocalization of recombinant CHMP4 paralogs in condensates of ALIX constructs

(A) ALIX and CHMP4 constructs used for co-localization experiments. Each construct is designated by a circled number. The positions of point mutations and the fluorophore conjugation sites are marked. Non-native residues are labeled in purple. Construct representing maltose binding protein ($MBP^{E64C}_{28\text{-}396}$; construct 6) was used as a negative control. **(B)** Primary sequence comparison of the C-terminal portions of CHMP4B and CHMP4C (UniProt entries: Q9H444 and Q96CF2, respectively). Purple asterisks denote the locations of engineered non-native cysteine residues. The unique insert region of CHMP4C (residues 201–218) is marked. Representative microscopy images and fluorescence intensity profiles showing the co-localization (or the lack thereof) of ATTO-647N labeled **(C–E)** $CHMP4C^{S191C}_{121\text{-}233}$, **(F–G)** $CHMP4B^{S184C}_{121\text{-}224}$, and **(I–K)** $MBP^{E64C}_{28\text{-}396}$ in the condensates made by Alexa-Fluor488-labeled ALIX constructs, namely $ALIX^{Strep}_{1\text{-}868*}$ (panels C, F, and I) , $PRD^{Strep}_{703\text{-}868*}$ (panels D, G, and J), and $PRD^{Strep}_{800\text{-}868}$ (panels E, H, and K). Uniform co-partitioning of CHMP4 paralogs in condensates of $ALIX^{Strep}_{1\text{-}868*}$ and $PRD^{Strep}_{703\text{-}868*}$ Strep was observed among all analyzed samples ($n \geq 3$ with ≥ 100 condensates per sample); also see Fig. 4.4.1 for panoramic images showing co-partitioning (or the lack thereof) of CHMP4 paralogs in condensates made by ALIX constructs, Fig. 4.4.2 for images at the respective fluorescent channels of droplets of ALIX-PRD constructs, and Fig. 4.4.3 for colocalization of an extended fragment of CEP55 in $PRD^{Strep}_{703\text{-}868*}$ droplets. **(L)** Representative microscopy images and fluorescence intensity profiles showing the co-localization of ATTO-647N labeled $CHMP4C^{S191C}_{121\text{-}233}$, and ATTO-390 labeled $CHMP4B^{S184C}_{121\text{-}224}$ in freshly prepared condensates of Alexa-Fluor488 labeled $ALIX^{Strep}_{1\text{-}868*}$. **(M)** Microscopy images and intensity profiles of the droplets shown in panel L upon incubation at room temperature for 2 h. White arrows mark the condensates that were used to generate the fluorescence intensity profiles. The individual proteins were first mixed, followed by the addition of 5% (w/v) PEG-4000 to induce phase separation. Experimental and buffer conditions were the same as described in Fig. 4.1.1 caption. Concentrations of ALIX constructs were 50 μM and the partner proteins were at 1 μM.

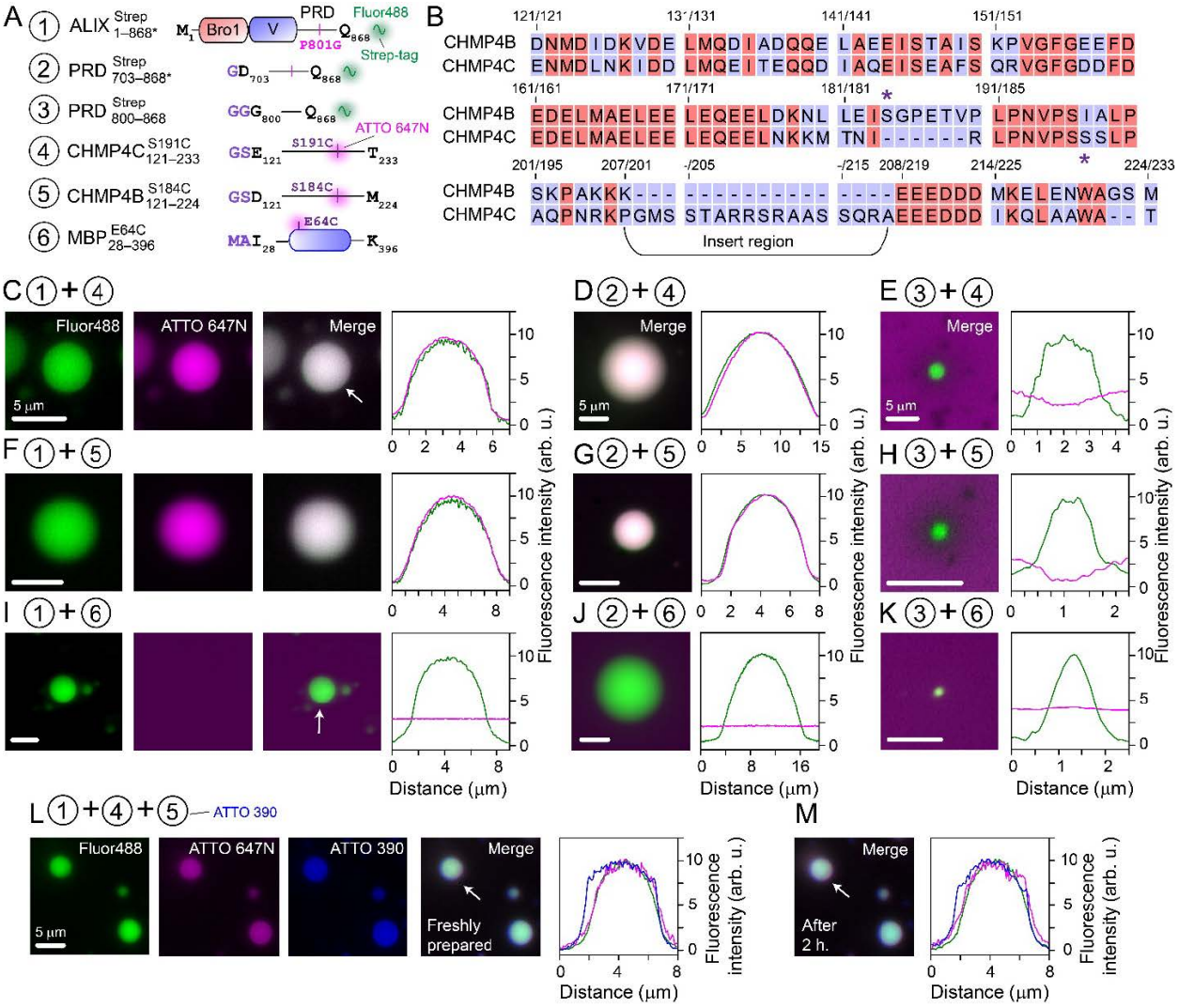
A
1 ALIX Strep 1–868*
2 PRD Strep 703–868*
3 PRD Strep 800–868
4 CHMP4C S191C 121–233
5 CHMP4B S184C 121–224
6 MBP E64C 28–396
Bro1
V
PRD
Fluor488
P801G
Strep-tag
ATTO 647N
B
CHMP4B DNMDIDKVDELMQDIADQQELAEEISTAISKPVGFGEEFD
CHMP4C ENMDLNKIDDLMQEITEQQDIAQEISEAFSQRVGFGDDFD
CHMP4B EDELMAELEELEQEELDKNLLEISGPETVPLPNVPSIALP
CHMP4C EDELMAELEELEQEELNKKMTNI------RLPNVPSSSLP
CHMP4B SKPAKKK---------------EEEDDDMKELENWAGSM
CHMP4C AQPNRKPGMSSTARRSRAASSQRAEEEDDDIKQLAAWA--T
Insert region
C 1+4
D 2+4
E 3+4
F 1+5
G 2+5
H 3+5
I 1+6
J 2+6
K 3+6
Fluor488
ATTO 647N
Merge
5 μm
Fluorescence intensity (arb. u.)
Distance (μm)
L 1+4+5 ATTO 390
ATTO 390
Freshly prepared
M
After 2 h.

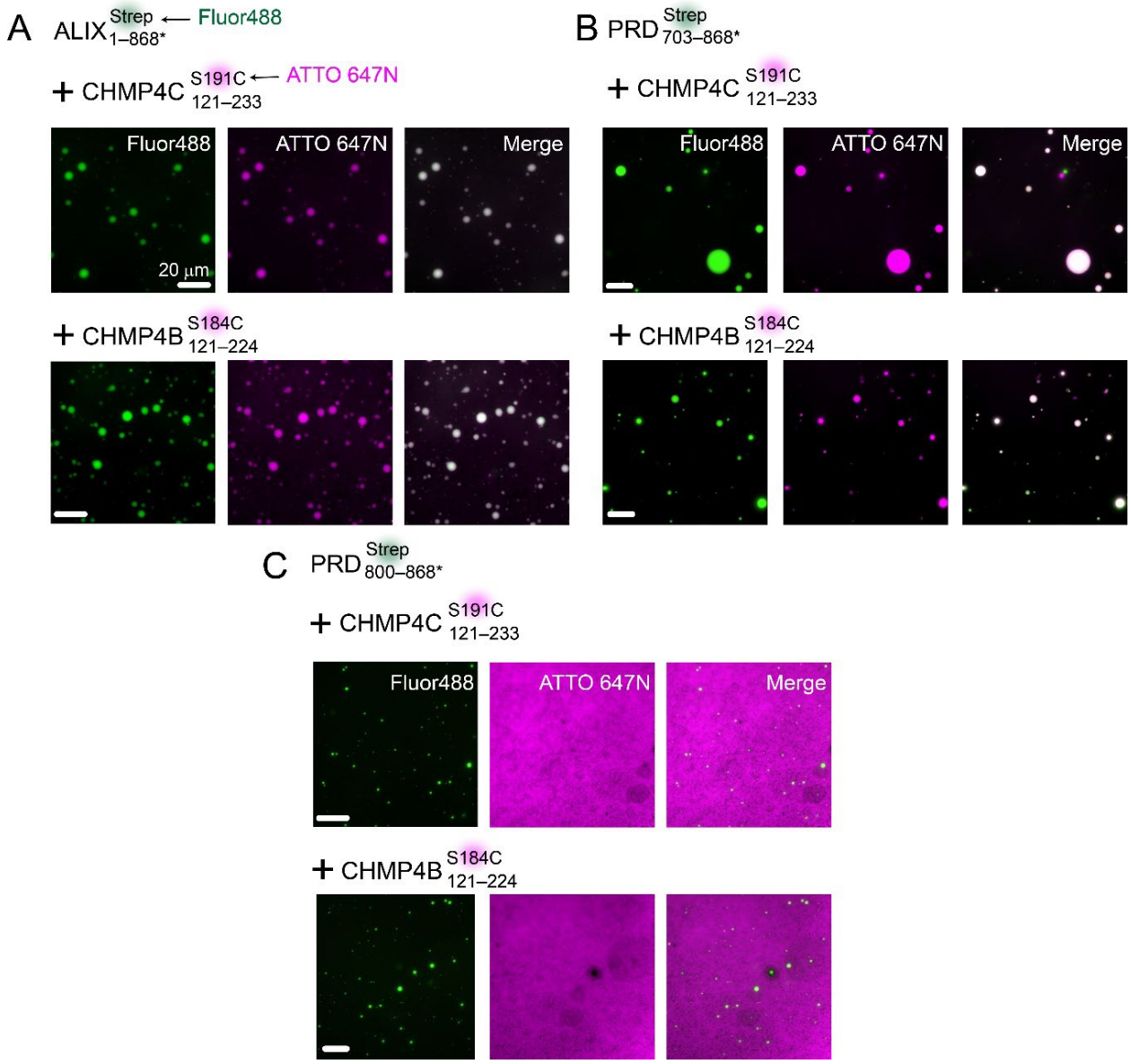

Figure 4.4.1: Panoramic images showing co-partitioning (or the lack thereof) of CHMP4 paralogs in condensates made by ALIX constructs

Representative fluorescence microscopy images showing colocalization of ATTO-647N labeled CHMP4 paralogs, $CHMP4C^{S191C}_{121\text{-}233}$ and $CHMP4B^{S184C}_{121\text{-}224}$, in Alexa-Fluor488-labeled droplets of **(A)** $ALIX^{Strep}_{1\text{-}868*}$, **(B)** $PRD^{Strep}_{703\text{-}868*}$, and a lack of their colocalization in Alexa-Fluor488-labeled $PRD^{Strep}_{800\text{-}868}$ droplets **(C)**. Colocalization or lack thereof of CHMP4 paralogs was verified over $n \geq 3$ replicates ($\geq$ 100 condensates per sample).

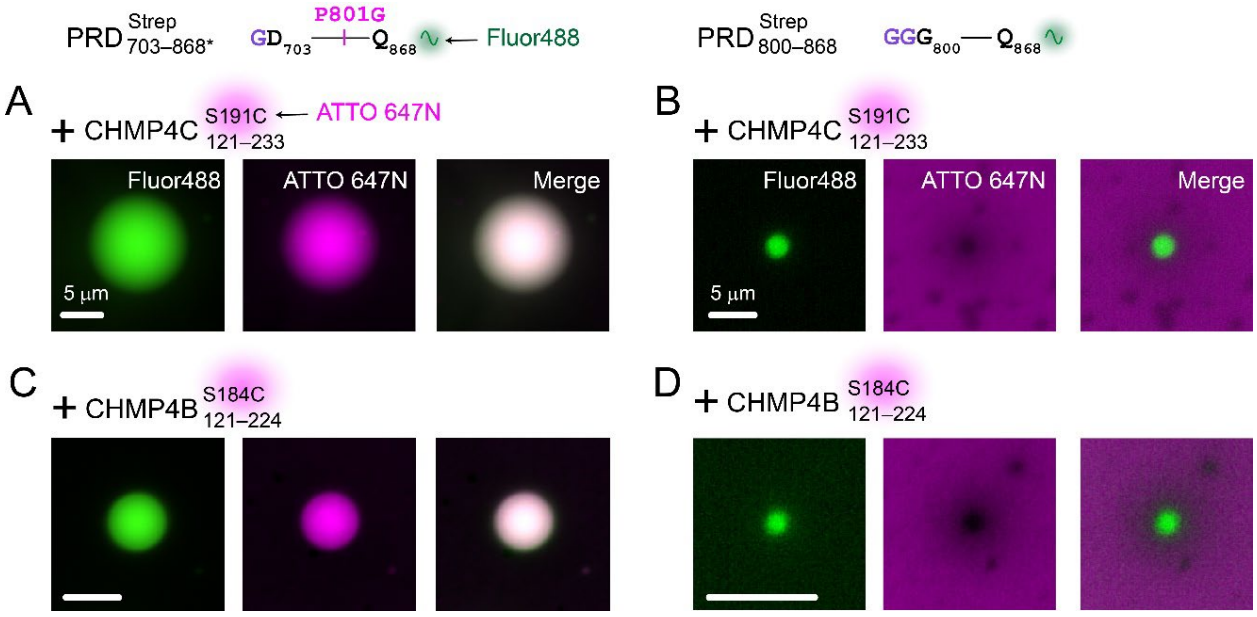

Figure 4.4.2: Co-partitioning of CHMP4 paralogs in condensates made by ALIX-PRD constructs

Representative fluorescence microscopy images showing colocalization of ATTO- 647N labeled CHMP4 paralogs, $CHMP4C^{S191C}_{121-233}$ and $CHMP4B^{S184C}_{121-224}$, in Alexa-Fluor488-labeled $PRD^{Strep}_{703-868*}$ droplets **(A and C)**, and a lack of their colocalization in Alexa-Fluor488- labeled $PRD^{Strep}_{800-868}$ droplets **(B and D)**.

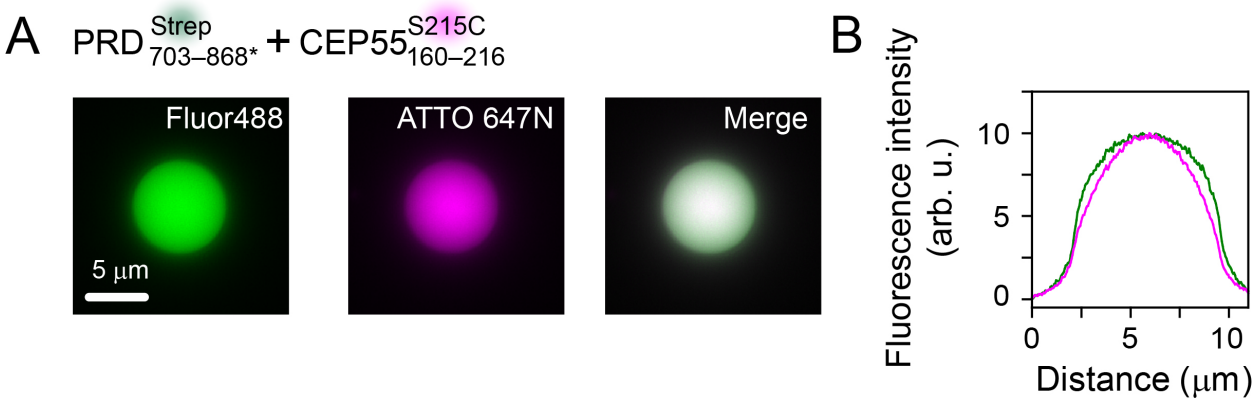

Figure 4.4.3: Co-partitioning of CEP55 in $PRD^{Strep}_{703-868*}$ condensates

(A) Representative fluorescence microscopy images showing colocalization of $CEP55^{S215C}_{160-216}$ in $PRD^{Strep}_{703-868*}$ droplets. **(B)** Corresponding fluorescence intensity profiles. The binding interface between the two proteins was mapped by X-ray crystallography [PDB entry: 3E1R (25)] and comprises residues 178–195 of CEP55 and 797–808 of ALIX-PRD. A ready colocalization of $CEP55^{S215C}_{160-216}$ in $PRD^{Strep}_{703-868*}$ droplets, indicates that P801G mutation did not interfere with these interactions.

4.5 NMR analysis of ALIX-CHMP4 interactions

To investigate ALIX–CHMP4 interactions, NMR titration experiments were performed where 3-molar equivalents of unlabeled $CHMP4C^{S191C}_{121\text{-}233}$ or $CHMP4B^{S184C}_{121\text{-}224}$ were added to $^{15}N/^{2}H$-labeled Bro1; corresponding experiments using $ALIX^{Strep}_{1\text{-}868*}$ were not feasible owing to its large molecular size (~100 kDa), which resulted in severe line broadening. Using NMR spectroscopy, we previously established that Bro1 retains its fold in solution (23). On the addition of CHMP4 proteins, large $^{1}H_N/^{15}N$ chemical-shift perturbations [$\Delta_{H/N}$ ~0.05–0.47 parts per million (ppm)] were observed for residues 54–72, 135–156, 201–227, and 333–349 of Bro1 (Fig. 4.5 A and Fig. 4.5.1). Fig. 4.5 B maps these perturbations onto the X-ray structure of the Bro1–CHMP4C peptide complex (10). Although the CHMP4C constructs used for these two studies were different, extended fragment for NMR (residues 121–233) vs. a peptide analog for X-ray (residues 221–233), there was an excellent agreement between their results as most chemical shift perturbations were localized in and around the X-ray binding interface between Bro1 and the CHMP4C peptide. However, two Bro1 regions that showed large perturbations with $CHMP4C^{S191C}_{121\text{-}233}$ (residues 54–72 and 347–349) were located ~15–25 Å away from the C-terminus of the CHMP4C peptide (cf. Fig. 4.5 B). These observations suggest that in addition to the binding site comprising the extreme C-terminal CHMP4C motif (residues 221–233), Bro1 binds to additional motif(s) present in residues 121–220 of $CHMP4C^{S191C}_{121\text{-}233}$. Because $^{1}H_N/^{15}N$ chemical shift perturbations in Bro1 resonances upon the addition of $CHMP4B^{S184C}_{121\text{-}224}$ were similar to those obtained using $CHMP4C^{S191C}_{121\text{-}233}$ (cf. Fig. 4.5 A) and since the C-terminal motifs of CHMP4B (residues 207–224) and CHMP4C (residues 221–233) bind to the same Bro1 site as determined by X-ray crystallography (3), we conclude that Bro1 also binds to additional motif(s) localized in residues 121–206 of $CHMP4B^{S184C}_{121\text{-}224}$.

To uncover the existence of interactions between the N-terminal portion of ALIX-PRD (residues 703–800) and CHMP4 paralogs, as suggested by our microscopy results (cf. Fig. 4.4 C–H), we performed titration experiments using unlabeled CHMP4 proteins and NMR-visible $PRD^{Strep}_{703\text{-}800}$. This region of ALIX-PRD is unstructured in its free form (22). The addition of 3-molar equivalent of $CHMP4C^{S191C}_{121\text{-}233}$ or $CHMP4B^{S184C}_{121\text{-}224}$ resulted in small but noticeable $^{1}H_N/^{15}N$ and $^{13}C'/^{15}N$ chemical shift changes in $PRD^{Strep}_{703\text{-}800}$ resonances, $\Delta_{H/N}$ and $\Delta_{C'/N}$ of 0.01–0.04 and 0.01–0.03 ppm, respectively (Fig. 4.5 C and Figs. 4.5.2–4.5.3). The affected PRD region encompassed residues 734–768, which overlaps with Src-kinase binding site on PRD [residues 752–757, cf. Fig. 4.1.1 A (19)]. This motif is highly basic owing to multiple arginine residues [theoretical isoelectric point (31), pI, ~12]. In contrast, both CHMP4 proteins used in this work are anionic (theoretical pI: 4–5). Since NMR experiments were performed at pH 6.5 (Methods), $PRD^{Strep}_{703\text{-}800}$ likely binds to CHMP4 proteins via electrostatic interactions. Because the $^{1}H_N/^{15}N$ chemical shift changes observed for $PRD^{Strep}_{703\text{-}800}$–CHMP4 interactions were smaller than those observed for Bro1–CHMP4 interactions, we conclude that the binding between $PRD^{Strep}_{703\text{-}800}$ and CHMP4 paralogs is weaker than Bro1–CHMP4 association, and that CHMP4-bound $PRD^{Strep}_{703\text{-}800}$ remains disordered. Altogether, NMR titration experiments uncovered the existence of additional interactions between ALIX domains (Bro1 and PRD) and CHMP4 constructs.

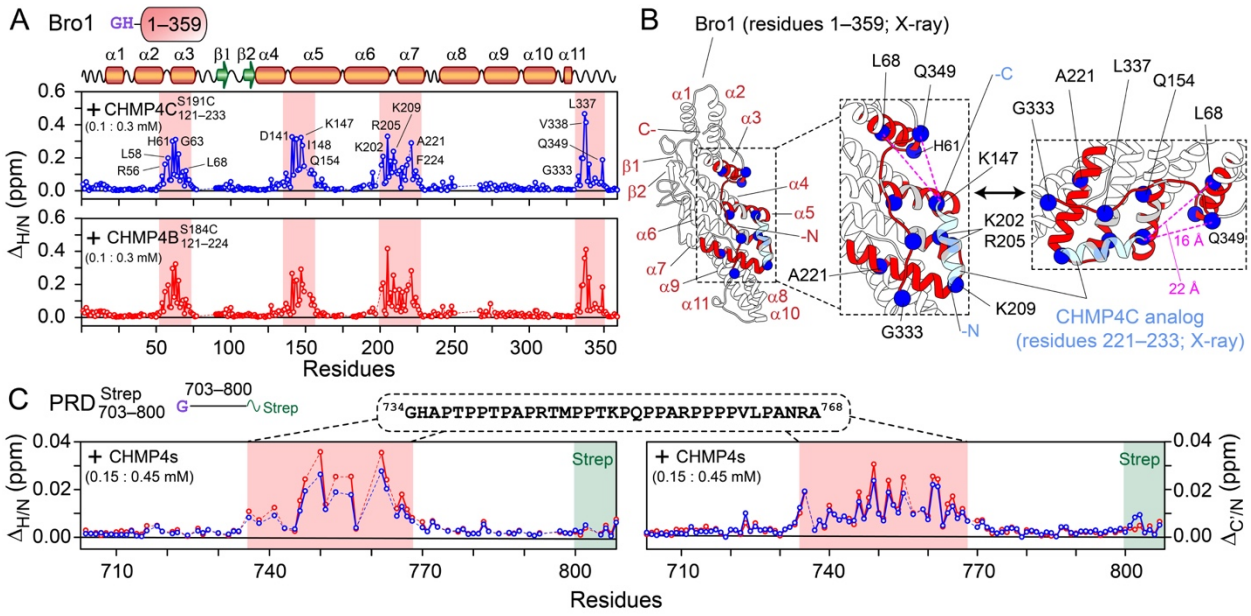

Figure 4.5: NMR analysis of ALIX-CHMP4 interactions

(A) $^{1}H_N/^{15}N$ chemical shift perturbation profiles of 100 μM $^{15}N/^{2}H$-labeled Bro1 on addition of 300 μM unlabeled CHMP4 constructs; $CHMP4C^{S191C}_{121-233}$ (upper; blue) and $CHMP4B^{S184C}_{121-224}$ (lower; red). Secondary structure elements are indicated above the panel. Red rectangles indicate regions that exhibit large chemical shift perturbations, a few of the affected residues are labeled. Dashed lines indicate proline residues or residues that could not be assigned unambiguously. **(B)** Ribbon diagram of the X-ray structure of the complex between Bro1 (white ribbons) and CHMP4C peptide analog [light blue ribbons] (10). Bro1 motifs that undergo large chemical shift changes in the presence of $CHMP4C^{S191C}_{121-233}$ (panel A, upper) are marked in red ribbons. A few affected residues are depicted by blue spheres. Gray ribbons indicate residues around the interaction site that could not be assigned unambiguously. Dashed magenta lines mark the distances between two representative Bro1 residues (L68 and Q349) and the C-terminus of the CHMP4C peptide analog. **(C)** $^{1}H_N/^{15}N$ and $^{13}C'/^{15}N$ chemical shift perturbation profiles of 150 μM $^{15}N/^{13}C$-labeled $PRD^{Strep}_{703-800}$ in the presence of 450 μM unlabeled CHMP4 constructs, the same color scheme as panel A. The primary sequence of the affected region (residues 734–768), marked by semitransparent red rectangles, is shown above the graphs. The position of the C-terminal Strep tag (residues 801–808) is denoted by semitransparent gray rectangles. All NMR experiments were performed at 30 ºC in 20 mM sodium phosphate, pH 6.5, 1 mM TCEP, and 2 mM EDTA at a spectrometer ^{1}H frequency of 800 MHz.

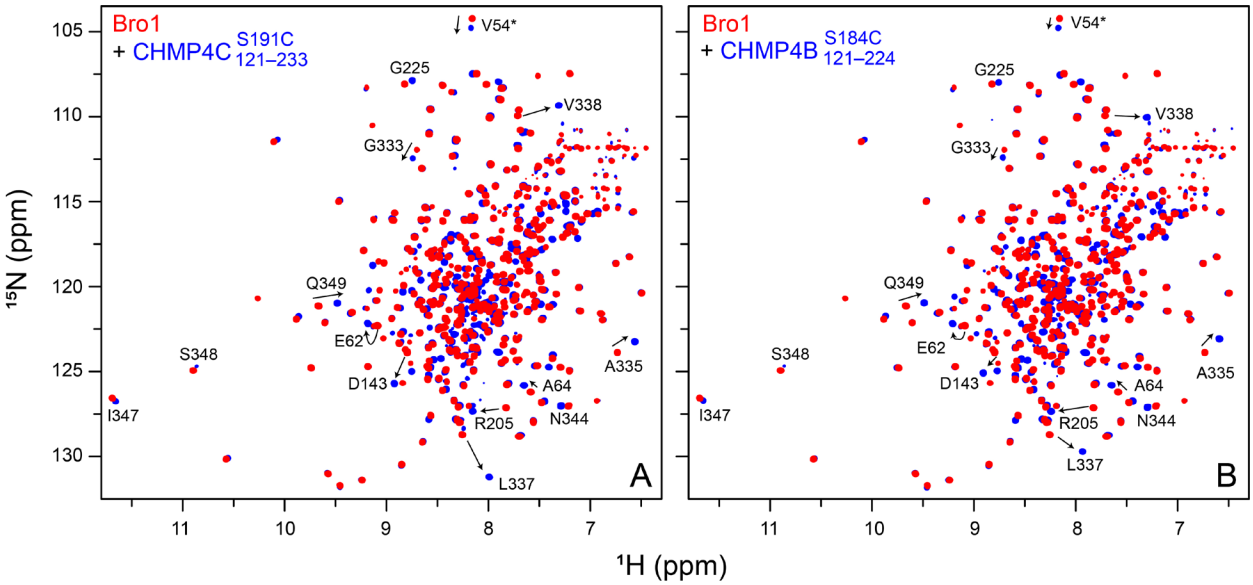

Figure 4.5.1: NMR analysis of interactions between ALIX-Bro1 and CHMP4 paralogs

Overlay of expanded region of the ^{1}H-^{15}N TROSY-HSQC correlation spectra of $^{15}N/^{2}H$-labeled 100 µM Bro1 in the absence (red) and presence (blue) of 300 µM CHMP4 paralogs, namely **(A)** $CHMP4C^{S191C}_{121-233}$ and **(B)** $CHMP4B^{S184C}_{121-224}$. Some isolated cross-peaks of Bro1 that exhibit changes in chemical shifts upon addition of CHMP4 paralogs are labeled. Folded cross-peaks of residue V54 are marked by asterisks. Buffer and experimental conditions were as follows: 20 mM sodium phosphate, pH 6.5, 1 mM TCEP, and 2 mM EDTA at 30 ºC.

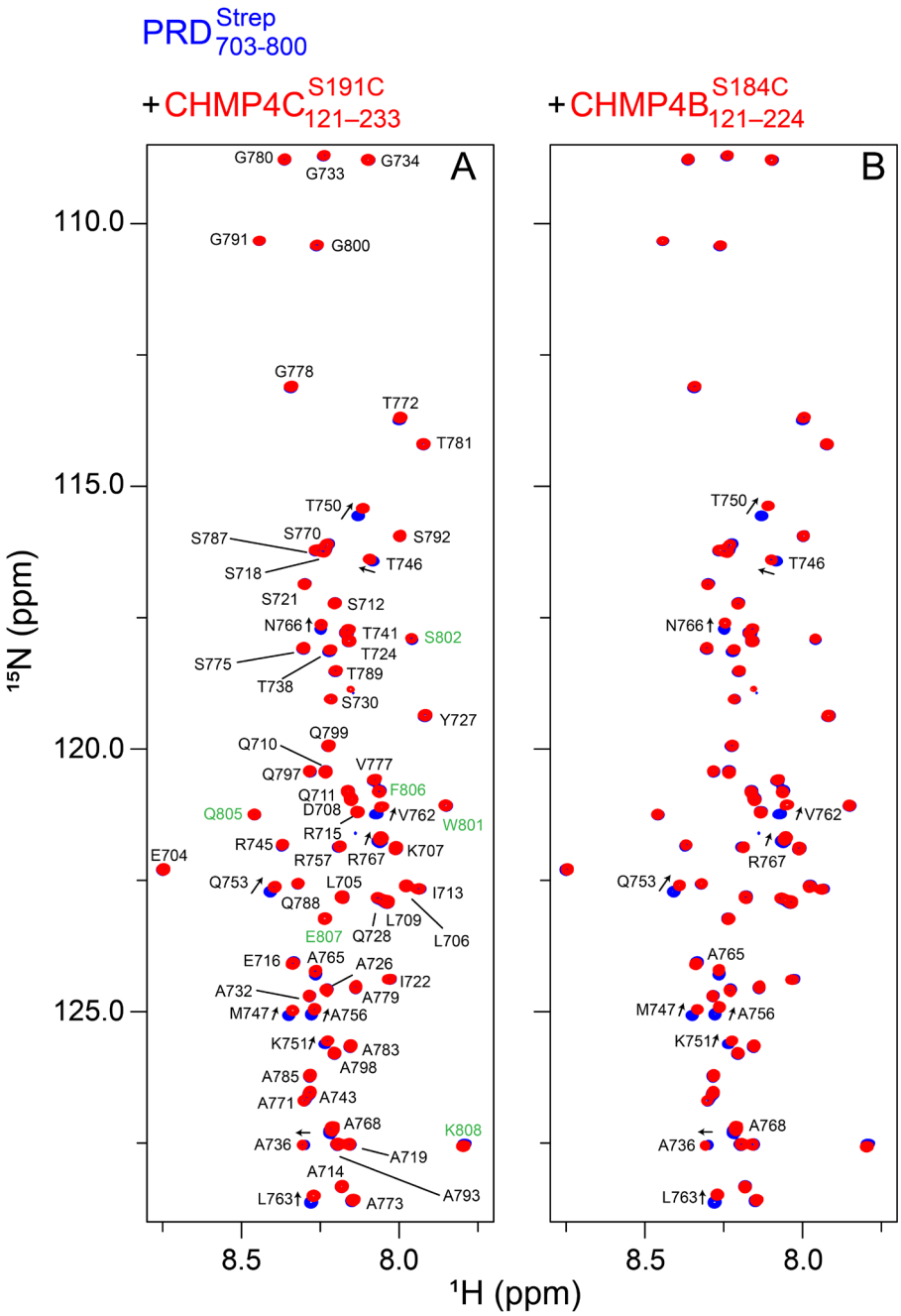

Figure 4.5.2: NMR analysis of interactions between $PRD^{Strep}_{703-800}$ and CHMP4 paralogs.

Overlay of expanded region of the ^{1}H-^{15}N TROSY-HSQC correlation spectra of $^{15}N/^{13}C$-labeled 150 µM $PRD^{Strep}_{703-800}$ in the absence (blue) and presence (red) of 450 µM CHMP4 paralogs, namely **(A)** $CHMP4C^{S191C}_{121-233}$ and **(B)** $CHMP4B^{S184C}_{121-224}$. Assignments of each cross-peaks are shown in panel A. Cross-peaks of the residues that undergo chemical shift changes upon addition of CHMP4 constructs are marked by arrows. Non-native residues of the C-terminal Strep tag are labeled in 15 green. Buffer and experimental conditions were as follows: 20 mM sodium phosphate, pH 6.5, 1 mM TCEP, and 2 mM EDTA at 30 ºC.

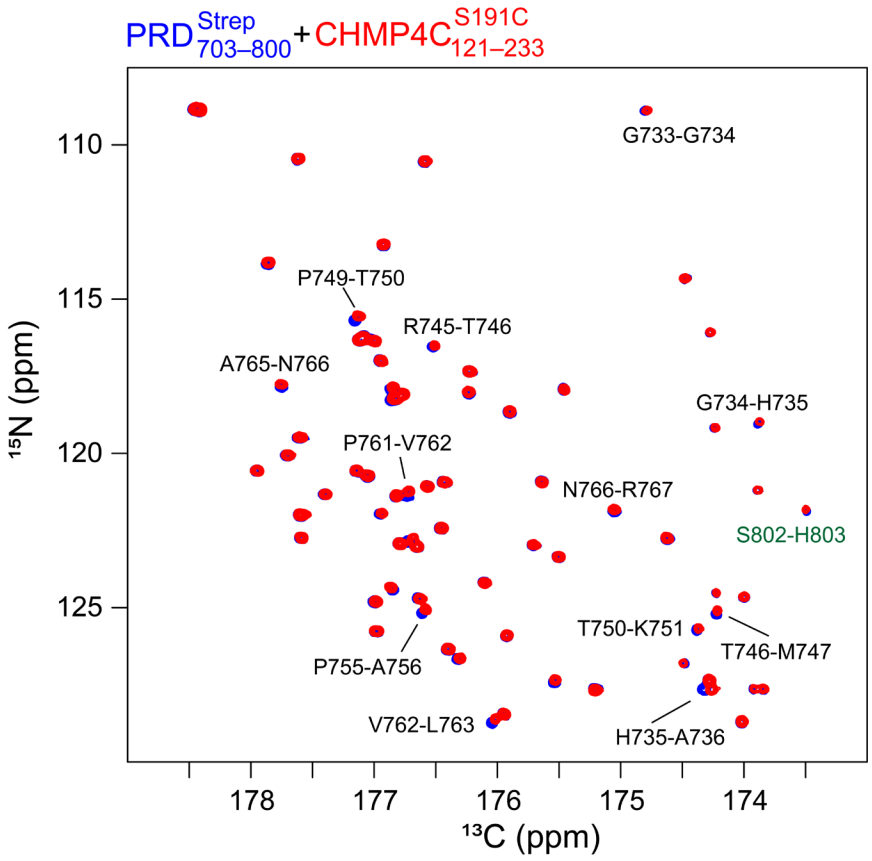

Figure 4.5.3: NMR analysis of interactions between $PRD^{Strep}_{703-800}$ and $CHMP4C^{S191C}_{121-233}$

Overlay of expanded region of the ^{13}C-^{15}N CON correlation spectra of $^{15}N/^{13}C$-labeled 150 µM $PRD^{Strep}_{703-800}$ in the absence (blue) and presence (red) of 450 µM $CHMP4C^{S191C}_{121-233}$. Note that the above-mentioned concentrations were chosen because of the following: (1) poor sensitivity of the carbon-detected ^{13}C-^{15}N CON experiment as compared to its proton-detected counterpart (69); and (2) the addition of > 450 µM CHMP4 paralogs to 150 µM $PRD^{Strep}_{703-800}$ led to sample precipitation. Cross-peaks of the residues that undergo chemical shift changes upon addition of $CHMP4C^{S191C}_{121-233}$ are marked. Cross-peaks of non-native residues of the C-terminal strep tag are labeled in green. Buffer and experimental conditions were as follows: 20 mM sodium phosphate, pH 6.5, 1 mM TCEP, and 2 mM EDTA at 30 °C.

4.6 Conformation and dynamics of CHMP4 paralogs in solution

To further explore interactions between CHMP4 paralogs and ALIX, we first analyzed CHMP4C$^{S191C}_{121-233}$ and CHMP4B$^{S184C}_{121-224}$ in their free forms. The structures of CHMP4 paralogs are not available as they are refractory to crystallography. Based on the structures of homologs, sequence-based and AlphaFold predictions, the CHMP4 paralogs are suggested to comprise six helices (α1–α6, Fig. 4.6 A and Fig. 4.6.1), with α1–α3 spanning their filament-forming N-terminal core domains (residues 1–120), and α4–α6 localized in their C-terminal tails (2, 4, 32-34). Cytosolic CHMP4 proteins are hypothesized to be in a closed conformation, because of intramolecular interactions between α5 and α1–α2. In the presence of activation factors (e.g., ALIX), CHMP4 paralogs likely undergo a conformational rearrangement, involving the dissociation of α5 from α1–α2, followed by merging α2 with α3, and a reorganization of their C-termini, triggering their subsequent polymerization. Surprisingly, far-ultraviolet (UV) circular dichroism (CD) spectra of CHMP4C$^{S191C}_{121-233}$ and CHMP4B$^{S184C}_{121-224}$ showed that both were largely disordered (Fig. 4.6 B). However, a slight dip at ~222 nm UV wavelength indicated that CHMP4C$^{S191C}_{121-233}$ exhibited a greater helical propensity than CHMP4B$^{S184C}_{121-224}$. These results were confirmed by AUC experiments (Fig. 4.6 C), which established that these two constructs yielded notably different best-fit frictional ratios (1.8 and 2.3 for CHMP4C$^{S191C}_{121-233}$ and CHMP4B$^{S184C}_{121-224}$, respectively), despite being different by only ~1 kDa. Consequently, both proteins were monomeric, with no indication of self-association, and although both were largely disordered, CHMP4C$^{S191C}_{121-233}$ exhibited a more compact conformation than CHMP4B$^{S184C}_{121-224}$.

Both CHMP4C$^{S191C}_{121-233}$ and CHMP4B$^{S184C}_{121-224}$ yielded high-quality ^{1}H-^{15}N transverse relaxation optimized spectroscopy–heteronuclear single quantum coherence (TROSY-HSQC) spectra and a narrow dispersion of chemical shifts of their backbone amide proton resonances (7.5–

8.8 ppm) indicated disordered conformations (Fig. 4.6.2). To further explore their conformational propensities, we recorded backbone chemical shifts, $^{3}J_{HN\text{-}H\alpha}$ couplings, and ^{15}N-transverse relaxation rates (R_2). Secondary chemical shifts ($\Delta\delta$), the differences between experimental and the corresponding predicted random-coil values (35, 36), are shown in Fig. 4.6.3. The region between residues 163–179 of CHMP4C$^{S191C}_{121\text{-}233}$ that corresponds to the predicted α5 motif in full-length CHMP4C exhibited elevated $\Delta\delta(^{13}C\alpha)$ values (0.5–1.5 ppm), indicating a stable helical conformation in this region; $\Delta\delta(^{13}C\alpha)$ values are the best reporters of local secondary structure. In contrast, $\Delta\delta(^{13}C\alpha)$ values of CHMP4B$^{S184C}_{121\text{-}224}$ were evenly distributed ~0 ppm, indicative of a random-coil conformation. To further examine these conformational differences, the secondary structures of CHMP4C$^{S191C}_{121\text{-}233}$ and CHMP4B$^{S184C}_{121\text{-}224}$ were determined from experimental backbone chemical shifts using TALOS-N (37); Fig. 4.6 D–E, upper. The helical propensity for residues 163–179 of CHMP4C$^{S191C}_{121\text{-}233}$ ranged between 0.6–0.96, confirming a stable helix in this region. In contrast, the helical propensity of residues 163–181 in CHMP4B$^{S184C}_{121\text{-}224}$ was 0.13–0.49, indicative of a transient helical character, even though the primary sequence of this region is nearly identical to that of CHMP4C$^{S191C}_{121\text{-}233}$ (cf. Fig. 4.4 B); helical propensities of residues 177–179 were 0.13–0.22, suggesting a possible bend at this location. These observations were complemented by experimental $^{3}J_{HN\text{-}H\alpha}$ couplings (Fig. 4.6 D, middle), which showed largely helical values ranging between 3.5–5.5 Hz for residues 161–178 of CHMP4C$^{S191C}_{121\text{-}233}$ that deviated considerably from the corresponding random coil values (~7 Hz) predicted using nearest-neighbor effects (38). Additionally, the ^{15}N-R_2 values of residues 159–182, measured at 800 MHz at 30 °C, were uniformly elevated (6–8 s-1; Fig. 4.6 D, lower), which established an ordered conformation of this motif. In contrast, residues 163–181 of CHMP4B$^{S184C}_{121\text{-}224}$ exhibited non-helical $^{3}J_{HN\text{-}H\alpha}$ couplings (~7 Hz), and slightly elevated ^{15}N-R_2 values (2–4 s^{-1}), indicating a lack of stable helical

configuration (Fig. 4.6 E). Residues 130–133 and 140–143 (α4), 207–209 (insert), and 225–230 (α6) of $CHMP4C^{S191C}_{121\text{-}233}$ exhibited helical propensities ranging between 0.25–0.56 (Fig. 4.6 D, upper), indicating that these motifs possess lower propensities for spontaneous helix formation than the region between residues 163–179 (α5); the labels in parentheses denote the corresponding proposed regions in full-length CHMP4C. Most notable among these were a few residues of the insert region of $CHMP4C^{S191C}_{121\text{-}233}$ that showed helical $^{3}J_{HN\text{-}H\alpha}$ couplings (~5 Hz, Fig. 4.6 D, middle), slightly elevated $^{15}N\text{-}R_2$ values (~4 s-1, Fig. 4.6 D, lower) and $\Delta\delta(^{13}C\alpha)$ shifts (~0.3 ppm, Fig. 4.6.3 A), indicating a partially ordered helix. This insert is highly basic owing to the presence of multiple arginine residues (theoretical pI ~12.5). It therefore may transiently interact with other acidic motifs of $CHMP4C^{S191C}_{121\text{-}233}$, e.g., residues 163–179 (theoretical pI ~3.7), stabilizing their conformation, and that the absence of this insert in $CHMP4B^{S184C}_{121\text{-}224}$ may result in a lack of a stable helix in the region between residues 163–181. To confirm these long-range contacts, we performed intramolecular paramagnetic relaxation enhancement (PRE) experiments (39-41) on two CHMP4C mutants, $CHMP4C^{G154C}_{121\text{-}233}$ and $CHMP4C^{M165C}_{121\text{-}233}$ (Fig. 4.6 F and Fig. 4.6.4). The attachment of a paramagnetic nitroxide spin label, (1-oxyl-2,2,5,5-tetramethyl-Δ3-pyrroline-3-methyl) methanethiosulfonate [MTSL], at individual residues C154 and C165 resulted in local signal attenuation and a notable attenuation in the $^{1}H_N/^{15}N$ cross-peaks of residues 200–212, confirming the transient long-range interactions between the acidic residues encompassing the α5 motif of CHMP4C and the basic residues of its insert. These findings are consistent with our AUC data (cf. Fig. 4.6 C), which showed that among the two CHMP4 paralogs, CHMP4C is more compact. For $CHMP4B^{S184C}_{121\text{-}224}$, in addition to the motif 163–181 (α5), residues 129–133 (α4) and 217–217 (α6) showed helical propensities ranging between 0.25–0.5 (Fig. 4.6 E, upper), indicating transient helices. Thus, both CHMP4 paralogs tested here are largely disordered with residual

helical propensities (Fig. 4.6 G), apart from the α5 motif of CHMP4C that forms a stable helix and the presence of transient long-range interactions between the basic residues of its insert and acidic residues in and around its α5 motif. Disordered proteins or regions are vital signaling hubs as their lack of structure facilitates dynamic protein–protein interactions of modest affinity but high specificity (42, 43). We argue that disordered C-terminal tails of CHMP4 paralogs will provide multiple interaction motifs and facilitate the formation of metastable CHMP4 filaments essential for membrane scission.

Figure 4.6: Conformation and dynamics of CHMP4 paralogs in solution

(A) Hypothetical models of inactive and active conformations of full-length CHMP4 paralogs (2, 4, 31, 32), originally described by Vietri et al (2); MIM = MIT interacting motif, which binds to the MIT domain containing proteins [e.g., VPS4] (62), MIR = membrane insertion region. Helix α5 (pink) is likely responsible for the autoinhibition of CHMP4 paralogs. **(B)** Far-UV CD spectra with the solid line and shaded region representing the mean and SD, respectively (5 scans) and **(C)** absorbance sedimentation c(*s*) profiles of $CHMP4C^{S191C}_{121-233}$ (blue), and $CHMP4B^{S184C}_{121-224}$ (red). Arrow points to the dip at ~222 nm in the CD spectrum of $CHMP4C^{S191C}_{121-233}$. The concentrations of proteins were ~10 and ~40 μM for CD and AUC, respectively. NMR analysis of **(D)** $CHMP4C^{S191C}_{121-233}$ and **(E)** $CHMP4B^{S184C}_{121-224}$, including TALOS-N derived helical propensities obtained from the assigned backbone chemical shifts (upper), a comparison between experimental $^{3}J_{HN-H\alpha}$ scalar couplings against random coil values (middle), and $^{15}N\text{-}R_2$ profiles measured at 30 ºC (also see Table 4.1). Unlike $CHMP4B^{S184C}_{121-224}$, $CHMP4C^{S191C}_{121-233}$ showed greater helical propensity for residues 163–179; highlighted by semitransparent magenta rectangle. The corresponding drop in $^{3}J_{HN-H\alpha}$ couplings and elevated $^{15}N\text{-}R_2$ values of this region confirmed the presence of a stable helix. The unique insert region of $CHMP4C^{S191C}_{121-233}$ (cf. Fig. 4.4 B) exhibited deviation from random coil $^{3}J_{HN-H\alpha}$ couplings and elevated $^{15}N\text{-}R_2$ values (highlighted by semitransparent magenta rectangles), indicating a residual helical structure. Additionally, residues of the regions showing elevated TALOS-N derived helical propensities (ranging between 0.25–0.56), indicating transient helical structures, are labeled. **(F)** Evidence of transient long-range interactions in CHMP4C paralog using experimental PRE profiles of $CHMP4C^{G154C}_{121-233}$ (upper) and $CHMP4C^{M165C}_{121-233}$ (lower). The locations of paramagnetic label, MTSL, are marked with dashed vertical lines. **(G)** Schematic of $CHMP4C^{S191C}_{121-233}$ (blue), and $CHMP4B^{S184C}_{121-224}$ (red) based on NMR results. Transient and stable helices are depicted as gray and magenta cylinders, respectively; numbers denote the corresponding residues. The positions of CHMP4 helices, based on the proposed models of full-length proteins (cf. panel A), are in parentheses.

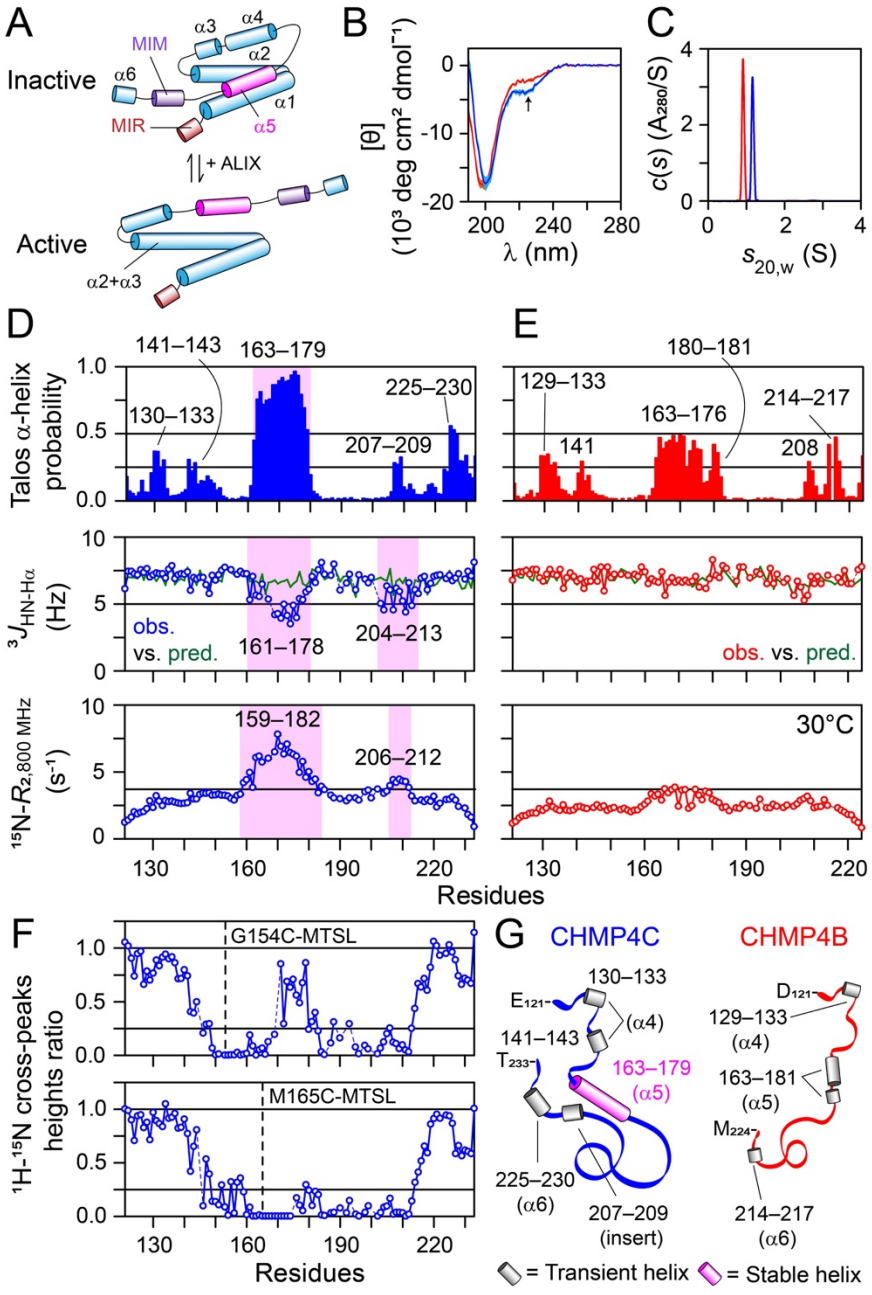
A
Inactive
α3
α4
MIM
α2
α6
α1
MIR
α5
+ ALIX
Active
α2+α3
B
[θ] (10³ deg cm² dmol⁻¹)
λ (nm)
C
c(s) (A280/S)
s20,w (S)
D
Talos α-helix probability
141–143
163–179
225–230
130–133
207–209
3JHN-Hα (Hz)
obs. vs. pred.
161–178
204–213
15N-R2,800 MHz (s-1)
159–182
206–212
E
180–181
129–133
163–176
214–217
141
208
obs. vs. pred.
30°C
Residues
F
1H-15N cross-peaks heights ratio
G154C-MTSL
M165C-MTSL
Residues
G
CHMP4C
CHMP4B
130–133
E121
(α4)
141–143
T233
163–179
(α5)
225–230
(α6)
207–209
(insert)
D121
129–133
(α4)
163–181
(α5)
M224
214–217
(α6)
= Transient helix
= Stable helix

Table 4.1: Residue-specific NMR parameters of CHMP4 fragments in free form

All NMR data were acquired at 30 °C in buffer containing 20 mM sodium phosphate, pH 6.5, 1 mM TCEP, and 2 mM EDTA. Helical propensities (α prop.) were calculated using Talos-N (37) from assigned backbone chemical shifts, namely $^{13}C\alpha$, $^{13}C\beta$, $^{13}C'$, ^{15}N, and $^{1}H_N$. Experimental $^{3}J_{HN\text{-}H\alpha}$ couplings were measured using WATERGATE-optimized 2D TROSY pulse sequence (67). Corresponding random coil values were predicted using the nearest-neighbor effects corrected for temperature (38). Experimental $^{3}J_{HN\text{-}H\alpha}$ couplings of overlapped residues and glycines were not considered. ^{15}N $R_1\rho$ measurements were carried out at 800 MHz on 0.5 mM proteins. Overlapped residues or residues that undergo resonance broadening due to rapid exchange were not considered.

$CHMP4C^{S191C}_{121\text{-}233}$					$CHMP4B^{S184C}_{121\text{-}224}$				
Res.	α prop.	$^{3}J_{HN\text{-}H\alpha}$ Pred.	$^{3}J_{HN\text{-}H\alpha}$ Exp.	$^{15}N\text{-}R_2$ (s^{-1})	Res.	α prop.	$^{3}J_{HN\text{-}H\alpha}$ Pred.	$^{3}J_{HN\text{-}H\alpha}$ Exp.	$^{15}N\text{-}R_2$ (s^{-1})
E121	0.178	6.591	6.138	1.229 ± 0.036	D121	0.128	6.926	6.778	1.147 ± 0.037
N122	0.072	7.037	7.426	1.392 ± 0.041	N122	0.032	7.214	7.306	1.288 ± 0.042
M123	0.054	6.988	7.426	1.613 ± 0.044	M123	0.015	6.988	7.394	1.553 ± 0.037
D124	0.035	6.989	7.258	2.010 ± 0.033	D124	0.027	6.972	7.394	1.705 ± 0.029
L125	0.063	6.902	7.178	1.858 ± 0.021	I125	0.047	7.764	7.482	1.724 ± 0.019
N126	0.151	7.418	7.554	1.975 ± 0.036	D126	0.076	6.897	7.218	1.884 ± 0.022
K127	0.065	6.802	7.346	2.027 ± 0.029	K127	0.025	6.742	7.57	1.926 ± 0.020
I128	0.062	7.528	7.634	2.251 ± 0.020	V128	0.056	7.661	7.57	1.906 ± 0.017
D129	0.206	7.181	7.01	2.828 ± 0.025	D129	0.335	6.927	6.954	2.253 ± 0.023
D130	0.368	7.042	7.178	2.322 ± 0.026	E130	0.331	6.707	6.69	2.112 ± 0.012
L131	0.366	6.727	7.306	3.205 ± 0.028	L131	0.346	6.55	7.218	2.290 ± 0.022
M132	0.247	7.07	7.258	2.801 ± 0.024	M132	0.263	7.07	7.57	2.811 ± 0.022
Q133	0.303	6.958	7.258	2.464 ± 0.031	Q133	0.282	7.101	7.218	2.397 ± 0.022
E134	0.09	6.429	6.93	2.846 ± 0.021	D134	0.179	6.764	7.13	2.218 ± 0.032
I135	0.032	7.441	7.594	2.771 ± 0.022	I135	0.084	7.722	7.57	2.115 ± 0.019
T136	0.038	7.747	7.842	2.816 ± 0.032	A136	0.075	6.119	6.154	2.525 ± 0.026
E137	0.041	6.498	6.89	2.726 ± 0.031	D137	0.046	6.746	6.954	2.140 ± 0.034
Q138	0.046	6.781	7.178	2.665 ± 0.033	Q138	0.034	6.958	7.306	2.094 ± 0.027
Q139	0.063	6.893	7.258	2.632 ± 0.026	Q139	0.071	6.75	7.042	2.149 ± 0.030
D140	0.083	6.764	7.218	2.656 ± 0.024	E140	0.204	6.446	6.69	2.366 ± 0.025
I141	0.306	7.722	7.386	2.693 ± 0.024	L141	0.293	6.771	6.866	2.405 ± 0.020
A142	0.22	5.923	6.01	3.391 ± 0.021	A142	0.146	6.057	6.154	2.312 ± 0.022
Q143	0.283	6.916	6.97	2.977 ± 0.034	E143	0.186	6.464	6.69	2.248 ± 0.030
E144	0.122	6.429	6.842	2.979 ± 0.026	E144	0.07	6.513	6.69	–
I145	0.149	7.517	6.97	3.304 ± 0.025	I145	0.051	7.517	7.57	2.323 ± 0.023
S146	0.143	6.957	6.97	3.417 ± 0.035	S146	0.038	6.954	6.69	2.540 ± 0.042
E147	0.182	6.59	6.426	3.384 ± 0.034	T147	0.038	7.634	7.746	2.326 ± 0.043
A148	0.153	6.091	5.762	3.423 ± 0.037	A148	0.026	5.955	5.978	2.449 ± 0.033
F149	0.129	7.208	7.138	3.256 ± 0.030	I149	0.017	7.599	7.746	2.114 ± 0.030

Table 4.1: Residue-specific NMR parameters of CHMP4 fragments in free form (continued)

$CHMP4C^{S191C}_{121-233}$					$CHMP4B^{S184C}_{121-224}$				
Res.	α prop.	$^3J_{HN-H\alpha}$ Pred.	$^3J_{HN-H\alpha}$ Exp.	^{15}N-R_2 (s^{-1})	Res.	α prop.	$^3J_{HN-H\alpha}$ Pred.	$^3J_{HN-H\alpha}$ Exp.	^{15}N-R_2 (s^{-1})
S150	0.08	7.146	6.762	3.261 ± 0.045	S150	0.017	6.816	6.954	2.248 ± 0.030
Q151	0.097	6.809	7.178	3.333 ± 0.035	K151	0.015	6.772	7.218	2.332 ± 0.034
R152	0.035	6.692	7.514	3.257 ± 0.028	P152	0.003	–	–	–
V153	0.023	7.749	7.722	3.257 ± 0.029	V153	0.017	7.623	7.218	2.175 ± 0.021
G154	0.008	–	–	3.191 ± 0.031	G154	0.00	–	–	2.277 ± 0.026
F155	0.017	7.349	7.554	3.009 ± 0.027	F155	0.019	7.349	7.13	2.122 ± 0.035
G156	0.008	–	–	2.886 ± 0.035	G156	0.009	–	–	2.002 ± 0.037
D157	0.015	7.049	7.218	3.236 ± 0.032	E157	0.023	6.571	7.218	2.140 ± 0.024
D158	0.03	7.33	7.426	3.327 ± 0.037	E158	0.038	6.818	7.042	2.156 ± 0.020
F159	0.024	7.373	7.258	4.193 ± 0.037	F159	0.036	7.196	7.746	2.393 ± 0.020
D160	0.021	7.28	7.258	4.413 ± 0.028	D160	0.006	7.28	7.394	2.561 ± 0.030
E161	0.11	6.702	5.306	4.940 ± 0.027	E161	0.036	6.702	6.514	2.814 ± 0.028
D162	0.451	6.717	7.05	3.836 ± 0.029	D162	0.091	6.717	6.866	3.349 ± 0.018
E163	0.757	6.707	5.642	6.061 ± 0.033	E163	0.319	6.707	6.69	3.191 ± 0.022
L164	0.812	6.55	5.554	6.162 ± 0.012	L164	0.471	6.55	6.602	3.331 ± 0.025
M165	0.718	7.224	6.474	5.720 ± 0.027	M165	0.388	7.224	7.394	2.893 ± 0.023
A166	0.748	5.779	–	–	A166	0.434	5.779	5.626	3.729 ± 0.022
E167	0.756	6.612	5.346	6.018 ± 0.044	E167	0.448	6.612	6.602	3.438 ± 0.029
L168	0.865	6.67	–	–	L168	0.485	6.67	6.954	3.673 ± 0.010
E169	0.865	6.784	4.185	6.490 ± 0.027	E169	0.433	6.784	6.602	3.857 ± 0.016
E170	0.894	6.53	4.265	7.811 ± 0.086	E170	0.487	6.53	6.778	2.422 ± 0.029
L171	0.919	6.67	3.929	6.906 ± 0.039	L171	0.481	6.67	6.602	3.639 ± 0.024
E172	0.888	6.731	4.969	6.333 ± 0.033	E172	0.252	6.731	6.778	3.663 ± 0.021
Q173	0.896	6.834	4.137	7.075 ± 0.053	Q173	0.371	6.834	6.602	2.276 ± 0.022
E174	0.937	6.298	3.513	6.429 ± 0.034	E174	0.446	6.298	6.69	2.473 ± 0.010
E175	0.964	6.53	4.889	6.305 ± 0.040	E175	0.387	6.53	7.042	3.689 ± 0.021
L176	0.934	6.725	3.977	6.176 ± 0.024	L176	0.378	6.813	6.242	3.244 ± 0.027
N177	0.793	7.418	5.386	4.959 ± 0.042	D177	0.131	6.978	–	2.916 ± 0.025
K178	0.692	6.53	5.306	5.760 ± 0.044	K178	0.14	6.779	6.154	3.544 ± 0.035
K179	0.529	6.368	5.89	4.599 ± 0.036	N179	0.221	7.246	6.866	3.429 ± 0.035
M180	0.192	6.659	6.098	5.012 ± 0.030	L180	0.418	6.942	8.282	2.956 ± 0.013
T181	0.07	7.605	7.05	4.275 ± 0.045	L181	0.356	7.072	7.13	2.802 ± 0.020
N182	0.05	7.457	6.594	4.457 ± 0.031	E182	0.176	6.915	6.954	2.680 ± 0.022
I183	0.031	7.436	7.554	3.437 ± 0.029	I183	0.03	7.557	7.842	2.324 ± 0.023
R184	0.009	7.227	8.09	3.914 ± 0.036	C184	0.007	7.294	7.658	2.375 ± 0.038
L185	0.014	6.853	7.218	3.679 ± 0.027	G185	0.005	–	–	2.090 ± 0.044
P186	0.012	–	–	–	P186	0.017	–	–	–
N187	0.02	7.114	7.138	3.257 ± 0.028	E187	0.017	6.318	6.69	2.317 ± 0.032

Table 4.1: Residue-specific NMR parameters of CHMP4 fragments in free form (continued)

$CHMP4C^{S191C}_{121-233}$					$CHMP4B^{S184C}_{121-224}$				
Res.	α prop.	$^3J_{HN-H\alpha}$ Pred.	$^3J_{HN-H\alpha}$ Exp.	^{15}N-R_2 (s^{-1})	Res.	α prop.	$^3J_{HN-H\alpha}$ Pred.	$^3J_{HN-H\alpha}$ Exp.	^{15}N-R_2 (s^{-1})
V188	0.005	7.819	7.97	3.052 ± 0.036	T188	0.017	7.444	7.746	2.270 ± 0.033
S190	0.012	6.688	6.031	3.000 ± 0.039	P190	0.003	–	–	–
C191	0.02	7.046	–	–	L191	0.004	6.727	6.954	2.471 ± 0.010
S192	0.011	7.103	6.542	2.833 ± 0.047	P192	0.009	–	–	–
L193	0.023	6.895	7.218	3.045 ± 0.038	N193	0.019	7.114	7.394	2.266 ± 0.051
N198	0.015	6.964	6.858	3.511 ± 0.035	A198	0.01	6.124	6.514	2.566 ± 0.034
R199	0.012	6.741	6.57	3.635 ± 0.028	L199	0.01	6.87	7.218	2.430 ± 0.031
K200	0.008	6.73	6.978	3.042 ± 0.025	P200	0.008	–	–	–
P201	0.018	–	–	–	S201	0.005	6.434	6.602	2.325 ± 0.054
G202	0.015	–	–	3.711 ± 0.035	K202	0.012	6.772	6.866	2.516 ± 0.036
M203	0.022	6.983	5.033	–	P203	0.011	–	–	–
S204	0.019	6.833	4.553	3.392 ± 0.049	A204	0.009	5.453	5.626	2.422 ± 0.037
S205	0.028	6.74	6.33	3.558 ± 0.074	K205	0.012	6.488	6.69	2.609 ± 0.021
T206	0.066	7.634	6.05	3.962 ± 0.061	K206	0.022	6.347	6.242	2.861 ± 0.037
A207	0.283	5.692	4.553	4.416 ± 0.042	K207	0.136	6.488	5.274	2.987 ± 0.038
R208	0.27	6.708	6.17	4.210 ± 0.035	E208	0.291	6.323	5.626	3.171 ± 0.032
R209	0.324	6.896	5.93	4.457 ± 0.042	E209	0.223	6.382	7.042	2.824 ± 0.038
S210	0.103	6.569	5.202	4.304 ± 0.036	E210	0.108	6.525	6.514	2.316 ± 0.025
R211	0.08	6.966	4.385	4.272 ± 0.040	D211	0.041	6.86	7.042	2.398 ± 0.034
A212	0.123	5.821	6.57	3.828 ± 0.037	D212	0.042	7.037	6.514	2.408 ± 0.032
A213	0.083	5.81	4.873	3.195 ± 0.040	D213	0.119	6.774	–	2.916 ± 0.025
S214	0.047	6.791	6.05	2.839 ± 0.049	M214	0.419	6.757	7.13	2.487 ± 0.026
S215	0.044	6.69	5.762	–	K215	–	6.671	–	–
Q216	0.045	6.809	6.938	2.900 ± 0.030	E216	0.472	6.471	–	–
R217	0.064	6.775	7.058	2.761 ± 0.034	L217	0.293	6.67	6.954	2.310 ± 0.023
A218	0.117	5.72	6.05	2.935 ± 0.027	E218	0.088	6.839	6.602	2.138 ± 0.023
E219	0.125	6.464	6.53	2.794 ± 0.028	N219	0.023	7.638	7.482	1.983 ± 0.043
E220	0.098	6.382	7.058	3.179 ± 0.029	W220	0.03	6.863	6.514	1.806 ± 0.033
E221	0.053	6.525	7.138	2.363 ± 0.029	A221	0.031	6.331	6.514	1.768 ± 0.032
D222	0.046	6.86	7.178	2.652 ± 0.023	G222	0.021	–	–	1.387 ± 0.029
D223	0.232	7.037	–	–	S223	0.128	6.705	7.546	1.218 ± 0.040
D224	0.214	7.025	6.898	2.921 ± 0.025	M224	0.333	6.926	7.762	0.826 ± 0.007
I225	0.559	7.48	7.138	2.941 ± 0.022	–	–	–	–	–
K226	0.529	6.815	6.738	3.117 ± 0.023	–	–	–	–	–
Q227	0.486	6.923	6.938	2.897 ± 0.032	–	–	–	–	–
L228	0.296	6.687	7.258	2.411 ± 0.027	–	–	–	–	–
A229	0.292	6.158	–	–	–	–	–	–	–
A230	0.336	6.218	6.858	2.292 ± 0.029	–	–	–	–	–

Table 4.1: Residue-specific NMR parameters of CHMP4 fragments in free form (continued)

$CHMP4C^{S191C}_{121-233}$					$CHMP4B^{S184C}_{121-224}$				
Res.	α prop.	$^3J_{HN-H\alpha}$ Pred.	$^3J_{HN-H\alpha}$ Exp.	^{15}N-R_2 (s^{-1})	Res.	α prop.	$^3J_{HN-H\alpha}$ Pred.	$^3J_{HN-H\alpha}$ Exp.	^{15}N-R_2 (s^{-1})
W231	0.199	6.821	7.426	1.813 ± 0.029	–	–	–	–	–
A232	0.168	6.221	7.098	1.611 ± 0.025	–	–	–	–	–
T233	0.333	7.606	8.106	0.914 ± 0.010	–	–	–	–	–

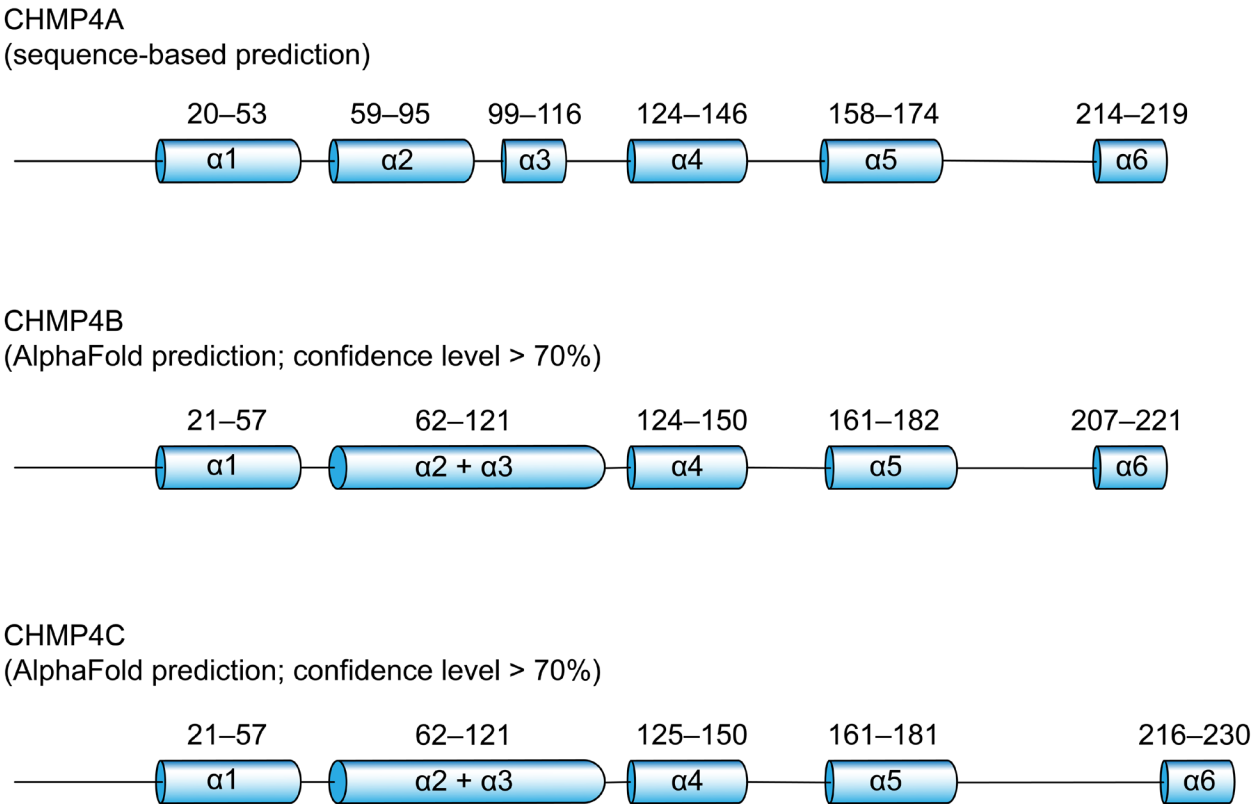

Figure 4.6.1: Predicted structural organization of human CHMP4 paralogs

Predictions based on primary sequence [CHMP4A, upper (33)] or AlphaFold (34) [CHMP4B, middle, and CHMP4C, lower]. Cylinders and labels represent the corresponding CHMP4 helices (α1–α6) whereas numbers above the cylinders represent corresponding CHMP4 residues. Note that among the three CHMP4 paralogs, cellular functions of CHMP4A are not known.

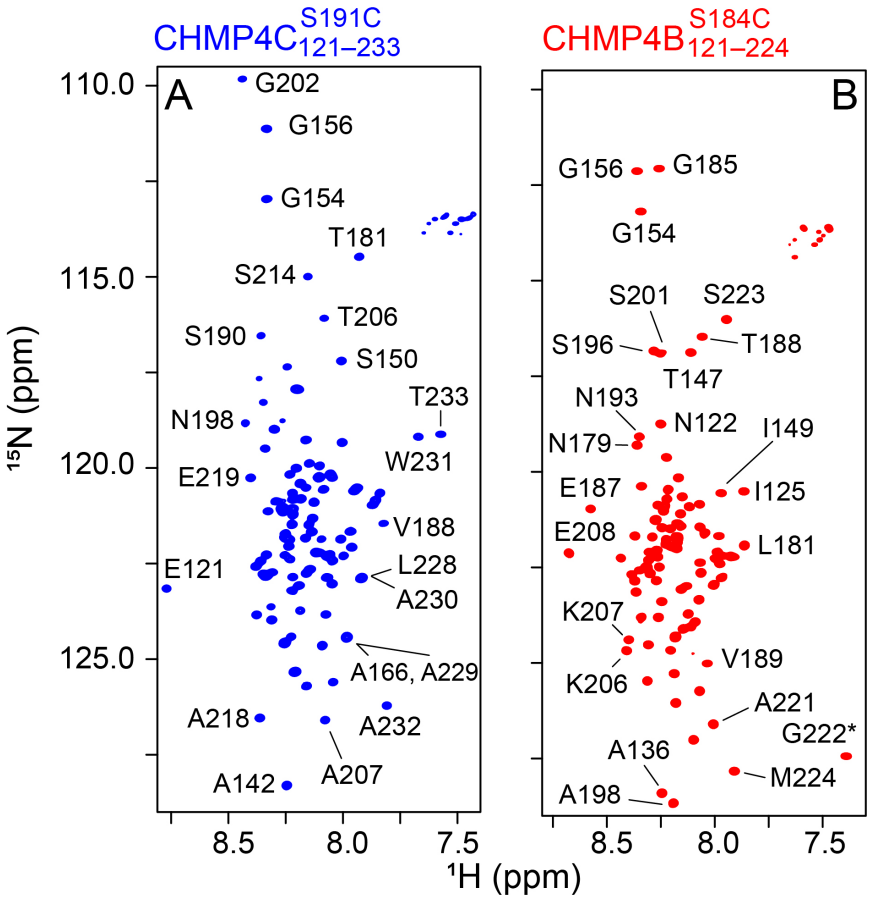

Figure 4.6.2: NMR spectra of CHMP4 paralogs

Expanded regions of the ^{1}H-^{15}N TROSY-HSQC correlation spectra of ^{15}N-labeled **(A)** CHMP4C$^{S191C}_{121-233}$ (blue) and **(B)** CHMP4B$^{S184C}_{121-224}$ (red). Some of the isolated cross-peaks are marked. Folded cross-peak of residue G222 (CHMP4B$^{S184C}_{121-224}$) is marked with an asterisk. Buffer and experimental conditions were as follows: 20 mM sodium phosphate, pH 6.5, 1 mM TCEP, and 2 mM EDTA at 30 ºC. Protein concentrations were 0.5 mM each.

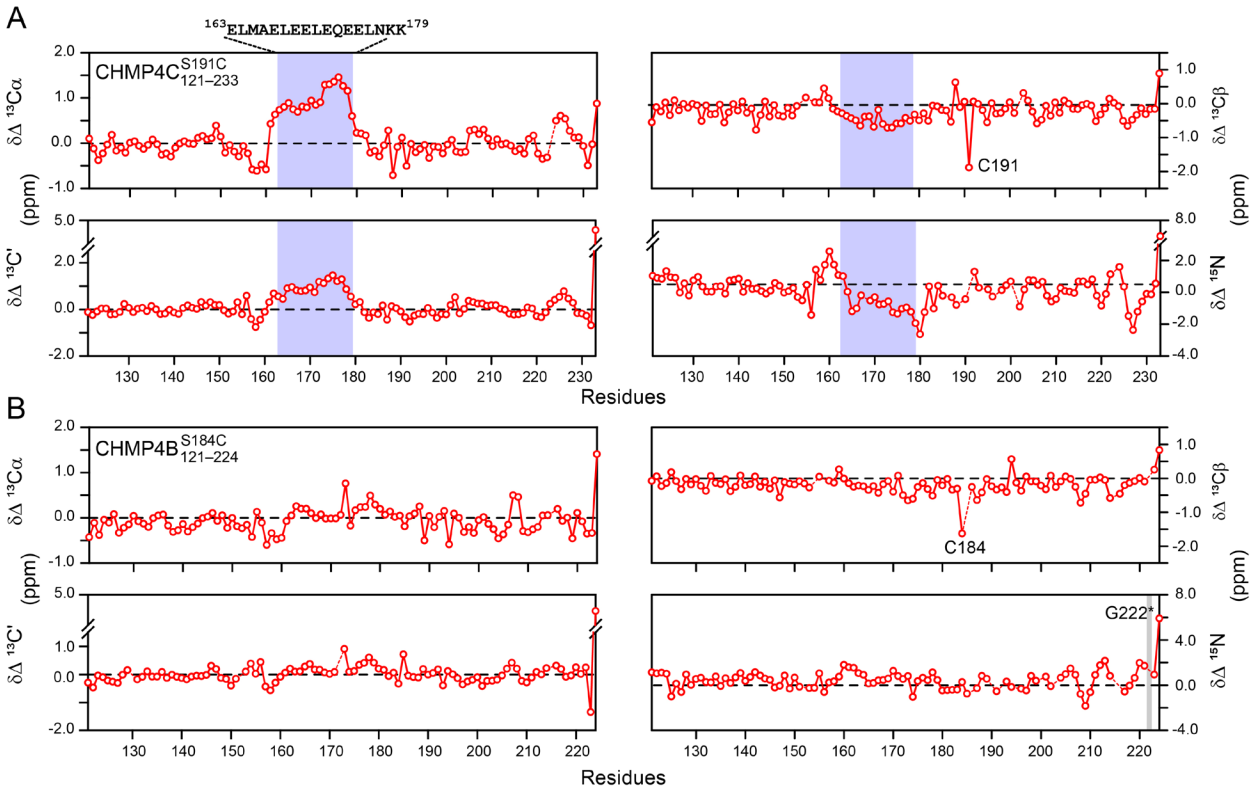

Figure 4.6.3: NMR analysis of CHMP4 paralogs

Secondary chemical shifts (Δδ), ^{13}Cα, ^{13}C', ^{13}Cβ and ^{15}N, of **(A)** CHMP4C$^{S191C}_{121-233}$, and **(B)** CHMP4B$^{S184C}_{121-224}$, derived from assigned backbone chemical shifts and the corresponding random coil values and correction factors of Poulsen and co-workers (35, 36). The region between residues 163–179 of CHMP4C$^{S191C}_{121-233}$, which forms a stable helix, is highlighted in semi-transparent blue rectangles. The Cβ chemical shifts of engineered cysteine residues, namely C191 of CHMP4C$^{S191C}_{121-233}$ and C184 of CHMP4B$^{S184C}_{121-224}$, were ca. 28 ppm, indicating that these two residues were reduced in solution (80). Δδ(^{15}N) of G222 of CHMP4B$^{S184C}_{121-224}$ was not considered because of its folded cross-peak (cf. Fig. 4.6.2).

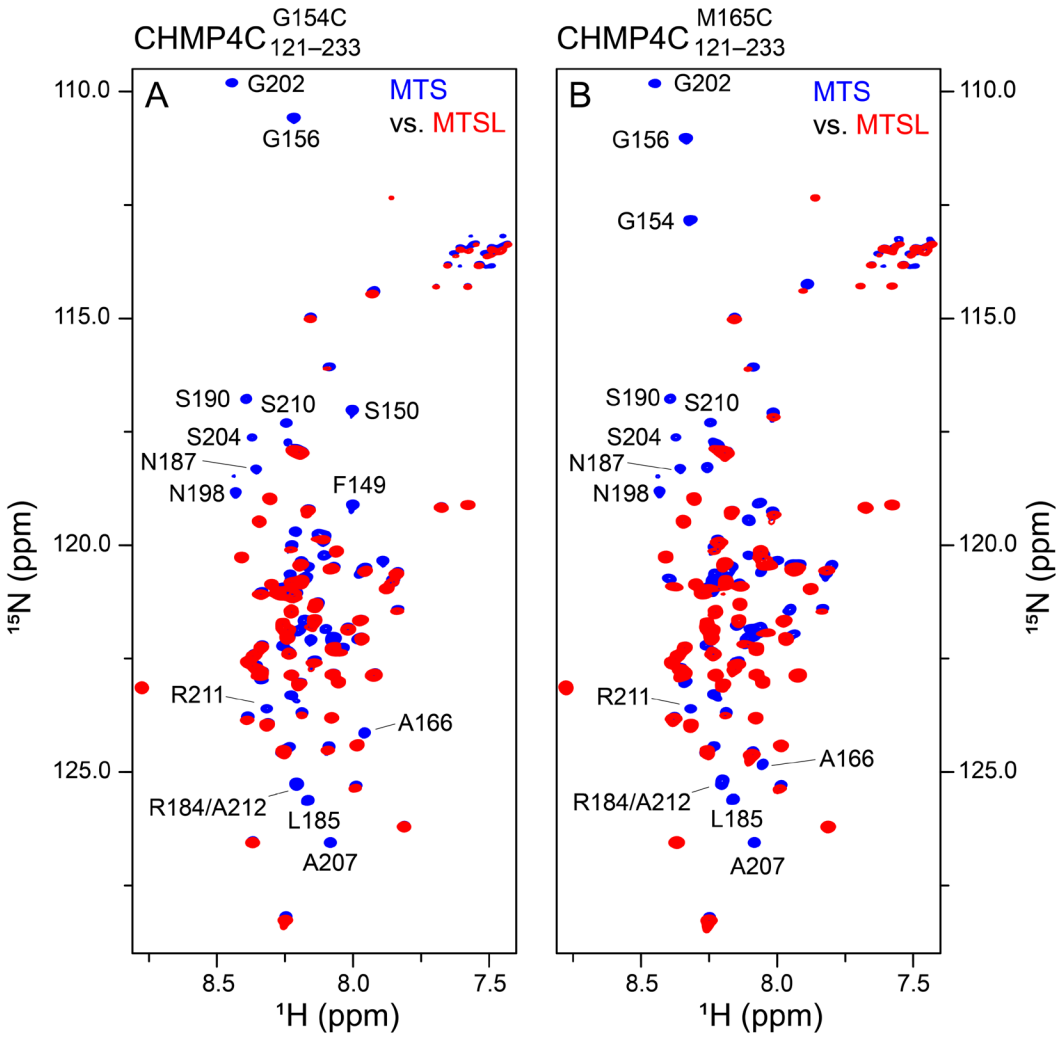

Figure 4.6.4: NMR-PRE analysis of the transient long-range interactions in CHMP4C constructs

Overlay of expanded regions of ^{1}H-^{15}N TROSY-HSQC spectra of diamagnetic MTS-labeled (blue) and paramagnetic MTSL-labeled (red) **(A)** CHMP4C$^{G154C}_{121-233}$ and **(B)** CHMP4C$^{M165C}_{121-233}$. A few of the isolated cross-peaks that undergo significant signal attenuation (^{1}H- ^{15}N cross-peak heights ratio < 0.25) due to the PRE effect are labeled; note that intramolecular PREs are exquisitely sensitive and have thus been used to identify transient long-range interactions in disordered proteins (39-41, 81, 82). All spectra were recorded at 800 MHz at 30 ºC. Buffer conditions were as follows: 20 mM sodium phosphate, pH 6.5, and 2 mM EDTA. Protein concentrations were 0.2 mM each.

4.7 Mechanism of ALIX-mediated CHMP4 activation

To further explore CHMP4–ALIX interactions, we performed NMR titration experiments where increasing concentrations of Bro1 or $PRD^{Strep}_{703\text{-}800}$ were added to NMR-visible CHMP4 constructs. Reductions in $^{1}H_N/^{15}N$ cross-peak heights of 150 μM ^{15}N-labeled CHMP4 proteins were observed with unlabeled Bro1 (Fig. 4.7 A–B and Fig. 4.7.1 A–B). Specifically, the cross-peaks of the α6 motifs of $CHMP4C^{S191C}_{121\text{-}233}$ and $CHMP4B^{S184C}_{121\text{-}224}$ (residues 220–233 and 209–224, respectively) were completely attenuated in the presence of 75 μM Bro1, indicating that these motifs represent high-affinity Bro1-binding sites. These results agree with a study that showed that residues 221–233 of CHMP4C and residues 207–224 of CHMP4B bind to Bro1 (3). Surprisingly, upon a stepwise increase in Bro1 concentration (75, 150, and 450 μM of Bro1; Fig. 4.7 A–B), the cross-peaks of residues 160–180 (α5) of $CHMP4C^{S191C}_{121\text{-}233}$ and residues 153–183 (α5) of $CHMP4B^{S184C}_{121\text{-}224}$ were progressively attenuated, establishing that these α5-motifs represent low-affinity sites for Bro1. These results are in excellent agreement with the above observations that showed that residues 54–72 and 347–349 of Bro1 bind to motifs located in the N-terminal portions of CHMP4 constructs (cf. Fig. 4.5 A–B). TALOS-N derived helical propensities obtained from the backbone chemical shifts of CHMP4 paralogs in the presence of Bro1 are shown in Fig. 4.7.2 A–B. Extensive line broadening precluded a detailed analysis of the helical propensities of the high and low-affinity CHMP4 sites in their Bro1-bound forms, and no noticeable changes were observed in regions that did not bind to Bro1. However, a gradual increase in ^{15}N-ΔR_2 values of residues surrounding the high and low-affinity sites indicates that these motifs are likely ordered in the presence of Bro1 (Fig. 4.7.2 C–D). Note that the high-affinity sites (α6 motifs) of CHMP4 paralogs form ordered helices with Bro1 as evidenced by X-ray crystallography (3) [cf. Fig. 4.1.1

A] and that ^{15}N-ΔR_2 or lifetime line broadening (44, 45) are the differences observed in ^{15}N-R_2 values of CHMP4 fragments with and without Bro1.

The titration experiments performed on 150 μM ^{15}N-labeled CHMP4 proteins and unlabeled $PRD^{Strep}_{703\text{-}800}$ (75, 150, and 450 μM) yielded negligible $^{1}H_N/^{15}N$ cross-peak attenuation but large chemical shift perturbations, especially with 450 μM $PRD^{Strep}_{703\text{-}800}$, a manifestation of fast exchange on the chemical shift time scale ($\Delta_{H/N}$ ~0.13–0.5 ppm; Fig. 4.7 C–D and Fig. 4.7.1 C–D). These chemical shift changes were considerably larger than the small perturbations observed for samples comprising 150 μM ^{15}N-labeled $PRD^{Strep}_{703\text{-}800}$ and 450 μM unlabeled CHMP4 paralogs (cf. Fig. 4.5 C), indicating that although CHMP4-bound $PRD^{Strep}_{703\text{-}800}$ remains disordered, the CHMP4 motifs that bind to $PRD^{Strep}_{703\text{-}800}$ form ordered bound conformations. The large chemical shift changes ($\Delta_{H/N} \geq 0.125$ ppm) observed in samples comprising 150 μM CHMP4 proteins and 450 μM $PRD^{Strep}_{703\text{-}800}$ were localized at residues 134–146, 152, 164–175 of $CHMP4C^{S191C}_{121\text{-}233}$ and residues 140–143 and 162–179 of $CHMP4B^{S184C}_{121\text{-}224}$ (cf. Fig. 4.7 C–D). In comparison, the C-terminal portions, residues 180 onwards, of both CHMP4 constructs showed minimal perturbations. A noticeable increase in TALOS-N-derived helical propensities (≥ 0.5) for residues 130–132 and 142–149 (α4) of $CHMP4C^{S191C}_{121\text{-}233}$ and residues 162–177 (α5) of $CHMP4B^{S184C}_{121\text{-}224}$ were observed with $PRD^{Strep}_{703\text{-}800}$ (Fig. 4.7 E–F). Furthermore, residues of the α5 motif of $CHMP4C^{S191C}_{121\text{-}233}$ that formed a stable helix in free form (cf. Fig. 4.6 D, upper), also displayed increased helicity in the presence of $PRD^{Strep}_{703\text{-}800}$, especially for residues 163–170 (helical propensity ~1). No marked changes in helicity were observed for the C-terminal portions, residues 180 onwards, of either CHMP4 constructs in the presence of $PRD^{Strep}_{703\text{-}800}$. Elevated ^{15}N-$\Delta R_2$ values (≥ 2.5 s-1) were obtained for residues 132–153 (α4) and 161–180 (α5) of $CHMP4C^{S191C}_{121\text{-}233}$ and residues 161–180

(α5) of $CHMP4B^{S184C}_{121-224}$ in the presence of $PRD^{Strep}_{703-800}$ (Fig. 4.7 G–H), establishing an increased ordering of their bound conformations. Therefore, in contrast to $CHMP4B^{S184C}_{121-224}$ where the binding to $PRD^{Strep}_{703-800}$ is localized around the α5 motif, the binding interface involves a substantially larger N-terminal portion of $CHMP4C^{S191C}_{121-233}$, namely α4 and α5 motifs, perhaps because folding of α5 helix is a prerequisite for the interactions of CHMP4 paralogs with ALIX-PRD. Because residues 734–768 of $PRD^{Strep}_{703-800}$ exhibit chemical shift changes with CHMP4 proteins (cf. Fig. 4.5 C), we conclude that residues 734–768 of ALIX-PRD bind to the above-mentioned N-terminal CHMP4 motifs. These results establish a large gain in helicity and structural order for CHMP4 paralogs upon their interactions with ALIX-PRD. To determine whether residual CHMP4 helices play a role in binding to ALIX-PRD, a phenomenon known as conformational selection or folding before binding (46-48), would require an extensive kinetic analysis, which is ongoing in our laboratory.

The results of titration experiments performed on samples comprising 30 μM $^{15}N/^{2}H$-labeled CHMP4 constructs and 90 μM unlabeled $ALIX^{Strep}_{1-868*}$ are shown in Fig. 4.7 I–J; unlike measurements mentioned-above, these experiments were carried out at lower concentrations to account for the increase in viscosity with $ALIX^{Strep}_{1-868*}$. A complete attenuation of $^{1}H_N/^{15}N$ cross-peak heights of residues 165–173 (α5) and 220–233 (α6) of $CHMP4C^{S191C}_{121-233}$ and residues 161–174 (α5) and 210–224 (α6) of $CHMP4B^{S184C}_{121-224}$ was observed with $ALIX^{Strep}_{1-868*}$. These results complement the above findings and confirm that ALIX binds to both α5 and α6 motifs of CHMP4 paralogs. To gain mechanistic insights, we generated an additional CHMP4C construct, $CHMP4C^{S191C,AAA}_{121-233}$, that carried three alanine substitutions in its α6 motif (I225A, L228A, and W231A; Fig. 4.7, Upper). A single alanine substitution for each of these three highly conserved hydrophobic residues was previously shown to abolish α6 (CHMP4) – Bro1 (ALIX) interactions

(3). The results of NMR titration experiments carried out using 30 μM $^{15}N/^{2}H$-labeled $CHMP4C^{S191C,AAA}_{121-233}$, with and without 90 μM unlabeled $ALIX^{Strep}_{1-868*}$ are shown in Figs. 4.7 K and 4.7.3. As expected, the cross-peaks of the α6 motif of $CHMP4C^{S191C,AAA}_{121-233}$, did not show any signal attenuation or chemical shift perturbations in the presence of $ALIX^{Strep}_{1-868*}$. Resonances of residues 163–172 (α5), however, underwent signal attenuation, albeit to a lower extent as compared to $CHMP4C^{S191C}_{121-233}$ + $ALIX^{Strep}_{1-868*}$ titration. These observations establish that, in the absence of α6 – $ALIX^{Strep}_{1-868*}$ hydrophobic interactions, the anionic α5 motif of CHMP4C can independently bind to ALIX. Thus, we propose that ALIX and full-length CHMP4 interactions will comprise hydrophobic (high-affinity) and electrostatic (low-affinity) associations, involving the α6 and α5 motifs of CHMP4 paralogs and Bro1 and PRD of ALIX (Fig. 4.7 L). These intermolecular interactions will, in turn, prevent the intramolecular association between α5 and the N-terminal CHMP4 motifs (α1–α2), thereby triggering the cascade of conformational changes resulting in CHMP4 activation (cf. Fig. 4.6 A). The thermodynamics of binding between CHMP4 paralogs and $ALIX^{Strep}_{1-868*}$ were characterized by isothermal titration calorimetry (ITC; Fig. 4.7 M-N). Excellent agreement was obtained by fitting the experimental isotherms to an independent-sites binding model in the software NanoAnalyze (TA Instruments), yielding the equilibrium dissociation constants, K_D, of 0.6 ± 0.1 μM for $CHMP4C^{S191C}_{121-233}$ – $ALIX^{Strep}_{1-868*}$ and 0.9 ± 0.1 μM for $CHMP4B^{S184C}_{121-224}$ – $ALIX^{Strep}_{1-868*}$ interactions (Table 4.2). Experimentally determined values of the parameter n (where n is the number of binding sites) were very close to unity, which established a 1:1 stoichiometry of these interactions. Similar K_D values were obtained for the interactions of Bro1 with $CHMP4C^{S191C}_{121-233}$ and $CHMP4B^{S184C}_{121-224}$ (0.9 ± 0.1, and 1.0 ± 0.2 μM, respectively; Table 4.2), implying that the association of CHMP4 paralogs and ALIX is primarily governed by the

Bro1 domain and that the interactions with ALIX-PRD are considerably weaker, consistent with the above NMR results. To determine the impact of salt on these interactions, we carried out additional ITC measurements in the presence of 150 mM NaCl, yielding a K_D of 6.1 ± 0.7 μM for $CHMP4C^{S191C}_{121-233}$ – $ALIX^{Strep}_{1-868*}$ interactions (Table 4.2). Similar ITC measurements carried out in the presence of 150 mM NaCl did not detect any noticeable $CHMP4C^{S191C,AAA}_{121-233}$ – $ALIX^{Strep}_{1-868*}$ interactions, which further confirmed the electrostatic association between the anionic α5 motif of CHMP4C and ALIX (Table 4.2). Overall, the above measured K_D values are notably stronger than those reported in a previous study (3), which used surface plasmon resonance to characterize the binding between CHMP4 analogs mimicking the α6 motifs and Bro1 (K_D ~40 μM), further corroborating that both α5 and α6 motifs of CHMP4 paralogs bind to ALIX (and Bro1), and that this larger binding interface is responsible for the increased binding affinity observed here.

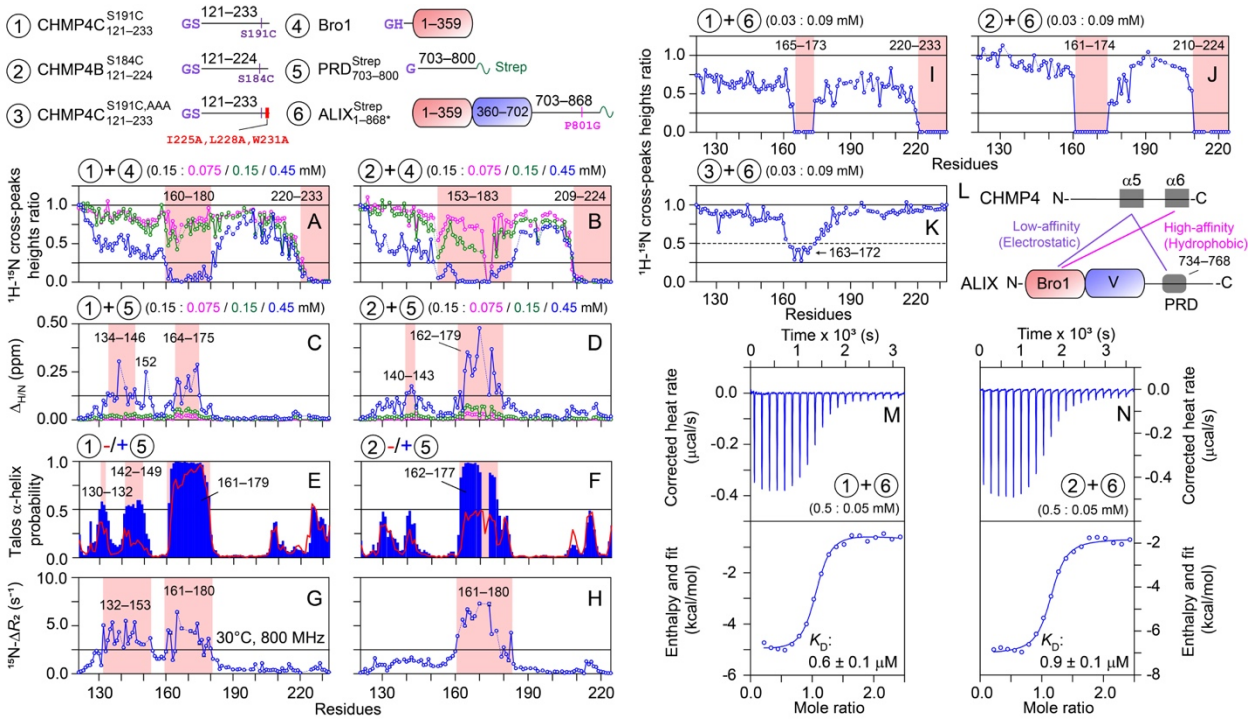

Figure 4.7: NMR and IITC analyses of CHMP4-ITC interactions

(Upper) Schemes of constructs used in these experiments. The reduction in $^{1}H_N/^{15}N$ cross-peak heights of 150 µM ^{15}N-labeled **(A)** $CHMP4C^{S191C}_{121-233}$ and **(B)** $CHMP4B^{S184C}_{121-224}$ as a function of increasing amount of unlabeled Bro1. The color scheme is as follows: CHMP4 fragments + Bro1 molar ratio = 1:0.5 (magenta), 1:1 (green), and 1:3 (blue). The perturbations in $^{1}H_N/^{15}N$ chemical shifts of 150 µM ^{15}N-labeled **(C)** $CHMP4C^{S191C}_{121-233}$ and **(D)** $CHMP4B^{S184C}_{121-224}$ as a function of increasing amount of unlabeled $PRD^{Strep}_{703-800}$; same color scheme as panels **A** and **B**. Dashed lines indicate proline residues or residues that could not be assigned unambiguously. TALOS-N derived helical propensities of **(E)** $CHMP4C^{S191C}_{121-233}$ and **(F)** $CHMP4B^{S184C}_{121-224}$, in the presence (blue bars) and absence (red lines; also see Fig. 4.6 D–E, upper) of $PRD^{Strep}_{703-800}$. Missing residues are shown as gaps. ^{15}N-ΔR_2 profiles measured on **(G)** $CHMP4C^{S191C}_{121-233}$ + $PRD^{Strep}_{703-800}$ and **(H)** $CHMP4B^{S184C}_{121-224}$ + $PRD^{Strep}_{703-800}$ samples at 800 MHz (30 ºC); ^{15}N-ΔR_2, lifetime line broadening (44, 45), are the differences observed in ^{15}N-R_2 values of CHMP4 fragments recorded with and without $PRD^{Strep}_{703-800}$. Protein concentrations were 150 µM ^{15}N-labeled CHMP4 paralogs and 450 µM unlabeled $PRD^{Strep}_{703-800}$; also see Fig. 4.6 D–E (lower) for ^{15}N-R_2 values of CHMP4 fragments recorded in the absence of $PRD^{Strep}_{703-800}$. The reduction in $^{1}H_N/^{15}N$ cross-peak heights of 30 µM $^{15}N/^{2}H$-labeled **(I)** $CHMP4C^{S191C}_{121-233}$, **(J)** $CHMP4B^{S184C}_{121-224}$, and **(K)** $CHMP4C^{S191C,AAA}_{121-233}$ in the presence of 90 µM unlabeled $ALIX^{Strep}_{1-868*}$. In all panels, the affected regions are highlighted with semitransparent red rectangles. **(L)** Scheme summarizing ALIX–CHMP4 interactions found in this study. ITC analyses of the titrations of 500 µM **(M)** $CHMP4C^{S191C}_{121-233}$ and **(N)** $CHMP4B^{S184C}_{121-224}$ into 50 µM $ALIX^{Strep}_{1-868*}$; also see Table 4.2.

Table 4.2: Summary of thermodynamic parameters for the interactions between CHMP4 paralogs and $ALIX^{Strep}_{1\text{-}868*}$ /Bro1 obtained by fitting ITC data to independent sites model

All ITC measurements were performed at 25 °C; ΔH = enthalpy and -TΔS = entropy of dissociation. Errors were calculated from two-three independent titrations, performed by varying the concentrations of involved proteins. To determine the impact of salt on $ALIX^{Strep}_{1\text{-}868*}$ – CHMP4C interactions, additional ITC measurements were carried out in the presence of 150 mM sodium chloride; note that all other ITC measurements were carried out in the absence of sodium chloride. For $ALIX^{Strep}_{1\text{-}868*}$ – $CHMP4C^{S191C,AAA}_{121\text{-}233}$ interactions, the sample concentrations were 1500 μM $CHMP4C^{S191C,AAA}_{121\text{-}233}$ and 300 μM $ALIX^{Strep}_{1\text{-}868*}$. All remaining measurements were preformed using 300-500 μM CHMP4 paralogs, $CHMP4C^{S191C}_{121\text{-}233}$ and $CHMP4B^{S184C}_{121\text{-}224}$, and 30-50 μM $ALIX^{Strep}_{1\text{-}868*}$ or Bro1.

	K_D (μM)	n	ΔH (kcal/mol)	-TΔS (kcal/mol)
$CHMP4C^{S191C}_{121\text{-}233}$				
+ $ALIX^{Strep}_{1\text{-}868*}$	0.6 ± 0.1	1.00 ± 0.02	-4.8 ± 0.2	-3.7 ± 0.3
+$ALIX^{Strep}_{1\text{-}868*}$ (with 150 mM NaCl)	6.1 ± 0.7	1.09 ± 0.01	-3.0 ± 0.2	-4.1 ± 0.3
+ Bro1	0.9 ± 0.1	1.20 ± 0.1	-5.0 ± 0.1	-3.3 ± 0.1
$CHMP4B^{S184C}_{121\text{-}224}$				
+ $ALIX^{Strep}_{1\text{-}868*}$	0.9 ± 0.1	1.05 ± 0.04	-6.4 ± 0.8	-1.8 ± 0.9
+ Bro1	1.0 ± 0.2	1.07 ± 0.06	-6.7 ± 0.03	-1.6 ± 0.1
$CHMP4C^{S191C,AAA}_{121\text{-}233}$ + $ALIX^{Strep}_{1\text{-}868*}$	No binding was detected			

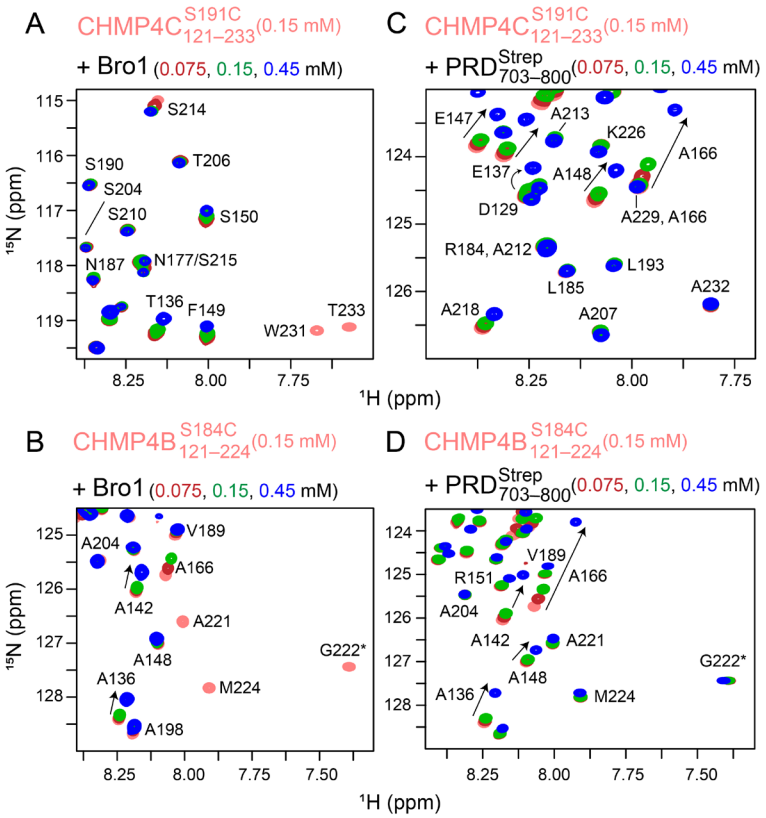

Figure 4.7.1: NMR analysis of interactions between CHMP4 paralogs and ALIX domains

Overlay of expanded regions of the ^{1}H-^{15}N TROSY-HSQC correlation spectra of ^{15}N-labeled **(A and C)** $CHMP4C^{S191C}_{121-233}$ and **(B and D)** $CHMP4B^{S184C}_{121-224}$ in the absence and presence of unlabeled ALIX domains, namely Bro1 and $PRD^{Strep}_{703-800}$. The concentrations of CHMP4 paralogs were 150 µM. The color scheme is as follows: CHMP4 paralogs in free form = light red, in the presence of 75, 150, and 450 µM of Bro1 / $PRD^{Strep}_{703-800}$ = dark red, green, and blue, respectively. A few of cross-peaks are marked. Cross-peaks of the residues that undergo chemical shift changes upon addition of $PRD^{Strep}_{703-800}$ are marked by arrows. Folded cross-peaks of residue G222 ($CHMP4B^{S184C}_{121-224}$) are marked with asterisks.

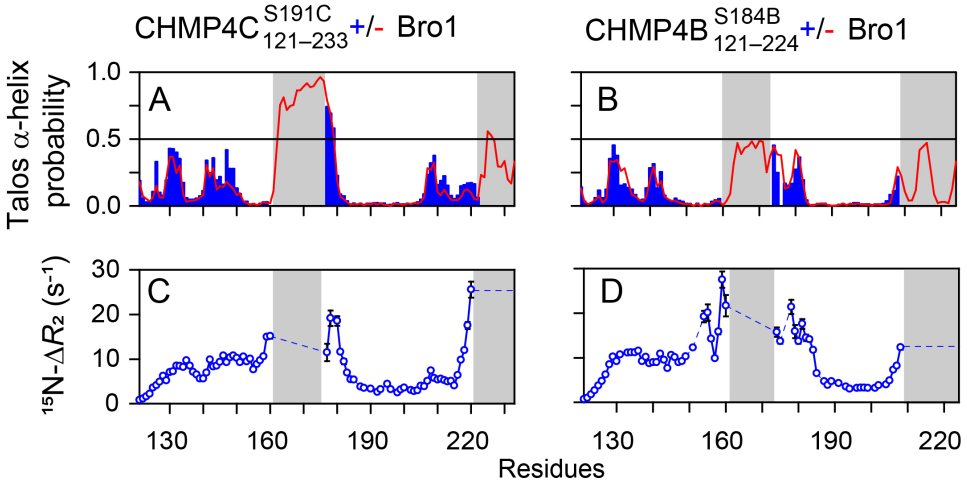

Figure 4.7.2: NMR analysis of CHMP4–Bro1 interactions

TALOS-N (37) derived helical propensities of **(A)** $CHMP4C^{S191C}_{121-233}$ and **(B)** $CHMP4B^{S184C}_{121-224}$, in the presence (blue bars) and absence (red lines) of Bro1; obtained from the corresponding assigned backbone chemical shifts, namely $^{13}C\alpha$, $^{13}C\beta$, $^{13}C'$, ^{15}N, and $^{1}H_N$. Residues that undergo resonance-line broadening in the presence of Bro1 are marked by semi-transparent grey rectangles. ^{15}N-ΔR_2 profiles of **(C)** $CHMP4C^{S191C}_{121-233}$ + Bro1 and **(D)** $CHMP4B^{S184C}_{121-224}$ + Bro1 samples at 800 MHz (30 °C). Protein concentrations were as follows: 150 μM ^{15}N-labeled CHMP4 paralogs and 450 μM non-labeled Bro1.

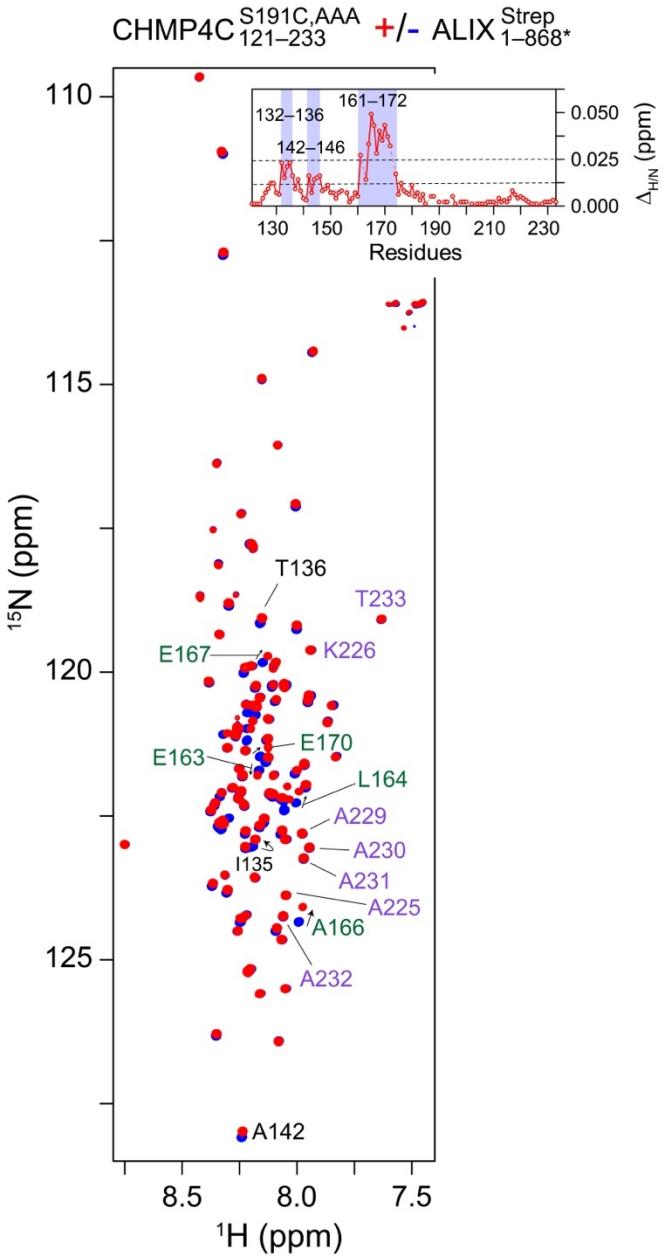

Figure 4.7.3: NMR analysis of CHMP4C$^{S191C,AAA}_{121-233}$–ALIX$^{Strep}_{1-868*}$ interactions

Overlay of expanded regions of the ^{1}H-^{15}N TROSY-HSQC correlation spectra of 30 μM ^{15}N/^{2}H-labeled CHMP4C$^{S191C,AAA}_{121-233}$ in the absence (blue) and presence (red) of 90 μM unlabeled ALIX$^{Strep}_{1-868*}$. A few of the cross-peaks of α5 motif that show signal attenuation upon addition of ALIX$^{Strep}_{1-868*}$ are marked in green (^{1}H-^{15}N cross-peak heights ratio = 0.25–0.5). Cross-peaks of α6 motif that did not show any signal attenuation are marked in magenta. A few other cross-peaks that show chemical shift perturbations are marked in black. **Inset:** Corresponding $^{1}H_N/^{15}N$ chemical shift perturbation profile; semi-transparent blue rectangles indicate regions that exhibit chemical shift perturbations ($\Delta_{H/N} \geq 0.0125$ ppm). Spectra were acquired at a spectrometer ^{1}H frequency of 800 MHz (30 °C). Buffer conditions were the same as those described in Fig. 4.5 caption.

4.8 Modulation of ALIX condensates by tyrosine phosphorylation and the impact of CHMP4C sequestration

Cellular ACBs are regulated by PTMs, specifically by Aurora-B-mediated (serine) phosphorylation of CHMP4C (11). Furthermore, ALIX-PRD fibrils dissolve and reform upon reversible tyrosine phosphorylation mediated by Src and PTP1B (22, 23). Hence, we asked if these PTMs can modulate $ALIX^{Strep}_{1\text{-}868*}$ condensates and the subsequent impact of the confinement of CHMP4 paralogs. Src-mediated hyperphosphorylation of $ALIX^{Strep}_{1\text{-}868*}$ was confirmed by western blotting and mass spectrometry (MS; Fig. 4.8 A–B). To explore the impact of tyrosine phosphorylation on ALIX's phase separation, 5 μM Src and 5 mM adenosine triphosphate (ATP) were mixed with $ALIX^{Strep}_{1\text{-}868*}$ condensates (50 μM), and the resultant changes in droplet morphologies were visualized by fluorescence microscopy (Fig. 4.8.1 A). After ~10 min., bursts of fluorescent light were seen emanating from larger $ALIX^{Strep}_{1\text{-}868*}$ droplets (≥ 5 μm in diameter), likely due to the disintegration of condensates into soluble species upon phosphorylation (Supplementary Files). After 30 min, no droplets were visible. Similar experiments performed without Src or ATP revealed minimal alterations in droplet morphologies with time (Fig. 4.8 C–D), thereby ruling out photobleaching as the cause of the droplet disappearance observed for samples mixed with both Src and ATP. These results were confirmed by turbidity assays (Fig. 4.8.1 B). Unlike negative controls, $ALIX^{Strep}_{1\text{-}868*}$ droplets without Src or ATP that displayed no changes in turbidity, a rapid loss of turbidity was observed in $ALIX^{Strep}_{1\text{-}868*}$ droplets mixed with Src and ATP with a half-time ($t_{1/2}$) of ~5 min, confirming the breakdown of higher-order ALIX multimers into soluble species upon phosphorylation. Because condensates of ALIX constructs displayed gel-like properties (e.g., slow fusion and little FRAP recovery), we propose that Src

accesses and phosphorylates the outer edges of these droplets, causing the phosphorylated species to slowly leach out, as evidenced by a gradual decrease in the droplet size with time; Supplementary Files captured using total internal reflection fluorescence (TIRF) microscopy. Hyperphosphorylated $ALIX^{Strep}_{1\text{-}868*}$ (50 μM) did not phase separate with PEG-4000 (Fig. 4.8.1 C). The addition of 50 nM PTP1B, however, resulted in the reformation of condensates as dephosphorylation proceeded in real-time; the latter was confirmed by western blotting (Fig. 4.8 E). The corresponding sigmoidal increase in turbidity ($t_{1/2}$ ~15 min) corroborated the restoration of condensates upon dephosphorylation, whereas samples without PTP1B showed no noticeable increase in turbidity (Fig. 4.8.1 D). These results establish that reversible tyrosine phosphorylation modulates ALIX's phase separation.

To assess the changes in Src-mediated dissolution of ALIX condensates comprising CHMP4 proteins, we performed microscopy experiments and turbidity assays on $ALIX^{Strep}_{1\text{-}868*}$ condensates containing increasing concentrations of $CHMP4C^{S191C}_{121\text{-}233}$. These measurements were performed using 0.5 μM Src (as opposed to 5 μM Src that was used in above experiments). Under these conditions, a gradual loss of turbidity was observed in $ALIX^{Strep}_{1\text{-}868*}$ condensates in the absence of $CHMP4C^{S191C}_{121\text{-}233}$ ($t_{1/2}$ ~35 min; Fig. 4.8.1 E). In the presence of 2.5 and 10 μM $CHMP4C^{S191C}_{121\text{-}233}$, the corresponding changes in turbidity were progressively minimal. Specifically, 10 μM $CHMP4C^{S191C}_{121\text{-}233}$ in $ALIX^{Strep}_{1\text{-}868*}$ condensates resulted in minimal alterations in droplet morphology and turbidity over a 90 min time-course (Fig. 4.8.1 E and Fig. 4.8.2). Therefore, the sequestration of CHMP4C in ALIX droplets modulates their Src-mediated dissolution (Fig. 4.8.1F), perhaps because both CHMP4C and Src compete for overlapping binding sites on ALIX-PRD (cf. Fig. 4.1.1 A and 4.5 C). To test this, we analyzed the changes in Src-mediated phosphorylation of $ALIX^{Strep}_{1\text{-}868*}$ condensates in the absence and presence of equimolar amount of $CHMP4C^{S191C}_{121\text{-}233}$ using

western blotting (Fig. 4.8.3). Unlike the sample without $CHMP4C^{S191C}_{121\text{-}233}$, a large decrease in band intensities of phosphorylated $ALIX^{Strep}_{1\text{-}868*}$ was observed in the presence of $CHMP4C^{S191C}_{121\text{-}233}$, establishing that colocalization of CHMP4C in ALIX droplets inhibits ALIX's phosphorylation by Src. We thus propose that the dissolution of ALIX aggregates confined within cellular ACBs can be tuned by changes in Src kinase expression and activity, further supporting the important role of Src-family kinases in cytokinetic abscission.

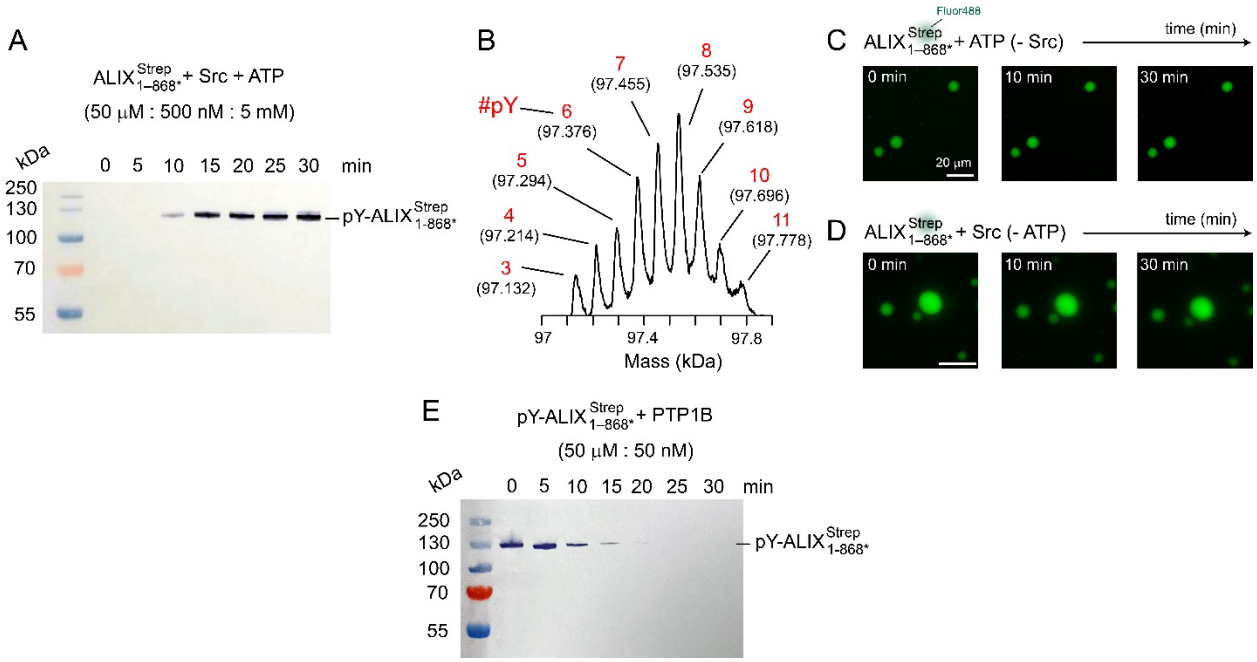

Figure 4.8: Dissolution and formation of ALIX condensates upon reversible tyrosine phosphorylation

(A) Time course of Src-mediated in vitro phosphorylation of $ALIX^{Strep}_{1\text{-}868*}$ by western blotting (the primary and secondary antibodies were phospho-tyrosine mouse monoclonal and goat anti-mouse IgG, respectively). The numbers in parenthesis represent the concentrations of $ALIX^{Strep}_{1\text{-}868*}$, Src, and ATP used for this experiment, namely 50 μM, 500 nM, and 5 mM, respectively. The gel-band for phosphorylated (pY) $ALIX^{Strep}_{1\text{-}868*}$ Strep is marked. Note that the corresponding band of phosphorylated Src is not detected because of its low nanomolar concentration, and that $ALIX^{Strep}_{1\text{-}868*}$ migrates anomalously on 4–12% Bis-Tris SDS-PAGE gel, likely due to its disordered PRD. **(B)** LC–ESI–TOFMS analysis of phosphorylated $ALIX^{Strep}_{1\text{-}868*}$ revealed hyperphosphorylated state of $ALIX^{Strep}_{1\text{-}868*}$ [ALIX carries 33 native tyrosine residues among which 11 are localized in the C-terminal portion of its PRD, residues 803 to 846 (23)]. The numbers in red represent the number of phosphorylated tyrosine residues, labeled as pY. The numbers in parentheses represent the corresponding masses in kDa. Representative control microscopy images establishing the lack of dissolution of Alexa-Fluor488- labeled $ALIX^{Strep}_{1\text{-}868*}$ Strep condensates in the absence of **(C)** Src, and **(D)** ATP. **(E)** Time course of dephosphorylation of 50 μM hyperphosphorylated $ALIX^{Strep}_{1\text{-}868*}$ by 50 nM PTP1B monitored by western blotting. The buffer conditions were as follows: 50 mM Tris, pH 7.5, 50 mM NaCl, 2 mM DTT, 5 mM $MgCl_2$ for the kinase reaction, and 20 mM HEPES, pH 7.5, 50 mM NaCl, 1 mM DTT, 1 mM EDTA for the phosphatase reaction. Both reactions were carried out at room temperature. Additionally, the phase-separation experiments shown in panels C and D were carried out in the presence of 5% (w/v) PEG-4000.

Figure 4.8.1: Dissolution and formation of ALIX condensates upon reversible tyrosine phosphorylation

(A) Time course of the dissolution of $ALIX^{Strep}_{1\text{-}868*}$ Strep condensates upon Src-mediated phosphorylation, monitored by fluorescence microscopy. The concentrations of $ALIX^{Strep}_{1\text{-}868*}$, Src, and ATP are specified in parenthesis. **(B)** Dissolution kinetics of $ALIX^{Strep}_{1\text{-}868*}$ condensates monitored by turbidity assay (OD_{330} nm). The solid line and shaded region represent the mean and SD, respectively (n = 3). $ALIX^{Strep}_{1\text{-}868*}$ condensates were incubated with Src + ATP (red), only Src (black), and only ATP (magenta); proteins and ATP concentrations were the same as in panel A. **(C)** PTP1B-mediated dephosphorylation of hyperphosphorylated $ALIX^{Strep}_{1\text{-}868*}$ (labeled as pY) resulted in the formation of $ALIX^{Strep}_{1\text{-}868*}$ condensates. Representative microscopy images at three time points are shown. **(D)** Kinetics of the formation of $ALIX^{Strep}_{1\text{-}868*}$ condensates monitored by turbidity assay. pY-$ALIX^{Strep}_{1\text{-}868*}$ (50 μM) was incubated with (blue) and without (red) PTP1B (50 nM), n = 3. **(E)** The changes in dissolution rates of $ALIX^{Strep}_{1\text{-}868*}$ condensates as a function of increasing concentration of $CHMP4C^{S191C}_{121\text{-}233}$, monitored by turbidity assay (n = 3). The concentrations of $ALIX^{Strep}_{1\text{-}868*}$, Src, and ATP are noted in parenthesis. The concentrations of $CHMP4C^{S191C}_{121\text{-}233}$ were as follows: 0 (red), 2.5 (orange), and 10 μM (blue). Inset: A representative microscopy image of $ALIX^{Strep}_{1\text{-}868*}$ droplets in the presence of 10 μM $CHMP4C^{S191C}_{121\text{-}233}$ upon 90 min incubation; also see Fig. 4.8 for images at the respective fluorescent channels as a function of time, and Fig. 4.8.2 for western blot analysis of changes in Src-mediated phosphorylation of $ALIX^{Strep}_{1\text{-}868*}$ droplets with and without $CHMP4C^{S191C}_{121\text{-}233}$. **(F)** Schematic of modulation of Src-mediated dissolution of ALIX condensates by CHMP4C. All above experiments were carried out at room temperature with 5% (w/v) PEG-4000. Buffer conditions are described in section 4.11.13. For fluorescence microscopy experiments, $ALIX^{Strep}_{1\text{-}868*}$ and $CHMP4C^{S191C}_{121\text{-}233}$ were labeled with Alexa-Fluor488 and ATTO-647N, respectively.

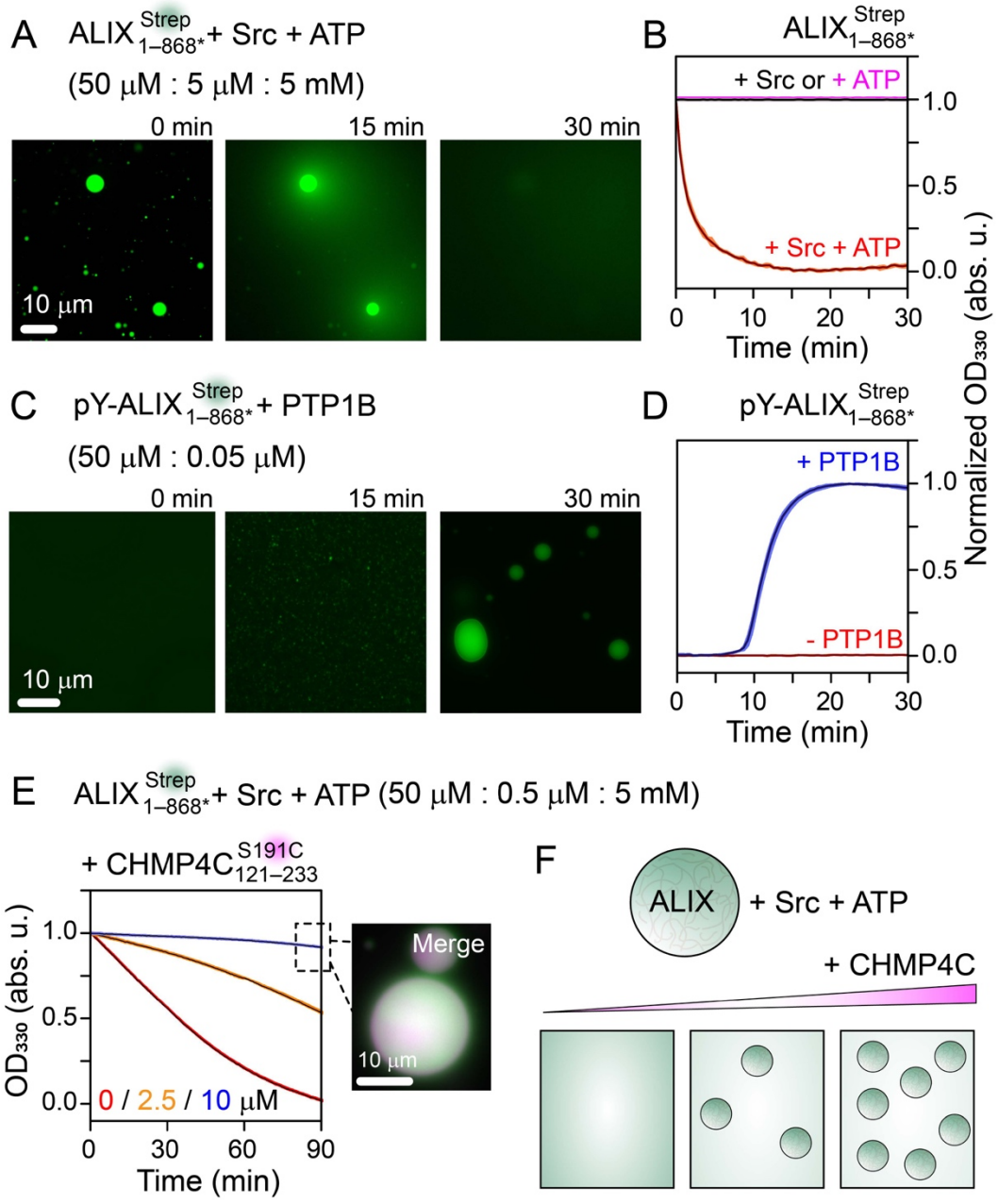
A
ALIX Strep 1–868* + Src + ATP
(50 μM : 5 μM : 5 mM)
0 min
15 min
30 min
10 μm
B
ALIX Strep 1–868*
+ Src or + ATP
+ Src + ATP
1.0
0.5
0.0
0
10
20
30
Time (min)
Normalized OD330 (abs. u.)
C
pY-ALIX Strep 1–868* + PTP1B
(50 μM : 0.05 μM)
0 min
15 min
30 min
10 μm
D
pY-ALIX Strep 1–868*
+ PTP1B
- PTP1B
1.0
0.5
0.0
0
10
20
30
Time (min)
E
ALIX Strep 1–868* + Src + ATP (50 μM : 0.5 μM : 5 mM)
+ CHMP4C S191C 121–233
OD330 (abs. u.)
1.0
0.5
0.0
0 / 2.5 / 10 μM
0
30
60
90
Time (min)
Merge
10 μm
F
ALIX
+ Src + ATP
+ CHMP4C

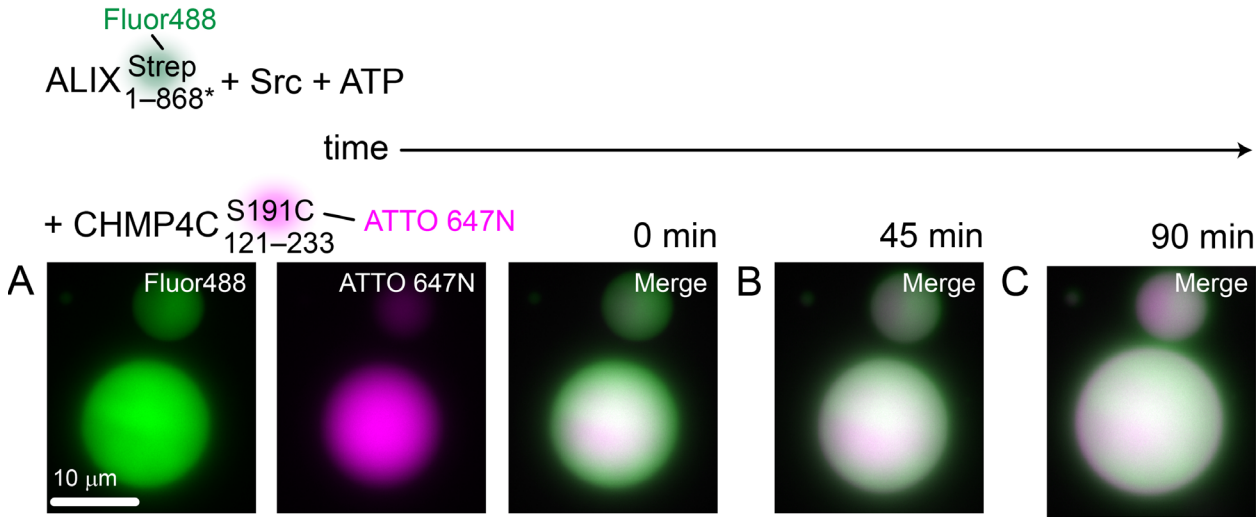

Figure 4.8.2: Time-course of the lack of Src-mediated dissolution of $ALIX^{Strep}_{1\text{-}868*}$ droplets in the presence of $CHMP4C^{S191C}_{121\text{-}233}$

Representative confocal images of Alexa-Fluor488-labeled $ALIX^{Strep}_{1\text{-}868*}$ condensates comprising $CHMP4C^{S191C}_{121\text{-}233}$ at three time points, namely 0 min **(A)**, 45 min **(B)**, and 90 min **(C)**. The following concentrations were used: 50 μM $ALIX^{Strep}_{1\text{-}868*}$, 10 μM $CHMP4C^{S191C}_{121\text{-}233}$, 500 nM Src, and 5 mM ATP in the presence of 5% (w/v) PEG-4000.

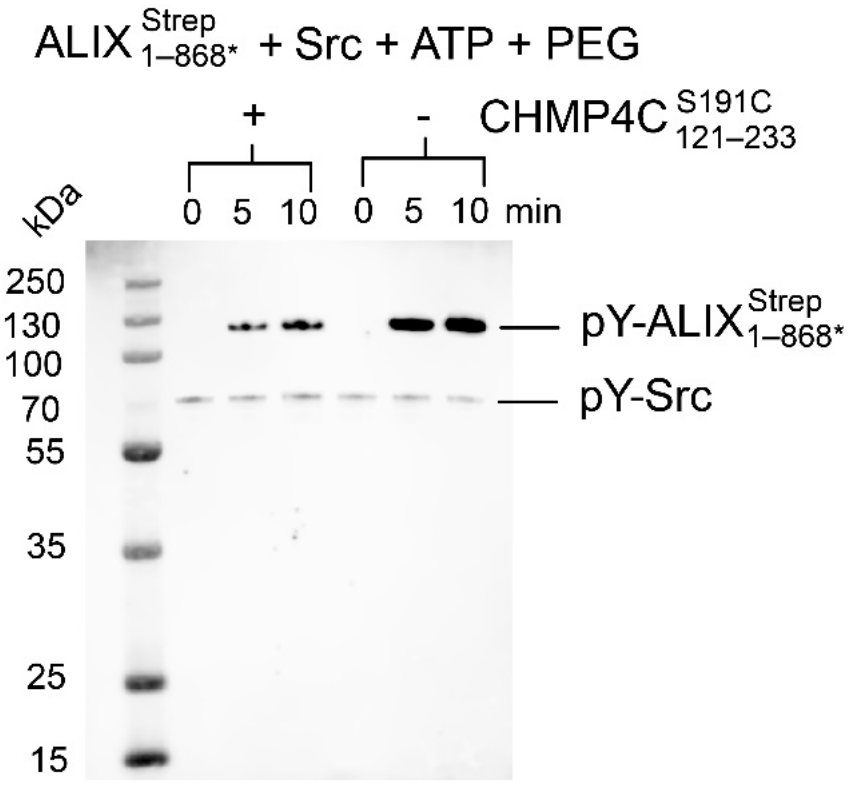

Figure 4.8.3: Western blot analysis of the changes in Src-mediated phosphorylation of $ALIX^{Strep}_{1-868*}$ droplets with and without $CHMP4C^{S191C}_{121-233}$

The primary and secondary antibodies were phospho-tyrosine mouse monoclonal and IRDye 800CW goat anti-mouse IgG, respectively. Blot was visualized using the Odyssey XF imaging system (LICOR Biosciences). The gel-bands for phosphorylated (pY) $ALIX^{Strep}_{1-868*}$ and Src are marked. The following protein concentrations were used: 50 μM $ALIX^{Strep}_{1-868*}$ with and without 50 μM $CHMP4C^{S191C}_{121-233}$, and 5 μM Src. Buffer and experimental conditions were as follows: 50 mM Tris, pH 7.5, 50 mM NaCl, 5 mM $MgCl_2$, 2 mM DTT, 5 mM ATP, 5% (w/v) PEG-4000, and room temperature.

4.9 Concluding remarks

In summary, ALIX phase separates into gel-like condensates in vitro and in vivo, mediated by the amyloidogenic portion of its PRD. Recombinant CHMP4B and CHMP4C readily colocalize in ALIX condensates. Both CHMP4 paralogs used in this study are largely disordered, except for the α5 motif of the CHMP4C, which forms a stable helix. ALIX binds to α5 and α6 motifs of CHMP4 proteins, elucidating the molecular basis of ALIX-mediated CHMP4 activation as the intermolecular ALIX–CHMP4 interactions will likely relieve intramolecular autoinhibitory interactions between α5 and α1–α2 motifs in full-length CHMP4 proteins, thereby triggering their activation. ALIX condensates are modulated by PTMs where tyrosine hyperphosphorylation and dephosphorylation of ALIX via Src and PTP1B lead to their dissolution and reformation. Based on these results, we argue that PTM-mediated phase separation of ALIX will contribute to the biogenesis and stability of cellular ACBs and propose a model to illustrate how ALIX's aggregation can control abscission timing (Fig. 4.9). Additionally, we note that the formation of phase-separated cellular compartments is primarily driven by the multivalent interactions of the sequestered biomolecules, often involving associations of their disordered regions (13). Eukaryotic PRDs frequently form such multivalent complexes due to their disordered nature and favorable binding properties (22). PRDs are also known to modulate cellular phase separation. For example, a recent report established that the PRD of microtubule-associated protein Tau drives its phase separation in vivo (49). Moreover, aromatic residues that are interspersed in the disordered protein regions promote phase separation through π-π stacking. In these regards, the importance of tyrosine residues was established by mutation and deletion studies (50-52) as well as by solution NMR analyses (53). PTMs, including tyrosine phosphorylation, are also known to regulate the formation and dissolution of biomolecular condensates. For example, phosphorylation of tyrosine residues

in RNA-binding proteins, namely cell cycle associated protein 1 [CAPRIN1] (54) and heterogeneous nuclear ribonucleoprotein 2 [hnRNPA2] (55), was shown to modulate their phase separation properties. The results presented here are in excellent agreement with these known observations. This is because the amyloidogenic portion of ALIX is enriched with proline and tyrosine residues (29% and 20%, respectively), which likely promote its phase separation via hydrophobic interactions, and that the introduction of negatively charged phosphoryl groups on tyrosine residues creates charge-charge repulsions, leading to condensate disassembly upon Src-mediated phosphorylation. Hence, the condensates of recombinant ALIX can likely be described as simple coacervates, driven by the intermolecular associations of the amyloidogenic portion of its PRD. Additionally, the above observations suggest how the stability and composition of cellular condensates can be modulated by reversible tyrosine phosphorylation. While a detailed structural investigation of these intermolecular associations in vitro and their dynamic interplay with the corresponding PTMs will provide vital physical insights and is a topic of ongoing investigation in our laboratory, we note that the mechanism of the formation and dissolution of such condensates in vivo will be staggeringly more complex. Altogether, the results presented in this study uncover the phase separation of ALIX and its plausible role in regulating the timing of cell division.

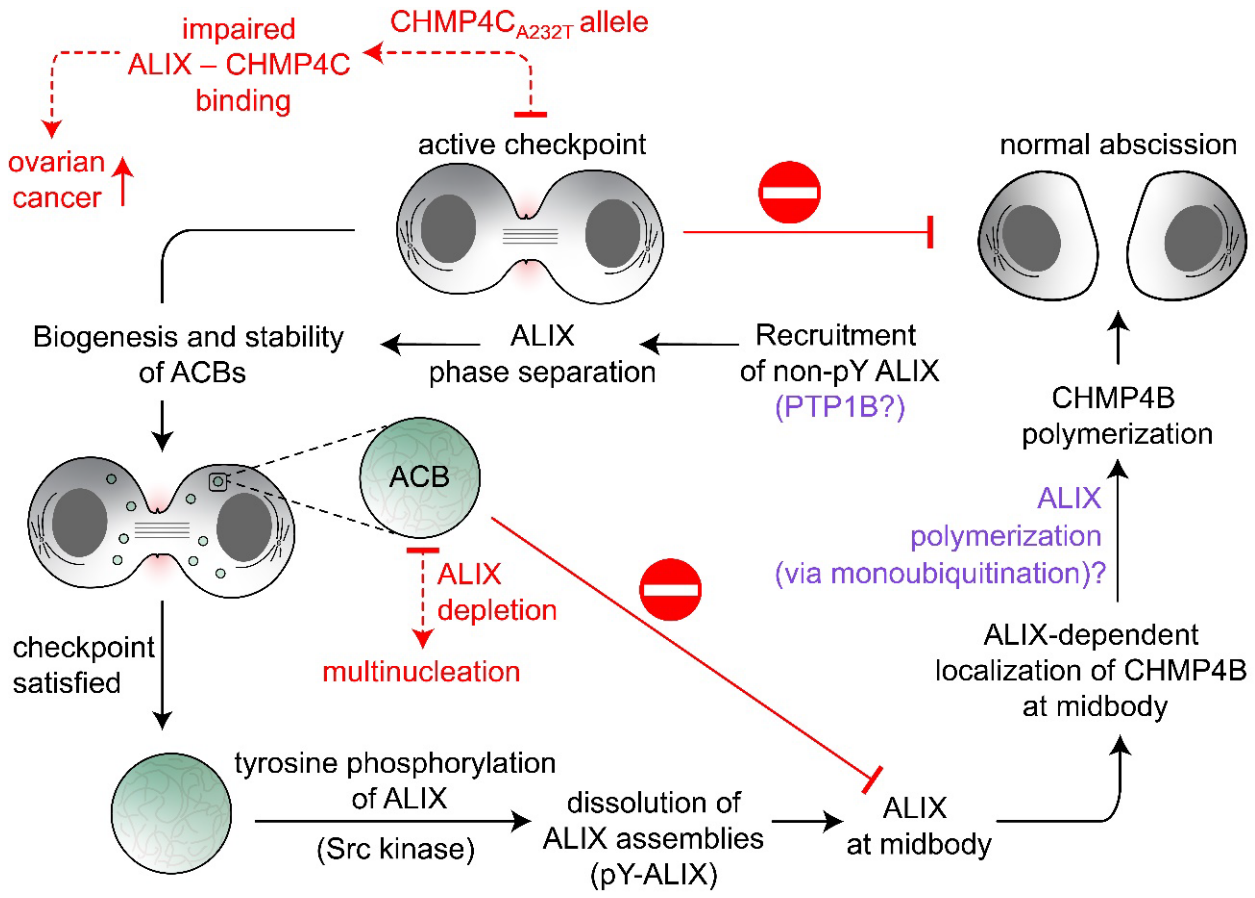

Figure 4.9: Proposed role of ALIX's phase separation in regulation of abscission

Based on the findings of current study and prior results (10, 11, 20, 73), we hypothesize that phase separation of non-phosphorylated (non-pY) ALIX will play a vital role in the biogenesis and stability of ACBs during the active abscission checkpoint (although PTP1B was used in current study, the exact identity of the tyrosine phosphatase that dephosphorylates ALIX in vivo is not known; noted with a question mark). The sequestration of ALIX in ACBs will delay the localization of ALIX and subsequently ALIX-mediated localization of CHMP4B at the midbody. We propose that upon the resolution of the checkpoint, hyperphosphorylation (pY) of ALIX by Src kinase will dissolve ALIX assemblies into monomers. Subsequent localization of hyperphosphorylated ALIX monomers at the midbody would result in ALIX-mediated localization of CHMP4B. ALIX, like other early-acting ESCRT-I factors that assemble into a scaffolding platform (74), may also polymerize into higher-order assemblies (marked by a question mark), facilitating the polymerization of CHMP4B filaments and thereby, CHMP4B-mediated membrane scission. We recently showed that monoubiquitination of ALIX via NEDD4-family E3 ligases, namely WWP2 and NEDD4L, promoted its fibrilization in vitro (75). Note that, like many ESCRT-proteins, ALIX is monoubiquitinated in vivo, which is important for its cellular functions (76, 77). Red dashed arrows represent known pathological aberrations in the shown processes, including the ovarian cancer-predisposing CHMP4C mutation that overrides the checkpoint due to its defective association with ALIX (10) and ALIX-depletion that results in multinucleated cells (73).

4.11 Experimental procedures

4.11.1 Data availability

All ALIX, CHMP4, and CEP55 plasmids tested in this study have been deposited in the Addgene repository, https://www.addgene.org (accession no. 180023 [$PRD^{Strep}_{800-868}$], 180024 [$ALIX^{Strep}_{1-868*}$], 180025 [$ALIX_{1–868*}$], 191191 [$ALIX^{mNGS}_{1-868}$], 191192 [$ALIX^{mNG}_{1-868*}$], 191193 [$ALIX^{mNG}_{1-702}$], 180026 [$CHMP4B^{S184C}_{121-224}$], 180027 [$CHMP4C^{S191C}_{121-233}$], 190783 [$CHMP4C^{G154C}_{121-233}$], 190784 [$CHMP4C^{M165C}_{121-233}$], 199242 [$CHMP4C^{S191C,AAA}_{121-233}$], 180029 [$PRD_{703-868*}$], and 186793 [$CEP55^{S215C}_{160-216}$]). Note that the remaining ALIX constructs were deposited in the Addgene repository as a part of our previously published works (22, 23) (accession no. 164444 [$PRD^{Strep}_{703-868*}$], 141344 [$PRD^{Strep}_{703-800}$], and 141345 [$PRD_{800–868}$]). The chemical shift assignments of $CHMP4B^{S184C}_{121-224}$ and $CHMP4C^{S191C}_{121-233}$ have been deposited in the Biological Magnetic Resonance Bank, https://bmrb.io (accession no. 51513 and 51514).

4.11.2 Materials

PEG-4000 was purchased from Sigma-Aldrich (catalog no. 81240). Streptavidin Alexa-Fluor488 conjugate was purchased from Thermo Fisher Scientific (catalog no. S32354). ATTO-390 maleimide, ATTO-488 NHS ester, and ATTO-647N maleimide were purchased from ATTO-TEC GmbH (catalog no. AD 390-41, AD 488-31, and AD 647N-41, respectively) and were dissolved in DMF at a concentration of 10 mM. ATP was purchased from Sigma-Aldrich (catalog no. A2383) and was dissolved and buffered in 100 mM Tris, pH 7.5, at a concentration of 100 mM. The phospho-tyrosine mouse monoclonal antibody was purchased from Cell Signaling Technology (catalog no. 9411). The secondary antibodies goat anti-mouse IgG and IRDye 800CW were purchased from Thermo Fisher Scientific (catalog no. G-21040 and NC9401841,

respectively). SDS-PAGE gels were purchased from Thermo Fisher Scientific (4–12% Bis-Tris gels, catalog no. NW04122BOX). Reagents for NMR isotopic enrichment were obtained from Cambridge isotope laboratories and Sigma-Aldrich. MTSL and MTS were purchased from Toronto Research Chemicals, Inc. (catalog no. O875000 and A167900, respectively).

4.11.3 Recombinant protein expression and purification

Codon-optimized constructs, $ALIX^{Strep}_{1\text{-}868*}$, $ALIX_{1–868*}$, $PRD_{703–868*}$, $PRD^{Strep}_{800\text{-}868}$, $CHMP4C^{S191C}_{121\text{-}233}$, $CHMP4C^{G154C}_{121\text{-}233}$, $CHMP4C^{M165C}_{121\text{-}233}$, $CHMP4C^{S191C,AAA}_{121\text{-}233}$, $CHMP4B^{S184C}_{121\text{-}224}$, and $CEP55^{S215C}_{160\text{-}216}$ were custom-synthesized from Azenta Life Sciences. The remaining constructs, $PRD^{Strep}_{703\text{-}868*}$, $PRD^{Strep}_{703\text{-}800}$, and $PRD_{800–868}$, were reported in our previous works (22, 23). ALIX-Bro1 and PTP1B were obtained from the Addgene repository, accession nos. 80641 (3) and 102719 (56), respectively. Constructs of Src kinase, $MBP^{E64C}_{28\text{-}396}$, and TEV protease were generous gifts from Albert van der Vliet (University of Vermont), G. Marius Clore (NIH), and David S. Waugh (NIH), respectively. See Fig. 4.1.2 for the design and subcloning of each recombinant construct tested in this study.

Src kinase, PTP1B, $PRD^{Strep}_{703\text{-}868*}$, $PRD^{Strep}_{703\text{-}800}$, TEV protease, and $MBP^{E64C}_{28\text{-}396}$ were expressed as described previously (22, 23, 45). All remaining constructs were expressed at 16 °C. Cells were grown at 37 °C in 1 L LB medium (MP Biomedicals, catalog no. 3002-036) at natural isotopic abundance or minimal M9 medium (22, 23) for isotopic labeling. About 30 min before induction, the temperature of the cell culture was reduced to 16 °C. Cells were induced with 1 mM IPTG at an absorbance of ~0.8 at 600 nm and harvested after ~24 h.

The purification schemes of ALIX-Bro1, Src kinase, PTP1B, and TEV protease are described previously (22, 23, 45). For $ALIX^{Strep}_{1\text{-}868*}$, cells were resuspended in a lysis buffer

containing 50 mM Tris, pH 8.0, 250 mM NaCl, 1 mM EDTA, and 1 mM DTT. Cells were lysed using EmulsiFlex-C3 (Avestin) before being cleared by centrifugation (48,380g, 30 min). The resultant supernatant was loaded onto a Strep-Tactin Sepharose column (Cytiva), pre-equilibrated with lysis buffer, and eluted in the same buffer containing 2.5 mM desthiobiotin. Eluted protein was diluted with a running buffer containing 50 mM Tris, pH 8.0, and 5 mM BME, and loaded onto a Q-Sepharose HP column (Cytiva) with a 0–1 M NaCl gradient in the same running buffer. Eluted protein was concentrated (Amicon ultra- 15, 30-kDa cutoff, EMD Millipore) and loaded onto a HiLoad 26/600 Superdex 200 pg column (Cytiva) pre-equilibrated with 50 mM Tris, pH 8.0, 50 mM NaCl, 1 mM EDTA, and 1 mM DTT. Relevant fractions were pooled, flash-frozen, and stored at -80°C. For the corresponding construct without the Strep tag, $ALIX_{1–868*}$, a similar protocol was used. The cell lysate was initially loaded onto a HisTrap column (Cytiva) pre-equilibrated with the lysis buffer mentioned-above (sans DTT) and eluted with a 0–1 M imidazole gradient. Eluted protein was further purified using a Q-Sepharose HP column as described above. Relevant fractions were mixed with TEV protease (molar ratio of 5:1) to cleave off the N terminal GB1 fusion tag. Proteolysis was performed at room temperature (~12 h) and assessed for completion using SDS-PAGE. The reaction mixture was loaded back onto a HisTrap column. The flow-through fractions of the hydrolyzed product were pooled, concentrated, and further purified using the above-mentioned sizing column, and subsequently stored at -80°C.

A purification scheme like the one used for $ALIX_{1–868*}$ was used for $CEP55^{S215C}_{160-216}$ and the CHMP4 constructs. Proteins were initially purified by nickel affinity chromatography (HisTrap column, Cytiva) followed by size exclusion chromatography (HiLoad 26/600 Superdex 75-pg column, Cytiva). The resultant fractions were mixed with TEV protease to cleave the N-terminal

GB1 fusion tag. After completion of proteolysis, the reaction mixture was purified using nickel affinity and size exclusion chromatography.

ALIX-PRD constructs, $PRD^{Strep}_{703\text{-}868*}$, $PRD^{Strep}_{703\text{-}800}$, and $PRD_{800–868}$, were purified by a combination of affinity chromatography and reverse-phase HPLC, as described previously (22, 23). A protocol similar to the one used for $PRD^{Strep}_{703\text{-}868*}$ was used for purification of $PRD^{Strep}_{800\text{-}868}$. Cells resuspended in 50 mM Tris, pH 8.0, and 6 M GdmCl were lysed by heat shock (80 °C for 5 min, followed by 10 min on ice) and cleared by centrifugation. The cell lysate was filtered through a 0.45 μm vacuum-driven filtration device (Stericup, Sigma- Aldrich) and loaded onto a HisTrap column, pre-equilibrated with lysis buffer. The bound protein was washed with 10 column volumes of refolding buffer containing 50 mM Tris, pH 8.0, and 250 mM NaCl, and eluted in the same buffer using a 0–1 M imidazole gradient. Eluted fractions were pooled and mixed with recombinant TEV protease (molar ratio 50:1) to cleave off the N-terminal GB1 fusion tag. Upon completion of proteolysis (assessed using SDS-PAGE gel), the precipitated product was solubilized in 3 M GdmCl and 5% (v/v) DMSO, and further purified using reverse phase HPLC (Jupiter 10 μm C18 300 Å column) using a 25–37% acetonitrile gradient comprising 0.1% TFA. Pooled eluted fractions were lyophilized and stored at -80 °C.

All protein constructs were verified by MS as described before (22, 23, 45).

4.11.4 Sedimentation velocity AUC

Sedimentation velocity experiments on $ALIX^{Strep}_{1\text{-}868*}$ Strep and CHMP4 paralogs were carried out at 50,000 rpm and 30 °C on a Beckman Coulter ProteomeLab XL-I analytical ultracentrifuge and An50-Ti rotor following standard protocols (59). Stock solutions of proteins, dialyzed into a buffer containing 20 mM sodium phosphate, pH 6.5, 1 mM TCEP, and 2 mM

EDTA, were diluted to ~40 μM, and loaded into 12 mm two-channel centerpiece cells. Sedimentation data were collected using optical detection systems for absorbance (280 nm) and interference (655 nm) and analyzed using our published protocols (22, 60-62).

4.11.5 Fluorophore labeling

$CHMP4C^{S191C}_{121-233}$, $CHMP4B^{S184C}_{121-224}$, and MBP^{E64C}_{28-396} were mixed with a 4-molar equivalent of ATTO-647N maleimide in 20 mM HEPES, pH 7.5, 50 mM NaCl, and 1 mM EDTA. The reaction was allowed to proceed for ~30 min before being quenched by the addition of 50- molar equivalent of BME. Unreacted dye was removed using a PD MidiTrap G-25 desalting column (Cytiva). A similar procedure was used to conjugate ATTO-390 to $CHMP4B^{S184C}_{121-224}$. For TIRF microscopy, $PRD^{Strep}_{703-868*}$ Strep was conjugated to ATTO-488 NHS ester. $PRD^{Strep}_{703-868*}$ Strep was mixed with a 4-molar equivalent of ATTO-488 NHS ester in 50 mM HEPES, pH 7.5, and 20% (v/v) DMSO. The reaction was allowed to proceed for ~30 min, followed by the addition of 6 M GdmCl. The unreacted dye was removed by dialyzing the reaction mixture in 20 mM CAPS, pH 10, and 50 mM NaCl (Slide-A-Lyzer G2 dialysis cassettes, Thermo Fisher Scientific). The fluorophore labeling efficiencies of $CHMP4C^{S191C}_{121-233}$, $CHMP4B^{S184C}_{121-224}$ and $PRD^{Strep}_{703-868*}$ were determined by UV-Vis absorbance (~95% efficiency in all samples). For Alexa-Fluor488 labeling, 0.2 mg/mL Streptavidin Alexa-Fluor488 conjugate was added to ALIX constructs carrying a C-terminal strep tag (the concentrations of ALIX constructs were 50 μM each). To monitor Src-mediated dissolution of $ALIX^{Strep}_{1-868*}$ condensates, the concentration of Alexa-Fluor488 conjugate was lowered to 0.02 mg/mL.

4.11.6 Phase separation of ALIX constructs

ALIX constructs ($ALIX^{Strep}_{1\text{-}868*}$ and $ALIX_{1–868*}$), were dialyzed in 20 mM HEPES, pH 7.5, 50 mM NaCl, 1 mM DTT, and 1 mM EDTA. Phase separation was initiated by the addition of 5% (w/v) PEG-4000. In all samples, the protein concentration was maintained at 50 μM. For ALIX-PRD constructs, $PRD^{Strep}_{703\text{-}868*}$, $PRD^{Strep}_{703\text{-}800}$ and $PRD^{Strep}_{800\text{-}868}$, lyophilized samples were reconstituted in 20 mM CAPS, pH 10, and 50 mM NaCl and concentrated to ~2 mM stock solutions. Phase separation was induced by a rapid dilution of corresponding samples in the above-mentioned HEPES buffer comprising 5% (w/v) PEG-4000 to a final protein concentration of 50 μM.

4.11.7 Microscopy

Condensate samples were applied to microscope slides (Thermo Fisher Scientific; catalog no. 12-550-003) and sandwiched between coverslips (VWR; catalog no. 48366-227). Slides were incubated for 5 min at room temperature before imaging to allow condensates to adhere to the glass surface. DIC microscopy was performed on a Nikon Ti2 widefield microscope equipped with a DS-Qi2 CMOS camera and a 100x/1.49NA oil DIC N2 Objective. The sample was excited by a 395/470/640 nm laser controlled by a Lumencor SpectraX for imaging of ATTO-390, Alexa-Fluor488, and ATTO-647N, respectively.

To determine the particle size, the condensates of $ALIX^{Strep}_{1\text{-}868*}$, $PRD^{Strep}_{703\text{-}868*}$, and $PRD^{Strep}_{800\text{-}868}$ were imaged in multiple 3x3 tile sets where each tile spanned an area of 100x100 μm2. Particles of an area ≥ 0.08 μm2 (with fluorescence above background) were identified using the analyze particles function in Fiji/ImageJ (63), and their diameters were determined assuming circular morphologies. For the corresponding constructs without the strep tag, particles were identified using condensate edges. To quantify ThT colocalization within the condensates, condensates of

$ALIX^{Strep}_{1\text{-}868*}$, $PRD^{Strep}_{703\text{-}868*}$, and $PRD^{Strep}_{800\text{-}868}$ were prepared with 20 μM ThT and imaged immediately using a 470 nm laser. Images for each construct were collected under identical laser power, gain, and exposure time to facilitate a quantitative comparison of ThT fluorescence.

In vitro FRAP experiments were performed on a Nikon point scanning confocal C2 with 2 GaAsP PMTs using a Plan Apo λ 60x/1.4 NA oil objective. Data collection consisted of six pre-photobleaching frames excited at 0.5% 488 nm laser power, followed by photobleaching with 2 iterations of 50% 488 nm laser power directed at the bleaching area for 10 s, and subsequently excited at 0.2% 488 nm laser power at 0.5 s intervals for 120 frames as post-photobleaching frames. Images were corrected for background fluorescence and intensity from the bleached region was normalized against an unbleached region on a nearby condensate of similar size.

Timelapse images of $ALIX^{Strep}_{1\text{-}868*}$ + Src + ATP and pY-$ALIX^{Strep}_{1\text{-}868*}$ + PTP1B reactions were acquired using an EVOS-M5000 imaging system (Thermo Fisher Scientific) equipped with a PlanApo N 60X oil objective and GFP and TagBFP LED cubes. All the above microscopy images were collected at ambient temperature and analyzed with Fiji/ImageJ (63).

TIRF microscopy for timelapse imaging of Src-mediated dissolution of $PRD^{Strep}_{703\text{-}868*}$ condensates was performed on a Nikon Eclipse Ti2-E equipped with an iXon Ultra 897 EMCCD camera (Andor) and Apo TIRF 60x/1.49 NA Oil DIC N2 Objective. The TIRF angle was controlled by the N-STORM illumination arm in the Nikon Elements software. The sample was excited by a 488 nm laser (10% laser power) controlled by an Agilent laser box. The excitation light is reflected by a quad dichroic and the emission is filtered by a quad emission filter (emission window 502–549 nm). Images were acquired at 15 s intervals for 1.5 h. The spinning disk pinhole was 50 μm.

4.11.8 Living cells

Plasmid of mNeonGreen in pcDNA3.1 was generated by PCR amplification from pmNeonGreen-N1 (Allele Biotechnology) using appropriate primers (Table 4.3). The BamHI/EcoRI digested PCR product was then ligated into BamHI/EcoRI-digested pcDNA3.1 backbone. Plasmids of $ALIX^{mNG}_{1\text{-}868*}$ and $ALIX^{mNG}_{1\text{-}702}$ were generated from $ALIX^{Strep}_{1\text{-}868*}$ plasmid by amplifying the respective segments using PCR and appropriate primers (Table 4.3). The resultant products were inserted into pcDNA3.1-mNG vector using Gibson assembly protocol and HiFi DNA assembly master mix (New England Biolabs; catalog no. E2621S). Plasmid of $ALIX^{mNG}_{1\text{-}868}$ was generated from $ALIX^{mNG}_{1\text{-}868*}$ using PCR and appropriate primers containing the point mutation primers (Table 4.3). All three ALIX constructs were verified by Sanger sequencing (Azenta Life Sciences).

HEK293T cells (ATCC, catalog no. CRL-3216) were cultured in Dulbecco's modified Eagle medium (Thermo Fisher Scientific, catalog no. 11-885-084) containing 4.5 g/l glucose, 10% fetal bovine serum (Thermo Fisher Scientific, catalog no. 26-140-079), and 1% v/v penicillin-streptomycin (Thermo Fisher Scientific, catalog no. 15-140-122). Cells were grown in humidified incubators (Heracell150) at 37 °C and with 5% carbon dioxide. Cells were checked for mycoplasma using Hoechst staining (Thermo Fisher Scientific; catalog no. 62249). For microscopy imaging, cells were plated on 35 mm glass-bottomed dishes (Cellvis, catalog no. D35-14-1.5-N). Cells were transfected 2–24 h with 500 ng of plasmid after plating using 1.5 μL PolyJet in vitro DNA transfection reagent (SignaGen Laboratories; catalog no. SL100688) and imaged ~24 h after transfection. Cell density was 50–80% confluent on the day of transfection.

For all live-cell imaging experiments, cells were washed and incubated in Hanks' balanced salt solution (Thermo Fisher Scientific; catalog no. 14065056) buffered with 20 mM HEPES, pH

7.4, and supplemented with 2 g/l glucose. Images were acquired on a Zeiss AxioObserver Z7 microscope equipped with a 40x1.4 N./A. oil-immersion objective, Prime 95B sCMOS camera (Photometrics) controlled by MetaFluor fluorescence ratio imaging software (Molecular Devices, LLC). Imaging was performed using the ET480/30x excitation filter with a T505dcxr dichroic mirror, and a ET535/50x emission filter. All filters were alternated by a Lambda 10-2 filter-changer (Sutter Instruments). Exposure times ranged between 50–500 ms. Raw fluorescence images were corrected by subtracting the background fluorescence intensity of a cell-free region from the emission intensities of ALIX-expressing cells.

In-cell FRAP experiments were performed on a Nikon Ti2 C2 confocal microscope equipped with a CSU-X1 spinning disc (Yokogawa), a 100x1.49 NA oil objective (Nikon), and 405/488/561/640 nm laser lines, dual Prime 95B sCMOS camera (Teledyne photometrics), Okolabs stage-top incubator, and OptiMicroscan FRAP box (Mad City Labs Inc.). The selected condensates were bleached for 500 ms with 405 nm laser (100% power) and observed using 488 nm laser and a single bandpass filter (525/36 nm) every 1 s for 3 min post-bleaching. Intensity data was collected using NISElements and normalized.

Table 4.3 Primers used for mammalian expression

Construct	Forward primer	Reverse primer
pmNeonGreenN1	TAAGCTTGGTACCGAGCT CGGATCCATGGTGAGCAA GGGCGAG	ACTGTGCTGGATATCTGCA GAATTCCATCACATCGGTA AAGGC
$ALIX^{mNG}_{1\text{-}868*}$	CTGGCTAGCGTTTAAACT TAAGCTTATGCATCACCA TCACCATCATGG	CTGGCTAGCGTTTAAACT TAAGCTTATGCATCACCA TCACCATCATGG
$ALIX^{mNG}_{1\text{-}702}$	CTGGCTAGCGTTTAAACT TAAGCTTATGCATCACCA TCACCATCATGG	CCTCGCCCTTGCTCACCA TGGATCCGCGTTCGGTTT TGCG
$ALIX^{mNG}_{1\text{-}868}$ (for P801G mutation)	GCCCCCCATATCCGACGTAC	GTCGGATATGGGGGGCCTTG

4.11.9 CD spectroscopy

CD measurements (178–280 nm, 1 nm data pitch, continuous scanning with 1 nm bandwidth, 60 nm/min, and 5 accumulations) with ~10 μM CHMP4 paralogs in 10 mM sodium phosphate, pH 6.5, were carried out in 1 mm quartz cuvettes (Thermo Fisher Scientific; catalog no. NC9651589) using an Aviv model 215 spectrometer. CD data were analyzed as described previously (23).

4.11.10 NMR Spectroscopy

Samples of ^{15}N-labeled or $^{15}N/^{13}C$-labeled or $^{15}N/^{2}H$ or $^{15}N/^{2}H/^{13}C$-labeled CHMP4 constructs, $^{15}N/^{13}C$-labeled $PRD^{Strep}_{703\text{-}800}$, and $^{15}N/^{2}H$-labeled or $^{15}N/^{13}C/^{2}H$-labeled Bro1 were prepared in a buffer comprising 20 mM sodium phosphate, pH 6.5, 1 mM TCEP, and 2 mM EDTA. An identical buffer (sans TCEP) was used for intramolecular PRE experiments. All NMR samples contained 7% (v/v) deuterium oxide (D2O).

NMR experiments were carried out at 30 °C on Bruker 600 and 800 MHz spectrometers equipped with z-gradient triple resonance cryoprobes. Spectra were processed using NMRPipe (64) and analyzed using the CCPN software suite (65). Sequential ^{1}H, ^{15}N, and ^{13}C backbone resonance assignments of CHMP4 constructs, in the absence and presence of Bro1/$PRD^{Strep}_{703-800}$, were carried out using TROSY-based three-dimensional (3D) triple resonance experiments (66). $^{3}J_{HN-H\alpha}$ couplings were measured on uniformly ^{15}N-labeled CHMP4 paralogs (0.5 mM each) using a WATERGATE-optimized 2D TROSY pulse sequence (67). ^{15}N-R_1 and $R_{1\rho}$ measurements (68) were carried out on uniformly ^{15}N-labeled CHMP4 paralogs (0.5 mM each) at 800 MHz using our previously described protocol (45). Intramolecular PREs were measured on two CHMP4C constructs ($CHMP4C^{G154C}_{121-233}$ and $CHMP4C^{M165C}_{121-233}$) from the peak height ratios between two 2D ^{1}H-^{15}N TROSY-HSQC spectra with paramagnetic (MTSL-labeled) and diamagnetic (labeled with acetylated diamagnetic analog of MTSL) samples, 0.2 mM each. The procedure for site-specific spin labeling is described in our previous work (23). Lifetime line-broadening (ΔR_2) values of CHMP4 constructs are given by the difference in ^{15}N-R_2 values obtained in the presence and absence of ALIX domains, Bro1 and $PRD^{Strep}_{703-800}$. NMR chemical shift perturbation experiments were performed using 0.15 mM ^{15}N-labeled CHMP4 constructs and unlabeled Bro1 and $PRD^{Strep}_{703-800}$ (0.075–0.45 mM). Similar experiments were carried out using 30 μM $^{15}N/^{2}H$-labeled CHMP4 constructs, namely $CHMP4C^{S191C}_{121-233}$, $CHMP4C^{S191C,AAA}_{121-233}$, and $CHMP4B^{S184C}_{121-224}$, and 90 μM unlabeled $ALIX^{Strep}_{1-868*}$. Perturbations were calculated as follows: $\Delta_{H/N}=\{(\Delta\delta_{HN})^2+(0.154\times\Delta\delta_N)^2\}^{1/2}$, where $\Delta\delta_{HN}$ and $\Delta\delta_N$ are the $^{1}H_N$ and ^{15}N chemical shift differences in ppm, respectively, between free and bound states. Additionally, chemical shift perturbation experiments were performed using 0.1 mM $^{15}N/^{2}H$-labeled Bro1 domain and 0.3 mM unlabeled CHMP4 constructs. The backbone resonance assignments for Bro1 were taken from our

previously published work (23) and further confirmed using TROSY-based 3D HNCA and HNCO experiments performed on samples comprising 0.5 mM $^{15}N/^{2}H/^{13}C$-labeled Bro1 and 1 mM CHMP4 paralogs, $CHMP4C^{S191C}_{121-233}$ and $CHMP4B^{S184C}_{121-224}$. Similar experiments were carried out using 0.15 mM $^{15}N/^{13}C$-labeled $PRD^{Strep}_{703-800}$ and 0.45 mM unlabeled CHMP4 constructs. Because of its high proline content (108 amino acids, ~28% proline residues), identical measurements were performed using 2D ^{13}C-^{15}N CON correlation experiments (69). The backbone resonance assignments for $PRD^{Strep}_{703-800}$ were obtained from our published work (22). $\Delta_{H/N}$ perturbations were calculated using the above-described formula. $\Delta_{C'/N}$ perturbations were calculated using $\Delta_{C'/N}=\left\{\left(0.3\times\Delta\delta_{C'}\right)^2+(0.154\times\Delta\delta_N)^2\right\}^{1/2}$, where $\Delta\delta_{C'}$ and $\Delta\delta_N$ are the ^{13}C' and ^{15}N chemical shift differences in ppm, respectively, between free and bound states.

4.11.11 Isothermal titration calorimetry (ITC)

ITC measurements were performed using a low-volume Affinity ITC calorimeter (TA Instruments). 1.6–2.6 µl aliquots of solutions containing between 300–500 µM CHMP4 paralogs, $CHMP4C^{S191C}_{121-233}$ and $CHMP4B^{S184C}_{121-224}$, were individually injected (20 injections) into a cell containing 30–50 µM $ALIX^{Strep}_{1-868*}$ or Bro1. The experiments were performed at 25°C in the same buffer that was used for NMR measurements. Additional measurements of interactions between $CHMP4C^{S191C}_{121-233}$ or $CHMP4C^{S191C,AAA}_{121-233}$ and $ALIX^{Strep}_{1-868*}$ were carried out in the presence of 150 mM NaCl (the remaining buffer composition was the same as above). Note that for $CHMP4C^{S191C,AAA}_{121-233}$ – $ALIX^{Strep}_{1-868*}$ interactions, the protein concentrations were 1500 µM $CHMP4C^{S191C,AAA}_{121-233}$ and 300 µM $ALIX^{Strep}_{1-868*}$. Results were analyzed using NanoAnalyze software (TA Instruments).

4.11.12 TEM

The solution comprising condensates of 50 μM $PRD^{Strep}_{703-868*}$ was incubated at room temperature for two days. TEM sample was prepared using our published protocol (70). TEM images were acquired using a JEM-1400Plus transmission electron microscope (JEOL) and recorded on a OneView digital camera (Gatan).

4.11.13 Reversible tyrosine phosphorylation of ALIX

To produce hyperphosphorylated (pY) $ALIX^{Strep}_{1-868*}$, 50 μM $ALIX^{Strep}_{1-868*}$, 5 μM Src, and 5 mM ATP were mixed in a buffer containing 50 mM Tris (pH 7.5), 50 mM NaCl, 5 mM $MgCl_2$, and 2 mM DTT. The reaction was allowed to proceed for ~18 h at 30 °C. Src was removed from the reaction mixture using a HisTrap column (Cytiva) pre-equilibrated with 50 mM Tris, pH 8, and 50 mM NaCl. The resultant flow-through fractions of $pYALIX^{Strep}_{1-868*}$ were pooled, and excess ATP and ADP were removed using a HiPrep 26/10 Desalting column (Cytiva) pre-equilibrated with 20 mM HEPES, pH 7.5, 50 mM NaCl, 1 mM DTT, 1 mM EDTA.

The reaction mixtures comprising $ALIX^{Strep}_{1-868*}$ + Src + ATP and pY-$ALIX^{Strep}_{1-868*}$ + PTP1B (and corresponding control samples) were loaded into 1 mm quartz cuvettes (Starna Cells, Inc.) and turbidity measurements were recorded at OD_{330} nm every 30 s using an Agilent Cary 50 Bio UV-Vis spectrophotometer. Reversible tyrosine phosphorylation of $ALIX^{Strep}_{1-868*}$ was also assessed using western blotting using our published protocol (22, 23).

4.12 Acknowledgements

We thank Z. Jiang, Y. Shen, J. H. Lee, J. Ying, J. L. Baber, P. A. Jennings, and I. Budin for useful discussions; X. Huang, Y. Su, T. Meerloo, E. Griffis, P. Guo, and A. Bobkov for

technical support. We acknowledge the use of facilities and instrumentation supported by the NIH for the UCSD Cellular and Molecular Medicine EM Core Facility; S10OD023527, and the UCSD Molecular Mass Spectrometry Facility; 1S10RR25636-1A1. This work was funded in part by a 2018 Development Award (to L. D.) from the SD-CFAR (an NIH-funded program; P30 AI036214), Collaborative Development Awards (to L. D.) from the HIVE center (an NIH-funded program; U54 AI150472) and the CHEETAH center (an NIH-funded program; P50 AI150464), by the Hellman fellowship (to L.D.), by NIH grant R35 GM147708 (to L.D.), an NSF graduate research fellowship under grant no. DGE-1650112 (to R.D.E.), by NIH grant R35 CA197622 (to J.Z.) and a research grant from Pfizer (to J.Z.). R.G. was supported by the Intramural Research Program at the NIDDK, NIH.

Chapter 4, in part, has been submitted for publication of the material as it may appear in: Elias, R. D., Zhu, Y., Su, Q., Ghirlando, R., Zhang, J., and Deshmukh, L. Reversible phase separation of ESCRT-protein ALIX through tyrosine phosphorylation. The dissertation author was the primary researcher and author of this paper.

4.13 References

1. Mierzwa, B., and Gerlich, D. W. (2014) Cytokinetic abscission: molecular mechanisms and temporal control. Dev. Cell 31, 525-538

2. Vietri, M., Radulovic, M., and Stenmark, H. (2020) The many functions of ESCRTs. Nat. Rev. Mol. Cell Biol. 21, 25-42

3. McCullough, J., Fisher, R. D., Whitby, F. G., Sundquist, W. I., and Hill, C. P. (2008) ALIX-CHMP4 interactions in the human ESCRT pathway. Proc. Natl. Acad. Sci. U. S. A. 105, 7687-7691

4. Tang, S., Buchkovich, N. J., Henne, W. M., Banjade, S., Kim, Y. J., and Emr, S. D. (2016) ESCRT-III activation by parallel action of ESCRT-I/II and ESCRT-0/Bro1 during MVB biogenesis. eLife 5, e15507

5. Steigemann, P., Wurzenberger, C., Schmitz, M. H., Held, M., Guizetti, J., Maar, S., and Gerlich, D. W. (2009) Aurora B-mediated abscission checkpoint protects against tetraploidization. Cell 136, 473-484

6. Nähse, V., Christ, L., Stenmark, H., and Campsteijn, C. (2017) The abscission checkpoint: Making it to the final cut. Trends Cell Biol. 27, 1-11

7. Petsalaki, E., and Zachos, G. (2021) The abscission checkpoint: A guardian of chromosomal stability. Cells 10

8. Carlton, J. G., Caballe, A., Agromayor, M., Kloc, M., and Martin-Serrano, J. (2012) ESCRT-III governs the Aurora B-mediated abscission checkpoint through CHMP4C. Science 336, 220-225

9. Pharoah, P. D. P., Tsai, Y.-Y., Ramus, S. J., Phelan, C. M., Goode, E. L., Lawrenson, K., Buckley, M., Fridley, B. L., Tyrer, J. P., Shen, H., Weber, R., Karevan, R., Larson, M. C., Song, H., Tessier, D. C., Bacot, F., Vincent, D., Cunningham, J. M., Dennis, J., Dicks, E., Aben, K. K., Anton-Culver, H., Antonenkova, N., Armasu, S. M., Baglietto, L., Bandera, E. V., Beckmann, M. W., Birrer, M. J., Bloom, G., Bogdanova, N., Brenton, J. D., Brinton, L. A., Brooks-Wilson, A., Brown, R., Butzow, R., Campbell, I., Carney, M. E., Carvalho, R. S., Chang-Claude, J., Chen, Y. A., Chen, Z., Chow, W.-H., Cicek, M. S., Coetzee, G., Cook, L. S., Cramer, D. W., Cybulski, C., Dansonka-Mieszkowska, A., Despierre, E., Doherty, J. A., Dörk, T., du Bois, A., Dürst, M., Eccles, D., Edwards, R., Ekici, A. B., Fasching, P. A., Fenstermacher, D., Flanagan, J., Gao, Y.-T., Garcia-Closas, M., Gentry-Maharaj, A., Giles, G., Gjyshi, A., Gore, M., Gronwald, J., Guo, Q., Halle, M. K., Harter, P., Hein, A., Heitz, F., Hillemanns, P., Hoatlin, M., Høgdall, E., Høgdall, C. K., Hosono, S., Jakubowska, A., Jensen, A., Kalli, K. R., Karlan, B. Y., Kelemen, L. E., Kiemeney, L. A., Kjaer, S. K., Konecny, G. E., Krakstad, C., Kupryjanczyk, J., Lambrechts, D., Lambrechts, S., Le, N. D., Lee, N., Lee, J., Leminen, A., Lim, B. K., Lissowska, J., Lubiński, J., Lundvall, L., Lurie, G., Massuger, L. F. A. G., Matsuo, K., McGuire, V., McLaughlin, J. R., Menon, U., Modugno, F., Moysich, K. B., Nakanishi, T., Narod, S. A., Ness, R. B., Nevanlinna, H., Nickels, S., Noushmehr, H., Odunsi, K., Olson, S., Orlow, I., Paul, J., Pejovic, T., Pelttari, L. M., Permuth-Wey, J., Pike, M. C., Poole, E. M., Qu, X., Risch, H. A., Rodriguez-Rodriguez, L., Rossing, M. A., Rudolph, A., Runnebaum, I., Rzepecka, I. K., Salvesen, H. B., Schwaab, I., Severi, G., Shen, H., Shridhar, V., Shu, X.-O., Sieh, W., Southey, M. C., Spellman, P., Tajima, K., Teo, S.-H., Terry, K. L., Thompson, P. J., Timorek, A., Tworoger, S. S., van Altena, A. M., van den Berg, D., Vergote, I., Vierkant, R. A., Vitonis, A. F., Wang-Gohrke, S., Wentzensen, N., Whittemore, A. S., Wik, E., Winterhoff, B., Woo, Y. L., Wu, A. H., Yang, H. P., Zheng, W., Ziogas, A., Zulkifli, F., Goodman, M. T., Hall, P., Easton, D. F., Pearce, C. L., Berchuck, A., Chenevix-Trench, G., Iversen, E., Monteiro, A. N. A., Gayther, S. A., Schildkraut, J. M., Sellers, T. A., Australian Cancer, S., and Australian Ovarian Cancer Study, G. (2013) GWAS meta-analysis and replication identifies three new susceptibility loci for ovarian cancer. Nat. Genet. 45, 362-370

10. Sadler, J. B. A., Wenzel, D. M., Strohacker, L. K., Guindo-Martínez, M., Alam, S. L., Mercader, J. M., Torrents, D., Ullman, K. S., Sundquist, W. I., and Martin-Serrano, J. (2018) A cancer-associated polymorphism in ESCRT-III disrupts the abscission checkpoint and promotes genome instability. Proc. Natl. Acad. Sci. U. S. A. 115, E8900-E8908

11. Strohacker, L. K., Mackay, D. R., Whitney, M. A., Couldwell, G. C., Sundquist, W. I., and Ullman, K. S. (2021) Identification of abscission checkpoint bodies as structures that regulate ESCRT factors to control abscission timing. eLife 10, e63743

12. Spector, D. L., and Lamond, A. I. (2011) Nuclear speckles. Cold Spring Harb. Perspect. Biol. 3, a000646

13. Shin, Y., and Brangwynne, C. P. (2017) Liquid phase condensation in cell physiology and disease. Science 357, eaaf4382

14. Boeynaems, S., Alberti, S., Fawzi, N. L., Mittag, T., Polymenidou, M., Rousseau, F., Schymkowitz, J., Shorter, J., Wolozin, B., Van Den Bosch, L., Tompa, P., and Fuxreiter, M. (2018) Protein phase separation: A new phase in cell biology. Trends Cell Biol. 28, 420-435

15. Murthy, A. C., N. L. Fawzi, N.L. (2020) The (un)structural biology of biomolecular liquid-liquid phase separation using NMR spectroscopy. J. Biol. Chem. 295, 2375-2384

16. Su, Q., Mehta, S., Zhang, J. (2021) Liquid-liquid phase separation: Orchestrating cell signaling through time and space. Mol. Cell 81, 4137-4146

17. Rai, A. K., Chen, J. X., Selbach, M., and Pelkmans, K. (2018) Kinase-controlled phase transition of membraneless organelles in mitosis. Nature 559, 211-216

18. Strom, A. R., and Brangwynne, C.P. (2019) The liquid nucleome – phase transitions in the nucleus at a glance. J. Cell Sci. 132

19. M. H. H. Schmidt, I. Dikic, O. Bögler, Src phosphorylation of Alix/AIP1 modulates its interaction with binding partners and antagonizes its activities. J. Biol. Chem. 280, 3414-3425 (2005).

20. Kasahara, K., Nakayama, Y., Nakazato, Y., Ikeda, K., Kuga, T., and Yamaguchi, N. (2007) Src signaling regulates completion of abscission in cytokinesis through ERK/MAPK activation at the midbody. J. Biol. Chem. 282, 5327-5339

21. Stuible, M., Abella, J. V., Feldhammer, M., Nossov, M., Sangwan, V., Blagoev, B., Park, M., and Tremblay, M. L. (2010) PTP1B targets the endosomal sorting machinery: . J. Biol. Chem. 285, 23899-23907

22. Elias, R. D., Ma, W., Ghirlando, R., Schwieters, C. D., Reddy, V. S., and Deshmukh, L. (2020) Proline-rich domain of human ALIX contains multiple TSG101-UEV interaction sites and forms phosphorylation-mediated reversible amyloids. Proc. Natl. Acad. Sci. U. S. A. 117, 24274-24284

23. Elias, R. D., Ramaraju, B., and Deshmukh, L. (2021) Mechanistic roles of tyrosine phosphorylation in reversible amyloids, autoinhibition, and endosomal membrane association of ALIX. J. Biol. Chem. 297, 101328

24. Woolstenhulme, C. J., Guydosh, N. R., Green, R., and Buskirk, A.R. (2015) High-precision analysis of translational pausing by ribosome profiling in bacteria lacking EFP. Cell Rep. 11, 13-21

25. Lee, H. H., Elia, N., Ghirlando, R., Lippincott-Schwartz, J., and Hurley, J. H. (2008) Midbody targeting of the ESCRT machinery by a noncanonical coiled coil in CEP55. Science 322, 576-580

26. Schmidt, T. G., and Skerra, A. (2007) The Strep-tag system for one-step purification and high-affinity detection or capturing of proteins. Nat Protoc 2, 1528-1535

27. Zhai, Q., Landesman, M. B., Chung, H.-Y., Dierkers, A., Jeffries, C. M., Trewhella, J., Hill, C. P., and Sundquist, W. I. (2011) Activation of the retroviral budding factor ALIX. J. Virol. 85, 9222-9226

28. Fezoui, Y., Hartley, D. M., Harper, J. D., Khurana, R., Walsh, D. M., Condron, M. M., Selkoe, D. J., Lansbury, P. T., Jr., Fink, A. L., and Teplow, D. B. (2000) An improved method of preparing the amyloid beta-protein for fibrillogenesis and neurotoxicity experiments. Amyloid 7, 166-178

29. Hou, L., Shao, H., Zhang, Y., Li, H., Menon, N. K., Neuhaus, E. B., Brewer, J. M., Byeon, I. J., Ray, D. G., Vitek, M. P., Iwashita, T., Makula, R. A., Przybyla, A. B., and Zagorski, M. G. (2004) Solution NMR studies of the A beta(1-40) and A beta(1-42) peptides establish that the Met35 oxidation state affects the mechanism of amyloid formation. J. Am. Chem. Soc. 126, 1992-2005

30. Shaner, N. C., Lambert, G. G., Chammas, A., Ni, Y., Cranfill, P. J., Baird, M. A., Sell, B. R., Allen, J. R., Israelsson, M., Davidson M. W., and Wang, J. (2013) A bright monomeric green fluorescent protein derived from Branchiostoma lanceolatum. Nat. Methods 10, 407-409

31. Gasteiger, E., Hoogland, C., Gattiker, A., Duvaud, S. e., Wilkins, M. R., Appel, R. D., and Bairoch, A. (2005) Protein Identification and Analysis Tools on the ExPASy Server. in The Proteomics Protocols Handbook (Walker, J. M. ed.), Humana Press, Totowa, NJ. pp 571-607

32. Bajorek, M., Schubert, H. L., McCullough, J., Langelier, C., Eckert, D. M., Stubblefield, W. M., Uter, N. T., Myszka, D. G., Hill, C. P., and Sundquist, W. I. (2009) Structural basis for ESCRT-III protein autoinhibition. Nat. Struct. Mol. Biol. 16, 754-762

33. Shim, S., Kimpler, L. A., and Hanson, P. I. (2007) Structure/function analysis of four core ESCRT-III proteins reveals common regulatory role for extreme C-terminal domain. Traffic 8, 1068-1079

34. Jumper, J., Evans, R., Pritzel, A., Green, T., Figurnov, M., Ronneberger, O., Tunyasuvunakool, K., Bates, R., Žídek, A., Potapenko, A., Bridgland, A., Meyer, C., Kohl, S. A. A., Ballard, A. J., Cowie, A., Romera-Paredes, B., Nikolov, S., Jain, R., Adler, J., Back, T., Petersen, S., Reiman, D., Clancy, E., Zielinski, M., Steinegger, M., Pacholska,

M., Berghammer, T., Bodenstein, S., Silver, D., Vinyals, O., Senior, A. W., Kavukcuoglu, K., Kohli, P., and Hassabis, D. (2021) Highly accurate protein structure prediction with AlphaFold. Nature 596, 583-589

35. Kjaergaard, M., Brander, S., and Poulsen, F. M. (2011) Random coil chemical shift for intrinsically disordered proteins: effects of temperature and pH. J. Biomol. NMR 49, 139-149

36. Kjaergaard, M., and Poulsen, F. M. (2011) Sequence correction of random coil chemical shifts: correlation between neighbor correction factors and changes in the Ramachandran distribution. J. Biomol. NMR 50, 157-165

37. Shen, Y., and Bax, A. (2013) Protein backbone and sidechain torsion angles predicted from NMR chemical shifts using artificial neural networks. J. Biomol. NMR 56, 227-241

38. Shen, Y., Roche, J., Grishaev, A., and Bax, A. (2018) Prediction of nearest neighbor effects on backbone torsion angles and NMR scalar coupling constants in disordered proteins. Protein Sci. 27, 146-158

39. Gillespie, J. R, and Shortle, D. (1997) Characterization of long-range structure in the denatured state of staphylococcal nuclease. I. paramagnetic relaxation enhancement by nitroxide spin labels. J. Mol. Biol. 268, 158-169

40. Dedmon, M. M., Lindorff-Larsen, K., Christodoulou, J., Vendruscolo, M., and Dobson, C.M. (2005) Mapping long-range interactions in α-Synuclein using spin-label NMR and ensemble molecular dynamics simulations. J. Am. Chem. Soc. 127, 476-477

41. Bertoncini, C. W., Jung, Y. S., Fernandez, C. O., Hoyer, W., Griesinger, C., Jovini, T. T., and Zweckstetter, M. (2005) Release of long-range tertiary interactions potentiates aggregation of natively unstructured α-synuclein. Proc. Natl. Acad. Sci. U.S.A. 102, 1430-1435

42. Tyukhtenko, S., Deshmukh, L., Kumar, V., Lary, J., Cole, J., Lemmon, V., and Vinogradova, O. (2008) Characterization of the neuron-specific L1-CAM cytoplasmic tail: naturally disordered in solution it exercises different binding modes for different adaptor proteins. Biochemistry 47, 4160-4168

43. Wright, P. E., and Dyson, H. J. (2015) Intrinsically disordered proteins in cellular signalling and regulation. Nat Rev Mol Cell Biol 16, 18-29

44. Fawzi, N. L., Ying, J., Ghirlando, R., Torchia, D. A., and Clore, G. M. (2011) Atomic-resolution dynamics on the surface of amyloid-β protofibrils probed by solution NMR. Nature 480, 268-272

45. Ramaraju, B., Nelson, S. L., Zheng, W., Ghirlando, R., and Deshmukh, L. (2021) Quantitative NMR study of insulin-degrading enzyme using amyloid-β and HIV-1 p6 elucidates Its chaperone activity. Biochemistry 60, 2519-2523

46. Fuxreiter, M., Simon, I., Friedrich, P., and Tompa, P. (2004) Preformed structural elements feature in partner recognition by intrinsically unstructured proteins. J. Mol. Biol. 338, 1015-1026

47. Arai, M., Sugase, K., Dyson, H. J., and Wright, P. E. (2015) Conformational propensities of intrinsically disordered proteins influence the mechanism of binding and folding. Proc. Natl. Acad. Sci. U. S. A. 112, 9614-9619

48. Mollica, L., Bessa, L. M., Hanoulle, X., Jensen, M. R., Blackledge, M., and Schneider, R. (2016) Binding mechanisms of intrinsically disordered proteins: Theory, simulation, and experiment. Front. Mol. Biosci. 3

49. Zhang, X., Vgers, M., McCarty, J., Rauch, J. N., Fredrickson, G. H., Wilson, M. Z., Shea, J. E., Han, S., and Kosik, K. S. (2020) The proline-rich domain promotes Tau liquid-liquid phase separation in cells. J. Cell Biol. 219

50. Jiang, H., Wang, S., Huang, Y., He, Y., Cui, H., Zhu, X., and Zheng, Y. (2015) Phase transition of spindle-associated protein regulate spindle apparatus assembly. Cell 163, 108-122

51. Lin, Y., Currie, S. L., and Rosen, M. K. (2017) Intrinsically disordered sequences enable modulation of protein phase separation through distributed tyrosine motifs. J Biol Chem 292, 19110-19120

52. Pak, C. W., Kosno, M., Holehouse, A. S., Padrick, S. B., Mittal, A., Ali, R., Yunus, A. A., Liu, D. R., Pappu, R. V., and Rosen, M. K. (2016) Sequence determinants of intracellular phase separation by complex coacervation of a disordered protein. Mol. Cell 63, 72-85

53. Kim, T. H., Payliss, B. J., Nosella, M. L., Lee, I. T. W., Toyama, Y., Forman-Kay, J. D., and Kay, L. E. (2021) Interaction hot spots for phase separation revealed by NMR studies of a CAPRIN1 condensed phase. Proc. Natl. Acad. Sci. U.S.A. 118, e2104897118

54. Kim, T. H., Tsang, B., Vernon, R. M., Sonenberg, N., Kay, L. E., and Forman-Kay, J. D. (2019) Phospho-dependent phase separation of FMRP and CAPRIN1 recapitulates regulation of translation and deadenylation. Science 365, 825-829

55. Ryan, V. H., Perikari, T. M., Naik, M. T., Saueressig, C. F., Lins, J., Dignon, G. L., Mittal, J., Hart, A. C., and Fawzi, N. L. (2021) Tyrosine phosphorylation regulates hnRNPA2 granule protein partitioning and reduces neurodegeneration. EMBO J. 40, e105001

56. Choy, M. S., Li, Y., Machado, L. E. S. F., Kunze, M. B. A., Connors, C. R., Wei, Y., Lindroff-Larsen, K., Page, R., and Peti, W. (2017) Conformational rigidity and protein dynamics at distinct timescales regulate PTP1B activity and allostery. Mol. Cell 65, 644-658.e645,

57. Huth, J. R., Bewley, C. A., Jackson, B. M., Hinnebusch, A. G., Clore, G. M., and Gronenborn, A. M. (1997) Design of an expression system for detecting folded protein

domains and mapping macromolecular interactions by NMR. Protein Sci. 6, 2359-236458.

58. Mith, P. K., Krohn, R. I., Hermanson, G. T., Mallia, A. K., Gartner, F. H., Provenzano, M. D., Fujimoto, E. K., Goeke, N. M., Olson, B. J., and Klenk, D. C. (1985) Measurement of protein using bicinchoninic acid. Anal. Biochem. 150, 76-85.

59. Zhao, H., Brautigam, C. A., Ghirlando, R., and Schuck, P. (2013) Overview of current methods in sedimentation velocity and sedimentation equilibrium analytical ultracentrifugation. Curr. Protoc. Protein Sci. Chapter 20, Unit20.12

60. Deshmukh, L., Schwieters, C. D., Grishaev, A., Ghirlando, R., Baber, J. L., and Clore, G. M. (2013) Structure and dynamics of full-length HIV-1 capsid protein in solution. J Am Chem Soc 135, 16133-16147

61. Deshmukh, L., Ghirlando, R.,and Clore, G.M. (2014) Investigation of the structure and dynamics of the capsid-spacer peptide 1-nucleocapsid fragment of the HIV-1 Gag polyprotein by solution NMR spectroscopy. Angew. Chem. Int. Ed. Engl. 53, 1025-1028

62. Deshmukh, L., Louis, J. M., Ghirlando, R., and Clore, G. M. (2016) Transient HIV-1 Gag-protease interactions revealed by paramagnetic NMR suggest origins of compensatory drug resistance mutations. Proc Natl Acad Sci U S A 113, 12456-12461

63. Schindelin, J., Arganda-Carreras, I., Frise, E., Kaynig, V., Longair, M., Pietzsch, T., Preibisch, S., Rueden, C., Saalfeld, S., Schmid, B., Tinevez, J. Y., White, D. J., Hartenstein, V., Eliceiri, K., Tomancak, P., and Cardona, A. (2012) Fiji: an open-source platform for biological-image analysis. Nature Methods 9, 676-682

64. Delaglio, F., Grzesiek, S., Vuister, G. W., Zhu, G., Pfeifer, J., and Bax, A. (1995) NMRPipe: a multidimensional spectral processing system based on UNIX pipes. J. Biomol. NMR 6, 277-293

65. Vranken, W. F., Boucher, W., Stevens, T. J., Fogh, R. H., Pajon, A., Llinas, M., Ulrich, E. L., Markley, J. L., Ionides, J., and Laue, E. D. (2005) The CCPN data model for NMR spectroscopy: development of a software pipeline. Proteins 59, 687-696

66. Clore, G. M., and Gronenborn, A. M. (1998) Determining the structures of large proteins and protein complexes by NMR. Trends Biotechnol. 16, 22-34

67. Roche, J., Ying, J., and Bax, A. (2016) Accurate measurement of 3JHNHα couplings in small or disordered proteins from WATERGATE-optimized TROSY spectra. J. Biomol. NMR 64, 1-7

68. Lakomek, N. A., Ying, J., and Bax, A. (2012) Measurement of ^{15}N relaxation rates in perdeuterated proteins by TROSY-based methods. J Biomol NMR 53(3):209-221.

69. Bastidas, M., Gibbs, E. B., Sahu, D., and Showalter, S. A. (2015) A primer for carbon-detected NMR applications to intrinsically disordered proteins in solution. Concepts Magn. Reson. A: Bridg. Educ. Res. 44, 54-66

70. Deshmukh, L., Ghirlando, R., and Clore, G. M. (2015) Conformation and dynamics of the Gag polyprotein of the human immunodeficiency virus 1 studied by NMR spectroscopy. Proc Natl Acad Sci U S A 112, 3374-3379

71. Zhai, Q., Landesman, M. B., Robinson, H., Sundquist, W. I., and Hill, C. P. (2011) Identification and structural characterization of the ALIX-binding late domains of simian immunodeficiency virus SIVmac239 and SIVagmTan-1. J. Virol. 85, 632-637

72. Wenzel, D. M., Mackay, D. R., Skalicky, J. J., Paine, E. L., Miller, M. S., Ullman, K. S., and Sundquist, W. I. (2022) Comprehensive analysis of the human ESCRT-III-MIT domain interactome reveals new cofactors for cytokinetic abscission. eLife 11, e77779

73. Morita, E., Sandrin, V., Chung, H. Y., Morham, S. G., Gygi, S. P., Rodesch, C. K., and Sundquist, W. I. (2007) Human ESCRT and ALIX proteins interact with proteins of the midbody and function in cytokinesis. EMBO J 26, 4215-4227

74. Flower, T. G., Takahashi, Y., Hudait, A., Rose, K., Tjahjono, N., Pak, A. J., Yokom, A. L., Liang, X., Wang, H.-G., Bouamr, F., Voth, G. A., and Hurley, J. H. (2020) A helical assembly of human ESCRT-I scaffolds reverse-topology membrane scission. Nat. Struct. Mol. Biol. 27, 570-580

75. Nelson, S. L., Li, Y., Chen, Y., and Deshmukh, L. (2023) Avidity-based method for the efficient generation of monoubiquitinated recombinant proteins. J. Am. Chem. Soc. 145, 7748-7752

76. Sette, P., Jadwin, J. A., Dussupt, V., Bello, N. F., and Bouamr, F. (2010) The ESCRT-associated protein Alix recruits the ubiquitin ligase Nedd4-1 to facilitate HIV-1 release through the LYPXnL L domain motif. J. Virol. 84, 8181-8192

77. B. Korbei (2022) Ubiquitination of the ubiquitin-binding machinery: how early ESCRT components are controlled. Essays Biochem. 66, 169-177

78. Tedeschi, A., Almagro, J., Renshaw, M. J., Messal, H. A., Behrens, A., and Petronczki, M. (2020) Cep55 promotes cytokinesis of neural progenitors but is dispensable for most mammalian cell divisions. Nat. Commun. 11, 1746

79. Lie-Jensen, A., Ivanauskiene, K., Malerød, L., Jain, A., Tan, K. W., Laerdahl, J. K., Liestøl, K., Stenmark, H., and Haglund, K. (2019) Centralspindlin recruits ALIX to the midbody during cytokinetic abscission in drosophila via a mechanism analogous to virus budding. Curr. Biol. 29, 3538-3548.e3537

80. Sharma, D., and Rajarathnam, K. (2000) 13C NMR chemical shifts can predict disulfide bond formation. J. Biomol. NMR 18, 165-171,

81. Jensen, M. R., Zweckstetter, M., Huang, J. R., and Blackledge, M. (2014) Exploring free-energy landscapes of intrinsically disordered proteins at atomic resolution using NMR spectroscopy. Chem. Rev. 114, 6632-6660

82. Kakeshpour, T., Ramanujam, V., Barnes, C. A., Shen, Y., Ying, J., and Bax, A. (2021) A lowly populated, transient β-sheet structure in monomeric Aβ1-42 identified by multinuclear NMR of chemical denaturation. Biophys. Chem. 270, 106531